Towards the molecular design of hydrotreating catalysts prepared with metallo-organic precursors

Thibault Alphazan

THÈSE

en vue de l'obtention du grade de

Docteur de l'Université de Lyon, délivré par l'École Normale Supérieure de Lyon

Discipline : Chimie

Laboratoire : IFP Energies nouvelles

École Doctorale de Chimie de Lyon (ED206)

présentée et soutenue publiquement le 25 octobre 2013

par Monsieur Thibault ALPHAZAN

Vers la conception moléculaire de catalyseurs d'hydrotraitement préparés à partir de précurseurs métallo-organiques

---

Directeur de thèse : M. Pascal RAYBAUD

Après l'avis de : M. Xavier CARRIER

Mme. Françoise MAUGE

Devant la commission d'examen formée de :

M. Daniel BIANCHI, IRCE Lyon, Université Lyon 1, Membre

Mme. Audrey BONDUELLE, IFP Energies nouvelles, Membre

M. Xavier CARRIER, LRS, Université Pierre et Marie Curie, Paris VI, Rapporteur

M. Christophe COPERET, ETH Zürich, Membre

Mme. Christèle LEGENS, IFP Energies nouvelles, Membre

M. Francis LUCK, TOTAL SA, Membre

Mme. Françoise MAUGE, ENSICAEN, Rapporteur

M. Pascal RAYBAUD, IFP Energies nouvelles, Directeur

Remerciements

Dans un premier temps, je remercie Messieurs D.Guillaume et F.Bertoncini de m'avoir accueilli au sein de leur division et de leur département à IFPEn. Merci aussi aux membres du jury, d'avoir accepté de juger mon travail de thèse, dans les rapports, comme lors de la soutenance. Un grand merci aussi à mon directeur, Pascal, pour son encadrement, et son implication dans ce projet de thèse. Des remerciements particuliers aussi pour Christophe, pour sa disponibilité, pour le désir d'aller toujours plus loin qu'il me transmettait, pour son accueil à l'ETH Zürich et ses conseils. Enfin, pour terminer avec l'équipe encadrante, je remercie très chaleureusement Christèle et Audrey pour leur patience lors des réunions hebdomadaires, pour leur capacité à supporter mes « oui, mais… » et pour leur intransigeance, qui m'a permis de toujours chercher à faire mieux (« ne pas faire aussi bien que quelqu'un de moyen, mais mieux que l'excellence ! », n'est-ce pas Audrey ? :D).

Je remercie aussi tous les collègues du département Sulfure, pour leur bonne humeur, leur aide au labo, les repas toujours plus sympas et leur soutien. Des remerciements tous particuliers à Nathalie, ma référente dès mon arrivée. Merci pour ta bonne humeur sans faille, ta zènitude, et ta gentillesse ! Au passage, un grand merci à Sylvie, et Anne : vous m'avez accueilli pendant mes 8 premiers mois, et partager votre bureau a vraiment été une chouette aventure ! (votre ficus est toujours vivant :D). Merci aussi à Julie (désolé pour mes taquineries un peu franches), Véro, Georges, Marie-Paule, avec qui j'ai pu passer de bons moments au labo. Merci aussi à tous ceux que je n'ai pas cités, mais à qui je pense en rédigeant ces mots.

Des remerciements aussi à Dani, pour tout le boulot que j'ai pu lui donner en début de thèse (pièces de verrerie un peu étranges), pour sa gentillesse, et sa disponibilité.

Pour continuer, je souhaite remercier toutes les personnes avec qui j'ai pu travailler, et surtout échanger. De chaleureux remerciements à « papa » Philou, qui a su me « botter les miches » quand il fallait, mais aussi me conseiller, et surtout m'écouter. La thèse n'aurait surement pas été la même sans toi. Vraiment, merci, merci beaucoup !

Merci à tous les membres du laboratoire IR/RMN, et plus particulièrement à Mathieu et Laurent. Merci pour votre implication lors des discussions, et pour la rapidité avec laquelle j'ai pu avoir vos résultats d'analyse. C'est aussi grâce à vous, que nous thésards, nous pouvons aller plus vite et « plus haut ».

Pareillement, un grand merci à toutes les personnes du laboratoire de microscopie : ça a toujours été un plaisir de passer dans votre grand bureau et discuter de la beauté et de l'intérêt (:D) de la microscopie. Merci en particulier à Anne-Lyse, pour sa formation, et son accompagnement tout au long de la thèse. J'en profite aussi pour remercier Anne-Sophie et Maria, qui ont beaucoup contribuées à rendre la thèse plus « sexy » grâce aux belles images STEM-HAADF obtenues (et ouai, mieux que les Danois :p !)

Pour continuer, un grand merci aussi au département Catalyse Homogène (H.Olivier-Bourbigou). Merci plus particulièrement aux techniciens, qui m'ont prêté du matériel, m'ont permis d'utiliser l'IR, la RMN et la GC/MS. J'ai très souvent été chez vous sans faire parti de votre département, et merci vraiment pour votre accueil !

Enfin, parce qu'il est impossible de remercier tout le monde nominativement, merci à tous les membres de la division Physique et Analyses, dont les résultats d'analyses m'ont été d'une aide précieuse pour arriver au bout de ce manuscrit.

Merci aux secrétaires (en particulier Valérie), pour leur soutien, leur aide et leur disponibilité.

Je tenais aussi à remercier toutes les personnes avec qui j'ai pu participer à des activités extra-professionnelles grâce au CE. Merci à Eric et Serge, pour les 2 années à la section renforcement musculaire, merci à toute l'équipe du groupe salsa, en particulier Daniel, Patrice, Nico, Agnès, Camille et Hélo (:D), et un grand, grand merci à Jérôme de la section SAE, pour m'avoir redonné le goût de l'escalade, que j'avais oublié depuis 15 ans.

Un merci tout particulier aux thésards et à l'ADIFP. La « famille thésard » m'a vraiment permis d'avancer, dans les bons comme les mauvais moments. Impossible ici de citer tout le monde, mais un merci particulier à certains avec qui j'ai pu passer des moments hors du commun, à IFPEn, comme en dehors. Merci aux fistons : Bob (co-bureau de folie, avec nos sessions F.Cabrel déprimantes, ou sessions musiques « de film » planifiées le soir, à partir de 18h30-19h), Guillaume (et nos sessions discussions en OFF, sur le parking Dolomite, après un badgeage à l'arrachée) et Fabien. Merci à tous ceux de la pause café de 18h, qui n'ont pas encore été nommés : Ema (wua !), Maxime (achhh !), Alex, Alban, Gabi, et les autres. D'ailleurs, merci à la machine à café, et sa copine la machine à grignoter, pour nous avoir offert (ou pas vraiment…) de quoi prendre des forces pour les dernières heures de boulot. Merci encore à certains et certaines pour les grandes discussions, et le soutien mutuel, notamment Laurette la bouclette.

Au passage, je remercie tous les collègues thésards et post-doc de l'ETH, pour leur accueil chaleureux à chacun de mes passages, et les bonnes soirées passées ensembles. Merci en particulier à Maria C., Maxime, Giuseppe, Georges, Karol, Martin, Victor, et surtout David et Florent ! Merci aussi à Esther, pour toutes les formalités administratives.

Merci aussi à mes amis/es, sans qui je n'aurais jamais réussi à tenir le coup ces trois ans, que ce soit grâce au sport, aux sorties, ou à des moments plus tranquilles (Fred, Emilie, Antoine, Caro, Laura du thé, Laurelineuuu, …). Et surtout, des remerciements tous particuliers à ma Joan…

Last but not least, je remercie profondément ma famille qui m'a toujours soutenu, et surtout mes parents, à qui je dois tout…

Table des matières

Remerciements **5**

Table des matières **9**

Introduction générale **14**

Partie I : Etude bibliographique **19**

Table des matières (bibliographie) **21**

I.1. Généralités sur les procédés d'hydrotraitement **23**

I.2. Les catalyseurs d'hydrotraitement couramment utilisés **25**

I.3. La phase sulfure **26**

I.3.a. Généralités et modèle(s) issu(s) de la littérature 26

I.3.b. Morphologie 2D de la phase sulfure 28

I.3.c. Généralités sur l'activité des catalyseurs en HDS et HYD 31

I.4. Préparation conventionnelle et activation des catalyseurs sulfures **33**

I.4.a. Préparation des phases oxydes supportées non promues 33

I.4.b. Préparation des phases oxydes supportées promues 34

I.4.c. Activation des catalyseurs 35

I.5. Apport de la Chimie de Surface Contrôlée (CSC) : catalyseurs préparés par voie non conventionnelle **37**

I.5.a. Caractérisation et préparation des supports 39

I.5.b. Utilisation de la méthode CSC (ou COMS) pour la préparation de catalyseurs ayant des sites actifs bien définis : généralités. 46

I.5.c. Catalyseurs d'hydrotraitement non promus, préparés par voie CSC 49

I.5.d. Catalyseurs d'hydrotraitement promus, préparés par voie CSC 52

I.6. Conclusion et stratégie de la thèse **56**

I.7. Références bibliographiques **61**

Part II. Experimental **69**

Outline (Part II) **71**

II.1. Products and materials **73**

II.2. Characterisation **73**

II.2.a. Nuclear magnetic resonance (NMR) 73

II.2.b. X-ray photoelectron spectroscopy (XPS) 74

II.2.c. Fourier transform infrared spectroscopy (FT-IR) 76

II.2.d. Carbon monoxide adsorption at 77K, monitored by FT-IR (IR(CO)) 77
II.2.e. Transmission electron microscopy (TEM) and Scanning transmission electron microscopy (STEM) 77
II.2.f. Other analyses 77
II.3. Preparation of supported W alkoxide materials 79
II.3.a. Preparation of ASA-supported materials 79
II.3.b. Preparation of SiO_2-supported materials 85
II.3.c. Preparation of Al_2O_3-supported materials 85
II.3.d. Preparation of conventional dried and calcined materials 86
II.4. Preparation of non-promoted sulphide materials (bulk) 87
II.5. Synthesis of non-promoted sulphide catalysts supported on ASA 87
II.6. Preparation of nickel-promoted materials 89
II.6.a. Preparation of conventional dried and calcined oxide materials 89
II.6.b. Preparation of CSC materials, prior to sulphidation 89
II.7. Preparation of nickel-promoted sulphide catalysts 92
II.8. Catalytic test 92
II.9. References 93

Part III. Preparation of non-promoted ASA-supported W catalysts: impregnation of W(V) and W(VI) alkoxides 95
Outline (Part III) 97
Introduction 99
III.1. Characterisation of molecular complexes of W(V) and W(VI) 99
III.1.a. Tungsten pentaethoxide - $W(OEt)_5$ 101
III.1.b. Tungsten hexaethoxide - $W(OEt)_6$ 103
III.1.c. Tungsten oxotetraethoxide - $[W(=O)(OEt)_4]_2$ 106
III.2. Preparation and characterisation of W-supported materials, from W(V) or W(VI) molecular precursors. 110
III.2.a. Characterisation of CSC materials by Infrared spectroscopy (IR) 110
III.2.b. Characterisation of CSC materials by X-ray photoelectron spectroscopy (XPS) 111
III.3. Characterisation of sulphide catalysts prepared from W(V) or W(VI) precursors ... 112
III.5. Conclusion 116
III.6. References 116

Part IV. Effect of tungsten loading on the nature of surface species obtained after impregnation of $[W(OEt)_5]_2$ on ASA 119
Outline (part IV) 121
Introduction 123
IV.1. Characterisation of CSC materials by X-ray photoelectron spectroscopy (XPS) 123
IV.2. Characterisation by Infrared spectroscopy (IR) 124

IV.3. Characterisation by Solid-State NMR spectroscopy (NMR) 126
IV.4. Insights into the characterisation of surface species 130
IV.4.a. Deposition of ethanol onto $SiO_{2\text{-}700}$, $Al_2O_{3\text{-}450}$ and $ASA_{\text{-}300}$. 130
IV.4.b. Location of W-containing species 133
IV.4.c. Detailed structure of W-containing species 137
IV.5. Discussion. 141
IV.5.a. Surface species for coverage below *ca.* 0.8 (± 0.1) W/nm² 141
IV.5.b. Surface species for coverage above *ca.* 0.8 (± 0.1) W/nm² 149
IV.6. Conclusion 150
IV.7. References 150

Part V. Evolution of catalysts during sulphidation: from surface species to active WS_2 phases 153
Outline (part V) 155
Introduction 157
V.1. Influence of the tungsten loading on conventional and CSC catalysts 157
V.1.a. Insights into the spreading of oxide species on ASA: the case of conventional materials 158
V.1.b. Characterisation by X-ray photoelectron spectroscopy (XPS) 164
V.1.c. Characterisation by Temperature-programmed reduction (TPR) 167
V.1.d. Characterisation by Transmission electron microscopy (Bright field mode) 171
V.1.e. Characterisation by Scanning transmission electron microscopy (High angle annular dark field) 172
V.1.f. Characterisation by Carbon monoxide adsorption at low temperature (77K), monitored by IR spectroscopy - IR(CO) 175
V.1.g. Catalytic results and discussion 179
V.1.h. Conclusion on the influence of the tungsten loading on the genesis and activity of the active phase of WS_2/ASA catalysts 189
V.2. Influence of the sulphidation temperature on CSC and conventional catalysts 190
V.2.a. Characterisation by X-ray photoelectron spectroscopy (XPS) 191
V.2.b. Characterisation by Transmission electron microscopy (TEM Bright field mode) 196
V.2.c. Characterisation by Scanning transmission electron microscopy (high angle annular dark field) - STEM-HAADF 199
V.2.d. Characterisation by Carbon monoxide adsorption at low temperature (77K), monitored by IR spectroscopy - IR(CO) 201
V.2.e. Catalytic results and Discussion 203
V.2.f. Conclusion on the influence of the sulphidation temperature on the genesis and activity of the active phase of WS_2/ASA catalysts 210
V.3. References 211

Part VI. Synthesis of supported NiWS phases by the use of $[W(OEt)_5]_2$ and molecular precursors of nickel 215

Outline (Part VI) 217

Introduction 219

VI.1. Impregnation of Ni-precursors onto ASA-supported alkoxide tungsten species..... 221

VI.1.a. Characterisation of supported NiW species by IR spectroscopy 221

VI.1.b. Characterisation of NiWS sulphide phases by X-ray photoelectron spectroscopy (XPS) 226

VI.1.c. Characterisation of NiWS sulphide phases by Transmission electron microscopy (TEM) 229

VI.1.d. Characterisation of NiWS sulphide phases by STEM-HAADF 230

VI.1.e. Characterisation of NiWS sulphide phases by CO adsorption at low temperature (77K) monitored by IR spectroscopy - IR(CO) 233

VI.1.f. Influence of the Ni content on properties of NiWS phases: the case of $Ni(acac)_2/[W(OEt)_5]_2$/ASA sulphide samples 235

VI.2. Impregnation of Ni-precursors onto a WS_2 phase, prepared at 350°C 238

VI.2.a. Preparation and characterisation by IR spectroscopy 239

VI.2.b. Characterisation by X-ray photoelectron spectroscopy (XPS) 241

VI.2.c. Characterisation by Transmission electron microscopy (TEM) 242

VI.3. Impregnation of a Ni-precursor onto a WS_2 phase, prepared at 23°C: study of the influence of the Ni content 243

VI.3.a. Characterisation by X-ray photoelectron spectroscopy (XPS) 244

VI.3.b. Characterisation by Transmission electronic microscopy (TEM) 246

VI.4. Characterisation of spent catalysts 248

VI.5. Catalytic results 252

VI.5.a. Benchmarking catalytic activities with conventional samples and industrial references 252

VI.5.b. Influence of the nickel precursor 254

VI.5.c. Influence of the preparation method: deposition of $Ni(acac)_2$ onto supported tungsten species (non sulphided) or onto sulphide ones, prepared at 23°C or 350°C 257

VI.5.d. Influence of the nickel content 259

VI.6. Discussion 262

VI.6.a. Morphology and edge decoration of NiWS crystallites 262

VI.6.b. Optimal parameters for NiWS phases: the balance between the amount of active sites and their intrinsic HYD strength 272

VI.7. Conclusion 278

VI.8. References 279

Part VII. General conclusion and perspectives 283

VII.1. General conclusion 283

VII.2. Perspectives 294

VII.3. References 296

Appendices 297

Outline of appendices 299

Appendix A: Tentative de dépôt sur ASA_{-300} de $W(CO)_6$ et d'un mélange « $W(CO)_6$ / $W(CO)_5(thf)$ ». **..... 301**

Appendix B: Decomposition of ^1H MAS solid state NMR spectra with Dmfit software. **..... 305**

Appendix C: Bar graphs obtained from TEM analyses of different non-promoted and Ni promoted catalysts. **..... 309**

Appendix D: IR and NMR spectra of samples obtained after contacting ethanol with SiO_{2-700}, Al_2O_{3-450}, and ASA_{-300}. **..... 317**

Appendix E: Contributions W 4f des catalyseurs WS_2/ASA préparés par voie CSC ou conventionnelle (séchés ou calcinés), en fonction de la température de sulfuration **..... 319**

Appendix F: Contribution W 4f des catalyseurs WS_2/ASA préparés par voie CSC ou conventionnelle (séché ou calciné), en fonction de la température de sulfuration **..... 320**

Résumé **..... 321**

Introduction générale

Le pétrole brut est transformé en raffinerie par une suite de procédés de séparation, de conversion et de dépollution. Tous ces procédés permettent *in-fine* d'obtenir des produits directement valorisables (méthane, butane, huiles, bitumes), des produits rassemblés dans le pool essence ou le pool Diesel, ou des molécules utilisables en pétrochimie.

Actuellement, l'appauvrissement des réserves pétrolières conventionnelles mondiales amène les producteurs à fournir des bruts de plus en plus lourds, et généralement plus chargés en hétéroatomes indésirables. Les raffineurs sont donc confrontés à deux défis majeurs : l'amélioration des procédés de conversion des coupes lourdes que constituent les résidus atmosphériques, ainsi que la mise aux spécifications des carburants (diminution des teneurs en soufre dans les carburants en dessous de 10 ppm, notamment). L'hydrotraitement (HDT) des produits raffinés est par conséquent une étape clé pour éliminer de ces impuretés, grâce à l'action combinée de catalyseurs et d'hydrogène dans des conditions plus ou moins sévères de température et pression.

Schématiquement, le pétrole brut est distillé à pression atmosphérique pour donner des produits légers comme le gaz, les essences, des produits intermédiaires dits «distillats moyens» type gazole et kérosène et des produits plus lourds : les «résidus atmosphériques». La distillation de ces résidus à pression réduite permet d'obtenir les «distillats sous vide» (DSV) servant de base pour la production de carburants. Les composés non distillés forment une coupe appelée «résidus sous vide» (RSV), et serviront à la production de fiouls lourds et bitumes.

Actuellement, la répartition entre produits lourds, produits légers et intermédiaires après distillation des bruts n'est plus en phase avec la demande du marché. En effet, la demande en fuels lourds étant bien trop faible, les distillats sous vide doivent être transformés en composés plus légers pouvant servir de base à la production d'essence ou Diesel. Par ailleurs, l'importante diésélisation des parcs automobiles mondiaux contraignent les raffineurs à produire de plus en plus de distillats moyens afin de les raffiner *in-fine* en kérosène et gazole répondant aux spécifications demandées.

Les procédés catalytiques d'hydrotraitement, permettent de retirer les hétéro-éléments (soufre, azote, oxygènes...) indésirables, et mettent en œuvre des catalyseurs dont la phase

active est une phase sulfure mixte préparée à partir de tungstène (W) ou de molybdène (Mo), promue par du nickel (Ni) ou du cobalt (Co). Parmi ces catalyseurs, les phases mixtes NiWS sont reconnues pour être plus actives que les phases NiMoS et CoMoS en hydrogénation des aromatiques. Elles sont aussi actives que les phases NiMoS en hydrodéazotation, et plus performantes que les phases CoMoS.

Néanmoins, la sulfuration limitée du W par rapport au Mo conduit les industriels à préférer les catalyseurs à base de Mo. Ces catalyseurs (à base de W) sont conventionnellement préparés par imprégnation à sec à l'aide de précurseurs hétéro-polyanions. Or ces méthodes de préparation sont pour partie à l'origine des limites observées de la sulfuration du précurseur oxyde. L'enjeu de cette thèse réside donc dans la compréhension et l'amélioration de la sulfuration de catalyseurs à base de W. La thèse a donc pour objectif la rationalisation des différentes étapes de préparation de catalyseurs d'hydrotraitement de type NiWS depuis la préparation jusqu'au test catalytique par une approche moléculaire, ce qui permettra de proposer de nouvelles voies pour lever le verrou majeur lié à la mauvaise sulfuration du W. Au cœur de cette approche se situe l'utilisation d'une méthode de préparation originale, ayant recours à des composés moléculaires métallo-organiques bien-définis comme précurseurs de la phase sulfurée W, combinée à une analyse poussée par spectroscopie multiples (IR, RMN, XPS) et chimie computationnelle.

L'étude qui a été menée au cours de la thèse est détaillée dans ce manuscrit, qui est divisé en six grandes parties :

Dans la 1ère partie, nous présentons une étude bibliographique centrée sur les catalyseurs sulfures, et la caractérisation de leur phase active. Parmi les diverses tentatives d'amélioration des catalyseurs d'hydrotraitement (Ni)W déposés sur support oxyde, nous développons plus particulièrement le mode de préparation par une approche dite *moléculaire*, ou de *"chimie de surface contrôlée"* (CSC). [Ballard, 1973; Yermakov and Kuznetsov, 1972; Basset and Choplin, 1983, Copéret *et al.*, 2003; Wegener *et al.*, 2011] Nous exposons ensuite les objectifs et la méthodologie de la thèse.

La 2ème partie est consacrée à la description des modes de préparation de tous les matériaux catalytiques et présente également les techniques analytiques.

La 3ème partie traite de la préparation, de la caractérisation et d'une première évaluation des performances catalytiques (hydrogénation du toluène) de catalyseurs non-promus supportés sur silice-alumine amorphe (ASA) dits WS_2/ASA. Ces catalyseurs ont été préparés par imprégnation d'alcoxydes de tungstène où le métal est au degré d'oxydation (V) ou (VI), et leurs

performances catalytiques sont comparées à celles de catalyseurs préparés par voies conventionnelles, afin de déterminer le potentiel de la méthode de préparation dite de chimie de surface contrôlée.

La 4ème partie présente l'étude approfondie de matériaux, préparés par voie CSC à partir d'alcoxyde de tungstène(V) déposé sur ASA. Nous montrons en particulier l'influence de la quantité de tungstène déposée sur la nature des espèces de surface, et proposons un ensemble de mécanismes réactionnels pouvant être à l'origine des espèces de surface observées.

La 5ème partie détaille l'évolution des espèces alcoxydes de W supportés sur ASA *non promus* après sulfuration vers la phase active WS_2. Ce chapitre permet la comparaison des catalyseurs CSC avec des références conventionnelles, séchées ou calcinées. Nous détaillons l'ensemble des résultats de caractérisation et tentons de corréler ces résultats aux différences d'activités observées en hydrogénation du toluène.

La 6ème et dernière partie présente la préparation, la caractérisation et l'évaluation catalytique de catalyseurs *promus NiWS* supportés sur ASA. Nous exposons les diverses voies de préparation suivies, les résultats de caractérisation des phases promues NiWS, ainsi que leurs performances catalytiques, qui sont mises en regard des analyses effectuées sur nos catalyseurs.

Nous terminons ce manuscrit par une conclusion générale et les perspectives envisagées pour la suite de ces travaux.

L'étude bibliographique (partie I) est rédigée en Français. Les autres parties sont rédigées en Anglais.

Références bibliographiques

Ballard, D.G.H., *Advances in Catalysis* (1973), **23**, 263-275

Basset, J.M. and Choplin, A., *Journal of Molecular Catalysis* (1983), **21**, 1-3, 95-108

Copéret, C.; Chabanas, M.; Petroff Saint-Arroman, R.; Basset, J.M., *Angewandte Chemie International Edition* (2003), **42**, 2, 156-181

Wegener, S.L.; Marks, T.J.; Stair, P.C, *Accounts of Chemical Research* (2011), **45**, 2, 206, 214

Yermakov Y.I. and Kuznetsov B.N. *Kinetika i Kataliz* (1972) 13, 1355-1356.

Partie I : Etude bibliographique

Table des matières (bibliographie)

Table des matières.....21

I.1. Généralités sur les procédés d'hydrotraitement.....23

I.2. Les catalyseurs d'hydrotraitement couramment utilisés.....25

I.3. La phase sulfure.....26
I.3.a. Généralités et modèle(s) issu(s) de la littérature.....26
I.3.b. Morphologie 2D de la phase sulfure.....28
I.3.c. Généralités sur l'activité des catalyseurs en HDS et HYD.....31

I.4. Préparation conventionnelle et activation des catalyseurs sulfures.....33
I.4.a. Préparation des phases oxydes supportées non promues.....33
I.4.b. Préparation des phases oxydes supportées promues.....34
I.4.c. Activation des catalyseurs.....35

I.5. Apport de la Chimie de Surface Contrôlée (CSC) : catalyseurs préparés par voie non conventionnelle.....37
I.5.a. Caractérisation et préparation des supports.....39
I.5.b. Utilisation de la méthode CSC (ou COMS) pour la préparation de catalyseurs ayant des sites actifs bien définis : généralités.....46
I.5.c. Catalyseurs d'hydrotraitement non promus, préparés par voie CSC.....49
I.5.d. Catalyseurs d'hydrotraitement promus, préparés par voie CSC.....52

I.6. Conclusion et stratégie de la thèse.....56

I.7. Références bibliographiques.....61

I.1. Généralités sur les procédés d'hydrotraitement

Le raffinage des produits pétroliers est un ensemble de procédés catalytiques mis en œuvre pour séparer, transformer et purifier les coupes pétrolières brutes en produits valorisables comme carburants ou en molécules utilisables en pétrochimie.

La **Figure 1** illustre la complexité du schéma de raffinage. Le pétrole brut est tout d'abord distillé à pression atmosphérique pour permettre d'obtenir séparément des produits légers (gaz, essences), des produits intermédiaires (distillats moyens) type gazole et kérosène et des produits plus lourds (résidus Atmosphériques). Une seconde distillation réalisée sous pression réduite permet d'obtenir une gamme de produits dits « distillats sous vide » (DSV), dont les points de coupe sont trop élevés pour être utilisés directement comme base carburants mais qui seront « craqués » dans les procédés de conversion pour être valorisés. Les composés non distillés dits « résidus sous vide » (RSV) servent notamment à la production de bitumes.

Deux procédés industriels permettent de transformer les DSV : le craquage catalytique, appelé FCC pour « Fluid Catalytic Cracking », qui permet d'obtenir majoritairement des essences de bonne qualité, et l'hydrocraquage qui permet de produire essentiellement des gazoles et kérosènes de bonne qualité. [Kaufmann *et al.*, 2000; Mochida and Choi, 2004; Raybaud and Toulhoat, 2013, Ed. Technip, Paris]. Les contraintes imposées par le marché (demande faible en produits lourds) et les spécifications environnementales (teneurs en S inférieures à 10 ppm dans les carburants) obligent donc les raffineries à améliorer les procédés d'hydrocraquage, de conversion des résidus lourds, et les procédés d'hydrotraitement (HDT), procédés clés destinés à se débarrasser des hétéroatomes indésirables. Tous ces procédés sont opérés grâce à l'action combinée de catalyseurs et d'hydrogène dans des conditions plus ou moins sévères (température, pression).

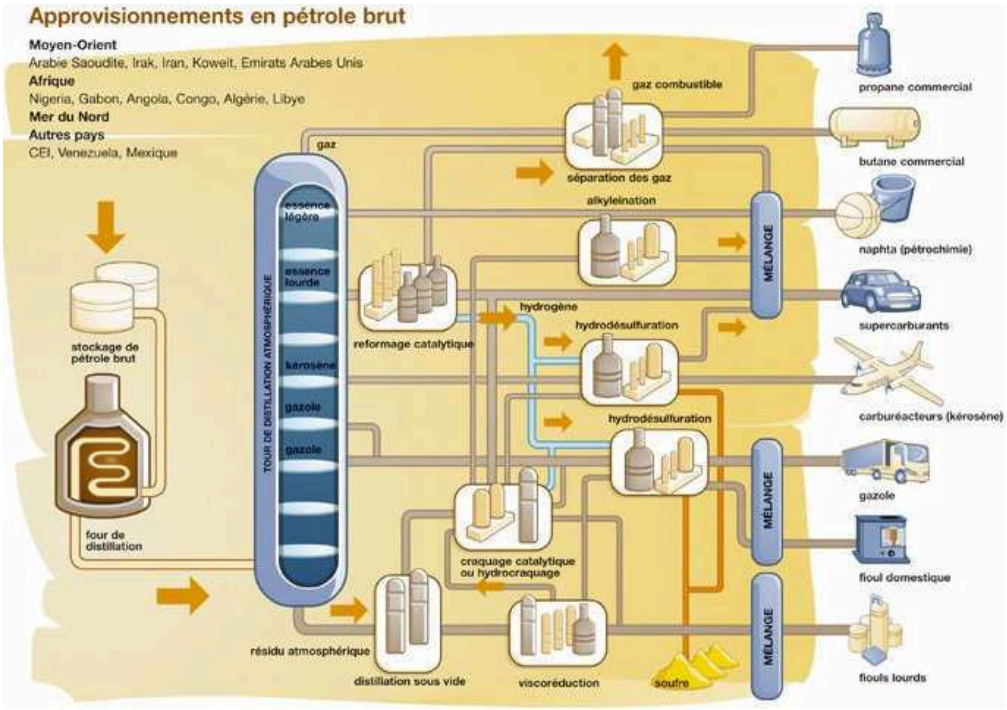

Figure 1 : schéma simplifié d'une raffinerie [energie.sia-partners.com]

La pollution atmosphérique engendrée par les rejets de SO_2, source des pluies acides, et l'empoisonnement des catalyseurs des pots catalytiques par le soufre issu de la combustion des carburants imposent notamment des réductions drastiques des taux de ce composé dans les carburants. Comme le soufre est l'hétéroatome le plus abondant dans les pétroles bruts [Schulz *et al.*, 1999] l'hydrodésulfuration (HDS) poussée devient une réaction majeure des raffineries, afin de respecter les normes européennes toujours plus drastiques : moins de 10 ppm de S dans les carburants depuis 2009. [Directive européenne 2009/30/CE]

L'azote est, quant à lui, présent dans des proportions 10 à 100 fois moins importantes que le soufre. L'élimination de ce composé (hydrodéazotation HDN) est absolument essentielle pour éviter l'empoisonnement des catalyseurs acides utilisés dans les procédés de conversion et notamment en hydrocraquage. Par ailleurs, il est probable que les futures normes européennes concernant les produits de combustion des composés azotés (NO_x) deviennent de plus en plus sévères, et incitent les raffineurs à diminuer les teneurs en azote dans les produits de raffinage (Norme Euro 6).

Parmi les procédés d'hydrotraitement, on peut aussi citer l'hydrodéoxygénation (HDO) et l'hydrodémétallation (HDM). L'HDO permet d'éliminer l'oxygène, notamment présent dans les coupes issues de la transformation de la biomasse. L'HDM des coupes de type résidus sous

vide permet de retirer les métaux tels que le nickel ou le vanadium, qui constituent des poisons pour les catalyseurs d'hydrotraitement en général.

Les procédés d'hydrotraitement comprennent aussi des procédés d'hydrogénation (HYD). Ils permettent d'éviter la formation de gommes (hydrogénation des oléfines), d'améliorer les propriétés des gazoles (amélioration de l'indice de cétane) ou d'hydrogéner des coupes lourdes (hydrogénation des aromatiques) avant hydrocraquage. La réaction d'hydrogénation des aromatiques est thermodynamiquement favorisée à haute pression d'hydrogène et faibles températures, mais cinétiquement favorisée à hautes températures. Pour réaliser ces réactions, des conditions opératoires présentant entre 30 et 150 bar d'H_2 et une température comprise entre 340°C et 410°C représentent un bon compromis.[Raybaud and Toulhoat, 2013, Ed. Technip, Paris]

I.2. Les catalyseurs d'hydrotraitement couramment utilisés

Les catalyseurs d'hydrotraitement couramment utilisés sont essentiellement des phases sulfures mixtes (car contenant au moins deux éléments) constituées de métaux du groupe VIB comme le molybdène et le tungstène, promus par des métaux du groupe VIII comme le nickel ou le cobalt. Les précurseurs de ces métaux sont déposés sur des supports oxydes présentant une surface spécifique importante comme la silice, l'alumine, ou les silice-alumines. Ils sont ensuite sulfurés pour générer la phase active.

Les catalyseurs d'hydrotraitement sont plus généralement préparés à partir de précurseurs de molybdène, notamment à cause de leur coût comparativement aux précurseurs à base de tungstène. A ce propos, la **Figure 2** illustre la diminution globale du prix du molybdène ces huit dernières années, *a contrario* de celui du tungstène. Néanmoins, sur des supports de type alumine et sur des charges très soufrées, c'est avant tout la meilleure sulfurabilité et la meilleure réactivité du molybdène [Raybaud and Toulhoat, 2013, Ed. Technip, Paris] qui le rend plus avantageux d'un point de vue industriel.

Figure 2: Cours du ferrotungstène (orange) et de l'oxyde de molybdène (gris) entre Novembre 2005 et Avril 2013. [infomine.com]

Cela peut expliquer pourquoi les phases NiWS supportées, bien que performantes en hydrogénation des aromatiques [Stanislaus and Cooper, 1994; Hensen *et al.*, 2007] et en HDN [Vazquez *et al.*, 1999], sont peu utilisées dans le domaine du raffinage. Par contre, dans l'enchainement de catalyseurs du procédé d'hydrocraquage et notamment dans un schéma « maxi sélectivité en gazole », les phases NiWS déposées sur silice-alumine sont très utilisées.

I.3. La phase sulfure

I.3.a. Généralités et modèle(s) issu(s) de la littérature

La phase sulfure présente une structure lamellaire, formée de feuillets de MS_2 (M = W, Mo). La morphologie 2D de ces feuillets, leur empilement moyen (≈ 2 à 4) et leur taille moyenne (≈ 3 à 6 nm) dépendent des conditions de sulfuration.

La sulfuration induit une modification profonde de la phase oxyde (**Figure 3**) : les ligands oxygène sont remplacés par des atomes de soufre et le métal passe d'un degré d'oxydation +VI à +IV. Cette transformation provoque une réorganisation des espèces de surface, ainsi qu'un changement de l'environnement cristallographique du métal qui passe d'une structure octaédrique à une structure trigonale prismatique.

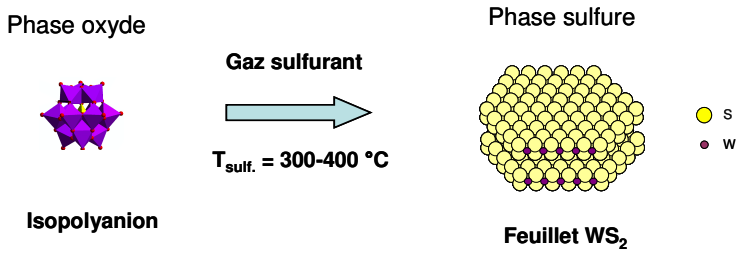

Figure 3: Schéma de principe de la transformation d'une phase oxyde en phase sulfure

Le procédé de sulfuration en phase gazeuse nécessite l'utilisation d'un composé soufré, très souvent du sulfure d'hydrogène (H_2S), pur ou dilué dans un autre gaz (N_2, H_2). En phase liquide, l'H_2S utilisé pour la sulfuration des matériaux oxyde peut aussi être produit *in-situ* par décomposition de composés soufrés (éventuellement présents dans les essences et Diesels), en présence de dihydrogène. Par ailleurs, la gamme de températures utilisées industriellement se situe entre 300°C et 400°C.

Parmi les différents modèles de phase active le modèle historique de Kasztelan *et al.* [Kasztelan *et al.*,1984] décrit des feuillets MoS_2 ayant une morphologie hexagonale ou rhomboédrique pour laquelle la présence de promoteur provoquerait une modification de structure. Les résultats obtenus par les auteurs ne permettent pas de conclure sur le rôle exact du promoteur, mais montrent que les différentes réactions d'hydrotraitement (HYD et HDS) sont limitées par le nombre de sites métalliques de bord, ou de coins. Ce modèle est en accord avec celui proposé par Topsøe *et al.* [Topsøe *et al.,* 1981, Topsøe and Brenner, 1983; Topsøe and Clausen, 1986] sur la base d'analyses de type spectroscopie Mössbauer sur des catalyseurs $CoMo/Al_2O_3$. Le modèle de Topsøe (catalyseur $CoMo/Al_2O_3$) illustré par la **Figure 4**, propose la présence de cristallites MoS_2 sur lesquelles le promoteur (cobalt) vient en décoration sur les bords des feuillets, ou leurs coins. La phase active, reconnue comme permettant les réactions d'HDT mentionnées précédemment, est la phase « Co-Mo-S » dite « phase mixte ». [Kasztelan *et al.*, 1983; van Veen *et al.*, 1992; Gandubert *et al.*, 2008] A ce propos, la terminologie « site mixte » désigne la juxtaposition, sur les bords des feuillets, d'un atome de molybdène (ou de tungstène) avec un atome de promoteur. Cependant, le catalyseur réel n'est pas idéal et tous les atomes introduits ne sont pas utilisés pour générer une phase mixte. Certains atomes de promoteur peuvent former des phases sulfures inactives, comme Co_9S_8 ou encore Ni_xS_y (NiS ou Ni_3S_2), et certains atomes de promoteurs peuvent migrer à l'intérieur du support pour former des structures de type spinelle $CoAl_2O_4$ ou encore, certaines espèces oxydes de Mo ou de W peuvent être réfractaires à la sulfuration et persister sous la forme de polyoxomolybdates ou

polyoxotungstates. La **Figure 4** illustre l'ensemble des espèces chimiques à la surface d'un catalyseur de type CoMo. Ce modèle, bien qu'étant issu de nombreux travaux réalisés sur les catalyseurs CoMo/Al_2O_3, est vraisemblablement transposable aux catalyseurs NiMo et (Co)NiW déposés sur silice, silice-alumine ou alumine.

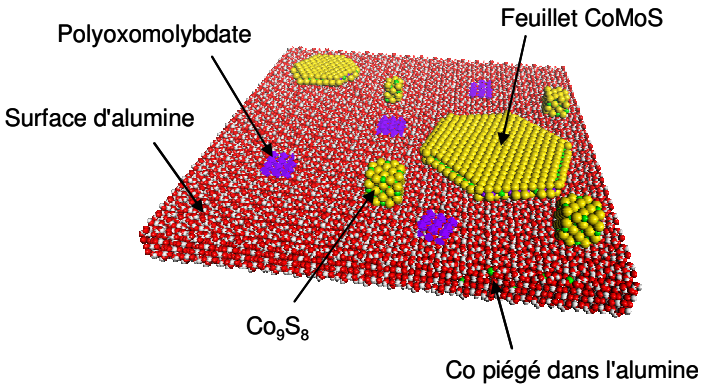

Figure 4 : Représentation schématique des différentes espèces de surface d'un catalyseur CoMo/Al_2O_3. En violet, Mo; en vert, Co, en jaune, S. [Raybaud and Toulhoat, 2013, Ed. Technip, Paris]

I.3.b. Morphologie 2D de la phase sulfure

En 2000, Helveg *et al.* [Helveg *et al.* 2000] ont publié les premiers clichés de microscopie à effet tunnel (scanning tunneling microscopy STM) montrant que des feuillets MoS_2 de catalyseurs non promus, déposés sur une surface d'or dont la phase cristallographique exposée est le plan (111), présentaient une structure triangulaire.

Par la suite, Schweiger *et al.* [Schweiger *et al.*, 2002] ont utilisé la théorie de la fonctionnelle de la densité (DFT) pour prédire la morphologie des feuillets MoS_2 non promus en fonction de la pression partielle en H_2S du système. Ils ont montré que pour une atmosphère très sulfurante, *i.e.* pour une pression partielle en H_2S ($p(H_2S)$) élevée, les feuillets MoS_2 adoptaient une géométrie triangulaire. Au contraire, dans des conditions proches de celles utilisées dans les procédés d'HDS ($p(H_2S)/p(H_2)$ compris entre 0,0025 et 0,15), la morphologie des feuillets devenait hexagonale. Leurs calculs théoriques ont ensuite été confirmés par les analyses STM effectuées par Lauritsen *et al.* en 2004. [Lauritsen *et al.,* 2004] La **Figure 5** présente deux modèles géométriques de feuillets MoS_2 : un modèle hexagonal et un triangulaire. La morphologie des cristallites dépend de la stabilité des bords M (M-edge, plan

cristallin (1 ;0 ;-1) [Moses *et al.*, 2007] ou S (S-edge, plan cristallin (-1 ;0 ;1) [Moses *et al.*, 2007]) l'un par rapport à l'autre.

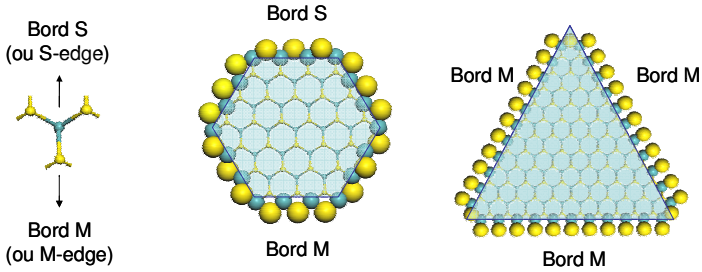

Figure 5 : Représentation schématique d'un feuillet MS_2 hexagonal ou triangulaire. Bleu : W ou Mo; jaune : S

Portela *et al.* [Portela *et al.*, 1995] on étudié l'influence de la pression partielle en H_2S sur la taille des cristallites MoS_2 de catalyseurs non promus MoS_2/Al_2O_3. Les auteurs ont montré que la pression partielle en H_2S modifie la taille des cristallites : l'étude du rapport atomique moyen Mo/Al obtenu par spectroscopie de type X-ray photoelectron spectroscopy (XPS) ainsi que des analyses d'adsorption d'oxyde d'azote suivie par spectroscopie infrarouge (IR) ont révélé qu'une sulfuration sous H_2S pur provoquait une augmentation de la taille des cristallites, par rapport à une sulfuration sous un mélange 15 $\%_{vol.}$ H_2S/H_2. Ces conclusions sont identiques à celles de Baubet [Baubet, PhD thesis, Lyon, 2013] qui a étudié par microscopie à transmission électronique (MET) des catalyseurs MoS_2/Al_2O_3, sulfurés sous H_2S pur, ou sous un mélange 15 $\%_{mol.}$ H_2S/H_2.

L'étude de catalyseurs promus CoMoS/Au(111) par STM (équipe de Lauritsen *et al.* [Lauritsen *et al.,* 2001] a permis d'observer que la présence du promoteur favorise une morphologie de feuillet plus hexagonale que triangulaire. Ces résultats expérimentaux ont été confirmés par les calculs DFT de Schweiger *et al.* en 2002. [Schweiger *et al.*, 2002] Ces derniers ont aussi montré que la variation de $p(H_2S)/p(H_2)$ aurait peu d'influence sur la stabilité des faces latérales Mo-edge et S-edge : la morphologie des cristallites MoS_2 d'un catalyseur promu resterait proche d'une structure hexagonale, quelle que soient les conditions sulfo-réductrices.

Des morphologies de feuillets sulfures hexagonales, triangulaires ou triangulaires tronquées (hexagonales déformées) ont donc été à la fois décrites par calculs DFT, et observées par STM. Parallèlement aux études de catalyseurs par STM, la morphologie 2D des cristallites MS_2 (M = Mo, W) a aussi été observée par MET. Cette technique, utilisée en mode transmission en champ clair (MET-BF pour bright field) permet de connaitre la longueur moyenne et l'empilement moyen des feuillets. Cependant, elle ne permet de visualiser que les cristallites positionnées parallèlement par rapport au faisceau d'électrons incidents. Le mode de détection en champ sombre (ou STEM-HAADF pour scanning transmission electron microscopy in high angle annular dark field) permet quant à lui d'observer les feuillets positionnés perpendiculairement à la direction des électrons incidents, mais aussi d'observer des feuillets « à plat », ce qui permet donc d'évaluer la morphologie 2D des feuillets, s'ils sont peu empilés.

Carlsson *et al.* [Carlsson *et al.*, 2006] ont réalisé des clichés STEM-HAADF de catalyseurs promus et non-promus (WS_2, MoS_2, NiWS et Co(Ni)MoS), déposés sur graphite (C). Ils retrouvent les variations de morphologies dues à l'influence du promoteur, précédemment décrites grâce aux travaux STM et aux calculs DFT. La **Figure 6** montre que l'ajout du promoteur, sur un catalyseur MoS_2/C dont les cristallites sont triangulaires ou triangulaires tronquées, entraine un changement morphologique vers une structure hexagonale déformée. Cependant, les variations de morphologie observées dans le cas du W sembleraient moins marquées : l'ajout du promoteur ne provoquerait qu'une troncature plus importante des angles des triangles WS_2 mais n'entrainerait pas un passage vers une structure proche d'un hexagone. Toutefois, l'analyse STEM-HAADF des systèmes NiWS est à ce jour moins poussée que celle des systèmes NiMoS dans la littérature. En parallèle, la mise en évidence de la localisation des atomes de promoteur sur les bords des feuillets sulfures par STEM-HAADF reste un défi. Les récents travaux récents travaux de microscopie STEM-HAADF de Deepak *et al.* [Deepak *et al.*, 2011], réalisés sur des nanofils de CoMoS et CoWS déposés sur alumine, ont cependant montré qu'il semblait possible de révéler la position des atomes de (W)Mo et de Co en bordure des nanofils sulfurés (et par conséquent, d'observer l'existence des fameux *sites mixtes*).

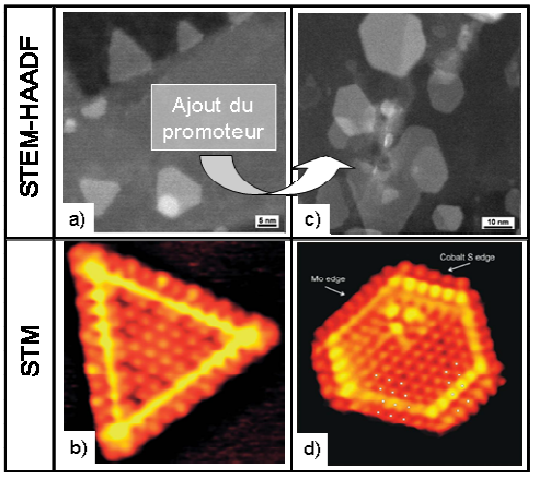

Figure 6 : Clichés STEM-HAADF [Carlsson *et al.*, 2006] et STM [Lauritsen and Besenbacher, 2006] de catalyseurs déposés sur graphite; a-b) MoS_2, c) NiMoS, d) CoMoS.

Pour résumer, ces travaux révèlent que la morphologie des feuillets dépend de la présence du promoteur, de la température de sulfuration ainsi que de la pression partielle en H_2S. Cependant, il convient de mettre en avant que la nature des supports utilisés pour les travaux expérimentaux de STM et STEM-HAADF relativise les résultats obtenus. En effet, les études ont été majoritairement effectuées sur des catalyseurs supportés sur des surfaces d'or ou de graphite, reconnues pour leurs plus faibles interactions « support - phase métallique ». L'étude de la morphologie 2D des feuillets sulfures présents sur des catalyseurs supportés sur support oxyde (silice, silice-alumine ou alumine) représente donc un réel intérêt à la vue du fait que ces matériaux sont communément employés dans l'industrie, et développent de plus fortes interactions avec les phases oxydes.

I.3.c. Généralités sur l'activité des catalyseurs en HDS et HYD

Les performances catalytiques des catalyseurs non promus, en particulier leurs activités (*i.e.* leur capacité à convertir des réactifs ciblés) sont faibles et l'ajout d'un promoteur permet d'améliorer d'un facteur *ca.* 10 leur activité en HDS et HYD. Cela traduit l'effet de synergie entre le promoteur (cobalt ou nickel) et la phase MoS_2 ou WS_2. Les travaux expérimentaux de Pecoraro et Chianelli [Pecoraro and Chianelli, 1981] couplés aux calculs de Toulhoat et Raybaud [Toulhoat and Raybaud, 1999] ont permis de définir une courbe en volcan (voir **Figure 7**) qui montre que l'activité d'un catalyseur dépend de l'énergie de liaison « métal – soufre » E_{M-S}, et qu'il existe un optimum d'énergie à environ 130 $kJ.mol^{-1}$. L'ajout du promoteur permet de

diminuer l'énergie de la liaison «métal - soufre» pour les catalyseurs NiMoS, d'environ 25 kJ.mol^{-1} par rapport à l'énergie plus élevée d'un catalyseur MoS_2. De même, l'ajout de Co permet de diminuer d'environ 30 kJ.mol^{-1} cette même énergie pour les catalyseurs CoMoS. Cependant, la plupart des travaux de la littérature montre que l'activité HDS des CoWS est très faible par rapport aux CoMoS, alors que leur énergie E_{M-S} diffère de moins de 5 kJ.mol^{-1}. Ce faible effet du promoteur dans le cas du tungstène pourrait provenir des difficultés rencontrées pour former une phase mixte «Co-W-S» lors de la sulfuration. Un effet de synergie a été en revanche trouvé dans les catalyseurs W promus au Ni (NiWS). Dans ce cas, l'énergie E_{M-S} pour un catalyseur NiWS est très proche de celle d'une phase NiMoS, située au sommet de cette courbe en volcan.

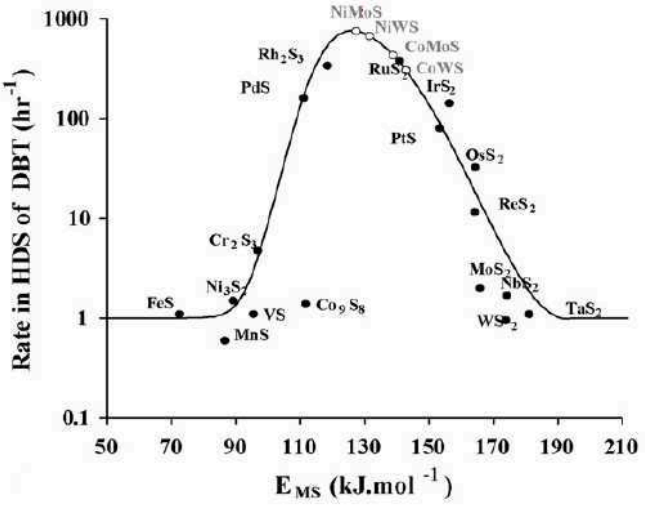

Figure 7 : Activité catalytique de différentes phases sulfures en HDS du dibenzothiophène, en fonction de l'énergie de liaison «métal-soufre» E_{M-S} [Pecoraro and Chianelli, 1981; Toulhoat and Raybaud, 1999]

L'activité des phases sulfures est liée aux atomes de bord M-edge et S-edge, encore appelés sites de bords (**Figure 5**). La quantité de ces sites actifs varie avec la morphologie 2D des feuillets, qui est dictée par la stabilité de chacun des bords. Que ce soit pour des réactions d'HDS, ou d'HYD, différents sites actifs comme différentes espèces interviendraient dans le processus catalytique. Selon l'étude de Moses *et al.* [Moses *et al.*, 2007], réalisée par calculs DFT sur des phases MoS_2, les réactions d'HYD, participant au mécanisme réactionnel de l'HDS du thiophène, seraient préférentiellement localisées sur les bords M-edge des feuillets. Dans le cas de phases CoMoS, une étude comparative [Gandubert *et al.*, 2008] entre expérience (catalyseurs $CoMo/Al_2O_3$) et calculs par DFT, révèlerait que pour une réaction d'HYD du

toluène, les sites actifs seraient principalement situés sur les bords M-edge. Par ailleurs, aucune étude n'a démontré que les sites de bords S-edge étaient totalement inactifs en HYD : leur influence, même moindre, peut donc être envisagée pour interpréter des résultats catalytiques. Les deux études précédentes mettent aussi en avant l'implication de différents sites : les CUS pour «coordinatively unsaturated sites», [Siegel, 1973; Gandubert *et al.*, 2008] ou les Brim. [Topsøe *et al.*, 2005; Moses *et al.*, 2007] Les CUS représentent des sites de bord avec une lacune en soufre, et sont supposés être impliqués dans l'adsorption des molécules soufrées, et dans la rupture des liaisons S-C (HDS). Les sites Brim, au contraire, représentent des sites proches du bord, localisés sur la partie supérieure des feuillets sulfures, et ne présentent pas de lacune en soufre. De plus, la présence d'espèces de type M-SH, encore appelée sulfhydryls, est aussi invoquée. Leur domaine de stabilité sur les bords des feuillets est, par exemple, discuté dans les travaux théoriques (DFT) de Prodhomme *et al.* [Prodhomme *et al.*, 2011] dans le cas des catalyseurs MoS_2. L'implication des espèces sulfhydryls, et des sites métalliques de bords (sans distinction M-edge ou S-edge) dans le processus d'hydrogénation est résumée dans les travaux de Guernalec *et al.* [Guernalec *et al.*, 2006], et leur modèle microcinétique de l'hydrogénation du toluène. Dans ce modèle, l'une des étapes comprend l'adsorption du cycle aromatique (toluène) sur un site métallique. Cette adsorption, dans le cas d'un site mixte CoMoS, seraient plus stable sur un atome de molybdène, d'après Gandubert *et al.* [Gandubert *et al.*, 2008]

I.4. Préparation conventionnelle et activation des catalyseurs sulfures

I.4.a. Préparation des phases oxydes supportées non promues

Les matériaux conventionnels à base de Mo et W sont obtenus par imprégnation à sec de précurseurs, comme l'heptamolybdate d'ammonium hydraté $(NH_4)_6Mo_7O_{24}$, xH_2O ou le métatungstate d'ammonium hydraté $(NH_4)_6H_2W_{12}O_{40}$, xH_2O, où les métaux (Mo ou W) sont rassemblés sous forme de clusters. En fonction des conditions de préparation (taux de chargement en métal, pH de la solution d'imprégnation), différentes espèces peuvent être formées à la surface des catalyseurs. Pour des matériaux séchés, préparés par dépôt de métatungstate d'ammonium sur alumine, l'espèce tungstate WO_4^{2-} est la seule mise en évidence tandis qu'après calcination, des phases oxyde WO_3 et polytungstate ont été révélées par spectroscopies XPS, Raman et IR [Ouafi *et al.*, 1988] Des espèces similaires sont recensées à la surface de catalyseurs préparés à partir de molybdène. [Kasztelan *et al.*, 1983]

I.4.b. Préparation des phases oxydes supportées promues

La préparation des catalyseurs promus peut être réalisée par imprégnations successives de la phase métallique ou du promoteur, par co-imprégnation des précurseurs, ou bien par imprégnation du promoteur sur une phase déjà sulfurée. Les précurseurs conventionnels les plus utilisés sont les dérivées nitrates, $Ni(NO_3)_2$, xH_2O ou $Co(NO_3)_2$, xH_2O. Il est aussi possible de déposer un hétéro-polycomposé réunissant le tungstène ou le molybdène, et le promoteur, au sein d'une même structure comme $Ni_4SiW_{11}O_{39}$. [Ben Tayeb, PhD thesis, Lille, 2009] L'étude du système promu NiW/Al_2O_3 par Reinhoudt *et al.* [Reinhoudt *et al.*, 2000] a permis de montrer, après calcination, la présence de nickel sous forme d'oxyde mixte plus ou moins fortement lié au support, ou de nickel sous forme de nickel-aluminate $NiAl_2O_4$. Le tungstène est quant à lui présent sous forme d'oxyde WO_3 et d'oxyde mixte avec le nickel Ni(WO). Une autre étude montre par ailleurs la présence d'oxyde de nickel NiO en faible quantité. [Hensen *et al.*, 2007]

De plus, les différents supports oxydes (silice, silice-alumine, alumine) utilisés pour la préparation de catalyseurs d'hydrotraitement n'ont pas la même influence sur les espèces oxydes de surface. La silice, par exemple, n'est pas couramment utilisée comme support de catalyseurs d'hydrotraitement. En effet, ce support présente une acidité quasiment nulle, et il est admis qu'il ne développe pas une très forte affinité avec les métaux, ce qui conduit généralement à des catalyseurs présentant une phase métallique peu dispersée. [Kim *et al.*, 1996] La silice-alumine et l'alumine sont plus communément utilisées, notamment de part leur acidité modérée ou forte, et de part la bonne dispersion du tungstène en surface. Cette meilleure répartition du tungstène sur la surface, comparé à un support silicique, a été associée à l'affinité du tungstène pour les parties aluminiques. [Vissenberg *et al.*, 2000; van der Meer *et al.*, 2004] Par ailleurs, l'étude de catalyseurs préparés sur silice-alumine a mis en évidence la présence d'espèces de surface similaire à celles observées sur alumine. [Dugulan *et al.*, 2010] Enfin, il convient de mentionner l'éventuelle « dissolution » du support, en présence d'espèces ioniques en solution, le cas le plus connu étant la dissolution partielle de l'alumine au contact d'une solution d'heptamolybdate d'ammonium, mis en évidence par Carrier *et al.* [Carrier *et al.*, 1997]

I.4.c. Activation des catalyseurs

L'activation des catalyseurs est réalisée lors de la sulfuration de la phase oxyde en phase sulfure, précédemment décrite partie I.3.a., durant laquelle le métal est réduit d'un degré d'oxydation +VI à un degré d'oxydation +IV, parallèlement à une réorganisation des espèces de surface (agglomération des atomes de tungstène pour former les feuillets WS_2).

Il est reconnu que pour des catalyseurs supportés sur alumine, le tungstène est plus difficilement sulfurable que le molybdène [Breysse *et al.* 1988]. Ce phénomène a été associé à l'énergie de liaison W-O-Al relativement élevée [Scheffer *et al.*, 1990] ainsi qu'à une liaison W-O plus difficile à rompre qu'une liaison Mo-O. [van der Vlies *et al.*, 2002a; van der Vlies et *al.*, 2002b] Dans le cas de catalyseurs à base de tungstène, préparés sur silice, Kim *et al.* [Kim *et al.*, 1996] décrivent la formation de feuillets sulfures plus empilés et moins bien dispersés que sur alumine. Dans le cas de matériaux préparés sur silice-alumine, [Hensen *et al.*, 2007] les phases sulfures obtenues sont similaires à celles obtenues sur alumine, en termes de longueur de feuillet, et d'activité catalytique en HDS. Les travaux réalisés à IFPEn [Raybaud and Toulhoat, 2013, Ed. Technip, Paris] sur des catalyseurs promus NiW supportés sur silice, silice-alumine (30 $\%_{pds.}$ SiO_2) et alumine et présentant 4,3 W/nm² et Ni/W = 0.4 at/at, ont permis de caractériser l'influence du support sur : la dispersion de la phase WS_2 à la surface du support (vue par XPS), la sulfurabilité du W, la formation de phase mixte «NiWS», la longueur moyenne et l'empilement moyen des feuillets. Ces résultats sont illustrés dans le **Tableau 1**. Comme observé auparavant par Kim *et al.*, [1996] plus un support est silicique, moins bonne est la répartition de la phase sulfure (vue par XPS), pour laquelle les feuillets sont plus longs et plus empilés. Cependant, la diminution de la quantité d'aluminium dans le support offre le bénéfice d'améliorer le taux de sulfuration du W (quantité de phase WS_2 observée par XPS supérieure) et d'accroitre la quantité de nickel engagée dans une phase mixte «NiWS».

Tableau 1 : Récapitulatifs des résultats d'analyses XPS et MET obtenus pour des catalyseurs NiWS/ASA préparés sur silice, silice-alumine (30 $\%_{pds.}$ SiO_2) *et al*umine.

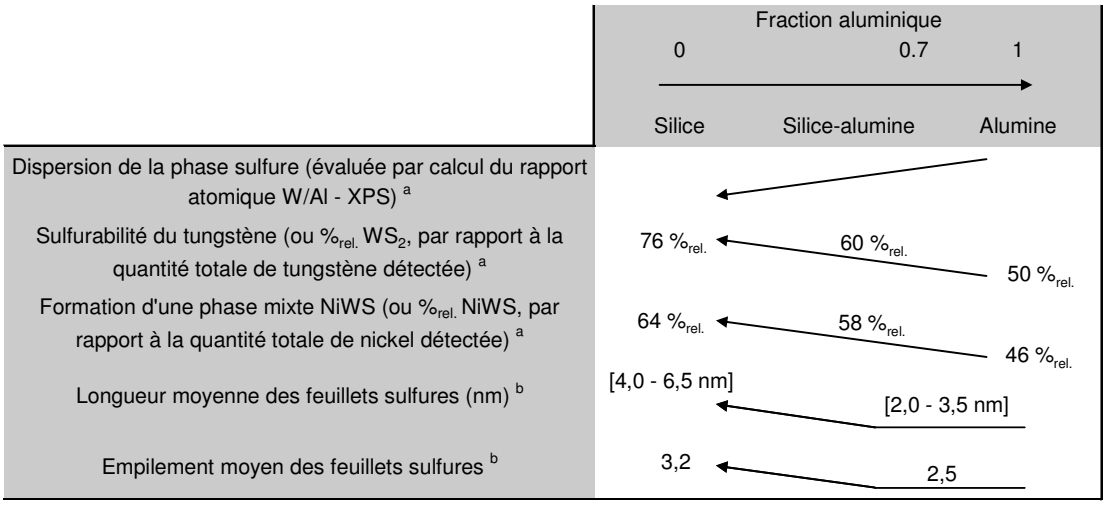

[a] obtenu par analyse XPS
[b] obtenu par microscopie électronique à transmission

L'étape de sulfuration, qui permet finalement de former la phase active des catalyseurs d'hydrotraitement, ne permet pas de convertir 100 % de la phase oxyde en phase sulfure. La spectroscopie EXAFS pour « extended X-ray absorption fine structure » [Hensen *et al.*, 2007] ainsi que la préparation de références adéquates et leur analyse par spectroscopie XPS, ont permis d'identifier trois différentes espèces chimiques présentes sur les catalyseurs sulfures, préparés à base de W : une espèce $W^{(IV)}$, attribuée à une phase sulfure WS_2, une phase réfractaire $W^{(VI)}$ attribuée à l'oxyde de départ, ainsi qu'une phase intermédiaire $W^{(V)}$. Le débat concernant l'attribution de cette dernière phase à des espèces de type WS_3 [Payen *et al.*, 1988; Sun *et al.*, 2001; Hensen *et al.*, 2007] ou oxysulfures type WO_xS_y [Payen *et al.*, 1988; Sun *et al.*, 2001; van der Vlies *et al.*, 2002a; Hensen *et al.*, 2007] est toujours ouvert.

A l'heure actuelle, il n'existe donc pas de solution satisfaisante pour sulfurer de manière optimale des catalyseurs conventionnels à base de W : la préparation de catalyseurs à partir de précurseurs conventionnels ne permet pas de sulfurer le tungstène à plus de 60$\%_{rel.}$ WS_2 sur silice-alumine (30 $\%_{pds.}$ SiO_2). Parmi les voies d'amélioration de la sulfuration du tungstène, on peut citer l'augmentation de la température de sulfuration. Le taux de sulfuration du W est alors augmenté [Reinhoudt *et al.*, 1998], au détriment de l'activité catalytique, ce qui est dû à l'effet de frittage des feuillets (augmentation de leur taille) qui diminue la quantité de phase active (atomes de bords). D'autres voies d'amélioration de la sulfuration sont envisageables, comme

l'utilisation de précurseurs non conventionnels. Ces précurseurs seraient de petite taille (mononucléaires ou petit cluster) avec l'objectif d'améliorer leur répartition sur la surface du support lors de l'imprégnation. Ils pourraient aussi contenir un à plusieurs atomes de W avec un degré d'oxydation plus proche de celui du tungstène sulfuré (*i.e.* $W^{(IV)}$), pour éventuellement faciliter la sulfuration du métal. Une recherche bibliographique a permis de mettre en évidence de nombreux travaux traitant du dépôt de W et d'autres métaux *via* des précurseurs non conventionnels, appelés précurseurs métallo-organiques. Leur utilisation pour préparer de nouveaux matériaux nécessite cependant une méthodologie de préparation peu employée dans le domaine catalyseurs d'hydrotraitement. Cette approche relativement atypique dans la préparation de catalyseurs d'hydrotraitement est décrite et illustrée dans la partie I.5.

I.5. Apport de la Chimie de Surface Contrôlée (CSC) : catalyseurs préparés par voie non conventionnelle

La préparation de catalyseurs à base de Mo et W peut être réalisée en remplaçant les précurseurs conventionnels par des complexes métallo-organiques. Un complexe métallo-organique est formé d'un métal entouré de ligands dont la nature (anionique : alkoxo (OR), amino (NR_2) mais aussi halogéno : Cl, Br ou neutre : alcools, amines, éthers…) et le mode de coordination (mono or multidentate) peuvent varier; ce qui détermine son degré d'oxydation et sa géométrie. Les complexes peuvent se présenter sous forme de monomères ou d'oligomères par l'intermédiaire de ligands pontants. Cette grande diversité de complexes métalliques permet d'avoir accès à des espèces aux propriétés physico-chimiques très différentes. On peut citer par exemple la tension de vapeur des composés, plus ou moins élevée suivant le type de ligands entourant le métal. Par ailleurs, les complexes métallo-organiques sont très souvent des espèces sensibles à l'air et à l'humidité, et doivent donc être manipulés en milieu inerte (atmosphère d'azote, argon ou hélium). Enfin, le dépôt de ces précurseurs peut être réalisé par plusieurs méthodes distinctes parmi lesquelles on retrouve l'imprégnation dans un solvant, ou le dépôt chimique en phase vapeur (ou CVD pour Chemical Vapour Deposition).

L'imprégnation à sec est réalisée suivant la même méthode que celle utilisée pour déposer les précurseurs conventionnels. Le complexe moléculaire est préalablement dissout dans un solvant et un volume de cette solution, identique au volume poreux du support, est ensuite imprégné sur le support. Par la suite, le catalyseur est séché, puis conditionné en boite à gants.

Le dépôt en phase vapeur est réalisé pour des composés dont la tension de vapeur est élevée. Ils sont aisément sublimables et peuvent donc être déposés sous phase vapeur sur le

support. Il existe de nombreuses méthodes de dépôt par voie CVD, les plus classiques étant le dépôt sous flux ou le dépôt en ampoule scellée. Le dépôt sous flux est généralement réalisé en lit fluidisé. Le précurseur, sous phase vapeur, est entrainé par un gaz vecteur et traverse un lit d'extrudés chauffés durant la durée de la manipulation. Le dépôt en ampoule scellée réunit quant à lui le précurseur et le support au sein d'un même contenant. Ces solides sont scellés dans une ampoule, sous vide partiel (quelques mbar de gaz neutre), et cette ampoule est chauffée durant un temps défini pour provoquer la sublimation du complexe et son dépôt sur le support.

L'utilisation de précurseurs non conventionnels permet d'envisager la préparation de catalyseurs par une approche dite de « chimie de surface contrôlée » (CSC), appelée traditionnellement « chimie organométallique de surface » (COMS) de part l'utilisation au départ de complexes organométalliques. [Ballard, 1973; Yermakov and Kuznetsov, 1973; Basset and Choplin, 1983; Copéret *et al.*, 2003, Wegener *et al.*, 2011] Cette approche requière le contrôle de l'état de surface du support, et le suivi étape par étape de la préparation du catalyseur. Chaque étape suivant le dépôt du composé doit être finement caractérisée, pour accéder à une compréhension des phénomènes chimiques au niveau moléculaire.

Lors de son dépôt sur un support oxyde, un précurseur métallo-organique peut se greffer ou être physisorbé. On appellera de manière général « greffage » lorsque le complexe moléculaire établit une liaison forte avec un(des) atome(s) de surface; il est souvent lié à la réaction d'échange entre un ou plusieurs des ligands anioniques du complexes avec un hydroxyle de surface du support oxyde (**Figure 8**). On appellera physisorption l'établissement d'interactions faibles de type van Der Waals entre une molécule et une surface.

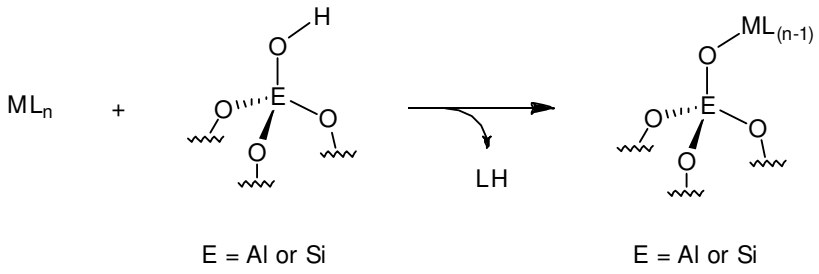

Figure 8 : Schéma d'un métal M greffé sur une surface.

Comme précisé auparavant, les complexes métallo-organiques utilisés pour les greffages sont généralement sensibles, mais ils présentent certains avantages. [Copéret *et al.*, 2003] Le

premier provient de la possibilité de préparer des catalyseurs avec des sites de surface de structure bien définie, là où les méthodes classiques ne fonctionnent pas. Le second avantage provient de la possibilité de déposer le métal de manière bien plus homogène sur la surface. L'utilisation de cette méthode de préparation permettrait de lever les interrogations sur la formation de la phase active, sa réactivité, les mécanismes de réaction, et les effets de synergie entre le promoteur et la phase métallique Mo ou W. De plus, comme les interactions entre promoteur et phase active ne sont pas encore totalement comprises, l'emploi de la voie CSC pour la préparation des catalyseurs promus pourrait être une solution pour mieux comprendre les effets de synergie identifiés pour les catalyseurs conventionnels. Enfin, l'un des enjeux de cette voie de préparation se situe dans le contrôle de l'état de surface du support, qui conditionne sa réactivité vis à vis des précurseurs.

I.5.a. Caractérisation et préparation des supports

Dans les parties précédentes, nous avons abordé l'utilisation de la silice, de l'alumine et de la silice-alumine comme support des catalyseurs d'hydrotraitement. La connaissance des propriétés texturales (surface spécifique, porosité) et de l'état de surface (taux d'hydroxylation, *i.e..* quantité de groupements hydroxyles OH présents en surface) de ces supports permet de mieux adapter les conditions de préparation des catalyseurs. Le contrôle du taux d'hydroxylation est en particulier très important dans le cas d'une approche dite moléculaire du dépôt d'espèces métalliques sur une surface. En effet, dans les conditions normales de température et de pression, les supports ont une surface plus ou moins hydratée et hydroxylée. La quantité d'hydroxyles de surface, ainsi que leurs types (décrits plus tard), modifient le comportement de chaque surface, et possèdent une signature spectroscopique spécifique permettant d'évaluer leurs interactions avec un précurseur métallique, notamment par spectroscopie FT-IR. Le contrôle du taux d'hydroxylation est réalisé par un traitement sous vide secondaire (10^{-5} mbar) ou sous flux d'un gaz inerte (azote, argon) à une température définie. Les différentes caractéristiques de la silice, de l'alumine et des silice-alumines sont décrites ci-dessous.

I.5.a.1. La silice – SiO_2

La silice est constituée d'un réseau tridimensionnel d'atomes de silicium dans un environnement tétraédrique SiO_4. En fonction des méthodes de préparation, la silice peut avoir une surface spécifique allant de *ca.* 10 à 1000 m^2/g. [Zuravlev, 2000]

A température ambiante, la silice, très polaire, a une surface recouverte d'eau en interaction avec des groupements hydroxyles appelés silanols SiOH. Au dessus de 140 °C, l'eau physisorbée est déplacée et laisse place à une surface très hydroxylés (> 4 OH/nm^2) Les hydroxyles de surface peuvent être divisés en trois groupes : silanols isolés SiOH (**Figure 9-a**) silanols vicinaux comportant des liaisons hydrogènes (provenant d'atomes de Si adjacents liés ou non par un pont oxygène (**Figure 9-b**), ou enfin des silanols géminaux $Si(OH)_2$ portés par un même atome de silicium (**Figure 9-c**). La surface présente aussi des groupements "siloxanes" Si-O-Si (**Figure 9-d**).

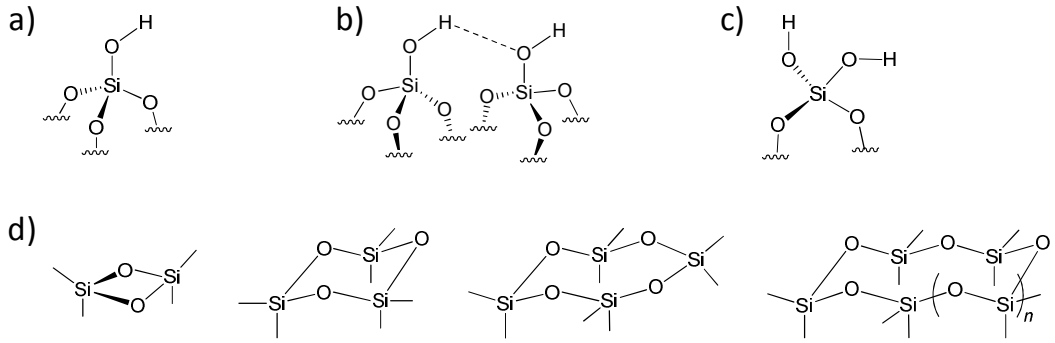

Figure 9: Différents hydroxyles de surface présents sur silice

Les fréquences des bandes de vibrations IR, caractéristiques des groupements OH, des ponts Si-O-Si et de l'eau en interaction avec la surface, sont résumées dans le **Tableau 2**.

Tableau 2 : Fréquences des bandes de vibrations IR remarquables pour un support silicique. [Vansant, 1995]

v (cm^{-1})	Attribution	Type de vibration
3750 - 3745	OH isolés	stretching
3742	OH geminaux	stretching
3730 - 3720	OH perturbés par H (SiOH voisin)	-
3660	SiOH liés par liaisons H moyennement fortes	-
3520	OH perturbés par O (SiOH voisin)	-
3400 - 2800	Eau adsorbée + OH liés par liaisons H fortes	-
2000 - 1870	Si - O - Si	Overtone des vibrations du skelette de la silice
1625	OH eau physisorbée	bending
1250 - 1020	Si - O - Si	asymmetrical stretching
935	Si-O pour SiOH isolés	stretching
870	OH	bending

Le type de silanols et leur concentration dépendent du type de silice, ainsi que de la température de traitement du support, sous vide ou sous gaz inerte. Le taux d'hydroxylation d'une silice amorphe, à température ambiante, est de l'ordre de 4 à 5 OH/nm² [Zuravlev, 2000] et celui-ci diminue de manière exponentielle avec la température à partir de 200°C (voir **Figure 10**). Par exemple, le taux d'hydroxylation de la surface est de 2,1, 1,4 et 0,8 OH/nm² après un traitement sous vide à 300, 500 et 700°C, respectivement. A 700°C, la surface comporte principalement des silanols isolés (> 90% et quelques silanols géminaux, *ca.* 5-10%) et des ponts siloxanes. Au-delà, la deshydroxylation s'accompagne d'une perte de surface spécifique, notamment pour une silice de flamme type Aerosil®, provenant de l'agrégation de particules. [Rascon *et al.*, 2011] Enfin, à des températures supérieures à 1200°C, la silice cristallise et ne comporte plus que des ponts siloxanes.

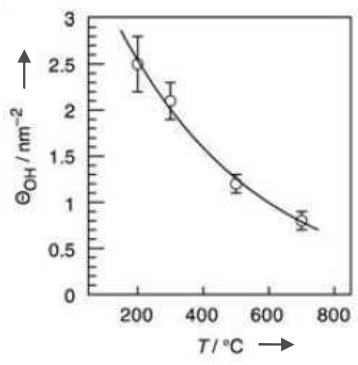

Figure 10 : Effet du prétraitement en température d'une silice sur le taux d'hydroxylation θ_{OH}. Adapté de la ref. [Rascon *et al.*, 2011]

I.5.b.2. L'alumine – Al_2O_3

Il existe huit formes cristallines d'alumines recensées à ce jour. Les alumines η, γ, δ, θ et α sont les plus connues et les plus employées mais nous ne détaillerons ici que le cas de l'alumine-γ. Deux modèles ont été proposés pour modéliser la structure de cette alumine-γ : un modèle spinelle [Pinto *et al.*, 2004; Menendez-Proupin and Gutiérrez, 2005] et un modèle non spinelle. [Krokidis *et al.*, 2001; Digne *et al.*, 2004] La différence entre les deux repose sur la présence ou non de défauts de sites dans la structure.

Comme pour la silice, Il existe différents types d'hydroxyles de surface pour l'alumine. Les premiers travaux de Knözinger *et al.* [Knözinger and Ratnasamy, 1978] proposent la présence d'aluminols isolés sur un Al tétraédrique (Al_{IV}), d'aluminols isolés sur un Al octaédrique (Al_{VI}), d'OH ponté entre un Al_{VI} et un Al_{IV}, d'OH coordonnés à 2 Al_{VI} et d'OH coordonnés à 3 Al_{VI}. Par la suite, la détermination des différents types d'OH et de leurs vibrations caractéristiques en spectroscopie IR ont été affinés par de nombreux travaux théoriques [Peri, 1965, Digne *et al.*, 2004] et expérimentaux.[Knözinger and Ratnasamy, 1978; Busca *et al.*, 1993] La **Figure 11-a**, qui montre le spectre IR d'une alumine-γ (chauffée sous vide, 10^{-5} mbar, à 500°C) dans la zone 3900-3500 cm^{-1}, met en évidence les vibrations d'élongation de différents OH observables, *i.e.* $\nu(Al_{IV} – OH) \approx 3795\ cm^{-1}$, $\nu(Al_{VI} – OH) \approx 3780\ cm^{-1}$, $\nu((Al_{VI})_3 – OH) \approx 3740\ cm^{-1}$, $\nu(Al_V – OH) \approx 3735\ cm^{-1}$and $\nu((Al_V)_2 – OH) \approx 3708\ cm^{-1}$.

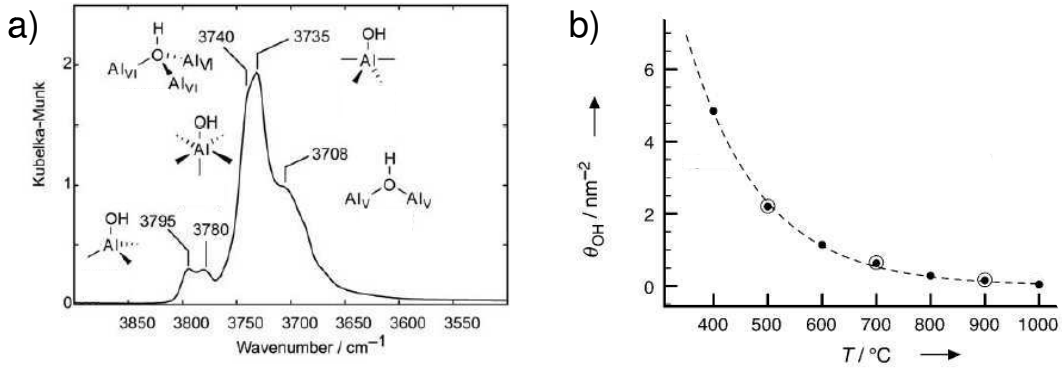

Figure 11 : a) Spectre infrarouge d'une alumine-γ deshydroxylée à 500°C sous vide (≈10^{-5} mbar). Adapté de la ref. [Rascon *et al.*, 2011]. b) Effet du prétraitement en température d'une alumine-γ sur le taux d'hydroxylation θ_{OH} mesuré par titration avec CH_3MgBr (●) ou intégration des bande OH du spectre IR (○). Adapté de la ref. [Wischert *et al.*, 2011]

Comme pour la silice, le taux d'hydroxylation d'une alumine-γ diminue de manière exponentielle avec la température de prétraitement au dessus de 200°C (**Figure 11.b**). [Wischer *et al.*, 2011] A 300°C, le taux d'hydroxylation avoisine 8 OH/nm², puis diminue à une valeur d'environ 3,2 OH/nm² à 450°C et 0,7 OH/nm^2 à 700 °C.

I.5.c.3. La silice-alumine – SiO_2-Al_2O_3

Les silice-alumines amorphes (ASA) sont des solides minéraux appartenant à la famille des aluminosilicates. Les zéolithes représentent la forme cristallisée de cette famille. Les silice-alumines sont composées de d'espèces siliciques, *et al*uminiques. La surface spécifique des silice-alumines avoisine les 150 à 400 m^2/g et peut atteindre 600 m²/g ou plus, dans le cas de supports mésostructurés.

Actuellement, la compréhension de la nature des sites de surfaces d'ASA reste un défi. La combinaison de résultats expérimentaux [Trombetta *et al.*, 1998; Gora-Marek *et al.*, 2005; Garrone *et al.*, 2006; Crépeau *et al.*, 2006] et de travaux théoriques [Garrone *et al.*, 2006; Chizallet *et al.*, 2009; Chizallet *et al.*, 2010] a récemment permis de déterminer la nature de différents groupements hydroxyles présents en surface. Ces hydroxyles sont présentés dans la **Figure 12**.

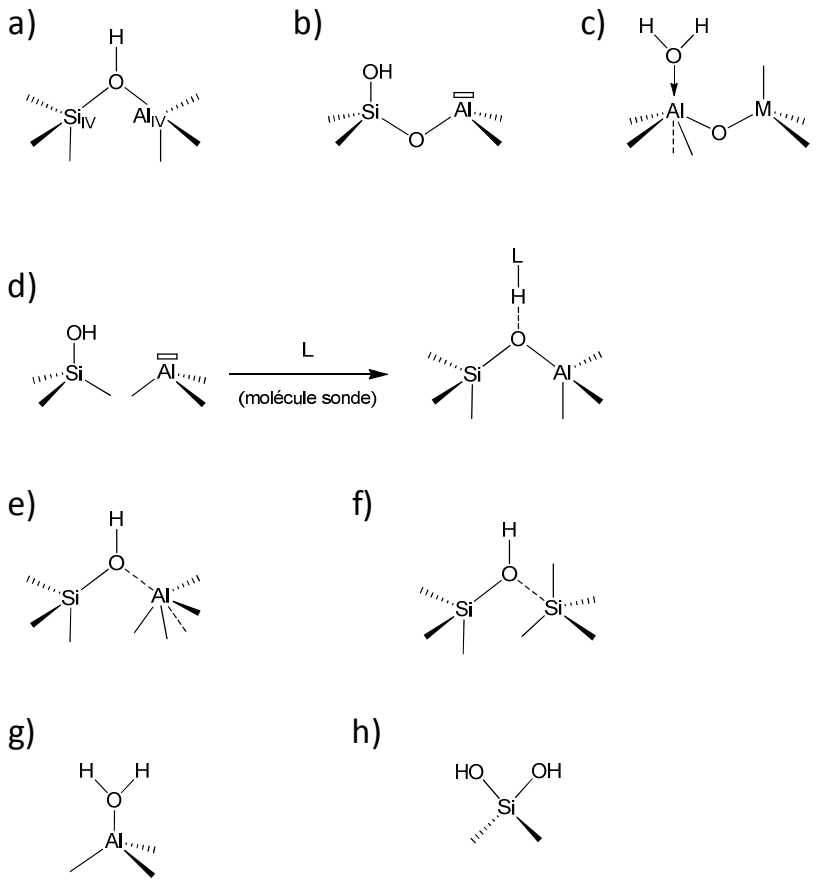

Figure 12 : Groupements hydroxyles d'une surface d' ASA, modèles proposés à partir de travaux expérimentaux (a–d) et calculs DFT (a, c, e, f, g, h) : (a) groupe pontant Si–(OH)–Al type zéolithe [Trombetta *et al.*, 1998; Gora-Marek *et al.*, 2005, (b) silanol au voisinage d'un atome d'aluminium Crépeau *et al.*, 2006, (c) molécule d'eau physisorbée sur un atome d'aluminium [Garrone *et al.*, 2006, (d) Pont Si–(OH)–Al induit par adsorption d'une molécule sonde [Trombetta *et al.*, 1998, (e) silanol pseudo-ponté sur un atome d'aluminium voisin (PBS–Al) [Chizallet and Raybaud, 2009; Chizallet and Raybaud, 2010] , (f) silanol pseudo-ponté sur un atome de silicium voisin (PBS–Si) [Chizallet *et al.*, 2010], (g) molécule d'eau adsorbée sur un aluminium [Chizallet and Raybaud, 2009; (f) silanols géminaux [Chizallet and Raybaud, 2009; Chizallet and Raybaud, 2010]. Adapté de Leydier *et al.* [Leydier *et al.*, 2011]

Sur cette figure, on note la présence de silanols géminaux (**Figure 12-h**), de silanols au voisinage d'un atome d'aluminium voisin de basse coordination (**Figure 12-b**), de silanols pseudo-pontés sur un atome d'aluminium voisin (PBS-Al pour pseudo-bridging silanol, **Figure 12-e**), et de silanols pseudo-pontés sur un atome de silicium voisin (PBS-Si, **Figure 12-f**). Une

surface hydratée présente aussi de l'eau physisorbée ou chimisorbée (et non désorbable en dessous de 500 à 700°C) sur des atomes d'aluminium (**Figure 12-c,g**). De plus, lorsque le taux de recouvrement de la surface dépasse 6,4 OH/nm², la présence de sites pontés Si–(OH)–Al [Chizallet and Raybaud, 2009] (**Figure 12-a**) a été mise en évidence.

Afin de proposer des interprétations quant à l'environnement local de certaines liaisons chimiques dans les alumino-silicates, il est possible de comparer les spectres IR des zéolithes et des ASA, bien qu'ils ne soient pas identiques. Sur les zéolithes, deux bandes de vibrations sont généralement observables dans la zone des hydroxyles : une bande caractéristique de la présence des silanols isolés à 3745 cm^{-1}, ainsi qu'une bande à 3610 cm^{-1}, caractéristiques des OH pontés des Si–(OH)–Al. Pour une ASA ayant subi un traitement thermique entre 300°C et 500°C sous vide (10^{-5} mbar), on observe sur le spectre IR (**Figure 13**) la présence de la bande caractéristique des silanols isolés à ν(OH) = 3743 cm^{-1}, ainsi qu'un massif large et plus ou moins intense, observé vers 3600 cm^{-1}. Ces signaux suggèrent respectivement la présence de nombreux silanols isolés, ainsi qu'une large distribution d'hydroxyles (pseudo)pontants. La présence d'eau est quant à elle marquée par un massif aux alentours de 3500 cm^{-1} et un pic observable vers 1626 cm^{-1}. Comme pour la silice, on retrouve les vibrations harmoniques des liaisons Si–O–Si des ponts siloxanes dans la région 2000-1000 cm^{-1}.

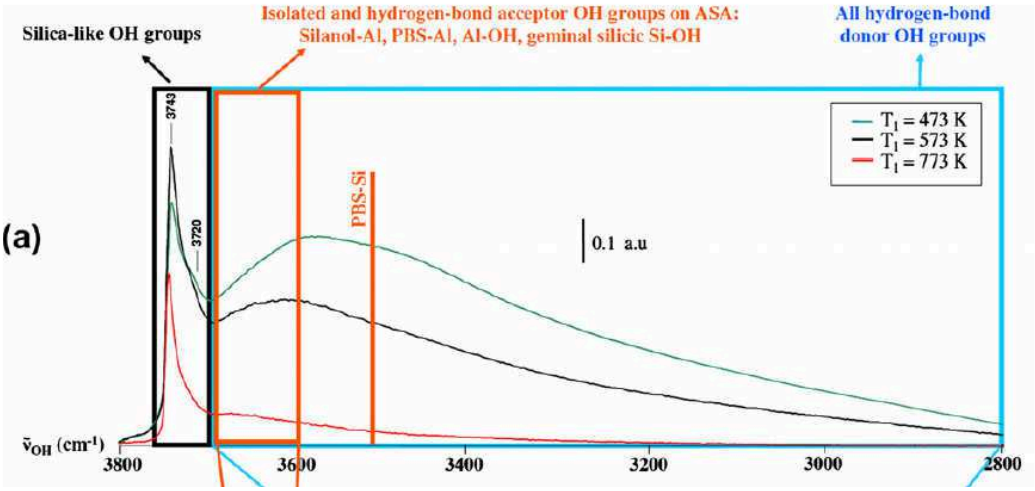

Figure 13 : Spectres FT-IR (transm.) d'une silice-alumine, prétraitée sous vide secondaire (10^{-5} mbar) [Leydier *et al.*, 2011]

Enfin, des mesures expérimentales du taux d'hydroxylation d'ASA par mesures potentiométriques ou par analyses thermogravimétriques ont révélé des taux d'OH allant de 3,9 OH/nm² à 6,4 OH/nm² pour une ASA non deshydroxylée. [Iengo *et al.*, 1998]

I.5.b. Utilisation de la méthode CSC (ou COMS) pour la préparation de catalyseurs ayant des sites actifs bien définis : généralités.

La voie de préparation CSC est utilisée permet de préparer des espèces de surface bien définies. Ces espèces de surface peuvent présenter une, ou plusieurs liaisons avec le support. Dans le cas d'une seule liaison « support - métal » on parle d'espèce monopodale. Si deux ou trois liaisons similaires sont observées, on parle respectivement d'espèce bipodale ou tripodale. La température de deshydroxylation du support est alors un facteur très important pour orienter le type de greffage des complexes organométalliques.

La méthode CSC a été employée pour la préparation de catalyseurs à base de métaux comme Mo, W ou Re, actifs en métathèse des oléfines. [Chabanas *et al.*, 2001, Mazoyer *et al.*, 2010; Leroux *et al.*, 2005a; Blanc *et al.*, 2007] Chabanas *et al.* [2001] ont par exemple préparé un catalyseur par imprégnation du complexe Re(≡C*t*Bu)(=CH*t*Bu)(CH_2*t*Bu)$_2$ sur une silice partiellement deshydroxylée à 700°C pour donner une espèce de surface du type [(≡SiO)Re(≡C*t*Bu)(=CH*t*Bu)(CH_2*t*Bu)] avec *t*Bu = $C(CH_3)_3$. A cette température, la silice n'expose principalement que des silanols isolés (voir I.V.a.1) qui vont réagir avec le rhenium Re pour établir une liaison « Si–O–Re » par départ d'un ligand néopentane (ou CH_3*t*Bu). Seule une espèce monopodale est formée. La même observation est faite lors du dépôt d'un complexe du type tungstène (VI) oxotetranéopentyl ou W(=O)(CH_2*t*Bu)$_4$ (néopentyl (Np) = CH_2*t*Bu$_3$) qui donne une espèce de surface monopodale du type [(≡SiO)W(=O)(CH_2*t*Bu)$_3$].[Mazoyer et a., 2010] Un exemple de l'influence significative du taux d'hydroxylation sur le type d'espèce de surface est illustré par les travaux de Lefort *et al.* [L.Lefort *et al.*, 2000] sur le dépôt de Ta(=CH*t*Bu)(CH_2*t*Bu)$_3$ sur des silices de plus en plus hydroxylées : $SiO_{2\text{-}700}$, $SiO_{2\text{-}500}$ et $SiO_{2\text{-}300}$. Sur $SiO_{2\text{-}700}$, l'espèce de surface monopodale [(≡SiO)Ta(=CH*t*Bu)(CH_2*t*Bu)$_2$] est majoritairement formée, comme montré **Figure 14**. Lorsque ce complexe est déposé sur $SiO_{2\text{-}300}$, une silice exposant un nombre plus important de groupements OH de surface, c'est l'espèce bipodale [(≡SiO)$_2$Ta(=CH*t*Bu)(CH_2*t*Bu)] qui est majoritaire (voir **Figure 14** aussi). Pour une silice deshydroxylée à une température intermédiaire, les auteurs rapportent la présence d'environ 50% de chacune de ces espèces sur la surface.

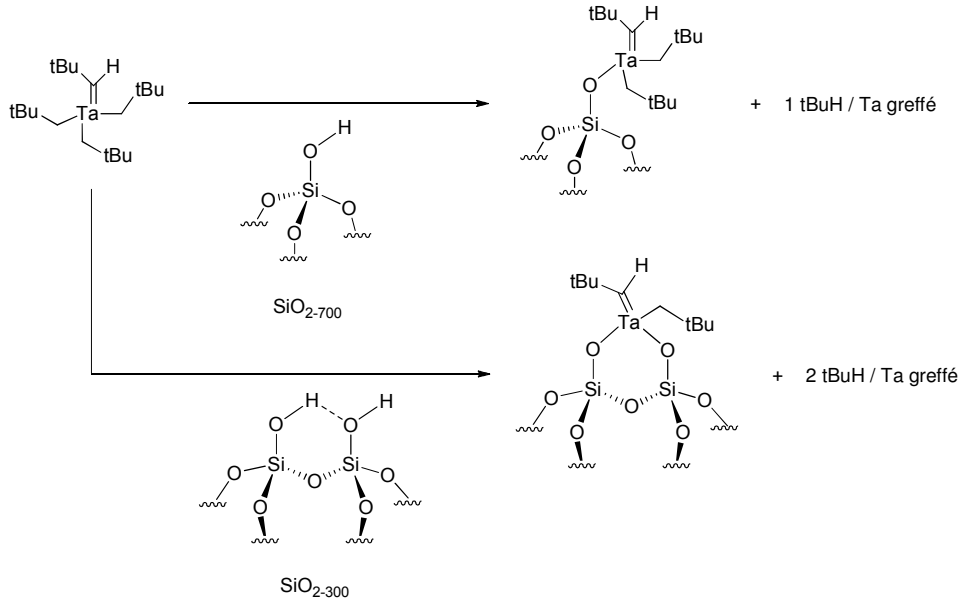

Figure 14 : Espèces de surface formées lors du greffage de Ta(=CHtBu)(CH_2tBu)$_3$ sur $SiO_{2\text{-}700}$ ou $SiO_{2\text{-}300}$.

La formation majoritaire d'espèces bipodales sur silice faiblement deshydroxylée ($SiO_{2\text{-}200}$) est aussi rapportée pour des complexes organométalliques du chrome ou du vanadium du type M(CH_2*t*Bu)$_4$ (M = Cr, V). Peu de travaux décrivent la préparation d'espèces tripodales en une seule étape. On peut citer le groupe de T.Marks (Wegener *et al.*, 2011) qui rapporte la préparation d'une espèce tripodale [(Al_SO)$_3$V(=O)] où Al_sO représente le support aluminique. Pour arriver à ce résultat, les auteurs ont greffé une solution de V(=O)(Mes)$_3$ (où Mes = mesithylène ou 1,3,5-trimethylbenzène) sur θ-$Al_2O_{3\text{-}400}$. Néanmoins, et malgré la précision des analyses généralement utilisées pour déterminer la structure des espèces de surface (Résonnance magnétique nucléaire (RMN) en phase solide, spectroscopie EXAFS, spectroscopie FT-IR, ou suivi quantitatif des étapes de greffage), les signaux observés ne sont malheureusement que moyennés, et éventuellement attribués à des espèces bipodales là où la surface n'est effectivement recouverte que d'espèces monopodales et tripodales. Par ailleurs, l'accès à des espèces tripodales peut être réalisé par traitement thermique sous hydrogène d'espèces monopodales. Par exemple, l'espèce monosiloxyperalkyl [(≡SiO)M(CH_2*t*Bu)$_3$] issues du greffage de complexes de métaux du groupe 4 (M = Ti [Rosier *et al.*, 1997], Zr [Corker *et al.*, 1996]) conduit à un mélange d'espèces comportant principalement une espèce tripodale (60-70%) (M = Ti [Bini *et al.*, 2006], Zr, [Rataboul *et al.*, 2004])

Leroux *et al.* [LeRoux *et al.*, 2005b] ont appliqué la méthode CSC pour le dépôt de [W(≡C*t*Bu)(CH_2*t*Bu)$_3$] sur alumine partiellement deshydroxylée à 500°C (ou $Al_2O_{3\text{-}500}$) afin de générer des catalyseurs de métathèse des alcanes à base de W. Une étude expérimentale [LeRoux *et al.*, 2005a] couplée à des calculs DFT [Joubert *et al.*, 2006] a montré qu'une espèce de surface monopodale du type [(Al_sO)W(≡C*t*Bu)(CH_2*t*Bu)$_2$] est obtenue, et qui traitée sous hydrogène donne un hydrure de W (*i.e.* WH/$Al_2O_{3\text{-}450}$), Ces espèces, en particulier l'hydrure de tungstène se sont révélés de très bons catalyseurs de métathèse des alcanes avec des performances supérieures à l'espèce de surface de référence l'hydrure de tantale supporté sur silice, [(≡SiO)$_2$TaH]. [Vidal *et al.*, 1997] On notera la préparation de catalyseurs similaires, déposés sur silice-alumine (Si/Al = 3 at/at) deshydroxylée à 500°C. Dans ce cas, [LeRoux *et al.*, 2007] le dépôt de W(≡CHtBu)(CH_2tBu)$_3$ donne une espèce de surface monopodale du type [(≡SiO)W(≡CHtBu)(CH_2tBu)$_2$] par réaction du complexe métallique avec les silanols du support, qui traité sous hydrogène, évolue vers un hydrure de tungstène supporté sur ASA. Ces catalyseurs se sont révélés aussi actif que sont homologue déposé sur $Al_2O_{3\text{-}500}$. Pour plus d'informations sur les précurseurs ou les supports utilisés, ainsi que sur les résultats catalytiques et les mécanismes associés à la métathèse des alcanes, le lecteur est invité à consulter le papier de Basset *et al.* [Basset *et al.*, 2010]

L'approche moléculaire du dépôt de complexe organométallique a aussi permis la préparation de catalyseurs actifs en polymérisation des oléfines. On peut notamment citer la préparation de catalyseurs à base de titane comme ceux préparés par Grau *et al.*, [Grau *et al.*, 2013] dans le cadre de l'amélioration de catalyseur Ziegler-Natta préparés sur $MgCl_2$, en présence de tétrahydrofurane (THF).

Pour terminer, il est intéressant d'évoquer le cas des complexes présentant des ligands alcoxydes, utilisés pour la préparation de catalyseurs d'époxydation (à partir de Ti(O*i*Pr)$_4$ [Fraile *et al.*, 1996]), de dépéroxidation (à partir de Ta(OMe)$_5$ [Petroff Saint-Arroman *et al.*, 2008]) ou de métathèse (à partir de Mo(≡NAr)(=CHCMe$_2$Ph)(OR)$_2$ où R = *t*Bu ou Ar [Rendón *et al.*, 2009]). Ainsi, le dépôt sur $SiO_{2\text{-}500}$ (voie CVD, à 70°C) d'un complexe comme V(=N*t*Bu)((CH_2*t*Bu))$_3$ ne comportant pas de ligand alcoxy, génère un mélange *quasi* équimolaire d'espèces monopodales et bipodales [Wolke *et al.*, 2001] par réaction d'un ou de deux ligand néopentyl alors que l'utilisation d'un précurseur comportant un ligand alcoxyde, V(=NtBu)((CH_2tBu))$_2$**(OtBu)** permet la formation d'une seule espèce de surface par échange sélectif du groupement CH_2*t*Bu par un ligand siloxy. Par ailleurs, dans le cas d'un oxo-alcoxyde comme le vanadinum oxo-triisopropoxyde, V(=O)(O*i*Pr)$_3$ où *i*Pr = CH(CH_3)$_2$, le dépôt sur des

silices deshydroxylées à 25°C comme à 500°C s'effectue par départ d'un ligand alcoxyde et ne permet d'obtenir majoritairement qu'une espèce monopodale du type [(≡SiO)V(=O)(OiPr)$_2$], comme montré **Figure 15**. La température de deshydroxylation, qui permet généralement d'orienter le type de greffage des complexes organométalliques (monopodal, bipodal), ne semble pas modifier le type d'espèce de surface obtenue dans ce dernier cas. [Copéret *et al.*, 2003]

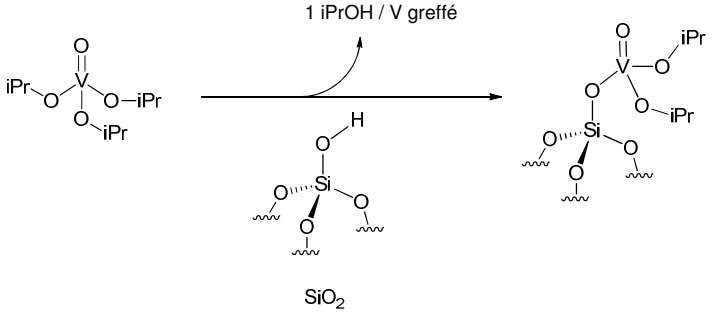

Figure 15 : Espèce de surface formée lors du dépôt de l'oxotriisopropoxyde de vanadium, sur silice.

I.5.c. Catalyseurs d'hydrotraitement non promus, préparés par voie CSC

Cette approche moléculaire a aussi été utilisée pour la préparation de catalyseurs d'hydrotraitement de type HDN [Harvey and Matheson, 1986], HYD [Thomas and Brenner, 1983; Eisen and Marks, 1994] ou HDS [Yermakov *et al.*, 1981, Yermakov *et al.*, 1984; Ishirara *et al.*, 1994; Choi, *et al.*, 2000; Larabi *et al.*, 2012]. Les supports les plus utilisés sont la silice et l'alumine.

Dans cette partie, les précurseurs métallo-organiques évoqués ne représentent qu'une infime partie des nombreuses espèces existantes. En effet, nous ne décrirons que l'utilisation de précurseurs carbonylés, du type $M^{(0)}(CO)_6$ (M = Mo, W) et de précurseurs homoleptiques (ayant un seul type de ligand) neutres, du type $M^{(x)}R_x$ (x = 2,4,5), avec M = W ou Mo et R étant un alkyl (C_nH_{2n+1}), ou un ligand anionique comme un alcène (C_nH_{2n}), ou un alcoxyde (OC_nH_{2n+1}).

D'après la littérature, il semblerait que l'imprégnation de précurseurs carbonylés $M(CO)_6$ (M = Mo, W) dans le pentane [Brenner and Burwell, 1978; Jaenicke and Loh, 1999] ou le benzène ne permette pas de déposer aisément d'importantes quantités de métal (< 2.2 $\%_{pds.}$ métal, sur

alumine [Davie *et al.*, 1972]), du fait de la faible solubilité de ces complexes et de leur faible réactivité vis-à-vis des groupements OH de surface. Cependant, ces composés sont photo-activables (irradiation sous UV) par échange de ligand avec, par exemple, du tétrahydrofurane (THF ou C_4H_8O) [Maeyama and Iwasawa, 1999] ou encore de la triphénylphosphine (PPh_3 ou $P(C_6H_5)_3$). [Baibich *et al.*, 1997; Sica *et al.*, 1999] Cette approche permet de remplacer facilement un ligand carbonyle par un ligand plus labile, qui pourra aisément être échangé lors de son dépôt sur le support. A titre d'exemple, Sica *et al.* [Sica *et al.*, 1999] rapporte le dépôt de W sur γ-$Al_2O_{3\text{-}450}$ par photo-irradiation d'une solution de pentane contenant le support, $W(CO)_6$ et PPh_3. Par spectroscopie FT-IR, les auteurs ont montré la présence de différentes espèces de tungstène adsorbées à la surface de l'alumine, mais n'ont pas étudié les interactions entre ces espèces et les hydroxyles du support. Compte tenu de la volatilité des complexes carbonylés, plusieurs travaux se sont intéressés au dépôt de ces complexes par voie CVD. La préparation par dépôt en phase vapeur permet typiquement de mieux contrôler la quantité de métal déposée et de potentiellement améliorer la dispersion [Suvanto *et al.*, 1998; Perez-Cadenas *et al.*, 2003], par un meilleur transport du précurseur au sein des pores du support ou par adsorption avec des sites spécifiques supposés bien dispersés [Suvanto *et al.*, 1998]. Les nombreuses études par spectroscopie FT-IR [Zecchina *et al.*, 1990; Busca *et al.*, 1993; Reddy and Brown, 1995; Suvanto *et al.*, 1999] réalisées sur les catalyseurs $M(CO)_6$/support préparés par CVD mettent toutes en évidence l'existence d'espèces $M(CO)_6$ physisorbées, mais présentent des divergences quant à la présence d'espèces sub-carbonyles $M(CO)_{6\text{-}x}$ greffées en surface. Il semblerait que la structure des espèces de surface soit dépendante des étapes de préparation (notamment le post traitement du catalyseur après dépôt du précurseur) et surtout de l'état de surface du support, notamment son taux d'hydroxylation et la présence de sites acides de Lewis Al^{3+} plus ou moins forts. De plus, les résultats catalytiques obtenus en HDS du thiophène ne révèlent pas systématiquement une amélioration de l'activité des catalyseurs. En particulier, Suvanto *et al.* [1999] ont montré que pour des catalyseurs $W(CO)_6/\gamma$-Al_2O_3, l'augmentation du taux de recouvrement en tungstène (W/nm^2) engendre une diminution de l'activité intrinsèque en HDS du thiophène ($mol_{(thiophène)}/mol_{(W)}$), probablement provoquée par moins bonne dispersion de la phase active sur le support à fort W/nm^2.

Il convient aussi de mentionner la possibilité de préparer du WS_2 massique par dépôt en couche mince, par réaction en phase gaz de $W(CO)_6$ ou de l'hexachlorure de tungstène (VI) WCl_6 avec de l'H_2S pur [Chung *et al.*, 1998], ou issu de la décomposition d'éthanedithiol $HS(CH_2)_2SH$. [Carmalt *et al.*, 2003]

Par ailleurs, l'imprégnation de précurseurs homoleptiques alkyles comme le tungstène tétra(η_3-1-butènyle) ($W(C_4H_7)_4$) paraît prometteuse. Yermakov *et al.* [1984] ont montré que le degré d'oxydation du métal greffé sur le support aurait une influence importante sur la sulfuration, la dispersion de la phase active, ainsi que sur l'activité catalytique. En particulier, pour un catalyseur WS_2/SiO_2, le processus de sulfuration est plus favorable en partant d'un métal à degré d'oxydation bas : une espèce de surface formée de W au degré d'oxydation +II étant plus facilement sulfurable qu'une espèce formée de $W^{(IV)}$ ou de $W^{(VI)}$. Une étude précédemment menée à IFPEn a montré qu'un catalyseur préparé à partir de tungstène (V) pentaéthoxyde $[W(OEt)_5]_2$ déposé sur silice-alumine amorphe (ASA, 30 $\%_{pds.}$ SiO_2) se sulfurait mieux qu'un catalyseur conventionnel calciné du type WO_3/ASA d'après des analyses XPS.

En HDS du thiophène Yermakov *et al.* [1984] ont mis en évidence que plus le degré d'oxydation du métal greffé est bas, plus l'activité intrinsèque de catalyseurs WS_2/SiO_2 est importante. Sur la **Figure 16**, le catalyseur sulfuré n°2, préparé initialement par réduction de $W^{(IV)}$ en $W^{(II)}$ a une activité presque 20 fois supérieure à celle du catalyseur conventionnel préparé par imprégnation d'un sel de W (droite n°5). Le catalyseur 4, préparé par voie organométallique puis calciné sous O_2, est lui aussi plus actif que son homologue conventionnel (catalyseur 5). Un travail similaire réalisé par imprégnation de $W(C_4H_7)_4$ sur alumine [1984] a confirmé l'amélioration des performances hydrodésulfurantes des catalyseurs préparés par une approche dite moléculaire.

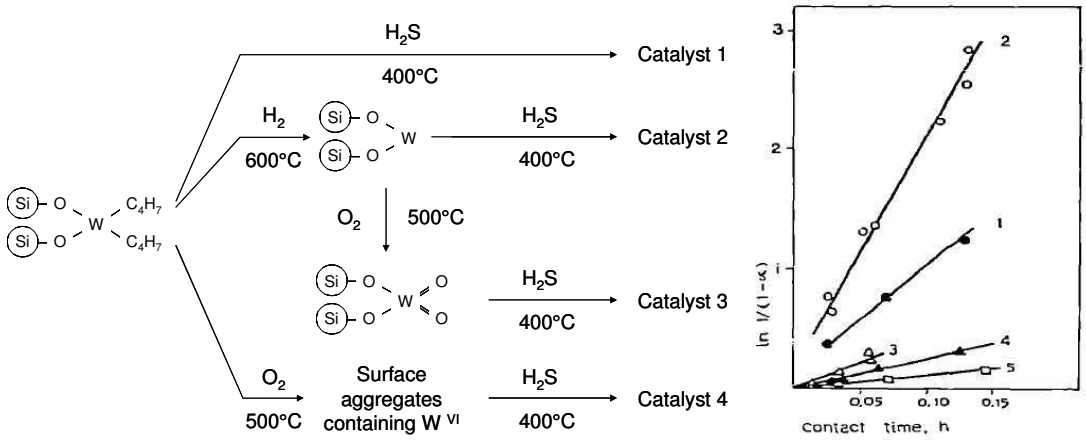

Figure 16 : A gauche : différentes voies de préparation de catalyseurs COMS sulfurés, à partir de $W(C_4H_7)_4$ sur SiO_2 – A droite : activité catalytique en HDS du thiophène des catalyseurs préparés suivant les différentes voie présentées. Le catalyseur 5 représente un catalyseur dit conventionnel, préparé à partir de $(NH_4)_2WO_4$. α représente le degré de conversion du thiophène.

En outre, l'emploi de précurseurs moléculaires permettrait de mieux répartir le W [Perez-Cadenas *et al.*, 2003] ($[W(OEt)_5]_2$/charbon actif) et la phase sulfure (WS_2/SiO_2 ou WS_2/ASA) [Yermakov *et al.*, 1981; Roukoss, 2009] à la surface du support, par rapport à une voie de préparation conventionnelle. Enfin, les caractéristiques structurales des feuillets semblent aussi être impactées par le degré d'oxydation du métal de départ. Pour un tungstène au degré +IV, il semblerait que la phase active soit composée de nanocristallites de taille inférieure à 1,0 nm et de monofeuillets allant de 1,5 à 5,0 nm. Pour un métal au degré d'oxydation inférieur, la taille moyenne est similaire alors que pour un degré d'oxydation supérieur ($W^{(VI)}$), la taille des cristallites observées est plus importante. [Yermakov *et al.*, 1984]

Les travaux présentés montrent que la préparation de catalyseurs d'hydrotraitement à base de W déposé par voie CSC permet généralement d'améliorer leur activité catalytique. Cela est notamment dû à la meilleure « sulfurabilité » de la phase métallique sur silice (comme sur alumine) en comparaison des catalyseurs conventionnels. Il semble aussi que cette voie non conventionnelle permette d'obtenir des tailles de cristallites différentes. Enfin, l'emploi de certains précurseurs métallo-organiques comme $[W(OEt)_5]_2$ a permis d'augmenter la dispersion des espèces de surface, sur les catalyseurs.

I.5.d. Catalyseurs d'hydrotraitement promus, préparés par voie CSC

Les méthodes de dépôt non conventionnelles de promoteurs sont identiques à celle utilisées pour le dépôt de la phase métallique Mo ou W.

Comme précisé précédemment, les précurseurs carbonylés sont aisément sublimables. Pour cette raison, certaines études, comme celle de Suvanto *et al.,* [1999] rapportent le dépôt par voie CVD de dicobalt (0) octacarbonyle, ou $Co_2(CO)_8$. La préparation de catalyseurs CoW/Al_2O_3 [Suvanto *et al.*, 1999] ou $CoMo/Al_2O_{3\text{-}600}$, [Kurhinen and Pakkanen, 2000] a permis de montrer que les solides obtenus sont actifs en HDS du thiophène, mais sont peu sélectifs.

Les équipes d'Okamoto [Okamoto *et al.*, 2005, Okamoto *et al.*, 2009] et Maugé [Maugé *et al.*, 1989, Maugé *et al.*, 1992] ont déposé du cobalt tricarbonyle nitrosyle, ou $Co(CO)_3NO$, par voie CVD directement sur un catalyseur sulfuré. Dans leur étude, Okamoto *et al.* [2009] ont tenté de mettre en évidence l'influence de la température de sulfuration des catalyseurs CoMoS et CoWS en HDS du thiophène. A cette température, et pour une sulfuration à P_{atm} avec un rapport H_2S/H_2 de 0.1, l'existence de deux types de phases mixtes Co-M-S (M = W, Mo) a été discutée. Pour des catalyseurs supportés sur silice, une phase dite de « type I » serait formée à

partir de 400°C tandis qu'une phase de type « type II » apparaîtrait à partir de 600°C. Toutefois, la notion de « type I » et « type II » demeure très vague, et ne se caractérise que très empiriquement par une meilleure activité hydrodésulfurante d'un type par rapport à l'autre. D'après Okamoto, la phase CoMoS de « type II » serait formée lorsque le promoteur est déposé sur une phase métallique parfaitement sulfurée. Les auteurs ont aussi mis en avant que l'influence des interactions «MoS_2–O–support» sur l'état électronique des feuillets MoS_2 conditionne l'état électronique des sites Co-Mo-S de bord, et ainsi, leur activité intrinsèque. La vitesse intrinsèque de conversion du thiophène des CoMoS « type I » serait deux fois plus importante que celle des «type I». De plus, les auteurs ont démontré que les Co-W-S dits de « type II » étaient 1,6 fois plus actifs que les Co-Mo-S en HDS du thiophène. Néanmoins, cela donne peu d'information sur la nature exacte des phases dites de « type II ».

L'équipe de Maugé *et al.* [1989, 1992] a montré que l'emploi de $Co(CO)_3NO$ permettait de multiplier par 2 l'activité HDS d'un catalyseur promu $CoMo/Al_2O_3$ préparé par voie CSC, mais n'en modifiait par l'activité hydrogénante. Cela illustre le fait que les réactions d'hydrogénation et d'hydrodésulfuration ne mettent pas en jeu les mêmes sites actifs. Cette observation est cohérente avec les travaux de Moses *et al.* [2007] et Gandubert *et al.* [2008] abordés partie I.3.c.

Enfin, il convient de mentionner l'emploi combiné de Metal-Organic framework (MOF) et de carbonyles ($Mo(CO)_6$, $Cr(CO)_6$) pour la préparation de catalyseurs promus non supportés. [Laribi *et al.*, 2012] Brièvement, le promoteur est contenu dans la charpente du MOF, comme pour [Ni_2(dhtp)] (H_4dhpt = acide 2,5-dihydroxyterephthalique). Le précurseur de Mo ou Cr est déposé par sublimation dans les pores du MOF, pour donner des espèces du type $M(CO)_3$, en interaction avec les cycles aromatiques de la charpente du support. La sulfuration du matériau dégrade le MOF pour donner un catalyseur massique du type NiMS (M = Cr, Mo) pour lequel seul le catalyseur préparé avec la combinaison Ni+Mo est actif. L'activité intrinsèque du NiMoS massique *ex*-MOF est 10 fois plus importante que celle d'un NiMoS massique conventionnel en HDS du dibenzothiophène, et 8 fois plus élevée en hydrogénation du naphtalène. Néanmoins, cette méthode de préparation doit être améliorée car les performances des catalyseurs *ex*-MOF restent inférieures de moitié à celle d'un $NiMoS/Al_2O_3$ conventionnel.

Parallèlement à l'emploi de la méthode CVD, certains auteurs ont étudié l'incorporation du promoteur par imprégnation. Vishwakarma *et al.* [Vishwakarma *et al.*, 2007] ont tenté de préparer des matériaux du type $CoW/\gamma\text{-}Al_2O_3$ par co-imprégnation $W(CO)_6$ et $Co_2(CO)_8$ dans le *n*-hexadécane, à l'aide d'ultrasons. Les auteurs n'ont cependant pas montré d'augmentation des activités HDS et HDN (coupe Light Gas Oil ou LGO) des phases CoWS préparées par voie

«sonochimique» par rapport aux références issues de précurseurs conventionnels. [Halbert *et al.*, 1991] L'imprégnation de $Co_2(CO)_8$ (en solution dans l'hexane) sur des catalyseurs pré-sulfurés (400°C, 10 % H_2S/H_2), préparés par calcination d'un matériau issu de l'imprégnation d'heptamolybdate d'ammonium sur $Al_2O_{3\text{-}500}$, produisent des phases CoMoS qui sont 1,3 fois plus actives que des phases NiMoS (supportées sur alumine) en HDS d'une charge de type gasoil. Elles sont cependant moins actives en HDN.

Yermakov *et al.* [1984] ont préparé des phases NiMoS et NiWS supportées sur SiO_2 ou Al_2O_3 par imprégnation du complexe $Ni(C_3H_5)_2$ solubilisé dans le pentane. Pour les catalyseurs préparés sur silice, l'ordre de dépôt du promoteur et du W(Mo) ne modifie pas significativement leur activité catalytique en HDS du thiophène à 300°C. Par ailleurs, le dépôt du promoteur sur une phase pré-sulfurée à 400°C sous H_2S pur permet d'obtenir, après une seconde sulfuration (mêmes conditions) un catalyseur 1,4 plus actif qu'un catalyseur préparé par dépôt du Ni sur une phase oxyde. Par ailleurs, ces catalyseurs du type $NiWS/SiO_2$ *ex.* $Ni/WS_{2\text{-}400}/SiO_2$, se sont révélés être plus de 3 fois plus actifs que les références conventionnelles préparées par co-imprégnation de sels de Ni et W. La **Figure 17** représente une comparaison de l'activité intrinsèque en HDS du thiophène (350°C) pour des catalyseurs NiW ou NiMo supportés sur silice ou alumine, préparés par voie conventionnelle et par voie CSC. Elle met en évidence que la vitesse intrinsèque d'HDS d'un catalyseur $NiWS/SiO_2$ (Ni déposé sur WS_2 CSC) est 2,5 fois plus importante que celle d'un catalyseur CSC à base de Mo, et à nouveau, plus de 3 fois supérieure à celle de son homologue dit «conventionnel». Les auteurs ont aussi mis en évidence que pour les catalyseurs conventionnels, la co-imprégnation des précurseurs de W et Ni apporte les meilleurs résultats catalytiques.

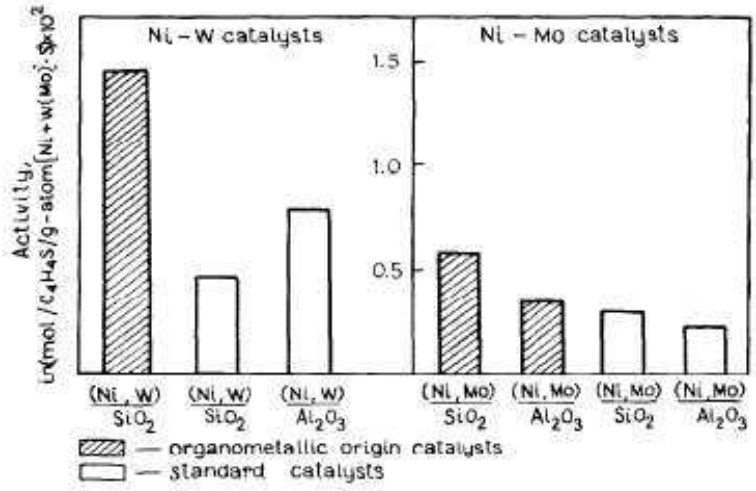

Figure 17 : Activité intrinsèque en HDS du thiophène à 350°C, de catalyseurs NiW et NiMo déposés sur silice ou alumine, en fonction de leur méthode de préparation (d'après Yermakov *et al.*[1984])

Des analyses MET [Zaikovskii *et al.*, 1984] pratiquées sur des catalyseurs NiWS CSC ont permis d'observer des feuillets WS_2 avec une longueur moyenne de 2,5 nm avec un empilement moyen de 2. La présence de particules de tailles inférieures à 1,0 nm, aussi observées par MET par d'autres auteurs, ont été attribuées à des nanoparticules de WS_2 [Zaikovskii *et al.*, 1984] ou à une phase oxysulfure non cristalline WO_xS_y . [Stockmann *et al.*, 1995; Reinhoudt *et al.*, 1998; Kooyman *et al.*, 2001] Okamoto *et al.* [2009] ont d'ailleurs observé que ces particules étaient moins visibles quand la température de sulfuration augmentait.

Des analyses XPS effectuées sur des catalyseurs supportés sur ASA (30 $\%_{pds.}$ SiO_2), préparés par co-imprégnation de $[W(OEt)_5]_2$ et nickel bis-méthylcyclopentadienyl ($Ni(1\text{-}MeCp)_2$), solubilisés dans l'hexane, ont confirmé la présence de phase WS_2, NiWS et NiS [Roukoss *et al.*, 2009]. L'utilisation de ces précurseurs a permis d'améliorer le taux de promotion (*i.e.* la quantité de Ni incorporée dans une phase NiWS) jusqu'à 17 % pour une phase WS_2 déposée par voie CSC. La quantité de phase NiS reste équivalente à celle observée sur des catalyseurs conventionnels.

Ainsi, la littérature montre donc que l'ajout du promoteur augmente significativement l'activité des catalyseurs sulfures. Cependant, il est nécessaire d'adapter la quantité de promoteur ajouté afin d'obtenir un rapport promoteur/métal optimal pour la réaction désirée. D'après les résultats présentés par Yermakov *et al.* [1984] sur des catalyseurs NiW et NiMo déposés sur silice, un rapport atomique Ni/M (at/at) proche de 0,4 (M = W, Mo) permet d'obtenir une activité catalytique maximale en HDS du thiophène (350°C). En HDS du dibenzothiophène, Halbert *et al.* [1991] montre que l'activité n'augmente plus pour des phases CoMoS supportées sur alumine qui présentent un rapport atomique Co/Mo situé entre 0,2 et 0,3.

On peut noter que dans le cas d'un catalyseur d'hydrogénation conventionnel, comme un catalyseur $CoMoS/Al_2O_3$, le rapport Co/Mo maximal à partir duquel la vitesse intrinsèque d'HYD du toluène ($mol_{(toluène)}/mol_{(Mo)}/h$) n'augmente plus se situe vers Co/Mo = 0,3 (at/at). [Gandubert *et al.*, 2008]. Un résultat similaire est obtenu par Marchand *et al.* [Marchand *et al.*, 2009] pour des phases $NiMoS/Al_2O_3$, avec un rapport maximal Ni/Mo (at/at) situé entre 0.2 et 0.3. De précédents travaux réalisés à IFPEn ont quand à eux montré que pour des catalyseurs conventionnels NiWS/ASA, le rapport optimal Ni/W (at/at) était situé entre 0,2 et 0,3. [Raybaud and Toulhoat, 2013, Ed. Technip, Paris] L'influence du support et du promoteur ne semblent

donc pas être significatifs sur la valeur de cet optimum promoteur/métal (ou P/M, avec P = Ni, Co et M = W, Mo).

I.6. Conclusion et stratégie de la thèse

Cette étude bibliographique a mis en avant que l'approche dite de «chimie de surface contrôlée» ou «CSC» est prometteuse pour élaborer de nouveaux catalyseurs d'hydrotraitement plus actifs que les catalyseurs conventionnels. Cette méthode de préparation permet d'améliorer la répartition de la phase métallique sur le support, d'obtenir une quantité plus importante de phase sulfure. De plus cette voie de synthèse entraine une amélioration significative de l'activité catalytique en HDS, aussi bien sur silice, que sur alumine. Le **Tableau 3** liste certains des précurseurs répertoriés dans cette étude bibliographique, leur utilisation, et les résultats d'intérêts.

Lors de la thèse, le support sélectionné pour préparer les premiers catalyseurs sera une silice-alumine amorphe (ASA, 30 $\%_{pds.}$ SiO_2). Ce choix est guidé par la bi-fonctionnalité intéressante des catalyseurs supportés sur ASA (acidité modérée due au support, et fonction hydro-déshydrogénante modérée de la phase sulfure), ainsi qu'aux résultats prometteurs obtenus lors de précédents travaux réalisés à IFPEn, en hydrogénation du toluène.

D'après les travaux présentés dans cette étude bibliographique, il apparait que le dépôt de précurseur de W en phase vapeur ne permet pas d'élaborer des catalyseurs WS_2 très actifs et aisément caractérisables. C'est pourquoi une méthode d'imprégnation sera privilégiée, avec un solvant organique adapté à chaque précurseur métallo-organique.

Comme les espèces de surface de type polyoxométallates (ou clusters de W, présent sur les catalyseurs conventionnels séchés) ou de type WO_3 (oxyde de grande taille, présent sur les catalyseurs calcinés) ne permettent pas d'obtenir d'importantes quantités de phase sulfure : 60$\%_{rel.}$ WS_2 sur ASA, pour un catalyseur NiW/ASA calciné, 4.3 W/nm², Ni/W = 0.4, il semble intéressant d'envisager le dépôt d'espèces de petite taille, pour bénéficier d'une meilleure répartition du tungstène sur la surface, et pour accéder à des taux de sulfuration plus élevés. Pour cela, on privilégiera l'emploi de précurseurs mono ou dinucléaires.

Le large choix de composés métallo-organiques disponibles permettra de sélectionner des précurseurs avec des ligands variés, pouvant réagir facilement avec les hydroxyles de surface du support (ASA), et développant des interactions « précurseur - support » probablement différentes de celles rencontrées jusqu'ici entre les précurseurs conventionnels et les supports couramment utilisés. De plus, l'emploi de molécules pour lesquelles les liaisons «métal – ligand» sont relativement labiles pourrait permettre d'augmenter le taux de sulfuration du tungstène, et éventuellement étudier la genèse de la phase sulfure.

Tableau 3 : Récapitulatif non exhaustif des précurseurs COMS utilisés dans la littérature, et leur intérêt.

Précurseur	Méthode de dépôt	Support	Application	Commentaires	Références
$W(CO)_6$	CVD	Al_2O_3	HDS	Augmentation du taux de recouvrement en W = diminution de la dispersion du W	Suvanto *et al.*, 1999
$Co(CO)_3NO$	CVD	SiO_2	HDS	Sulfuration plus aisée, activité intrinsèque des phases CoWS supérieure à celle des phasesCoMoS	Okamoto *et al*., 2009
$Co(CO)_3NO$	CVD	Al_2O_3	HDS	Promoteur organométallique = activité intrinsèque des phases CoMoS X 2 en HDS - pas d'amélioration de l'activité HYD	Maugé *et al.*, 1989
$W(OEt)_5$	n-hexane	ASA	HDS	Augmentation du taux de sulfuration du W et de la dispersion de WS_2 en surface	Roukoss, 2009
$W(CO)_6$	n-hexadécane + ultrasons	Al_2O_3	HDS	Pas de différence d'activité (HDS) *vs.* catalyseurs conventionnels	Vishwakarma *et al.*, 2007
$W(C_4H_7)_4$	pentane	SiO_2	HDS	Meilleure sulfuration du W et augmentation "dispersion" de WS_2 en surface + activité HDS	Yermakov *et al.*, 1984
$Ni(MeCp)_2$	n-hexane	ASA	HYD	Augmente la quantité de phase promue	Roukoss, 2009
$Ni(C_3H_5)_2$	pentane	SiO_2	HDS	Phase $NiWS_{(CSC)}$: vitesse intrinsèque HDS *X* 3 *vs.* NiWS conventionnels	Yermakov *et al.*, 1984
$Co_2(CO)_8$	n-hexadécane + ultrasons	Al_2O_3	HDS	Pas d'augmentation significative de l'activité HDS (phase CoWS)	Vishwakarma *et al.*, 2007
$Co_2(CO)_8$	hexane	Al_2O_3	HDS/HDN	Meilleure activité HDS pour des catalyseurs $Co_{(CSC)}/MoS_2$ Rapport Co/Mo (at/at) = 0,2-0,3 optimal pour les réactions d'HDS. Moins bonnes performances HDN que les ref. classiques.	Halbert *et al.*, 1991
$Co_2(CO)_8$	CVD	Al_2O_3	HDS	Augmentation de l'activité intrinsèque en HDS	Suvanto *et al.*, 1999
$W(CO)_6$	CVD	Al_2O_3	-	Présence de $W(CO)_6$ physisorbé en surface	Suvanto *et al.*, 1999; Reddy and Brown, 1995; Zecchina *et al.*, 1990
$W(CO)_6 + PPh_3$	Pentane + ultraviolets	Al_2O_3	-	Dépôt facilité par photo-irradiation du complexe en présence de PPh_3	Baibich *et al*., 1997
$W(CO)_6 + PPh_3$	Pentane + ultraviolets	Al_2O_3	Conversion de NO en N_2		Sica *et al.*, 1999
$W(OEt)_5$	n-hexane	Charbon actif	Isomérisation du 1-butène	Dispersion du W améliorée	Perez-Cadenas *et al.*, 2003
$W(CO)_6$	CVD	Charbon actif			Perez-Cadenas *et al.*, 2003

Afin d'étudier la réactivité de complexes métallo-organiques pour lesquels le tungstène présente deux états d'oxydation extrêmes, nous avons sélectionné des précurseurs dans lesquels le métal possède un degré d'oxydation 0, +V et +VI, mais nous étudierons plus particulièrement ceux au sein desquels le métal est au degré d'oxydation +V ou +VI. On emploiera donc au moins un précurseur où le tungstène est partiellement réduit (degré d'oxydation +V), afin de vérifier si son utilisation permet de mieux sulfurer le W. Enfin,

l'utilisation d'un précurseur moléculaire où le tungstène est au degré d'oxydation +VI permettra notamment de comparer l'effet de la nucléarité du précurseur de W, en s'affranchissant d'un éventuel effet du degré d'oxydation. Une liste des précurseurs étudiés est présentée **Figure 18**.

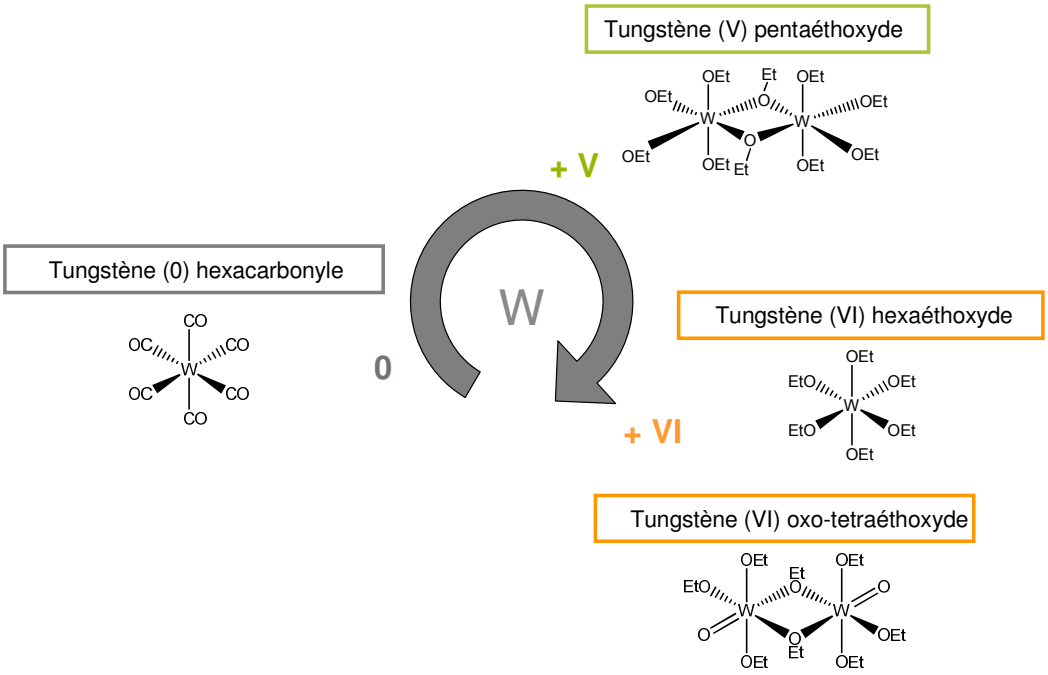

Figure 18 : Liste de différents précurseurs métallo-organiques de W, présélectionnés pour être déposés sur ASA.

Dans le cas de la préparation de catalyseurs promus NiW, on pourra envisager d'introduire le précurseur de Ni en co-imprégnation avec le précurseur de W, ou directement sur une phase oxyde de tungstène, ou bien encore directement sur une phase pré-sulfurée. Le dépôt par imprégnation sera privilégié, comme pour la préparation des matériaux non promus.

Une fois les matériaux préparés (imprégnation, séchage…), ils seront convertis en catalyseurs (après sulfuration) et des tests catalytiques sur molécule modèle (hydrogénation du toluène en présence d'aniline) permettront de discriminer les meilleurs précurseurs métalliques. Nous chercherons à mettre en évidence le moteur de la sulfuration en nous appuyant sur une approche combinant caractérisations spectroscopiques (IR, XPS) et microscopie électronique (TEM-BF, STEM-HAADF), afin d'évaluer la force motrice du processus de sulfuration des

espèces CSC, comparativement aux espèces conventionnellement rencontrées, de type hétéro-polyanioniques ou oxyde de tungstène (WO_3).

La spectroscopie IR et la modélisation moléculaire (au travers du monomère $W(OEt)_5$) permettront de vérifier si le précurseur déposé est greffé ou simplement physisorbé à la surface du support. L'étude par spectroscopie IR avant et après dépôt du précurseur donnera des informations quant aux interactions entre les hydroxyles du support, et le précurseur. L'analyse du spectre permettra aussi de visualiser les bandes de vibrations apparues après dépôt du précurseur, et de les attribuer aux espèces présentes sur le matériau.

La spectroscopie XPS permettra quant à elle d'estimer le degré d'oxydation des espèces de surface, et de quantifier les différentes phases observées. Cela permettra d'améliorer la compréhension des composés présents sous forme oxyde comme sous forme sulfure (WS_2, WO_xS_y, WO_3). Nous pourrons aussi accéder à la répartition du tungstène sur le support (vue par XPS), notamment par le calcul du rapport atomique moyen W/Al (ou W/Si). Enfin, pour les catalyseurs promus cette technique permettra aussi de déterminer la quantité de promoteur engagé dans une phase mixte « NiWS » et de connaitre le rapport atomique moyen Ni/W dans les feuillets WS_2.

De plus, l'analyse par microscopie électronique à transmission permettra d'accéder aux caractéristiques des cristallites WS_2 : longueur moyenne et empilement moyen. La réalisation d'analyses par STEM-HAADF sera un plus pour accéder à la morphologie 2D des cristallites. Cette analyse sera couplée à l'approche de modélisation moléculaire pour interpréter les tendances observées.

Comme précisé en introduction, la partie II de ce manuscrit sera consacrée aux différentes techniques expérimentales et à la description de la préparation des matériaux et des catalyseurs utilisés. Les parties III, IV et V traiteront de la préparation et de la caractérisation des matériaux non sulfurés, et des catalyseurs non promus respectifs (sulfurés), à base de tungstène. Cette étude sera complétée par la partie VI, qui présentera la préparation et la caractérisation des matériaux et catalyseurs promus par du nickel. Enfin, une conclusion générale regroupera les résultats essentiels de ces travaux, et permettra de proposer des perspectives.

Par ailleurs, l'étude du dépôt de $W(CO)_6$ sur ASA et alumine est disponible dans les annexes.

I.7. Références bibliographiques

Baibich, I.M.; Dos Santos, J.H.Z.; Stedile, F.C.; Santarosa, V. E. and Baumvol, I.J.R., *Polyhedron* (1997), **16**, 1937-1943

Basset, J.M. and Choplin, A., *Journal of Molecular Catalysis* (1983), **21**, 1-3, 95-108

Basset, J.M.; Copéret, C.; Soulivong, D.; Taoufik, M. and Thivolle-Cazat, J., *Account of Chemical Research* (2010), **43**, 2, 323-334

Ben Tayeb, PhD thesis, Université des Sciences et Technologies de Lille (2009)

Blanc, F.; Berthoud, R.; Salameh, A.; Basset, J.M.; Copéret, C.; Singh, R. and Schrock, R.R., *Journal of the American Chemical Society* (2007), **129**, 8434

Brenner, A. and Burwell Jr, L., *Journal of Catalysis* (1978), 52, 353-363

Breysse, M.; Cattenot, M.; Decamp, T.; Frety, Roger; Gachet, C.; Lacroix, M.; Leclercq, C.; de Mourgues, L., Portefaix, J.L.; Vrinat, M.; Houari, M.; Grimblot, J.; Kasztelan, S.; Bonnelle, J.P.; Housni, S.; Bachelier, J. and Duchet, J.C., *Catalysis Today* (1988), **4**, 39-55

Busca, G.; Lorenzelli, V.; Ramis, G. and Willey, R. J., *Langmuir* (1993), **9**, 1492-1499

Carlsson, A.; Brorson, M. and Topsøe, H., *Journal of Microscopy* (2006), **223**, 3, 179-181

Carrier, X.; Lambert, J. F. and Che, M., *Journal of the American Chemical Society* (1997), **119**, 10137-10146

Chizallet, C. and Raybaud, P. *Angewandte Chemie International Edition* (2009), **48**, 16, 2891-2893

Choi, J.S.; Petit-Clair, C. and Uzio, D., Controlled surface modification of alumina-supported Mo and Co-Mo sulfides by surface organometallic chemistry, *Proceedings of the 8th International Symposium*, 143, Edition Gaigneaux, E. (2000), 585-592, Elsevier

Chung, J.W.; Dai, Z.R. and Ohuchi, F.S., *Journal of Crystal Growth* (1998), **186**, 137-150

Copéret, C.; Chabanas, M.; Petroff Saint-Arroman, R. and Basset, J.M., *Angewandte Chemie International Edition* (2003), **42**, 2, 156-181

Corker, J.; Lefebvre, F.; Lécuyer, C.; Dufaud, V.; Quignard, F.; Choplin, A.; Evans, J. and Basset, J.M., *Science* (1996), **271**, 5251, 966-969

Crépeau, G.; Montouillout, V.; Vimont, A.; Mariey, L.; Cseri, T. and Maugé, F., *The Journal of Physical Chemistry B* (2006), **110**, 31, 15172-15185

Davie, E.S.; Whan, D.A. and Kemball, C., *Journal of Catalysis* (1972), **24**, 272-282

Deepak, F.L.; Esparza, R.; Borges, B.; Lopez-Lozano, X. and Jose-Yacaman, M., *ACS Catalysis* (2011), **1**, 5, 537-543

Digne, M.; Sautet, P.; Raybaud, P.; Euzen, P. and Toulhoat, H., *Journal of Catalysis* (2004), **226**, 54-68

Directive européenne 2009/30/CE de 2009 modifiant la directive 98/70/CE de 1998

Dugulan, A.I.; Hensen, E.J.M. and van Veen, J.A.R., *Catalysis Today* (2010), **150**, 3-4, 224-230

E.S. Davie, E.S., Whan, D.A. and Kemball, C., *Journal of Catalysis* (1972), **24**, 2, 272-282

Eisen, S. and Marks, T.J., *Journal of Molecular Catalysis* (1994), **86**, 23-50

Fraile, J.M.; García, J.; Mayoral, J.A.; Proietti, M.G. and Sánchez, M.C., *The Journal of Physical Chemistry* (1996), **100**, 50, 19484-19488

Gandubert, A.D.; Krebs, E.; Legens, C.; Costa, D.; Guillaume, D. and Raybaud, P. *Catalysis Today* (2008), **130**, 1, 149–159

Garrone, E.; Onida, B.; Bonelli, B.; Busco, C. and Ugliengo, P., *The Journal of Physical Chemistry B* (2006), **110**, 19087-19092

Gora-Marek, K.; Derewinski, M.; Sarv, P. and Datka, J., *Catalysis Today* (2005), **101**, 131-138

Grau, E; Lesage, A.; Norsic, S.; Copéret, C.; Monteil, V. and Sautet, P., *ACS Catalysis* (2013), **3**, 52

Guernalec, N.; Geantet, C.; Raybaud, P.; Cseri, T.; Aouine, M. and Vrinat, M., *Oil & Gas Science and Technology – Rev. IFP* (2006), **61**, 4, 515-525

Halbert, T.R.; Ho, T.C.; Stiefel, E.I.; Chianelli, R.R. and Daage, M., *Journal of Catalysis* (1991), **130**, 1, 116-129

Harvey, T.G.; and Matheson, T.W., *Journal of Catalysis* (1986), **101**, 2, 253-261

Helveg, S.; Lauritsen, J.V.; Laegsgaard, E.; Stensgaard, I.; Norskov, J.K.; Clausen, B.S.; Topsøe, H. and Besenbacher, F. *Physical Review Letters* (2000), **84**, 5, 951-954

Hensen, E.J.M.; van der Meer, Y.; van Veen, J.A.R. and Niemantsverdriet, J.W., *Applied Catalysis A: General* (2007), **322,** 0, 16-32

http://energie.sia-partners.com

Iengo, P.; Di Serio, M.; Solinas, V.; Gazzoli, D.; Salvio, G. and Santacesaria, E., *Applied Catalysis A: General* (1998), **170**, 225-244

Ishihara, A.; Nomura, M. and Kabe, T., *Journal of Catalysis* (1994), **150**, 1, 212-216

Jaenicke, S. and Loh, W. L., *Catalysis Today* (1999), **49**, 123-130

Joubert, J.; Delbecq, F; Sautet, P.; Le Roux, E.; Taoufik, M.; Thieuleux, C.; Blanc, F.; Copéret, C.; Thivolle-Cazat, J. and Basset J.M., *Journal of the American Chemical Society* (2006), **128**, 9157

Kasztelan, S.; Grimblot, J.; Bonnelle, J.P.; Payen, E.; Toulhoat, H. and Jacquin,Y. *Applied Catalysis* (1983), **7**, 1, 91-112

Kasztelan, S.; Toulhoat, H.; Grimblot, J. and Bonnelle, J. P., *Applied Catalysis* (1984), **13**, 127-159

Kaufmann, T.G.; Kaldor, A.; Stuntz, G.F.; Kerby, M.C. and Ansell, L.L., *Catalysis Today* (2000), **62**, 1, 77-90

Kim, D.S.; Ostromecki, M. and Wachs, I.E., *Journal of Molecular Catalysis A: Chemical* (1996), **106**, 1-2, 93-102

Knözinger, H. and Ratnasamy, P., *Catalysis Reviews, Science and Engineering* (1978), **17**, 31

Kooyman, P.J.; Hensen, E.J.M.; De Jong, A.M.; Niemantsverdriet, J.W.; and van Veen, J.A.R., *Catalysis Letters* (2001), **74**, 1-2, 49-53

Krokidis, X.; Raybaud, P.; Gobichon, A.E.; Rebours, B.; Euzen, P. and Toulhoat, H., *The Journal of Physical Chemistry B* (2001), **105**, 5121-5130

Kurhinen, M. and Pakkanen, T.A., *Applied Catalysis A: General* (2000), **192**, 1, 97-103

Larabi, C.; Nielsen, P.K.; Helveg, S.; Thieuleux, C.; Johansson, F.B.; Brorson, M. and Quadrelli, E.A., *ACS Catalysis* (2012), **2***,* 4, 695-700

Lauritsen, J.V.; Bollinger, M.V.; Laegsgaard, E.; Jacobsen, K.W.; Nørskov, J.K.; Clausen, B.S.; Topsøe, H.; and Besenbacher,F. *Journal of Catalysis* (2004), **221**, 2, 510–522

Lauritsen, J.V.; Helveg, S.; Laegsgaard, E.; Stensgaard, I.; Clausen, B.S.; Topsøe, H. and Besenbacher, F., *Journal of Catalysis* (2001), **197**, 1, 1-5

Le Roux, E.; Taoufik, M.; Baudouin, A., Copéret, C.; Thivolle-Cazat, J.; Basset J.M.; Maunders, B.M. and Sunley, G.J., *Advanced Synthesis & Catalysis* (2007), **349**, 231

Le Roux, E.; Taoufik, M.; Chabanas, M.; Alcor, D.; Baudouin, A.; Copéret, C.; Thivolle-Cazat, J.; Basset, J.M.; Lesage, A.; Hediger, S. and Emsley, L., *Organometallics* (2005), **24**, 17, 4274-4279

Le Roux, E.; Taoufik, M.; Copéret, C.; de Mallmann, A.; Thivolle-Cazat, J.; Basset, J.M., Maunders, B.M. and Sunley G.J., *Angewandte Chemie International Edition* (2005), **44**, 6745

Lefort, L.; Chabanas, M; Maury, O; Meunier, D.; Copéret, C.; Thivolle-Cazat, J. and Basset, J.M., *Journal of Organometallic Chemistry* (2000), **593-594**, 96.

Leydier, F.; Chizallet, C.; Chaumonnot, A.; Digne, M.; Soyer, E.; Quoineaud, A.A.; Costa, D. and Raybaud, P., *Journal of Catalysis* (2011), **284**, 215-229

Maeyama, K. and Iwasawa, N., *The Journal of Organic Chemistry* (1999), **64**, 1344-1346

Marchand, K.; Legens, C.; Guillaume, D.; and Raybaud, P., *Oil & Gas Science and Technology – Rev. IFP* (2009), **64**, 6, 719-730

Maugé, F.; Vallet, A.; Bachelier, J.; Duchet, J.C. and Lavalley, J.C., *Catalysis Letters* (1989), **2**, 1, 57-61

Maugé, F. and Lavalley, J.C., *Journal of Catalysis* (1992), **137**, 69-76

Mazoyer, E.; Merle, N.; de Mallmann, A.; Basset, J.M.; Berrier, E.; Delevoye, L.; Paul, J.F.; Nicholas, C.P.; Gauvin, R.M. and Taoufik, M., *Chemical Communications* (2010), **46**, 47, 8944-8946

Menéndez-Proupin, E. and Gutiérrez, G., *Physical Review B* (2005), **72**, 035116

Mochida, I.and Choi, K.H., *Journal of the Japan Petroleum Institute* (2004), **47**, 3, 145-163

Moses, P.G.; Hinnenman, B., Topsøe, H. and Nørskov, J.K. *Journal of Catalysis* (2007), **248**, 8, 188-203

Norme euro 6. Règlement (UE) n°459/2012 de la commission du 29 mai 2012 modifiant le règlement (CE) n°715/2007 du Parlement Européen et du Conseil ainsi que le règlement (CE) n° 692/2008 de la Commission en ce qui concerne les émissions des véhicules particuliers et utilitaires legers

Okamoto, Y.; Kato, A.; Usman, Sato, K.; Hiromitsu, I. and Kubota, T. *Journal of Catalysis* (2005), **233**, 1, 16-25

Okamoto, Y.; Kato, A.; Usman; Rinaldi, N.; Fujikawa, T.; Koshika, H.; Hiromitsu, I. and Kubota, T., *Journal of Catalysis* (2009), **265**, 2, 216-228

Ouafi, D.; Maugé, F.; Lavalley, J.C.; Payen, E.; Kasztelan, S.; Houari, M.; Grimblot, J. and Bonnelle, J.P., *Catalysis Today* (1988), **4**, 1, 23-37

Payen, E.; Kasztelan, S.; Grimblot, J. and Bonnelle, J.P. *Catalysis Today* (1988), **4**, 57-70

Pecoraro, T.A. and Chianelli, R.R., *Journal of Catalysis* (1981), **67**, 2, 430-445

Perez-Cadenas, A.F.; Moreno-Castilla, C.; Maldonado-Hodar, F.J. and Fierro, J.L.G., *Journal of Catalysis* (2003), **217**, 30-37

Peri, J. B., *The Journal of Physical Chemistry* (1965), **69**, 220-230

Petroff Saint-Arroman, R.; Didillon, B.; de Mallmann, A.; Basset, J.M. and Lefebvre, F., *Applied Catalysis A: General* (2008), **337**, 1, 78-85

Pinto, H.P.; Nieminen, R.M. and Elliot, S.D., *Physical Review B* (2004), **70**, 125402, 1-11

Portela, L.; Grange, P. and Delmon, B., *Journal of Catalysis* (1995), **156**, 2, 243-254

Prodhomme, P.Y.; Raybaud, P. and Toulhoat, H. *Journal of Catalysis* (2011), **280**; 178–195

Rascon, F.; Wischert, R. and Copéret, C., *Chemical Science* (2011), **2**, 8, 1449-1456

Rataboul, F.; Baudouin, A.; Thieuleux, C.; Veyre, L.; Copéret, C.; Thivolle-Cazat, J.; Basset, J.M.; Lesage, A. and Emsley, L., *Journal of the American Chemical Society* (2004), **126**, 39, 12541-12550

Raybaud, P. and Toulhoat, H., Catalysis by transition metal sulphides (2013), Editions Technip, Paris

Reddy, K. P. and Brown, T. L., *Journal of the American Chemical Society* (1995), **117**, 2845-2854

Reinhoudt, H.R.; Crezee, E.; van Langeveld, A.D.; Kooyman, P.J.; van Veen, J.A.R. and Moulijn, J.A., *Journal of Catalysis* (2000), **196**, 2, 315-329

Reinhoudt, H.R.; van Langeveld, A.D.; Kooyman, P.J.; Stockman, R.M.; Prins, R.; Zandbergen, H.W. and Moulijn, J.A., *Journal of Catalysis* (1998), **179**, 2, 443-450

Rendón, N.; Berthoud, R.; Blanc, F.; Gajan, D.; Maishal, T.; Basset, J.M.; Copéret, C.; Lesage, A.; Emsley, L.; Marinescu, S.C.; Singh, R. and Schrock, R.R., *Chemistry - A European Journal* (2009), **151**, 5083

Rosier, C.; Niccolai, G.P. and Basset, J.M., *Journal of the American Chemical Society* (1997), **119**, 50, 12408–12409

Scheffer, B.; Dekker, N.J.J.; Mangnus, P.J. and Moulijn, J. A., *Journal of Catalysis* (1990), **121**, 31-46.

Schulz, H.; Bohringer, W.; Ousmanov, F. and Waller, P., *Fuel Processing Technology* (1999), **61**,1-2, 5-41

Schweiger, H.; Raybaud, P. and Toulhoat, H., *Journal of Catalysis* (2002), **212**, 1, 33-38

Schweiger, H.; Raybaud, P.; Kresse, G. and Toulhoat, H., *Journal of Catalysis* (2002), **207**, 1, 76-87

Sica, A. M.; Dos Santos, J.H.Z.; Baibich, I.M. and Gigola, C.E., *Journal of Molecular Catalysis A: Chemical* (1999), **137**, 287-295

Siegel, S., *Journal of Catalysis* (1973), **30**, 139-145

Stanislaus, A. and Cooper, B.H., *Catalysis Reviews* (1994), **36**, 1, 75-123

Stockmann, R.M.; Zandbergen, H.W.; van Langeveld, A.D. and Moulijn, J.A., *Journal of Molecular Catalysis A: Chemical* (1995), **102**, 3, 147, 161

Sun, M.; Bürgi, T., Cattaneo, R. and Prins, R., *Journal of Catalysis* (2001), **197**, 172-181

Suvanto, M. and Pakkanen, T.A., *Applied Catalysis A: General* (1998), **166**, 1 105-113

Suvanto, M.; Räty, J. and Pakkanen, A., *Applied Catalysis A: General* (1999), **181**, 189-199

Thomas, T.J. and Brenner, A., *Journal of Molecular Catalysis* (1983), **18**, 2, 197-202

Topsøe, H. and Clausen, B.S., *Applied Catalysis* (1986), **25**, 1-2, 273-293.

Topsøe, H.; Clausen, B.S.; Candia, R.; Wivel, C. and Morup, S. *Journal of Catalysis* (1981), **68**, 2, 433-452

Topsøe, H.; Hinnemann, B.; Nørskov, J.K.; Lauritsen, J.V.; Besenbacher, F.; Hansen, P.L.; Hytoft, G.; Egeberg, R.G. and Knudsen, K.G., *Catalysis Today* (2005), **107–108**, 12–22

Topsøe, N.Y. and Topsøe, H., *Journal of Catalysis* (1986), **84**, 2, 386-401

Toulhoat, H. and Raybaud, P., *Catalysis Today* (1999), **50**, 3-4, 629-636

Trombetta, M.; Busca, G.; Rossini, S.; Piccoli, V.; Cornaro, U.; Guercio, A.; Catani, R. and Willey, R.J., *Journal of Catalysis* (1998), **179**, 581-596

van der Meer, Y.; Hensen, E.J.M.; van Veen, J.A.R. and van der Kraan, A.M., *Journal of Catalysis* (2004), **228**, 2, 433, 446

van der Vlies, A. J.; Prins, R. and Weber, T., *The Journal of Physical Chemistry B* (2002), **106**, 36, 9277-9285

van der Vlies, A.J.; Kishan, G.; Niemantsverdriet, J.W., Prins, R. and Weber, T., *The Journal of Physical Chemistry B* (2002), **106**, 13, 3449-3457

van Veen, J.A.R.; Gerkema, E.; van der Kraan, A.M.; Hendriks, P.A.J.M. and Beens, H., *Journal of Catalysis* (1992), **133**, 1, 112-123.

Vansant, E.F., Characterization and Chemical modification of the silica surface, Elsevier, New-York, 1995

Vazquez, P.; Pizzio, L.; Blanco, M.; Caceres, C.; Thomas, H.; Arriagada, R.; Bendezu, S.; Cid, R. and Garcia, R., *Applied Catalysis A: General* (1999), **184**, 2, 303-313

Vidal, V.; Théolier, A.; Thivolle-Cazat, J. and Basset, J.M., *Science* (1997), **276**, 5309, 99-102

Vishwakarma, S.K.; Sundaramurthy, V.; Dalai, A.K. and Adjaye, J., *Industrial & Engineering Chemistry Research* (2007), **46**, 14, 4778-4786

Vissenberg, M.J.; J. Joosten, L.J.M.; Heffels, M.M.E.H.; van Welsenes, A.J.; (San) de Beer, V. H. J.; van Santen, R.A. and van Veen, J.A.R., *The Journal of Physical Chemistry* B (2000), **104**, 35, 8456–8461

Wegener, S.L.; Marks, T.J. and Stair, P.C, *Accounts of Chemical Research* (2011), **45**, 2, 206, 214

Wischert, R.; Copéret, C.; Delbecq, F. and Sautet, P., *Angewandte Chemie International Edition* (2011), **50**, 14, 3202-3205

Wolke, S.I.; Buffon, R. and Filho, U.P.R., *Journal of Organometallic Chemistry* (2001), **625**, 101

Yermakov Y.I. and Kuznetsov B.N. *Kinetika i Kataliz* (1972), **13**, 1355-1356.

Yermakov, Y.I.; Kuznetsov, B.N.; Startsev, A.N.; Zhdan, P.A.; Shepelin, A.P.; Zaikovskii, V.I.; Plyasova, L.M. and Burmistrov, V.A., *Journal of Molecular Catalysis* (1981), **11**, 2-3, 205-214

Yermakov, Y.I.; Startsev, A.N. and Burmistrov, V.A., *Applied Catalysis* (1984), **11**, 1, 1-13

Zaikovskii, V.I.; Plyasova, L.M.; Burmistrov, V.A.; Startsev, A.N. and Yermakov,Y.I., *Applied Catalysis* (1984), **11**, 1, 15-27

Zecchina, A.; Bordiga, S.; Escalona Platero, E. and Otero Arean, C., *Journal of Catalysis* (1990), **125**, 568-570

Zuravlev, L.T., *Colloids and Surfaces A: Physicochemical and Engineering Aspects* (2000), **173**, 1-38

Part II. Experimental

Outline (Part II)

Outline (Part II) **71**

II.1. Products and materials **73**

II.2. Characterisation **73**
II.2.a. Nuclear magnetic resonance (NMR) 73
II.2.b. X-ray photoelectron spectroscopy (XPS) 74
II.2.c. Fourier transform infrared spectroscopy (FT-IR) 76
II.2.d. Carbon monoxide adsorption at 77K, monitored by FT-IR (IR(CO)) 77
II.2.e. Transmission electron microscopy (TEM) and Scanning transmission electron microscopy (STEM) 77
II.2.f. Other analyses 77

II.3. Preparation of supported W alkoxide materials **79**
II.3.a. Preparation of ASA-supported materials 79
II.3.b. Preparation of SiO_2-supported materials 85
II.3.c. Preparation of Al_2O_3-supported materials 85
II.3.d. Preparation of conventional dried and calcined materials 86

II.4. Preparation of non-promoted sulphide materials (bulk) **87**

II.5. Synthesis of non-promoted sulphide catalysts supported on ASA **87**

II.6. Preparation of nickel-promoted materials **89**
II.6.a. Preparation of conventional dried and calcined oxide materials 89
II.6.b. Preparation of CSC materials, prior to sulphidation 89

II.7. Preparation of nickel-promoted sulphide catalysts **92**

II.8. Catalytic test **92**

II.9. References **93**

II.1. Products and materials

All experiments were carried out by using standard Schlenk and glove-box techniques. Solvents were purified and dried by a solvent purification system (SPS-M-Braun) before being freeze-pumped and stored over 4 Å molecular sieves under argon. Dry ethanol was purchased from Sigma Aldrich, and was also degassed and stored over 4 Å molecular sieves under argon. $[W(OEt)_5]_2$ (94%), $W(OEt)_6$, $Ni(1\text{-}MeCp)_2$ (97%) and ammonium tetrathiotungstate were obtained from Alfa Aesar. $W(CO)_6$ (99%) and anhydrous $Ni(acac)_2$ (95%) were purchased from Strem, $Ni(NO_3)_2,xH_2O$ from Sigma Aldrich, and $CH_3{}^{13}CH_2OH$ (99% ^{13}C labelled) from Cortecnet. Ammonium metatungstate was obtained from AXENS. $W(O)(OEt)_4$ was prepared as described in the literature [Lomonosov, 1985]. All chemical products were used as received. γ-Al_2O_3, SiO_2 and amorphous SiO_2-Al_2O_3 (30 $\%_{wt.}$ SiO_2) were purchased from industrial partners. $SiO_{2\text{-}700}$ (Aerosil®) was kindly obtained from F.Heroguel, from ETH Zürich.

II.2. Characterisation

II.2.a. Nuclear magnetic resonance (NMR)

Solution NMR spectra were recorded on an AM-300 Brüker spectrometer. All chemical shifts are reported in (δ) ppm *vs.* $SiMe_4$ and were measured relative to residual ^1H or ^{13}C resonance in the deuterated solvents [Fulmer *et al.*, 2010].

All solid-state NMR spectra (performed at IFPEn) were recorded on a Bruker Avance 400 spectrometer equipped with a standard 4-mm CPMAS double-bearing probe head and operating at 75.47 and 300.18 MHz for ^{13}C and ^1H respectively. Solid-state NMR spectra recorded at ETH Zurich were recorded on a Bruker Avance 700, equipped with a standard 4-mm CPMAS double-bearing probe head and operating at 176.05 and 700.13 MHz for ^{13}C and ^1H. The samples were introduced in the rotor made of zirconia in a glove box and tightly closed. Compressed air was used for both bearing and driving the rotors. Anisotropic dipolar interactions were suppressed by rotating the sample about an axis oriented at 54.74° with respect to the external field, called the Magic Angle Spinning (MAS). In ^1H MAS spectra, the delay between each scans was fixed from 1 to 10 s, to allow for the complete relaxation of the ^1H nuclei. For ^{13}C CPMAS NMR experiments, a typical cross-polarization (CP) sequence was used to improve the signal/noise ratio: 90° rotation of the ^1H magnetization (impulsion length, 3.8 μs), and then contact between carbon and proton during T_c ranging from 1.2 to 1.5 ms, and

finally recording of the spectrum under high-power decoupling. The recycling delay between each scans was fixed to 20 s. ^{13}C-^{1}H Heteronuclear Correlation (HETCOR) MAS NMR analyses were performed at ETH Zurich. Typically, more than 1.5k scans were recorded for the HETCOR spectra, using a Decoupling Using Mind Boggling Optimization (DUMBO) NMR sequence [Brown *et al.*, 2004], with 128 increments, a recycling delay of 1 sec, and a contact time between carbon and proton set to 1.5 ms. Chemical shifts are given with the respect to TMS. All chemical shifts are reported in (δ) ppm

II.2.b. X-ray photoelectron spectroscopy (XPS)

XPS sampling of the sulphide catalysts was performed in a glove box under argon atmosphere, with controlled oxygen and water level in order to avoid their partial reoxidation. The samples were crushed and pressed onto an indium foil attached to the sample holder *via* a double side carbon tape. The sample holder was then moved directly to the introduction chamber of the XPS spectrometer, thanks to the special connection between the glove box and the XPS spectrometer. XPS spectra were recorded on a Kratos Axis Ultra instrument with an Al monochromator source (1486.6 eV) and a hemi-spherical analyzer operating at fixed pass energy of 40 eV. The measurements were made at ambient temperature in steps of 0.05 eV for nickel, 0.1 eV for sulphur and 0.1 eV for tungsten, and at a pressure lower than 1.10^{-6} Pa in the sample analysis chamber. Binding energies (BE) of the various elements were referenced to the C 1s level of the contamination carbon at 284.6 eV. The curves were integrated applying a Shirley type baseline for sulphur and tungsten, and linear type baseline for nickel, carbon, oxygen, and aluminium. A Tougaard type baseline was used for silicium. The collected spectra were analyzed by using Vision2 XPS software. Decomposition of the S 2p, W 4f and Ni 2p XPS spectra were performed using the appropriate oxide and sulphide references as supported monometallic catalysts. The methodology, similar to that developed for CoMo [Gandubert *et al.*, 2006; Gandubert *et al.*, 2008] and NiMo [Guichard *et al.*, 2008], has already been described elsewere [Ben Tayeb *et al.*, 2010]

Briefly, the relative atomic concentration C_i of the atom i was obtained from the measurement of the corresponding total peak area A_i and the use of appropriate sensitivity factor RSF furnished by the constructor.

To approach the relative atomic surface concentrations, all the atoms detected on the surface were taken into account in **Eq. 1**.

$$C_i = \frac{A_i / RSF_i}{\sum_{i=1}^{i=n} (A_i / RSF_i)} \qquad \textbf{Eq. 1}$$

For one atom, the signal obtained can be decomposed into different contributions relative to various chemical species. The calculation of the respective contribution of each peak area will lead to the knowledge of the relative proportion of each chemical form for a given atom. For example, in the case of W, W 4f photopeak decomposition exhibits 3 contributions attributed to W(VI) oxide (W $4f_{7/2}$ = 36.0 eV, W $4f_{5/2}$ = 38.1 eV), to W(IV) sulphide (W $4f_{7/2}$ = 32.2 eV, W $4f_{5/2}$ = 34.3 eV) [Kim *et al.*, 1996; Reinhoudt *et al.*, 2000; Sun *et al.*, 2001; Zuo *et al.*, 2004] and to W(V) oxisulphide WO_xS_y (W $4f_{7/2}$ = 33.5 eV, W $4f_{5/2}$ = 35.5 eV) [Hensen *et al.*, 2007]. Note this latter contribution as also been tentatively attributed to WS_3 species [Coulier *et al.*, 2002; Hensen *et al.*, 2007]. The relative amount of WS_2 phase, also called **"level of sulphidation"** is given by **Eq. 2**:

$$WS_2 = \frac{A_{WS2}}{A_{WS2} + A_{WOxSy} + A_{WO3}} x100 \qquad \textbf{Eq. 2}$$

The sulphidation level is described as the relative amount of W in a WS_2 phase.

Average results found for peculiar binding energies (BE) of W 4f and S 2p photopeaks are summarized as follows:

	BE (eV) W $4f_{7/2}$ – **W(IV)**	BE (eV) W $4f_{7/2}$ – **W(VI)**	FWHM (eV) **W(IV)**	ΔBE (eV) (W $4f_{7/2}$ **W(IV)** – S $2p_{3/2}$ **(S-II)**
Mean value	32.2	35.9	1.2	129.6
±	0.1	0.1	0.1	0.1

In the case of Ni atoms detected as Ni(II), NiWS and Ni_xS_y, the **"promotion level"** expressed as the relative amount of Ni incorporated in NiWS phase is given by **Eq. 3**:

$$Ni\ promotion\ level\ [\%] = \frac{A_{NiWS}}{A_{Ni\ total}}\ x\ 100 \qquad \textbf{Eq. 3}$$

with $A_{Ni\ total} = A_{NiWS} + A_{Ni(II)} + A_{NixSy}$ the experimental XPS area of, respectively, NiWS, Ni(II) and Ni_xS_y species. We can then deduce the effective amount of NiWS phase noted C_{NiWS} by multiplying the relative value with the total Ni content (4).

$$C_{NiWS} = C_{Ni\ total}\ x\ \frac{Ni\ promotion\ level}{100} \qquad \textbf{Eq. 4}$$

Average results found for peculiar binding energies (BE) of W 4f and Ni 2p photopeaks are summarized as follows:

	BE (eV) Ni $2p_{3/2}$ **NiWS**	BE (eV) Ni $2p_{3/2}$ **Ni_xS_y**	BE (eV) Ni $2p_{3/2}$ **Ni(II)**	ΔBE (eV) W $4f_{7/2}$ **W(IV)** *vs.* Ni $2p_{3/2}$ **(NiWS)**	ΔBE (eV) Ni $2p_{3/2}$ **NiWS** *vs.* Ni $2p_{3/2}$ **Ni_xS_y**	FWHM **(NiWS)** / FWHM **(Ni_xS_y)**
Mean value	853.7	852.6	856.4	821.5	1.1	1.5
Sdt. err.	0.1	0.1	0.2	0.1	0.1	0.2

II.2.c. Fourier transform infrared spectroscopy (FT-IR)

FT-IR spectra of self–supporting pellets (*ca.* 2.03 cm^2) were recorded at IFPEn on a ThermoFisher Scientific Nicolet Nexus 2 spectrometer, equipped with a mercury-cadmium-telluride (MCT) detector cooled with liquid nitrogen. The IR cell was equipped with CaF_2 windows, allowing *in-situ* studies, in a transmission mode. FT-IR spectra were also recorded at ETH Zurich on a Bruker Alpha FT-IR spectrometer in either transmission, or diffuse reflectance infrared Fourier transform spectroscopy (DRIFT) modes. FT-IR spectra of chemical products were performed on a Spectrum one FT-IR spectrometer, in attenuated total reflectance mode (ATR, ZnSe diamond). Typically, 32 scans were accumulated for each spectrum (resolution, 4 cm^{-1}). All IR analyses were performed in transmission mode, unless otherwise stated.

II.2.d. Carbon monoxide adsorption at 77K, monitored by FT-IR (IR(CO))

Carbon monoxide adsorption analyses at 77 K, monitored by FT-IR, were performed with a ThermoFisher Scientific Nicolet Nexus 2 apparatus, using an IR cell equipped with CaF_2 windows, in transmission mode. Prior to analysis, self-supporting pellets (*ca.* 2.03 cm^{-2}) were prepared under controlled atmosphere in a glovebox. Sulphide samples were often dark and proved to absorb a lot the IR signal, dramatically degrading its quality. Therefore, they were most of the time diluted with α-Al_2O_3 (S_{BET} < 10m^2/g) to improve the sample transparency. Before measurements using CO as probe molecule, the samples were outgassed under vacuum (1,3.10^{-4} Pa) and cooled down to 77 K. The spectrum of the empty cell was recorded as background reference. Adsorption experiments of CO probe molecule were carried out at low temperature, by pulse of increasing amount of CO from 0.12 to 300 µmol. The spectrum of sample without CO adsorption was assigned as the reference spectrum.

II.2.e. Transmission electron microscopy (TEM) and Scanning transmission electron microscopy (STEM)

TEM micrographs were obtained with a 200 kV JEOL-2010 transmission electron microscope equipped with a digital camera. For sample preparation, extrudates were crushed into a fine powder, a small amount of which being ultra sonically diluted in ethanol. Two drops of this solution were deposited on a carbon-coated Cu grid, rinsed with ethanol, and the solvent was evaporated under infrared light.

Scanning transmission electron microscopy (STEM) in high angle annular dark field (HAADF) experiments were performed at the Institut de Physique et Chimie des Matériaux de Strasbourg (IPCM Strasbourg) with a Cs aberration corrected scanning transmission electron microscope operating at 200 kV.

II.2.f. Other analyses

Fourier transform (FT) Raman spectroscopy was performed at ETH Zurich on a Raman spectrometer equipped with a Diodo Pumped ND: YAG Laser PSU.

Textural properties were used to calculate the pore distribution and the specific surface area of the materials. They were obtained using a Micromeritics ASAP 2420 apparatus. Prior to nitrogen adsorption, samples were outgassed for six hours to remove the adsorbed water and gases. Note that before outgassing, samples were loaded under inert atmosphere (glovebox) if sensitive. Conventional samples were outgassed at 500°C (5°C/min), while CSC samples were

outgassed at 25°C to avoid any degradation. BET and BJH methods were used [Lynch, 2001] to calculate pore distribution and specific surface area.

Elemental analyses (E.A) were used to quantify W, Ni, C and/or H. They were performed at either the CNRS Central Analysis Service of Solaize (France), at Pasher laboratories (Germany) or at IFPEn (by X-ray fluorescence XRF with a Thermo ARL Advant'x apparatus). In the case of conventional or CSC materials analysed at IFPEn, thus not analysed under inert conditions, samples were calcined so as to know to precise ignition weight loss of the materials prior to analysis. Corresponding results were corrected with the ignition weight loss.

Gas-phase chromatography analyses (GC) were performed on a Hewlett-Packard 5890 series II gas chromatograph equipped with a flame ionisation detector and a capillary column CP-Wax 52 CB (10 m X 0.1 mm). Typically, gas phases were analysed by injecting *ca.* 500 µl of gas. Liquid phases were analysed by injecting *ca.* 0.1 µl of liquid. Gas-phase chromatography coupled with mass spectra analyses (GC/MS) were collected with gas chromatograph Agilent 6890 N equipped with autosamplers and fitted with a PONA column (50 m, 0.20 mm diameter, 0.50 µm thick) or with a HP-5MS column (30 m, 0.25 mm diameter, 0.25 µm thick), coupled with an Agilent 5975B inert XL EI/CI MSD mass spectrometer.

Temperature-programmed reductions (TPR) were performed with a Micromeritics AutoChem 2910 analyser equipped with a TCD detector. The samples (*ca.* 0.5 g) were packed in a U-shaped quartz tube in a glove box, and the sealed tube was attached to the analyser under inert gas flushing. Gas mixture of 5%H_2/Ar with a flow rate of 20mL/min and temperature ranging from 36°C to 1000°C (5°C/min) were used for reductions.

X-ray powder diffraction (XRD) analyses were performed at room temperature, on a PANanalytical X'PertPro X-ray diffractometer, equipped with a CuKα raditation (λ = 1.5418 Å) in a Bragg Brentano geometry. The incident beam was focused to the sample through a programmable divergence slit to ensure a constant irradiation length of about 10 mm on the sample. The diffracted beam was directed through an anti-scattering programmable slit, a 0.2 mm reception slit and a (002) graphite monochromator before reaching the punctual detector. The samples (about 0.5 g of powder) were prepared in a rotating sample holder, and analysed in a range from 2θ = 2 to 2θ = 70°, with a step of 0.05° and a counting time of 12 seconds per step.

II.3. Preparation of supported W alkoxide materials

II.3.a. Preparation of ASA-supported materials

Preparation and characterisation of amorphous silica-alumina, partially dehydroxylated at 300°C, referred as ASA_{-300}

Silica-alumina with a specific area of 229 m²/g was calcined for 6h under air (static conditions), using a ramp of 5°C/min up to 300°C. Then, the solid was partially dehydroxylated at 300°C under high vacuum (5.10^{-5} mbar) for *ca.* 16 h. The system was cooled down to 140°C using a ramp of *ca.* 10°C/min, and the extrudates were stored in glovebox. After this treatment, the specific area was 228 m²/g. OH densities were measured by titration of OH by quantification of CH_4 evolved after contacting ASA suspended in diethylether with CH_3MgBr (1.3 M).[Cartes, 2012] Results: 1.22 mmol OH/g *e.g.* 3.2 OH/nm². **IR** (DRIFT): 3743 (isolated SiOH), 3554 (vbr), 1987, 1852, and 1621 (Si-O-Si) cm^{-1}.

Preparation and characterisation of amorphous silica-alumina, partially dehydroxylated at 500°C, referred as ASA_{-500}

Silica-alumina with a specific area of 229 m²/g was calcined for 6h under air (static conditions), using a ramp of 5°C/min up to 300°C. Then, the system was heated up to 500°C using a ramp of 5°C/min for the solid to be partially dehydroxylated (500°C) under high vacuum (5.10^{-5} mbar) for *ca.* 16 h. The system was cooled down to 140°C using a ramp of 10°C/min, and the extrudates were stored in glovebox. After this treatment, the specific area was 225 m²/g. OH densities were measured as previously described for ASA_{-300}.[Cartes, 2012] Results: 0.95 mmol OH/g *e.g.* 2.5 OH/nm². **IR** (DRIFT): 3743 (isolated SiOH), 3555 (br), 1980, 1855, and 1615 (Si-O-Si) cm^{-1}.

II.3.a.1. Screening of surface complexes obtained by impregnation of W(V) and W(VI) molecular precursors

Synthesis of $W(OEt)_6$-G-0.9/ASA_{-300} *(grafting)*

After stirring 0.474 g of $W(OEt)_6$ with CH_2Cl_2 (15 mL) for 2 h at 40°C, an aliquot of 11.2 mL of the solution was used to impregnate 1.99 g of ASA_{-300} heated at 40°C. After 15 min at 40°C, the reaction mixture was cooled down to room temperature and gently stirred for 16 h.

Extrudates were dried under high vacuum (5 10^{-5} mbar) for 2 h to give an off white solid, stored in the glovebox. **IR** (DRIFT): 2980, 2936, 2902, 2882, 1473 (w), 1448 (m), 1397 (sh), 1385 (s), 1358 (w) cm^{-1}. **^{1}H MAS** solid state NMR: 1.2 (W-O-$CH_2C\mathbf{H_3}$ + O_{ASA}-$CH_2C\mathbf{H_3}$), 3.8 (O_{ASA}-$C\mathbf{H_2}CH_3$), 5.1 (W-O-$C\mathbf{H_2}CH_3$). **^{13}C CPMAS** solid state NMR: 15 (W-O-$CH_2\mathbf{C}H_3$ + O_{ASA}-$CH_2\mathbf{C}H_3$), 58 (O_{ASA}-$\mathbf{C}H_2CH_3$), 75 (W-O-$\mathbf{C}H_2CH_3$). **E.A**: 5.64 $\%_{wt.}$ W, *e.g.* 0.9 (±0.1) W/nm²

Synthesis of $[W(OEt)_5]_2$-G-0.7/ASA_{-500} *(grafting)*

The sample was provided by M.A. Cartes (2012, ETH Zürich). **IR** (DRIFT): 100 % grafting on isolated SiOH, 2976, 2931, 2895, 2872, 1468, 1444, 1385, 1352 cm^{-1}. **E.A**: 4.41 $\%_{wt.}$ W, *e.g.* 0.7 (±0.1) W/nm².

Synthesis of $W(OEt)_6$-G-0.7/ASA_{-500} *(grafting)* [Cartes 2012]

IR (DRIFT): 100 % grafting on isolated SiOH, 2976, 2931, 2895, 2872, 1468, 1444, 1385, 1358 cm^{-1}. **E.A**: 4.64 $\%_{wt.}$ W, *e.g.* 0.7 (±0.1) W/nm².

Synthesis $[W(O)(OEt)_4]_2$-G-0.8/ASA_{-500} *(grafting)* [Cartes, 2012]

IR (DRIFT): 100 % grafting on isolated SiOH, 2979, 2935, 2899, 2880; 1472, 1447, 1384, 1357 cm^{-1}. **E.A**: 5.47 $\%_{wt.}$ W.

II.3.a.2. Influence of the W-loading on surface complexes obtained by incipient wetness impregnation of $[W(OEt)_5]_2$

Synthesis of $[W(OEt)_5]_2$-IWI-0.2/ASA_{-300} by incipient wetness impregnation. *Representative procedure*

After stirring 0.141 g of $[W(OEt)_5]_2$ in cyclohexane (2 mL) for 10 min, an aliquot of 280 µl of the solution was used to impregnate 0.491 g of ASA_{-300} extrudates. After 16 h of maturation, the extrudates were dried under high vacuum (5 10^{-5} mbar) for 2 h to give an off-white solid, which was stored in the glovebox. **IR** (DRIFT): 3743, 2982, 2937, 2905, 2877, 1448, 1396, 1387, 1359, 1268, 1258, 1243 cm^{-1}. **^{1}H MAS** solid state NMR: 1.0 (W-O-$CH_2C\mathbf{H_3}$ + O_{ASA}-$CH_2C\mathbf{H_3}$), 3.8 (O_{ASA}-$C\mathbf{H_2}CH_3$), 5.0 (W-O-$C\mathbf{H_2}CH_3$). **^{13}C CPMAS** solid state NMR: 15 (W-O-$CH_2\mathbf{C}H_3$ + O_{ASA}-$CH_2\mathbf{C}H_3$), 59 (O_{ASA}-$\mathbf{C}H_2CH_3$), 76 (W-O-$\mathbf{C}H_2CH_3$).

Synthesis of $[W(OEt)_5]_2$-IWI-0.5/ASA_{-300}

The material was prepared according to the procedure described above, with 0.871 g of $[W(OEt)_5]_2$ and 9.5 g of ASA_{-300}. An off-white solid was obtained. **IR** (DRIFT): 3743, 2981, 2937,

2904, 2879, 1447, 1396, 1387, 1359, 1268, 1261, 1246 cm^{-1}. **^{1}H MAS** solid state NMR: 1.0 (W-O-$CH_2C\mathbf{H_3}$ + O_{ASA}-$CH_2C\mathbf{H_3}$), 3.8 (O_{ASA}-$C\mathbf{H_2}CH_3$), 5.0 (W-O-$C\mathbf{H_2}CH_3$). **^{13}C CPMAS** solid state NMR: 15 (W-O-$CH_2\mathbf{C}H_3$ + O_{ASA}-$CH_2\mathbf{C}H_3$), 59 (O_{ASA}-$\mathbf{C}H_2CH_3$), 75 (W-O-$\mathbf{C}H_2CH_3$). **E.A**: 3.33 $\%_{wt.}$ W, *e.g.* 0.5 (±0.1) W/nm².

Synthesis of $[W(OEt)_5]_2$-IWI-0.8/ASA_{-300}

The material was prepared according to the procedure described above, with 0.645 g of $[W(OEt)_5]_2$ and 3.945 g of ASA_{-300}. An off-white solid was obtained. **IR** (DRIFT): 2978, 2934, 2897, 2877, 2747, 2705, 1469, 1446, 1394, 1387, 1382, 1356, 1268, 1259, 1251 cm^{-1}. **^{1}H MAS** solid state NMR: 1.2 (W-O-$CH_2C\mathbf{H_3}$ + O_{ASA}-$CH_2C\mathbf{H_3}$), 3.8 (O_{ASA}-$C\mathbf{H_2}CH_3$), 5.0 (W-O-$C\mathbf{H_2}CH_3$). **^{13}C CPMAS** solid state NMR: 16 (W-O-$CH_2\mathbf{C}H_3$ + O_{ASA}-$CH_2\mathbf{C}H_3$), 59 (O_{ASA}-$\mathbf{C}H_2CH_3$), 71 (W-O-$\mathbf{C}H_2CH_3$). **E.A**: 5.03 $\%_{wt.}$ W, *e.g.* 0.8 (±0.1) W/nm².

Synthesis of $[W(OEt)_5]_2$-IWI-1.7/ASA_{-300}

The material was prepared according to the procedure described above, with 3.359 g of $[W(OEt)_5]_2$ and 10.16 g of ASA_{-300}. A light brown/yellowish solid was obtained. **IR** (DRIFT): 2978, 2934, 2897, 2869, 2742, 2700, 1468, 1444, 1394, 1380, 1354, 1246, 1241 cm^{-1}. **^{1}H MAS** solid state NMR: 1.2 (W-O-$CH_2C\mathbf{H_3}$ + O_{ASA}-$CH_2C\mathbf{H_3}$), 3.8 (O_{ASA}-$C\mathbf{H_2}CH_3$), 5.0 (W-O-$C\mathbf{H_2}CH_3$). **^{13}C CPMAS** solid state NMR: 19 (W-O-$CH_2\mathbf{C}H_3$ + O_{ASA}-$CH_2\mathbf{C}H_3$), 59 (O_{ASA}-$\mathbf{C}H_2CH_3$), 69 (W-O-$\mathbf{C}H_2CH_3$). **E.A**: 10,89 $\%_{wt.}$ W, *e.g.* 1.7 (±0.1) W/nm².

Synthesis of $[W(OEt)_5]_2$-IWI-3.0/ASA_{-300}

The material was prepared according to the procedure described above. A solution (0.50 mL) of a cyclohexane with 0.393 g of $[W(OEt)_5]_2$ was prepared. An aliquot of 0.25 mL of the solution was used to impregnate *ca.* 0.4 g of ASA_{-300}. A light brown/yellowish solid was obtained. **IR** (DRIFT): 2972, 2929, 2891, 2869, 2741, 2699, 1733 (w), 1600 (w), 1469 (m), 1445 (m), 1379 (s), 1359 (m) cm^{-1}.

Synthesis of $[W(OEt)_5]_2$-IWI-3.7/ASA_{-300}

The material was prepared according to the procedure described above, with 3.347 g of $[W(OEt)_5]_2$ and 5.346 g of ASA_{-300}. A light brown/yellowish solid was obtained. **IR**: 100% grafting on isolated SiOH. **E.A**: 21.0 %wt. W, *e.g.* 3.7 (±0.1) W/nm².

Synthesis of $[W(OEt)_5]_2$-IWI-4.0/ASA_{-300}

The material was prepared according to the procedure described above. 0.50 mL of the solution was used to impregnate 0.479 g of ASA_{-300}. A light brown/yellowish solid was obtained.

IR (DRIFT): 2976, 2931, 2896, 2871, 2741, 2697, 1658 (vw), 1608 (vw). 1468 (m), 1445 (m), 1379 (s), 1351 (m) cm^{-1}.

Synthesis of $[W(OEt)_5]_2$-IWI-5.0/ASA_{-300}

The material was prepared according to the procedure described above, with 0.457 g of $[W(OEt)_5]_2$ and 489.3 mg of ASA_{-300}. A brown/yellowish solid was obtained. **IR** (DRIFT): 2976, 2931, 2893, 2871, 2741, 2697, 1658 (vw), 1608 (vw), 1468 (m), 1445 (m), 1379 (s), 1352 (m) cm^{-1}.

II.3.a.3. Investigation of the structure of surface species as a function of W-loading by using ^{13}C labelled $[W(OEt*)_5]_2$ (carbon-13 labelled on the methylene carbon).

Synthesis of ^{13}C labelled pentaethoxide tungsten (V), referred as $[W(OEt^*)_5]_2$

$[W(OEt)_5]_2$ and 5 *equiv.* of $CH_3{}^{13}CH_2OH$ were stirred for 6 h. After evacuation of ethanol under vacuum (10^{-2} mbar), the reaction mixture was dried (2 h, 10^{-5} mbar), affording a solution containing a white precipitate. After filtration, the solution contained pure $[W(OEt^*)_5]_2$, 20-30% labelled in position 1. **Yield**: 86 %. **IR** (ATR): 2969, 2926, 2892, 2862, 2732 (vw), 2693 (vw), 1737 (vw), 1466, 1441, 1372, 1348, 1275, 1146, 1092 (m), 1054 (s), 1041 (sh), 907, 630, 531 cm^{-1}. **^{1}H NMR** (CD_2Cl_2, 298K): 1.22 (t, W-O-$CH_2C\mathbf{H_3}$, J(H-H)=7 Hz), 4.77 (q, W-O-$C\mathbf{H_2}CH_3$, , J(H-H)=7 Hz), 4.53 (q, W-O-$^{13}C\mathbf{H_2}CH_3$, J(H-H)=7 Hz), 5.00 (q, W-O-$^{13}C\mathbf{H_2}CH_3$, J(H-H)=7 Hz), J(^{13}C-H)=144 Hz. **^{13}C{1H} NMR** (CD_2Cl_2, 298K): 18.0 (W-O-$CH_2\mathbf{C}H_3$), 68.0 (W-O-$\mathbf{C}H_2CH_3$).

Synthesis of ^{13}C labelled $[W(OEt^*)_5]_2$-IWI-0.2/ASA_{-300}. *Representative procedure for incipient wetness impregnation*

After stirring 0.159 g of carbon-13 labelled $[W(OEt^*)_5]_2$ in cyclohexane (V_{sol} = 2 mL) for 10 min, an aliquot of 800 µl of the solution was used to impregnate 1.457 g of ASA_{-300} extrudates. After 16 h of maturation, the extrudates were dried under high vacuum (5 10^{-5} mbar) for 2 h to give an off white solid, which was stored in the glovebox. **IR**: 3744 (m), 3532 (vbr), 2982, 2937, 2901, 2879, 1471 (vw), 1459 (sh), 1450 (m), 1396 (sh), 1386 (m), 1359 (vw) cm^{-1}. **^{1}H MAS** solid state NMR: 1.1 (O_{ASA}-$CH_2C\mathbf{H_3}$ + W-O-$CH_2C\mathbf{H_3}$), 1.7 (SiOH), 3.7 (O_{ASA}-$C\mathbf{H_2}CH_3$) 4.9 (W-O-$C\mathbf{H_2}CH_3$). **^{13}C MAS** solid state NMR: 14 (O_{ASA}-$CH_2\mathbf{C}H_3$ + W-O-$CH_2\mathbf{C}H_3$), 58 (O_{ASA}-$\mathbf{C}H_2CH_3$), 75 (W-O-$\mathbf{C}H_2CH_3$). **E.A:** 1.69 $\%_{wt.}$ W, *e.g.* 0.2 (±0.1) W/nm².

Synthesis of ^{13}C labelled $[W(OEt^*)_5]_2$-IWI-0.5/ASA_{-300}

After stirring 0.162 g of carbon-13 labelled $[W(OEt^*)_5]_2$ in cyclohexane (V_{sol} = 1 mL) for 10 min, an aliquot of 430 µl of the solution was used to impregnate 0.801 g of ASA_{-300} extrudates. After 16 h of maturation, the extrudates were dried under high vacuum (5 10^{-5} mbar) for 2 h to give an off white solid, which was stored in the glovebox. **IR**: 3744 (w), 3532 (vbr), 2982, 2937, 2901, 2879, 1471 (w), 1459 (sh), 1447 (m), 1396 (sh), 1385 (m), 1358 (vw) cm^{-1}. **^{1}H MAS** solid state NMR: 1.0 (O_{ASA}-$CH_2C\mathbf{H_3}$ + W-O-$CH_2C\mathbf{H_3}$), 3.7 (O_{ASA}-$C\mathbf{H_2}CH_3$), 4.9 (W-O-$C\mathbf{H_2}CH_3$). **^{13}C MAS** solid state NMR: 15 (O_{ASA}-$CH_2\mathbf{C}H_3$ + W-O-$CH_2\mathbf{C}H_3$), 59 (O_{ASA}-$\mathbf{C}H_2CH_3$), 73 (W-O-$\mathbf{C}H_2CH_3$). **E.A:** 3.49 $\%_{wt.}$ W, *e.g.* 0.5 (±0.1) W/nm².

Synthesis of ^{13}C labelled $[W(OEt^*)_5]_2$-IWI-0.6/ASA_{-300}

After stirring 0.225 g of carbon-13 labelled $[W(OEt^*)_5]_2$ in cyclohexane (V_{sol} = 1 mL) for 10 min, an aliquot of 460 µl of the solution was used to impregnate 804 mg of ASA_{-300} extrudates. After 16 h of maturation, the extrudates were dried under high vacuum (5 10^{-5} mbar) for 2 h to give an off white solid, which was stored in the glovebox. **IR**: 3742 (vw), 3462 (vbr) 2980, 2936, 2900, 2877, 1487 (sh), 1472 (w), 1457 (sh), 1447 (w), 1394 (sh), 1383 (m), 1359 (w) cm^{-1}. **^{1}H MAS** solid state NMR: 1.1 (O_{ASA}-$CH_2C\mathbf{H_3}$ + W-O-$CH_2C\mathbf{H_3}$), 3.8 (O_{ASA}-$C\mathbf{H_2}CH_3$) 5.0 (W-O-$C\mathbf{H_2}CH_3$). **^{13}C MAS** solid state NMR: 16 (O_{ASA}-$CH_2\mathbf{C}H_3$ + W-O-$CH_2\mathbf{C}H_3$), 59 (O_{ASA}-$\mathbf{C}H_2CH_3$), 73 (W-O-$\mathbf{C}H_2CH_3$). **E.A**: 4.08 $\%_{wt.}$ W, *e.g.* 0.6 (±0.1) W/nm².

Synthesis of ^{13}C labelled $[W(OEt^*)_5]_2$-IWI-0.7/ASA_{-300}

After stirring 0.088 g of carbon-13 labelled $[W(OEt^*)_5]_2$ in cyclohexane (V_{sol} = 370 µL) for 10 min, the solution was used to impregnate 0.602 g of ASA_{-300} extrudates. After 16 h of maturation, the extrudates were dried under high vacuum (5 10^{-5} mbar) for 2 h to give an off white solid, which was stored in the glovebox. **IR**: 3462 (vbr) 2979, 2936, 2900, 2877, 1472 (w), 1457 (sh), 1447 (w), 1394 (sh), 1383 (m), 1357 (w) cm^{-1}. **^{1}H MAS** solid state NMR: 1.2 (O_{ASA}-$CH_2C\mathbf{H_3}$ + W-O-$CH_2C\mathbf{H_3}$), 3.8 (O_{ASA}-$C\mathbf{H_2}CH_3$) 5.0 (W-O-$C\mathbf{H_2}CH_3$). **^{13}C MAS** solid state NMR: 16 (O_{ASA}-$CH_2\mathbf{C}H_3$ + W-O-$CH_2\mathbf{C}H_3$), 59 (O_{ASA}-$\mathbf{C}H_2CH_3$), 72 (W-O-$\mathbf{C}H_2CH_3$). **E.A**: 4.64 $\%_{wt.}$ W, *e.g.* 0.7 (±0.1) W/nm².

Synthesis of ^{13}C labelled $[W(OEt^*)_5]_2$-IWI-0.9/ASA_{-300}

After stirring 0.315 g of carbon-13 labelled $[W(OEt^*)_5]_2$ in cyclohexane (V_{sol} = 1 mL) for 10 min, an aliquot of 800 µL of the solution was used to impregnate 1.461 g of ASA_{-300} extrudates. After 16 h of maturation, the extrudates were dried under high vacuum (5 10^{-5} mbar) for 2 h to give an off white solid, which was stored in the glovebox. **IR**: 3532 (vbr), 2982, 2928, 2901, 2879, 2746, 2698, 1734 (vw), 1607 (w), 1484 (sh), 1469 (w), 1446 (m), 1396 (sh), 1380 (s),

1355 (m) cm^{-1}. **^{1}H MAS** solid state NMR: 1.2 (O_{ASA}-$CH_2C\mathbf{H_3}$ + W-O-$CH_2C\mathbf{H_3}$), 3.7 (O_{ASA}-$C\mathbf{H_2}CH_3$), 4.9 (W-O-$C\mathbf{H_2}CH_3$). **^{13}C MAS** solid state NMR: 14 (O_{ASA}-$CH_2\mathbf{C}H_3$), 16 (W-O-$CH_2\mathbf{C}H_3$), 58 (O_{ASA}-$\mathbf{C}H_2CH_3$), 68, 70 & 75 (W-O-$\mathbf{C}H_2CH_3$). **E.A**: 5.91 $\%_{wt.}$ W, *e.g.* 0.9 (±0.1) W/nm².

Synthesis of ^{13}C labelled $[W(OEt^*)_5]_2$-IWI-2.0+/ASA_{-300}

After mixing 0.230 g of carbon-13 labelled $[W(OEt^*)_5]_2$ with cyclohexane (V_{sol} = 360 µL) for 1 min, an aliquot of 330 µL of the solution was used to impregnate 0.578 g of ASA_{-300} extrudates. After 16 h of maturation, the extrudates were dried under high vacuum (5 10^{-5} mbar) for 2 h to give a light brown/yellowish solid, which was stored in the glovebox. **IR** (DRIFT) 3545 (vbr), 2973, 2931, 2892, 2869, 2738 (vw), 2700 (vw), 1734 (vw), 1600 (vw), 1482 (sh), 1468, 1445, 1377, 1352 cm^{-1}. **^{1}H MAS** solid state NMR: 1.2 (O_{ASA}-$CH_2C\mathbf{H_3}$ + W-O-$CH_2C\mathbf{H_3}$), 3.8 (O_{ASA}-$C\mathbf{H_2}CH_3$), 4.8 (W-O-$C\mathbf{H_2}CH_3$). **^{13}C MAS** solid state NMR: 17 (O_{ASA}-$CH_2\mathbf{C}H_3$), 18 (W-O-$CH_2\mathbf{C}H_3$), 58 (O_{ASA}-$\mathbf{C}H_2CH_3$), 68 & 70 (W-O-$\mathbf{C}H_2CH_3$).

Synthesis of ^{13}C labelled $[W(OEt^*)_5]_2$-G-0.5/ASA_{-300} *(grafting)*

After stirring 0.336 g of carbon-13 labelled $[W(OEt^*)_5]_2$ (0.82 mmol, 1.5 *equiv.*) with cyclohexane (1.5 mL) for 10 min, the solution was used to impregnate 0.446 g of ASA_{-300} extrudates (0.54 mmol OH, 1.22 mmol OH/g(ASA)). The mixture was slowly stirred for 16 h and the solid was washed 3 times (30min) with cyclohexane before being dried under high vacuum (5 10^{-5} mbar) for 2 h, to give an off white solid, stored in the glovebox. **IR**: 100 % grafting on isolated SiOH, 2978, 2934, 2898, 2875, 1470, 1447, 1382, 1355 cm^{-1}. **^{1}H MAS** solid state NMR: 1.1 (W-O-$CH_2C\mathbf{H_3}$ + O_{ASA}-$CH_2C\mathbf{H_3}$), 3.8 (O_{ASA}-$C\mathbf{H_2}CH_3$), 5.0 (W-O-$C\mathbf{H_2}CH_3$). **^{13}C CPMAS** solid state NMR: 18 (W-O-$CH_2\mathbf{C}H_3$ + O_{ASA}-$CH_2\mathbf{C}H_3$), 60 (O_{ASA}-$\mathbf{C}H_2CH_3$), 72 (W-O-$\mathbf{C}H_2CH_3$). **^{27}Al MAS** NMR: 70 (Al_{IV}), 11 (Al_{VI}). **E.A**: 3.54 $\%_{wt.}$ W, *e.g.* 0.5 (±0.1) W/nm².

Synthesis of ^{13}C labelled Et^*OH/ASA_{-300}

After stirring 0.221 g of a mixture of carbon-13 labelled ethanol and non labelled ethanol (50/50 vol/vol) with cyclohexane (V_{sol} = 1 mL) for 10 min, an aliquot of 550 µL of the solution was used to impregnate 1.001 g of ASA_{-300}. After 16 h of maturation, the extrudates were dried under high vacuum (5 10^{-5} mbar) for 16 h to give an off white solid, stored in the glovebox. Subsequent washing with 3 mL of cyclohexane was performed. The solid was dried under high vacuum (5 10^{-5} mbar) for 2 h to give an off white solid. **IR**: 3743 (isolated SiOH, 35 % consumed), 2978, 2937, 2904, 1484, 1448, 1390 cm^{-1}. **^{1}H MAS** solid state NMR: 1.0 (O_{ASA}-$CH_2C\mathbf{H_3}$), 1.7 (Si**O**H) 3.7 (O_{ASA}-$C\mathbf{H_2}CH_3$). **^{13}C CPMAS** solid state NMR: 15 (O_{ASA}-$CH_2\mathbf{C}H_3$), 59 (O_{ASA}-$\mathbf{C}H_2CH_3$).

II.3.b. Preparation of SiO_2-supported materials

Preparation of silica partially dehydroxylated at 700°C, referred as $SiO_{2\text{-}700}$

Silica was prepared as described in the literature and provided by F. Héroguel (ETH Zürich). Characteristic: 200 m²/g, 0.8 OH/nm^2 and **IR**: 3740 (isolated SiOH), 3652 (br, H-bonded SiOH), 1983, 1866, 1638 (Si-O-Si) cm^{-1}

Synthesis of ^{13}C labelled $[W(OEt^*)_5]_2$-G-0.7/$SiO_{2\text{-}700}$ *(grafting)*

After stirring 0.115 g of carbon-13 labelled $[W(OEt^*)_5]_2$ (0.28 mmol, 3.4 *equiv.*) with cyclohexane (1.5 mL) for 10 min, the solution was used to impregnate 0.308 g of silica powder dehydroxylated at 700ºC (0.08 mmol OH, 0.27 mmol OH/g(SiO_2)). The mixture was gently stirred for 16 h, and the solid was washed 3 times (30 min) with cyclohexane before being dried under high vacuum (5 10^{-5} mbar) for 2 h, to give an off white solid, stored in the glovebox. **IR**: 100 % grafting on isolated SiOH, 2978, 2934, 2898, 2875, 1470, 1447, 1382, 1355 cm^{-1}. **^{1}H MAS** solid state NMR: 1.0 (W-O-$CH_2C\mathbf{H_3}$ + O_{SiO2}-$CH_2C\mathbf{H_3}$), 3.6 (O_{SiO2}-$CH_2C\mathbf{H_3}$), 4.7 (W-O-$C\mathbf{H_2}CH_3$).**^{13}C CPMAS** solid state NMR: 15 (W-O-$CH_2C\mathbf{H_3}$ + O_{SiO2}-$CH_2\mathbf{C}H_3$), 59 (O_{SiO2}-$\mathbf{C}H_2CH_3$), 72 (W-O-$\mathbf{C}H_2CH_3$). **E.A**: 4.30 %$_{wt.}$ W, *e.g.* 0.7 (±0.1) W/nm².

Synthesis of EtOH/$SiO_{2\text{-}700}$

The sample was provided by M.A. Cartes (2012, ETH Zürich). **IR**: 3740 (isolated SiOH, 50 % consumed), 2983, 2938, 2906, 1486, 1448, 1395, 1370 cm^{-1}. **^{1}H MAS** solid state NMR: 1.0 (O_{SiO2}-$CH_2C\mathbf{H_3}$), 1.7 (SiO**H**), 2.6 (CH_2CH_3-O**H**), 3.7 (O_{SiO2}-$C\mathbf{H_2}CH_3$). **^{13}C CPMAS** solid state NMR: 14 (O_{SiO2}-$CH_2\mathbf{C}H_3$), 58 (O_{SiO2}-$\mathbf{C}H_2CH_3$).

II.3.c. Preparation of Al_2O_3-supported materials

Preparation of alumina partially dehydroxylated at 450°C, referred as $Al_2O_{3\text{-}450}$

γ-alumina (2 g) with a specific surface of 289 m²/g was calcined under air (static conditions) for 16h using a ramp of 5°C/min up to 500°C. Then, air was evacuated for *ca.* 30 min under high vacuum (5.10^{-5} mbar), and the solid was cooled down to 140°C (20°C/min). Afterwards, alumina was stored in the glovebox. Subsequently, 1 g of solid was contact with a vapour of distilled/degassed water, and heated up to 300°C using a ramp of 5°C/min for 30 min. Then, the temperature was increased up to 450°C (5°C/min) and the residual vapour of water was evacuated under high vacuum for 16h at 450°C. Finally, alumina was cooled down to 140°C (20°C/min) and was stored in the glovebox. OH density: between 3.0 and 3.5 OH/nm² according

to the literature [Rascon *et al.*, 2011]. **IR**: 3793 (vw), 3771, 3756, 3730, 3684, 3636, 3588 (w, vbr), 1364 cm^{-1}

Synthesis of ^{13}C labelled $[W(OEt^{*})_5]_2$-G-0.5/Al_2O_{3-450} *(grafting)*

After stirring 0.419 g of carbon-13 labelled $[W(OEt^{*})_5]_2$ (1.02 mmol, 1.5 *equiv.*) with cyclohexane (1.5 mL) for 10 min, the solution was used to impregnate 0.451 g of Al_2O_{3-450} extrudates (0.69 mmol OH, *ca.* 1.54 mmol OH/g(Al_2O_3)). The reaction mixture was slowly stirred for 16 h and the solid was washed 3 times (30 min) with cyclohexane before being dried under high vacuum (5 10^{-5} mbar) for 2 h, to give an off white solid, stored in the glovebox. **IR**: 2969, 2934, 2898, 2875, 1470, 1447, 1382, 1355 cm^{-1}. **^{1}H MAS** solid state NMR: 1.1, 4.4. **^{13}C CPMAS** solid state NMR 18 (W-O-$CH_2C\mathbf{H_3}$ + O_{Al2O3}-$CH_2\mathbf{C}H_3$), 60 (O_{Al2O3}-$\mathbf{C}H_2CH_3$), 72 (W-O-$\mathbf{C}H_2CH_3$). **^{27}Al MAS** NMR: 70 (Al_{IV}), 39 (Al_V), 11 (Al_{VI}). **E.A**: 4.41 $\%_{wt.}$ W, *e.g.* 0.5 (±0.1) W/nm².

Synthesis of $Et^{*}OH/Al_2O_{3-450}$

After mixing 86 µL of carbon-13 labelled ethanol with cyclohexane (V_{sol} = 275 µL) for 1 min, an aliquot of 180 µL of the solution was used to impregnate 0.225 g of Al_2O_{3-450} extrudates. After 16 h of maturation, the extrudates were dried under high vacuum (5 10^{-5} mbar) for 16 h to give an off white solid, Subsequent washing with 3 mL of cyclohexane was performed. The, the solid was dried under high vacuum (5 10^{-5} mbar) for 2 h to give an off white solid. **IR**: 3729, 3707, 3668, 3559 OH group: 61% consumed. 2963, 2929, 2892, 2871, 1491, 1448, 1382 cm^{-1}. **^{1}H MAS** solid state NMR: 1.3, 4.0. **^{13}C CPMAS** solid state NMR: 18 (O_{Al2O3}-$CH_2\mathbf{C}H_3$), 58 (O_{Al2O3}-$\mathbf{C}H_2CH_3$). **^{27}Al** MAS NMR: 70 (Al_{IV}), 39 (Al_V), 11 (Al_{VI}).

II.3.d. Preparation of conventional dried and calcined materials

Conventional dried and calcined materials were prepared by incipient wetness impregnation of an aqueous solution of ammonium metatungstate on ASA (co-impregnation) followed by a maturation step of 16 h. Subsequent drying at 120°C gave the sample referred as “dried”. “Calcined” materials were obtained by subsequent calcination under air, at atmospheric pressure, with a flow rate of 1.5 L/g(cat)/h, at 450°C for 2 h.

II.4. Preparation of non-promoted sulphide materials (bulk)

Synthesis of bulk WS_2

$[W(OEt)_5]_2$ (*ca.* 200 mg) was loaded into a small glass holder, which was placed in a sulphidation cell. After 4 h of sulphidation at atmospheric pressure, at 23°C, with a 15 $\%_{mol.}$ H_2S/H_2 mixture, the temperature was raised to 150°C (2°C/min). The system was finally cooled down to room temperature (20°C/min) , and evacuated at *ca.* 1 mbar for 20 min. A brown powder was obtained, and was subsequently treated with a 15 $\%_{mol.}$ H_2S/H_2 mixture at 600°C (using a ramp of 5°C/min) for 6 h. The system was cooled down, and evacuated at *ca.* 1 mbar for 20 min. The resulting metallic grey powder was stored in the glovebox. **XPS**: 92 $\%_{rel.}$ WS_2.

II.5. Synthesis of non-promoted sulphide catalysts supported on ASA

Synthesis of WS_2-ex.$[W(OEt)_5]_2$-G-0.7/ASA_{-500} at $T_{sulph.}$ = 350°C. *Representative Procedure*

About 2 g of $[W(OEt)_5]_2$-G-0.7/ASA_{-500} were placed in a sulphidation cell under argon (glovebox). The cell was plugged to the sulphidation apparatus, and the gas outlet was purged with argon. Then, a mixture of H_2S/H_2 (15 $\%_{mol}$. H_2S, 1 atm) with a flow rate of 2 L/g(cat)/h, was passed onto the catalysts which was heated up to 350°C, using a ramp of 5°C/min. After 2 h at 350°C, the sulphide gas was switched to argon (same flow rate), and the system was cooled down to 250°C (12°C/min). After 2 h at 250°C, the system was cooled down to 120°C (20°C/min). At 120°C, the cell was evacuated for 5 min at *ca.* 1 mbar and cooled down to room temperature (vide infra). The resulting sulphide material (black solid) was either sealed in ampoules or directly stored in glovebox. **XPS**: 71 $\%_{rel}$ WS_2

Synthesis of WS_2-ex.$W(OEt)_6$-G-0.7/ASA_{-500} at $T_{sulph.}$ = 350°C

The sample was prepared according to the procedure described above, at a sulphidation temperature of 350°C. **XPS**: 72 $\%_{rel}$ WS_2

Synthesis of WS_2-ex.$[W(O)(OEt)_4]_2$-G-0.8/ASA_{-500} at $T_{sulph.}$ = 350°C

The sample was prepared according to the procedure described above, at a sulphidation temperature of 350°C. **XPS**: 72 $\%_{rel}$ WS_2

Synthesis of WS_2-ex.$[W(OEt)_5]_2$-IWI-0.5/ASA_{-300} at $T_{sulph.}$ = 350°C

The sample was prepared according to the procedure described above, at a sulphidation temperature of 350°C. **XPS**: 76 $\%_{rel}$ WS_2

Synthesis of WS_2-ex.$[W(OEt)_5]_2$-IWI-1.7/ASA_{-300} at $T_{sulph.}$ = -25°C

About 1 g of $[W(OEt)_5]_2$-IWI-1.7/ASA_{-300} was placed in a sulphidation cell under argon (glovebox). The system was cooled down and maintained at -25°C in a cold bath of acetone. After 30 min, the sulphidation step was started by passing a mixture of H_2S/H_2 (15%$_{mol.}$ H_2S) at a flow rate of 2 L/g(cat)/h at atmospheric pressure for 2 h. Then, the gas inlet was switched to argon (same flow rate) for 2 h and allowed to return to room temperature. Finally, the cell was evacuated during 1 hour at *ca.* 1 mbar, and the light brown solid catalyst was stored inside the glovebox. **XPS**: 30 %$_{rel}$ WS_2

Synthesis of WS_2-ex.$[W(OEt)_5]_2$-IWI-1.7/ASA_{-300} at $T_{sulph.}$ = 23°C

About 1 to 2 g of $[W(OEt)_5]_2$-IWI-1.7/ASA_{-300} were placed in a sulphidation cell under argon (glovebox), at room temperature. The cell was plugged on the sulphidation apparatus, the gas outlet was purged under argon, and the inlet was set to a mixture of H_2S/H_2 (15 %$_{mol.}$ H_2S) with a flow rate of 2 L/g(cat)/h (atmospheric pressure), for 2 h. Afterwards, the gas inlet was switched to argon (same flow rate) for 2 h, at the same temperature. Finally, the cell was evacuated during 1 h at *ca.* 1 mbar and the brown solid was stored inside a glovebox. **XPS**: 49 %$_{rel}$ WS_2

Synthesis of WS_2-ex.$[W(OEt)_5]_2$-IWI-1.7/ASA_{-300} at $T_{sulph.}$ = 50°C

About 1 to 2 g of $[W(OEt)_5]_2$-IWI-1.7/ASA_{-300} was placed in a sulphidation cell under argon (glovebox). The cell was plugged on the sulphidation apparatus, the gas outlet was purged under argon, and the inlet was set to a mixture of H_2S/H_2 (15 %$_{mol}$. H_2S) with a flow rate of 2 L/g(cat)/h (atmospheric pressure). After 2 h at 50°C, the gas inlet was switched to argon (2 L/g(cat)/h) and the reaction conditions kept constant for 2 h. Finally, the cell was evacuated for 1 h at *ca.* 1 mbar, and the black solid was stored inside a glovebox. **XPS**: 58 %$_{rel}$ WS_2

Synthesis of WS_2-ex.$[W(OEt)_5]_2$-IWI-1.7/ASA_{-300} at $T_{sulph.}$ = 150°C

The sample was prepared according to the same procedure as WS_2-ex.$[W(OEt)_5]_2$-IWI-1.7/ASA_{-300} (T_{sulph} = 50°C), at a sulphidation temperature of 150°C. **XPS**: 68 %$_{rel}$ WS_2.

Synthesis of WS_2-ex.$[W(OEt)_5]_2$-IWI-1.7/ASA_{-300} at $T_{sulph.}$ = 250°C

The sample was prepared according to the same procedure as WS_2-ex.$[W(OEt)_5]_2$-G-0.7/ASA_{-500} (representative one), at a sulphidation temperature of 250°C. **XPS**: 75 %$_{rel}$ WS_2.

Synthesis of WS_2-ex.$[W(OEt)_5]_2$-IWI-1.7/ASA_{-300} at $T_{sulph.}$ = 350°C

The sample was prepared according to the representative procedure, at a sulphidation temperature of 350°C. **XPS**: 85 %$_{rel}$ WS_2.

Synthesis of WS_2-ex.$[W(OEt)_5]_2$-IWI-1.7/ASA_{-300} at $T_{sulph.}$ = 450°C

The sample was prepared according to the representative procedure, at a sulphidation temperature of 450°C. **XPS**: 82 $\%_{rel}$ WS_2.

Synthesis of WS_2-ex.$[W(OEt)_5]_2$-IWI-1.7/ASA_{-300} at $T_{sulph.}$ = 600°C

The sample was prepared according to the representative procedure, at a sulphidation temperature of 600°C. **XPS**: 87 $\%_{rel}$ WS_2

Synthesis of sulphide catalysts based on conventional oxide dried or calcined catalyst were prepared according to the representative procedure (from 23°C to 600°C)

II.6. Preparation of nickel-promoted materials

II.6.a. Preparation of conventional dried and calcined oxide materials

Conventional dried and calcined materials were prepared by incipient wetness impregnation of an aqueous solution of ammonium metatungstate and nickel nitrate on ASA (co-impregnation) followed by a maturation step of 16 h. Subsequent drying at 120°C gave the sample referred as “dried”. “Calcined” materials were obtained by subsequent calcination under air, at atmospheric pressure, with a flow rate of 1.5 L/g(cat)/h, at 450°C for 2 h.

II.6.b. Preparation of CSC materials, prior to sulphidation

Synthesis of $Ni(acac)_2$/ASA_{-300}

$Ni(acac)_2$ (0.160 g) was stirred in hot toluene (75 to 80°C) for 3 h (2 mL, 0.31 mol/L) to give an homogeneous emerald green solution. ASA_{-300} (0.910 g) was impregnated with 460 µL of this hot solution under manual stirring. After 16 h of maturation, the solvent was evacuated under high vacuum (5 10^{-5} mbar) for 2 h to give light green extrudates, which were stored in the glovebox. **IR** (DRIFT): 3742 (isolated SiOH, 66 % consumed), 3084, 3006, 2930, 1600, 1581 (sh), 1533, 1517 (sh), 1407 (sh) cm^{-1}. **EA**: 0.93 $\%_{wt.}$, *e.g.* 0.4 (±0.1) Ni/nm².

Synthesis of Ni(1-MeCp)$_2$/ASA$_{-300}$

Ni(1-MeCp)$_2$ (0.114 g) was stirred for 15 min in cyclohexane (2 mL; 0.26 mol/L) to give a dark green solution. An aliquot of 620 µL of this solution was taken to impregnate 1.20 g of ASA$_{-300}$, which turned immediately dark green. After 16 h of maturation, the solvent was evacuated under high vacuum (5 10^{-5} mbar) for 2 h to give dark green extrudates, which were stored in the glovebox. **IR**: 3742 (isolated SiOH, 50 % consumed), 3113, 3088, 2934, 2872, 1511, 1383 cm^{-1}. **EA**: 1.02 $\%_{wt.}$, *e.g.* 0.4 (±0.1) Ni/nm².

II.6.b.1. Deposition of nickel precursors onto tungsten surface species

Synthesis of Ni(acac)$_2$-IWI-0.21/[W(OEt)$_5$]$_2$-IWI-1.7/ASA$_{-300}$. *Representative procedure*

Ni(acac)$_2$ (0.456 g) was stirred for 3 h in hot toluene (75 to 80°C) (5 ml, 0.33 mol/L) to give an emerald green solution. An aliquot (410 µL) of this hot solution was used to impregnate 1.565 g of [W(OEt)$_5$]$_2$-IWI-1.7/ASA$_{-300}$, which turned green. After 16 h of maturation, the solvent were evacuated under high vacuum (5 10^{-5} mbar) for 2 h to give light green extrudates, which were stored in the glovebox. Traces of an off-white product were observed on the glassware. **E.A**: 10.17 $\%_{wt.}$ W, *e.g.* 1.6 (±0.1) W/nm²; 0.68 $\%_{wt.}$ Ni, *e.g.* Ni/W = 0.21.

Synthesis of Ni(acac)$_2$-IWI-0.44/[W(OEt)$_5$]$_2$-IWI-1.7/ASA$_{-300}$

The sample was prepared according to the same procedure. **E.A**: 9.52 $\%_{wt.}$ W, *e.g.* 1.5 (±0.1) W/nm²; 1.35 $\%_{wt.}$ Ni, *e.g.* Ni/W = 0.44.

Synthesis of Ni(acac)$_2$-IWI-1.00/[W(OEt)$_5$]$_2$-IWI-1.7/ASA$_{-300}$

The sample was prepared according to the same procedure, with 2 successive impregnations of a toluene solution of Ni(acac)$_2$ (0.64 mol/L, same target as for Ni/W ≈ 0.4 (at/at)). **E.A**: 9.26 $\%_{wt.}$ W, *e.g.* 1.5 (±0.1) W/nm²; 2.96 $\%_{wt.}$ Ni, *e.g.* Ni/W = 1.00.

Synthesis of Ni(1-MeCp)$_2$-IWI-0.21/[W(OEt)$_5$]$_2$-IWI-1.7/ASA$_{-300}$

Ni(1-MeCp)$_2$ (0.166 g) was stirred in 3 mL of cyclohexane for 15 min to give a dark green solution. An aliquot of 780 µL of this solution was slowly added to impregnate 1.50 g of [W(OEt)$_5$]$_2$-IWI-1.7/ASA$_{-300}$, which turned dark green. After 16 h of maturation, the solvent was evacuated under high vacuum (5 10^{-5} mbar) for 2 h to give dark extrudates, which were stored in the glovebox.

Synthesis of $Ni(NO_3)_2$-IWI-0.30/$[W(OEt)_5]_2$-IWI-1.7/ASA_{-300}

$Ni(NO_3)_2$ (0.488 g) was stirred in 5 mL of ethanol for 15 min to give a colourless solution. An aliquot of 600 µL of this solution was slowly added to impregnate 1.49 g of $[W(OEt)_5]_2$-IWI-1.7/ASA_{-300}, which turned light green. After 16 h of maturation, the solvent was evacuated under high vacuum (5 10^{-5} mbar) for 2 h to give green extrudates, which were stored in the glovebox. **E.A**: 9.56 $\%_{wt.}$ W, *e.g.* 1.6 (±0.1) W/nm²; 0.92 $\%_{wt.}$ Ni, *e.g.* Ni/W = 0.30.

Synthesis of $Ni(acac)_2$-0.22/W(POM)-IWI-1.8/ASA

$Ni(acac)_2$ (0.478 g) was stirred for 3 h in hot toluene (75 to 80°C) (5 ml, 0.40 mol/L) to give an emerald green solution. An aliquot (1.2 mL) of this hot solution was used to impregnate 2.95 g of a conventionally prepared ASA supported dried oxide phase (referred as W(POM)-IWI-1.8/ASA, 11.4 $\%_{wt.}$ W) The solid turned green. After 16 h of maturation, the solvent was evacuated under high vacuum (5 10^{-5} mbar) for 2 h to give light green extrudates. **E.A**: 11.09 $\%_{wt.}$ W, *e.g.* 1.8 (±0.1) W/nm²; 0.78 $\%_{wt.}$ Ni, *e.g.* Ni/W = 0.22.

II.6.b.2. Deposition of nickel precursors onto tungsten sulphide materials

Synthesis of $Ni(acac)_2$-IWI-0.20/$WS_{2\text{-}350°C}$/ASA_{-300}

$Ni(acac)_2$ (0.341 g) was stirred for 3 h in hot toluene (75 to 80°C) (5 mL, 0.27 mol/L) to give an emerald green solution. An aliquot (900 µL) of this hot solution was used to impregnate 1.72 g of a dark sulphide material referred as $WS_{2\text{-}350°C}$/ASA_{-300}.,Dark extrudates were obtained. After 16 h of maturation, the solvent was evacuated under high vacuum (5 10^{-5} mbar) for 2 h to give a dark solid, stored in the glovebox. **E.A**: 9.89 $\%_{wt.}$ W, *e.g.* 1.7 (±0.1) W/nm²; 0.66 $\%_{wt.}$ Ni, *e.g.* Ni/W = 0.20.

Synthesis of $Ni(acac)_2$-IWI-0.24/$WS_{2\text{-}23°C}$/ASA_{-300}

$Ni(acac)_2$ (0.345 g) was stirred for 3 h in hot toluene (75 to 80°C) (5 ml, 0.27 mol/L) to give a emerald green solution. An aliquot (800 µL) of this hot solution was used to impregnate 1.575 g of a brown sulphide material, prepared at 23°C (referred as $WS_{2\text{-}23°C}$/ASA, see preparation on WS_2-ex.$[W(OEt)_5]_2$-IWI-1.7/ASA_{-300} at $T_{sulph.}$ = 23°C). Brown extrudates were obtained. After 16 h of maturation, the solvent was evacuated under high vacuum (5 10^{-5} mbar) for 2 h to give a brown solid, stored in the glovebox. Traces of an off-white product were observed on the glassware. **E.A**: 10.03 $\%_{wt.}$ W, *e.g.* 1.6 (±0.1) W/nm²; 0.79 $\%_{wt.}$ Ni, *e.g.* Ni/W = 0.24.

Synthesis of $Ni(acac)_2$-IWI-0.44/$WS_{2\text{-}23°C}$/$ASA_{\text{-}300}$

$Ni(acac)_2$ (0.692 g) was stirred for 3 h in hot toluene (75 to 80°C) (5 ml, 0.54 mol/L) to give a emerald green solution. An aliquot (790 µL) of this hot solution was used to impregnate 1.536 g of a brown sulphide material, prepared at 23°C (referred as $WS_{2\text{-}23°C}$/ASA). Brown extrudates were obtained. After 16 h of maturation, the solvent was evacuated under high vacuum (5 10^{-5} mbar) for 2 h to give a brown solid, stored in the glovebox. Traces of an off-white product were observed on the glassware.

Synthesis of $Ni(acac)_2$-IWI-0.85/$WS_{2\text{-}23°C}$/$ASA_{\text{-}300}$

The sample was prepared with 2 successive impregnations of a toluene solution of $Ni(acac)_2$ (0.54 mol/L). The first one of the two impregnations was performed on 1.58 g of a brown sulphide material, prepared at 23°C (referred as $WS_{2\text{-}23°C}$/ASA). **E.A**: 9.17 $\%_{wt.}$ W, *e.g.* 1.5 (±0.1) W/nm²; 2.49 $\%_{wt.}$ Ni, *e.g.* Ni/W = 0.85.

II.7. Preparation of nickel-promoted sulphide catalysts

Sulphide materials, either prepared *via* a CSC or a conventional method, were prepared according to the representative procedure, with a sulphidation temperature of 350°C

II.8. Catalytic test

Catalytic activity measurements in toluene hydrogenation (HYD) were carried out in a 16 fixed beds unit reactor *Flowrence* from *Avantium* using *ca.* 450 µl of catalyst. The mass required was calculated from the density of the whole extrudate, unless otherwise stated. Zirconia-based materials are used in the top and the bottom of the reactor in order to correctly set the catalyst bed and fill the void space.

The model feed was composed of dimethyldisulphide (DMDS 5.8 $\%_{wt.}$) and toluene (20 $\%_{wt.}$), cyclohexane (74.2 $\%_{wt.}$) and aniline (0.5 $\%_{wt.}$). DMDS is decomposed to CH_4 and H_2S, which maintain the sulphided state of catalyst during test. The hydrogen to feed ratio (H_2/HC) was 450 NL/L during test and *in situ* pre-sulphidation step. In order to avoid cracking reactions of catalysts and measure a more accurate value of hydrogenation, the catalysts were tested in the presence of aniline to moderate the acidity [Ben Tayeb *et al.*, 2010]. To this end, aniline was added to the feed and the operating conditions were adapted to allow hydrogenation (and

isomerisation) reactions without cracking products formation. The experimental condition was strictly similar for all tests.

Note that the *in situ* pre-sulphidation of the catalysts was conducted at a liquid hourly space velocity (LHSV) of 4 h^{-1} with a total pressure of 6 MPa for 2.5 h, during which the temperature increased from 70°C to 350 °C with a ramp of 2 °C/min. Then, the liquid hourly space velocity was turned down to 2 h^{-1}. Liquid products of the reaction were analyzed by gas chromatography using a DB1 column. Each reactor was analyzed six times over the course of 9 hours (one analysis per reactor per 90 minutes). One strong inconvenient for non-conventional (CSC) catalysts was that *in-situ* pre-sulphidation causes an important leaching of metal species. Indeed, the sulphidation step begins around 70°C, when toluene and aniline are still liquid. As toluene, cyclohexane and aniline proved to leach the metal from the surface, the feed, under its liquid state, cleaves "ASA-O-W" bonds before tungsten oxide species being transformed into WS_2 slabs, strongly bonded to the support.

Therefore, catalysts were pre-sulphided *ex-situ* prior to catalytic tests. These sulphide catalysts were loaded into reactors under inert conditions (glovebox) and tested following the same procedure as described earlier: one sulphidation step (liquid phase) and then, the test step. Considering that the sulphidation step of the test modifies the sulphide phase of each catalyst, spent catalysts were recovered after test, quickly stored under argon and analysed by XPS and TEM.

II.9. References

Ben Tayeb, K.; Lamonier, C.; Lancelot, C.; Fournier, M.; Payen, E.; Bonduelle, A. and Bertoncini, F., *Catalysis Today* (2010), **150**, (3–4), 207-212

Brown, S.P.; Lesage, A.; Elena B. and Emsley, L., *Journal of the American Chemical Society* (2004), **126,** 41, 13230-13231.

Cartes, M.A.; post doctoral position, ETH Zürich

Fulmer, G. R.; Miller, A. J. M.; Sherden, N. H.; Gottlieb, H. E.; Nudelman, A.; Stoltz, B. M.; Bercaw, J. E. and Goldberg, K. I., *Organometallics* (2010), **29**, 2176

Gandubert, A.D.; Legens, C.; Guillaume, D.; and Payen, E., *Surface and Interface Analysis* (2006), **38**, 4, 206-209.

Gandubert, A.D.; Krebs, E.; Legens, C.; Costa, D.; Guillaume, D. and Raybaud, P., *Catalysis Today* (2008), **130**, 1, 149-159.

Guichard, B.; Roy-Auberger, M.; Devers, E.; Legens, C. and Raybaud, P., *Catalysis Today* (2008), **130**, 1, 97-108.

Hensen E.J.M., van der Meer Y., van Veen J.A.R. and Niemantsverdriet J.W., *Applied Catalysis A: General* (2007), **322**, 0, 16-32.

Heroguel, F. PhD position, ETH Zürich

Kim, C.H.; Yoon, W.L.; Lee, I.C. and Woo, S.I., *Applied Catalysis* A: General, **144**, 159-175

Lmonosov, M.V. Moscow State University. Translated from *Koordinatsionnaya Khimiya* (1985), **11**, 11, 1521-1528

Lynch, J., Analyse physico-chimique des catalyseurs industriels (2001), Editions Technip, Paris

Rascon, F.; Wischert, R. and Copéret, C., *Chemical Science* (2011), **2**, 8, 1449-1456

Reinhoudt, H.R.; Crezee, E.; van Langeveld, A.D.; Kooyman, P.J.; van Veen, J.A.R. and Moulijn, J.A., *Journal of Catalysis*, (2000), **196**, 2, 315-329

Sun, M.; Bürgi, T., Cattaneo, R. and Prins, R. *Journal of Catalysis* (2001), **197**, 172-181

Zuo, D.; Vrinat, M.; Nie, H.; Maugé, F.; Shi, Y.; Lacroix, M. and Li, D., *Catalysis Today* (2004), **93-95**, 1, 751-760

Part III. Preparation of non-promoted ASA-supported W catalysts: impregnation of W(V) and W(VI) alkoxides

Outline (Part III)

Outline (Part III) **97**

Introduction **99**

III.1. Characterisation of molecular complexes of W(V) and W(VI) **99**

III.1.a. Tungsten pentaethoxide - $W(OEt)_5$ 101

III.1.b. Tungsten hexaethoxide - $W(OEt)_6$ 103

III.1.c. Tungsten oxotetraethoxide - $[W(=O)(OEt)_4]_2$ 106

III.2. Preparation and characterisation of W-supported materials, from W(V) or W(VI) molecular precursors. **110**

III.2.a. Characterisation of CSC materials by Infrared spectroscopy (IR) 110

III.2.b. Characterisation of CSC materials by X-ray photoelectron spectroscopy (XPS) ... 111

III.3. Characterisation of sulphide catalysts prepared from W(V) or W(VI) precursors **112**

III.4. Benchmarking catalytic activities with conventionally prepared catalysts **114**

III.5. Conclusion **116**

III.6. References **116**

Introduction

The aim of this chapter is to evaluate the effect of the structure of different tungsten precursors on the resulting hydrogenating catalysts performances. This is meant to choose a molecular precursor and the detailed characterisation and evaluation of the catalytic performance of the thus-prepared catalyst. In particular, we will look into the effect of the structure of the molecular precursor on the surface species obtained after grafting, and of the resulting sulphide phases obtained after sulphidation on to the catalytic activity. Following the characterisation of tungsten(V) and tungsten(VI) alkoxides molecular precursor by Fourier Transform Infrared (FT-IR) and Nuclear Magnetic Resonance (NMR) spectroscopies, we will describe the preparation and characterisation of materials before and after sulphidation, analysed by IR spectroscopy as well as by X-ray Photoelectron Spectroscopy (XPS), to finish by an evaluation of the catalytic activity.

III.1. Characterisation of molecular complexes of W(V) and W(VI)

The physical properties of metal alkoxides $[M(OR)_x]_n$ are strongly influenced by the type of alkyl group R, as well as by the preferential coordination number of the metal. Only a few homoleptic metal alkoxides, *e.g.* metallo-organic complexes containing identical ligands, have been structurally characterised in the literature. The majority of the complexes which structure were determined usually contain other ligands beside the alkoxy group [Cotton *et al.*, 1985]. The alkoxy ligand RO^- can adopt several binding modes to metal and behaves as terminal (**Figure 19-a**) or bridged ligand (**Figure 19-b**).

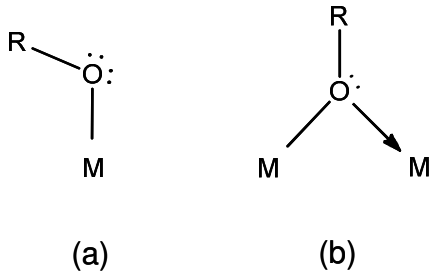

Figure 19 : binding modes of alkoxy ligands

Most of the homoleptic metal alkoxides which are soluble in common organic solvent tend to form oligomers with low degree of oligomerization (*e.g.* n = 2, 3, or 4) [Bradley, 1958]. Moreover, it has been proposed that for the less bulky alkoxy group, the metal uses the bridging propensity of the ligand to achieve the smallest oligomer compatible, with the metal atoms attaining their preferred coordination number. To minimize the complexity of polynuclear complexes, it is necessary to maximize the number of bridging ligands, by forming face-sharing or edge-sharing polyhedra. Besides, the steric effect of the ligand RO^- plays an important role. By increasing the chain branching or the size of the R-group, steric effects can prevent alkoxy-bridging mode leading to mononuclear complexes.

In the early 50's, Bradley [Bradley *et al.*, 1953] proposed a theory for metal alkoxides structure based on consideration of molecular weight data, enthalpy and entropy. From this theory, $W(OMe)_6$ would tend to be monomeric with an octahedral structure, while Nb linked to methoxo groups would be a dimer exhibiting edge-sharing octahedra, as shown on **Figure 20**.

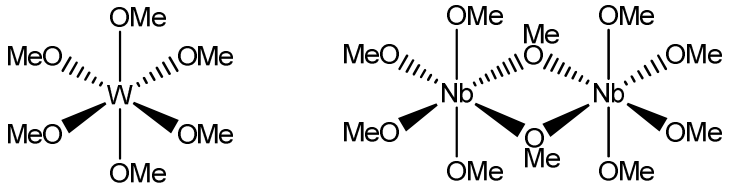

(3-IV) (3-V)

Figure 20: structural types adopted by $W(OMe)_6$ and $[Nb(OMe)_5]_2$ from Bradley's theory

Therefore, the structure of the alkoxy complexes used in this study will depend on the steric effect of ethoxo groups as well as the tungsten ability to form stable structures with five or six ethoxo ligands. The characterisation of $W(OEt)_5$, $W(OEt)_6$ and $W(=O)(OEt)_4$ is presented in the following part.

III.1.a. Tungsten pentaethoxide - $W(OEt)_5$

$W(OEt)_5$ is a commercial compound, provided by Alfa Aesar. It is moisture and oxygen sensitive. Contact with H_2O and molecular oxygen causes polycondensation of tungsten species and oxidation of tungsten, respectively.

First, we characterised the tungsten precursor (409.15 g/mol) by mass spectrometry (electronic impact, direct introduction). Isotopic peak of W at M/Z = 409.08 confirmed the presence of the complex, as well as several fragment ions formed in the apparatus.

Structural characterisation of tungsten pentaethoxide by X-ray has not been achieved as far as we know. Alkoxides compounds with close molecular formula were, however, crystallized and characterised in the literature. $W_2(\mu\text{-}OEt)_2(OEt)_4Cl_4$ [Cotton *et al.*, 1981] as well as $W_2(\mu\text{-}OMe)_2(OMe)_8$ [Bryan *et al.*, 1991] exhibited edge-sharing octahedral structures with bridging ligands. Therefore, we can assume that tungsten pentaethoxide forms a dimer with the formula $W_2(\mu\text{-}OEt)_2(OEt)_8$, also denoted $[W(OEt)_5]_2$, and exhibits two bridging ethoxy ligands (see **Figure 21**), as previously supposed by Bryan and co-workers.

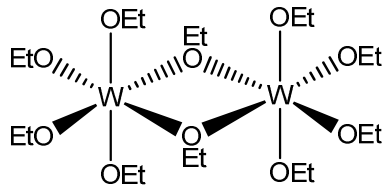

Figure 21: Structure of $[W(OEt)_5]_2$

III.1.a.1. Infrared spectroscopy (IR)

IR analysis of $[W(OEt)_5]_2$ was performed with an attenuated total reflectance (ATR) accessory, which allow the samples to be examined directly in the liquid (or the solid) state without further preparation. The IR spectrum, shown in **Figure 22**, exhibits the characteristic vibration bands of alkoxide ligands, *e.g.* ν(CH) in the 3000-2800 cm^{-1} region, as well as δ(CH) in the 1500-1250 cm^{-1} region. ν(C-O) vibrations are visible between 1150 and 900 cm^{-1}. We have not been able to assign CO vibrations to terminal or bridging ligands. In the literature however, Ta(V), Nb(V) and U(V) alkoxides exhibit $\nu(C\text{-}O)_{bridg}$ between 1030-1024 cm^{-1}, and

$\nu(C\text{-}O)_{term}$ between 917-905 cm^{-1} and between 1120-1056 cm^{-1}. Moreover, vibration of "tungsten-oxygen" bond, $\nu(M\text{-}O)$, were tentatively attributed to IR vibration band at 582 cm^{-1} and 615 cm^{-1}.[Reagan and Brubaker, 1970] On the IR spectrum of our product, the strong vibrations between 550 and 520 cm^{-1} could be in line with a $\nu(M\text{-}O)$ vibration, as reported for other ethoxo complexes [Bradley, 2001].

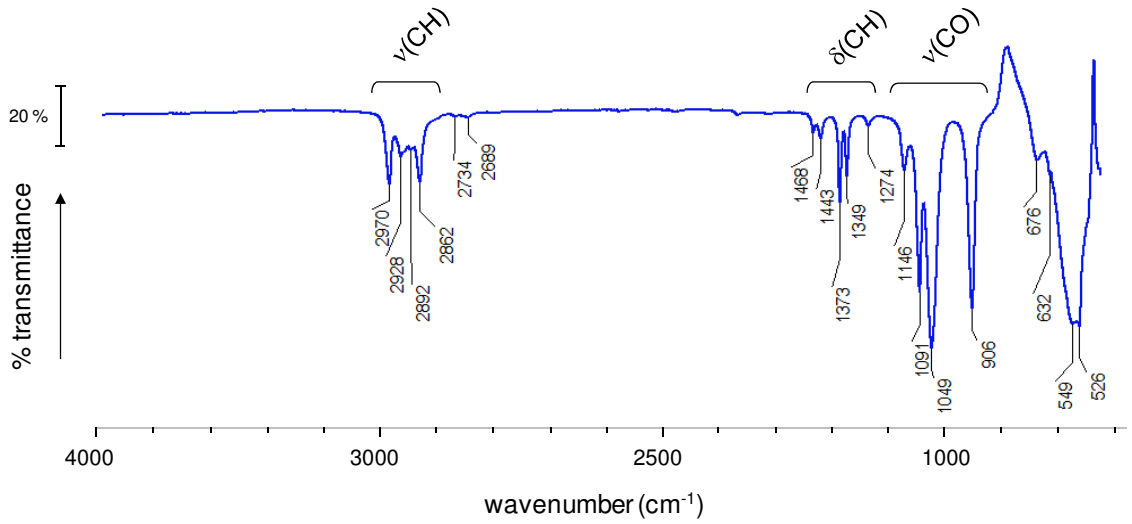

Figure 22: IR spectrum (ATR) of commercial $[W(OEt)_5]_2$

III.1.a.2. Nuclear Magnetic Resonance spectroscopy (NMR)

While tungsten pentaethoxide would be paramagnetic in its monomeric form, $W(OEt)_5$, because of the d1 configuration of the metal centre, the absence of EPR signal [Reagan and Brubaker, 1970] and the presence of sharp peak in NMR spectra shows that $[W(OEt)_5]_2$ is diamagnetic [Chisholm *et al.*, 1995]. The spectra obtained by proton NMR, denoted ^1H NMR; and proton decoupled ^{13}C NMR, denoted $^{13}C\{^1H\}$, are shown in **Figure 23**. Peaks attribution is summarized in **Table 1**. The ^1H NMR spectrum (CD_2Cl_2, 298K) shows a triplet at δ = 1.22 ppm assigned to W-O-$CH_2C\mathbf{H_3}$ and a quadruplet at δ = 4.77 ppm assigned to W-O-$C\mathbf{H_2}CH_3$ as reported in the literature [Reagan and Brubaker, 1970]. $^{13}C\{^1H\}$ NMR spectrum (CD_2Cl_2, 298K) exhibits two peaks, attributed to W-$OCH_2\mathbf{C}H_3$, δ = 18.8 ppm, and to W-O-$\mathbf{C}H_2CH_3$, δ = 70.1 ppm. Note that one could have expected a different spectrum, where bridging and terminal alkoxy ligands exhibit different chemical shifts. However, as the tungsten pentaethoxide is necessarily

diamagnetic and in its dimeric form, the experimental NMR spectrum clearly speaks for a rapid intramolecular exchange between bridging and terminal alkoxy ligands.

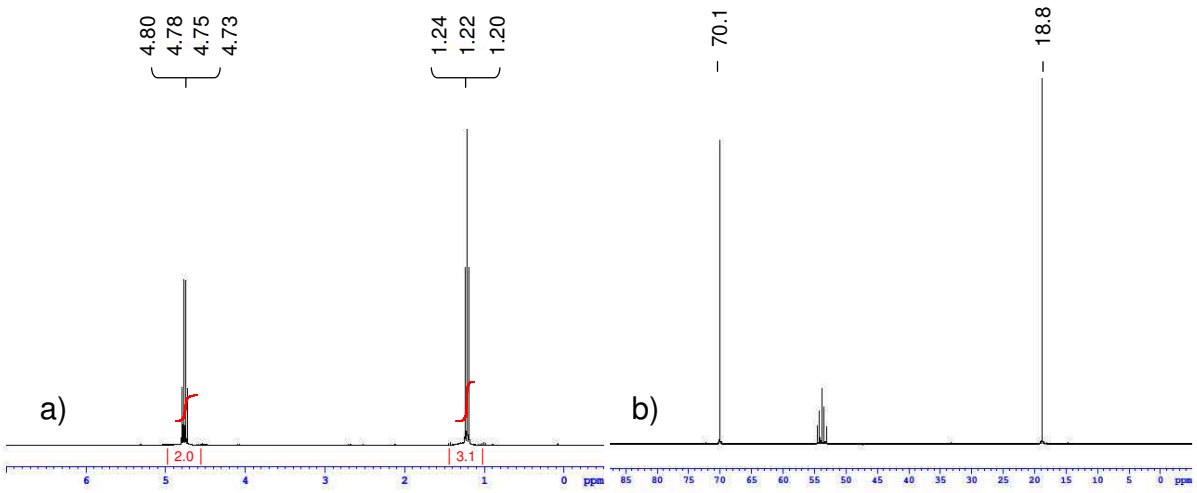

Figure 23: NMR spectra (298K, $CDCl_2$) of commercial $[W(OEt)_5]_2$: a) ^1H spectrum, and b) $^{13}C\{^1H\}$ spectrum.

Table 1: ^1H and $^{13}C\{^1H\}$ NMR data obtained on $[W(OEt)_5]_2$

	δ(CH_3) ppm W-O-CH_2-**CH_3**		δ(CH_2) ppm W-O-**CH_2**-CH_3	
	^1H	$^{13}C\{^1H\}$	^1H	$^{13}C\{^1H\}$
$[W(OEt)_5]_2$	1.22, *triplet*	18.8	4.77, *quadruplet*	70.1

No XPS could be recorded because the sample was liquid. All data are however consistent with a dimeric structure.

III.1.b. Tungsten hexaethoxide - $W(OEt)_6$

$W(OEt)_6$ is also a commercial compound (Alfa Aesar), oxygen and moisture sensitive. Its structure is supposed to be monomeric as the corresponding methoxy complex $W(OMe)_6$ [Bradley *et al.*, 1977] exhibits a monomeric structure with a W in an octahedral environment (see **Figure 24**).

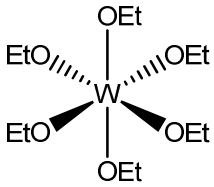

Figure 24: supposed structure of $W(OEt)_6$

III.1.b.1. Infrared (IR) and Raman spectroscopy

IR analysis (ATR) of $W(OEt)_6$ is very close to this discussed for $[W(OEt)_5]_2$. The IR spectrum of $W(OEt)_6$ (shown **Figure 25**) exhibits the characteristic vibration bands of alkoxy ligands: ν(CH) in the 3000-2800 cm^{-1} region, as well as δ(CH) in the 1500-1250 cm^{-1} region and ν(C-O) between 1150 and 900cm^{-1}. Two new bands are visible at ν = 1123 cm^{-1} and ν = 787 cm^{-1}. The first one is assigned to a C-O stretching mode, active for $W(OEt)_6$ .The band at ν = 787cm^{-1} is assigned to a W=O bond of the oxo-derivative impurity $W(=O)(OEt)_4$. Raman spectroscopy also evidences the presence of the oxo compound, exhibiting a ν(W=O) vibration at ν = 788 cm^{-1} (see **Figure 26**). These oxo-derivatives of metal alkoxides usually come from hydrolysis of alkoxides with the formation of hydroxo derivatives, which condense to form the oxo-ligand. Bradley, 2001]

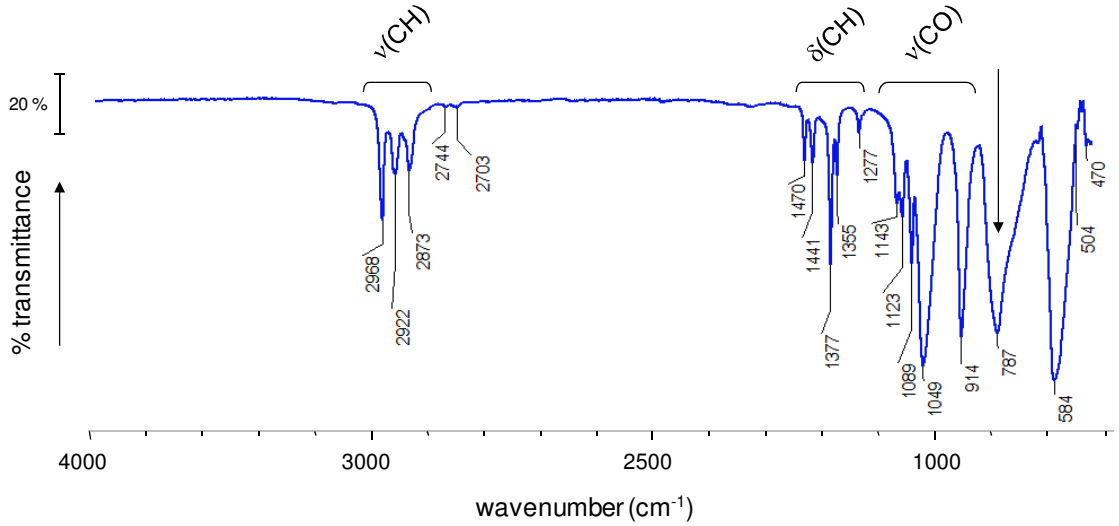

Figure 25: IR spectrum (ATR) of commercial $W(OEt)_6$

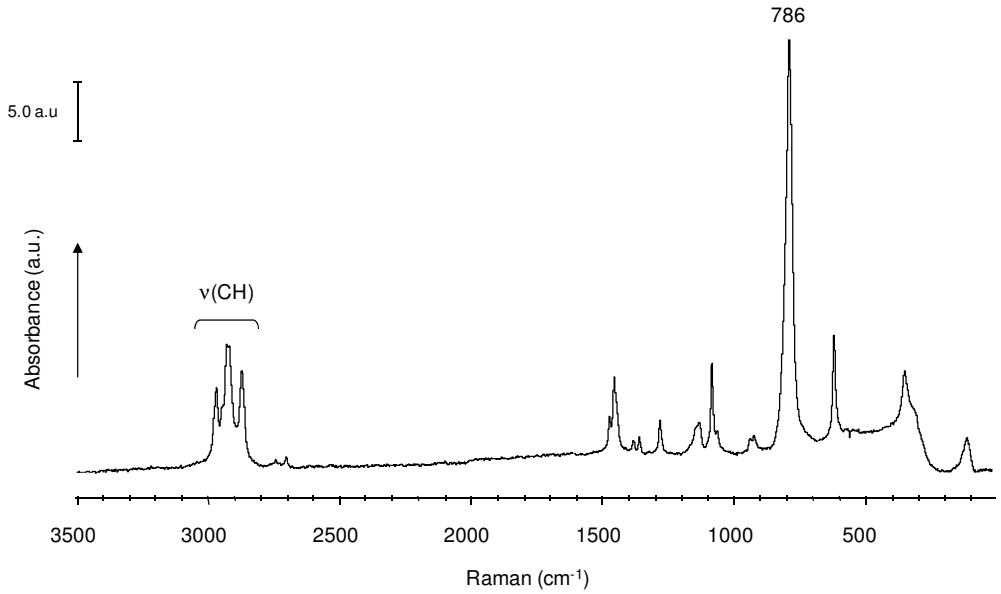

Figure 26: Raman spectrum of commercial $W(OEt)_6$

III.1.b.2. Nuclear magnetic resonance spectroscopy (NMR)

The ^1H and $^{13}C\{^1H\}$ NMR spectra (CD_2Cl_2, 298K) of $W(OEt)_6$ are shown **Figure 27**. Peaks assignment is summarized in **Table 2**. The ^1H NMR spectrum exhibits resolved multiplets as well as broad peaks. The triplet at δ = 1.22 ppm is assigned to CH_3 groups of ethoxy ligands. A quadruplet at δ = 4.76 ppm is assigned to CH_2 groups of ethoxy ligands [Bradley, 1972]. Then, as we will explain it latter with **Figure 31-a**, the two broad peaks, at δ = 1.32 ppm and δ = 4.77 ppm are assigned to ethoxy ligands of $[W(O)(OEt)_4]_2$. The presence of non-negligible amount of this degradation product, already detected by IR, has been confirmed by $^{13}C\{^1H\}$ NMR. The $^{13}C\{^1H\}$ spectrum (CD_2Cl_2, 298K) exhibits 4 peaks, which have been attributed as follows. δ = 18.8 ppm ($W(OEt)_6$, W-O-CH_2**C**H_3), δ = 70.1 ppm ($W(OEt)_6$, W-O-**C**H_2CH_3) and δ = 18.2 ppm ($[W(O)(OEt)_4]_2$, W-O-CH_2**C**H_3), δ = 72.4 ppm ($[W(O)(OEt)_4]_2$, W-O-**C**H_2CH_3).

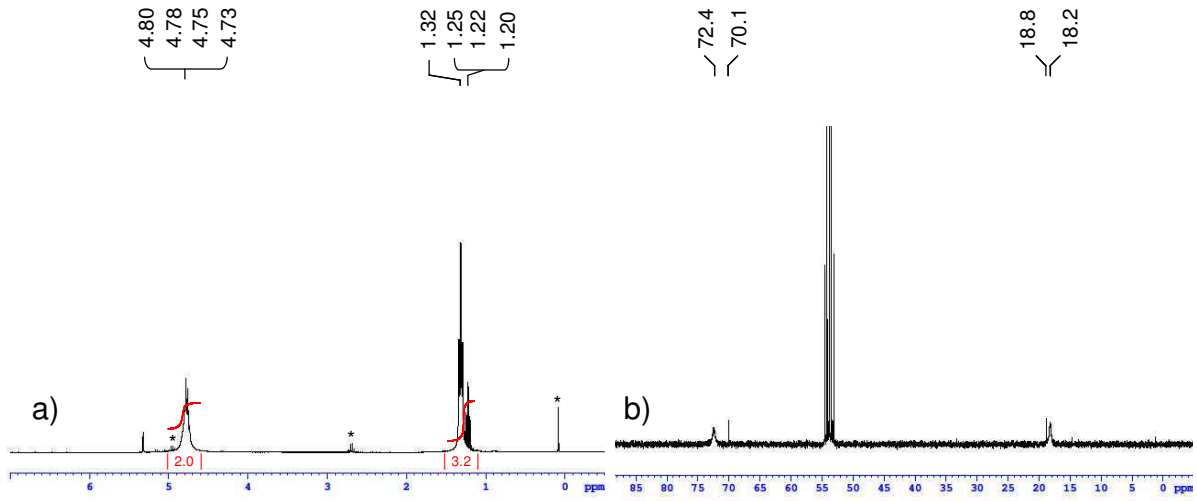

Figure 27: NMR spectra (298K, $CDCl_2$) of commercial $W(OEt)_6$: a) ^1H spectrum, and b) $^{13}C\{^1H\}$ spectrum. (∗ stands for impurities)

Table 2: ^1H and $^{13}C\{^1H\}$ NMR data obtained on $W(OEt)_6$

	δ(CH_3) ppm W-O-CH_2-**CH_3**		δ(CH_2) ppm W-O-**CH_2**-CH_3	
	^1H	$^{13}C\{^1H\}$	^1H	$^{13}C\{^1H\}$
$W(OEt)_6$	1.22, *triplet*	18.8	4.76, *quadruplet*	70.1
$[W(O)(OEt)_4]_2$[a]	1.32, *triplet*	18.2	4.77, *broad peak*	72.4

[a] Impurity

III.1.c. Tungsten oxotetraethoxide - $[W(=O)(OEt)_4]_2$

$[W(=O)(OEt)_4]_2$ was kindly provided by M.Cartes (synthesized during her post doctoral position at ETH Zürich) as part of our on-going collaboration. The oxo-derivative synthesis is available in the experimental section (part II).

From the literature, oxo-derivatives of tungsten tend to adopt different nuclearities. $W(O)(OtBu)_4(thf)$ has been reported as mononuclear species [Cotton *et al.*, 1985]. Clegg's team [Clegg *et al.*, 1992] synthesised and characterised various oxo-alkoxides with formula $W(O)(OR)_4$ (R = Me, Et). X-ray characterisation of $W_2(O)_2(\mu\text{-}OMe)_2(OMe)_6$ has shown that this compound was a dimeric molecule, adopting a distorted edge-shared bi-octahedral structure

featuring terminal oxo ligand trans to the bridged-methoxo group. According to the work of Clegg, $[W(O)(OEt)_4]_2$ can adopt a bi-octahedral geometry as depicted in **Figure 28.**

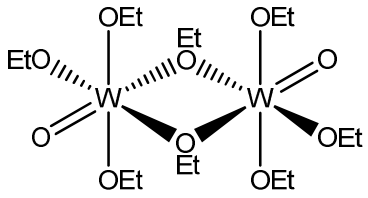

Figure 28: proposed structure of $[W(O)(OEt)_4]_2$ by Clegg and co-workers [Clegg *et al.*, 1992]

III.1.c.1. Infrared (IR) and Raman spectroscopy

The IR spectrum (ATR) of $[W(O)(OEt)_4]_2$ (see **Figure 29**) exhibits the characteristic vibration bands of alkoxide ligands: ν(CH) in the 3000-2800 cm^{-1} region, as well as δ(CH) in the 1500-1250 cm^{-1} region and ν(C-O) between 1150 and 900 cm^{-1}, including the vibration at ν = 1123 cm^{-1}. The vibration positioned at ν = 788 cm^{-1} is assigned to the W=O bond stretching by comparison with the reported data for $[W(O)(OEt)_4]_2$. [Clegg *et al.*, 1992]

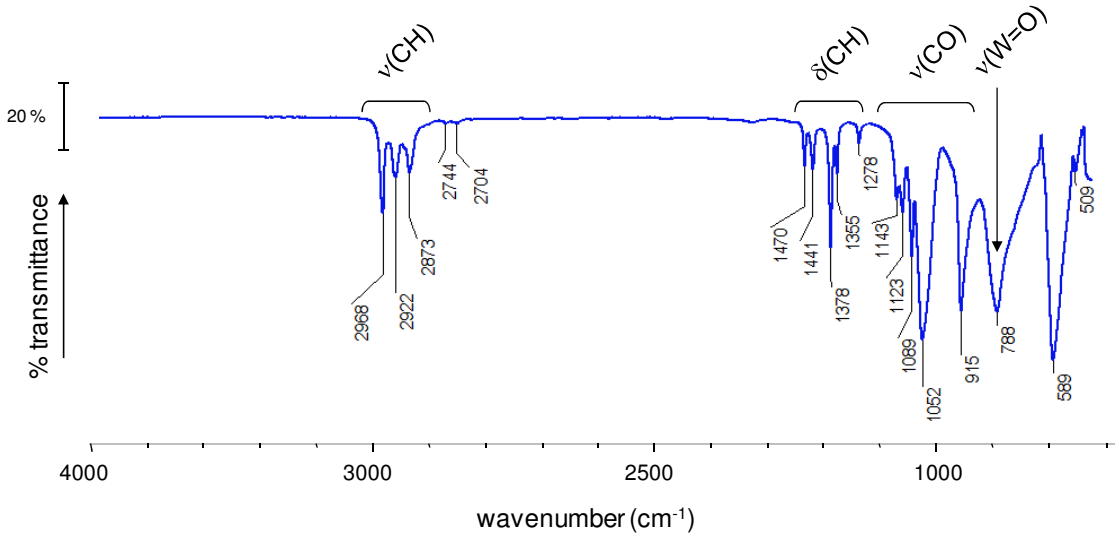

Figure 29: IR spectrum (ATR) of $[W(O)(OEt)_4]_2$

Besides, the characterisation of $[W(O)(OEt)_4]_2$ by Raman spectroscopy, shown in **Figure 30**, highlights a band at 788 cm^{-1}, assigned to W=O.

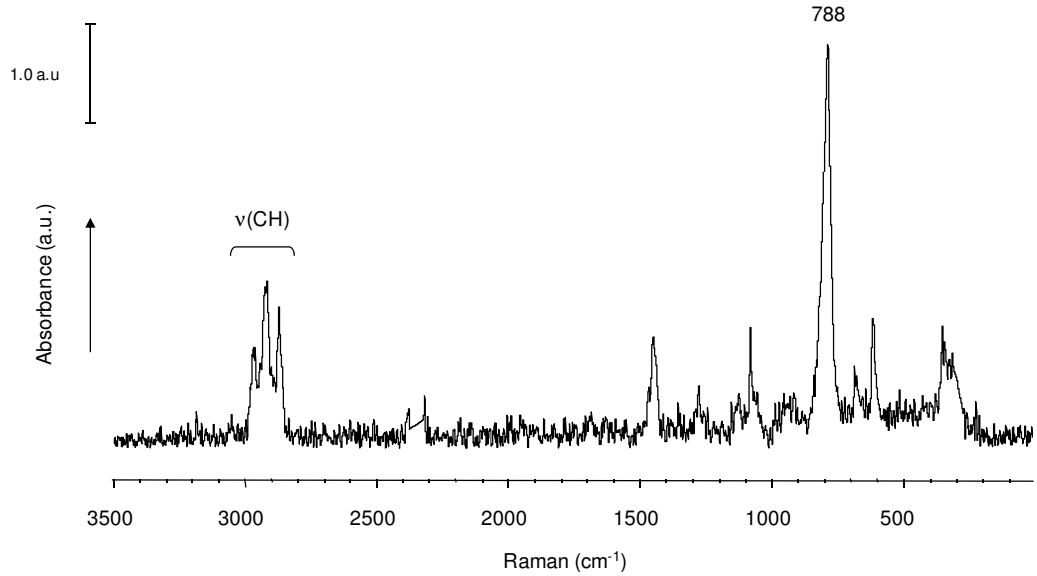

Figure 30: Raman spectrum of $[W(O)(OEt)_4]_2$

III.1.c.2. Nuclear magnetic resonance spectroscopy (NMR)

The ^1H and $^{13}C\{^1H\}$ NMR spectra (CD_2Cl_2, 298K) of $[W(O)(OEt)_4]_2$ are shown **Figure 31**, and peaks assignment is summarized in **Table 3**), On the ^1H NMR spectrum, broad resonances of methyl (δ = 1.32 ppm) and methylene protons (δ = 4.78 ppm) are visible. The $^{13}C\{^1H\}$ NMR spectrum (CD_2Cl_2, 298K) contains two main peaks at δ = 18.2 ppm and δ = 72.4 ppm, respectively assigned to the beta-carbon and alpha-carbon of the ethoxo ligands. Traces of $W(OEt)_6$ are visible (asterisks).

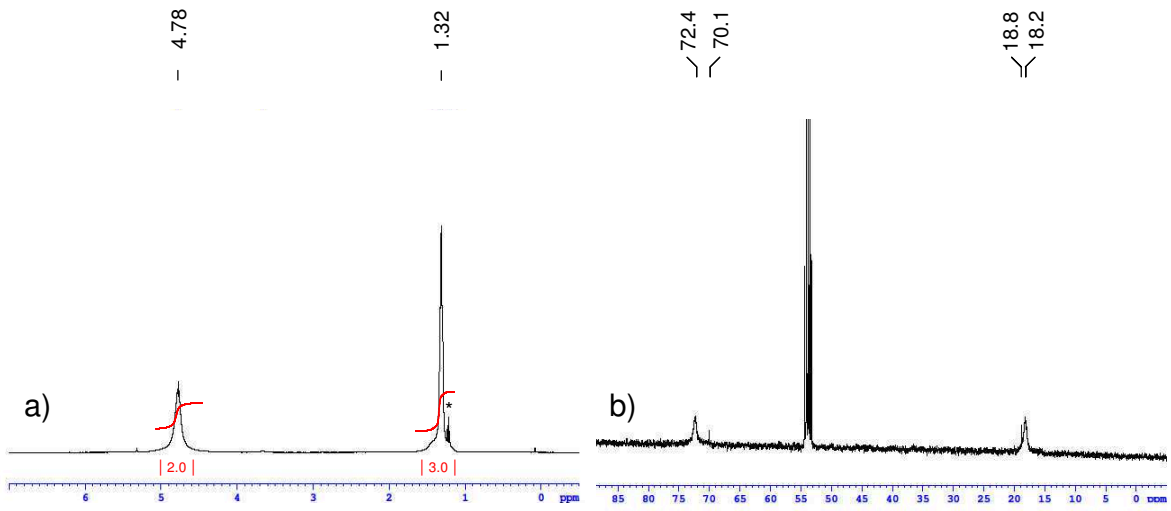

Figure 31: NMR spectra (298K, CD_2Cl_2) of $W(O)(OEt)_4$. : a) ^1H spectrum, and b) $^{13}C\{^1H\}$ spectrum. [Cartes, 2012].

Table 3: ^1H and $^{13}C\{^1H\}$ NMR data obtained on $[W(O)(OEt)_4]_2$

	$\delta(CH_3)$ ppm W-O-CH_2-**CH_3**		$\delta(CH_2)$ ppm W-O-**CH_2**-CH_3	
	^1H	$^{13}C\{^1H\}$	^1H	$^{13}C\{^1H\}$
$[W(O)(OEt)_4]_2$	1.32, *triplet*	18.2	4.78, *broad peak*	72.4
$W(OEt)_6$[a]	1.22, *triplet*	18.8	4.76, *quadruplet*	70.1

[a] Impurity

No elemental analysis of $[W(O)(OEt)_4]_2$ was performed.

As a conclusion, we showed that commercially available $W(OEt)_6$, interesting as a mononuclear species was not pure and contained non-negligible amount of $[W(O)(OEt)_4]_2$. The oxo-derivative was purer than $W(OEt)_6$, and probably exhibited a dimeric structure. Finally, $[W(OEt)_5]_2$ was the purest of tungsten derivatives we analysed.

III.2. Preparation and characterisation of W-supported materials, from W(V) or W(VI) molecular precursors.

Different materials were prepared, by deposition of $[W(OEt)_5]_2$, $W(OEt)_6$ and $[W(O)(OEt)_4]_2$ onto amorphous silica-alumina partially dehydroxylated at 300°C or 500°C under vacuum. Samples impregnations were performed by Incipient Wetness Impregnation (*IWI*) or by grafting (*e.g.* stoechiometric impregnation followed by several washing steps). Thermal pretreatments of silica-alumina supports are described in part II, as well as their characterisation.

The three materials prepared by *grafting* (G) were kindly prepared by M.Cartes at ETH Zürich, and are referred as follows:

- $[W(OEt)_5]_2$-*G*-0.7/ASA_{-500} with *ca.* 0.7 W/nm²
- $W(OEt)_6$-*G*-0.7/ASA_{-500} with *ca.* 0.7 W/nm²
- $[W(O)(OEt)_4]_2$-*G*-0.8/ASA_{-500} with *ca.* 0.8 W/nm²

Note that the W-loadings of the samples reported in this study were calculated on the basis of the support surface area, which is *ca.* 227 m²/g for ASA_{-500}.

III.2.a. Characterisation of CSC materials by Infrared spectroscopy (IR)

Figure 32 shows the IR spectra (4000 cm^{-1} - 1400 cm^{-1}) of samples prepared by grafting, *e.g.* $[W(OEt)_5]_2$-*G*-0.7/ASA_{-500}, $W(OEt)_6$-*G*-0.7/ASA_{-500} and $[W(O)(OEt)_4]_2$-*G*-0.9/ASA_{-500}. On the spectra, the vibration band attributed to isolated silanols $\nu(OH)_i$ at 3743 cm^{-1} disappears upon deposition of the precursors. Moreover, apparition of the characteristic features of alkoxy complexes, *e.g.* ν(CH) and δ(CH) bands, is attributed to the presence of ethoxo ligands, linked to surface tungsten. We can conclude that tungsten complexes are probably grafted on surface hydroxyles.

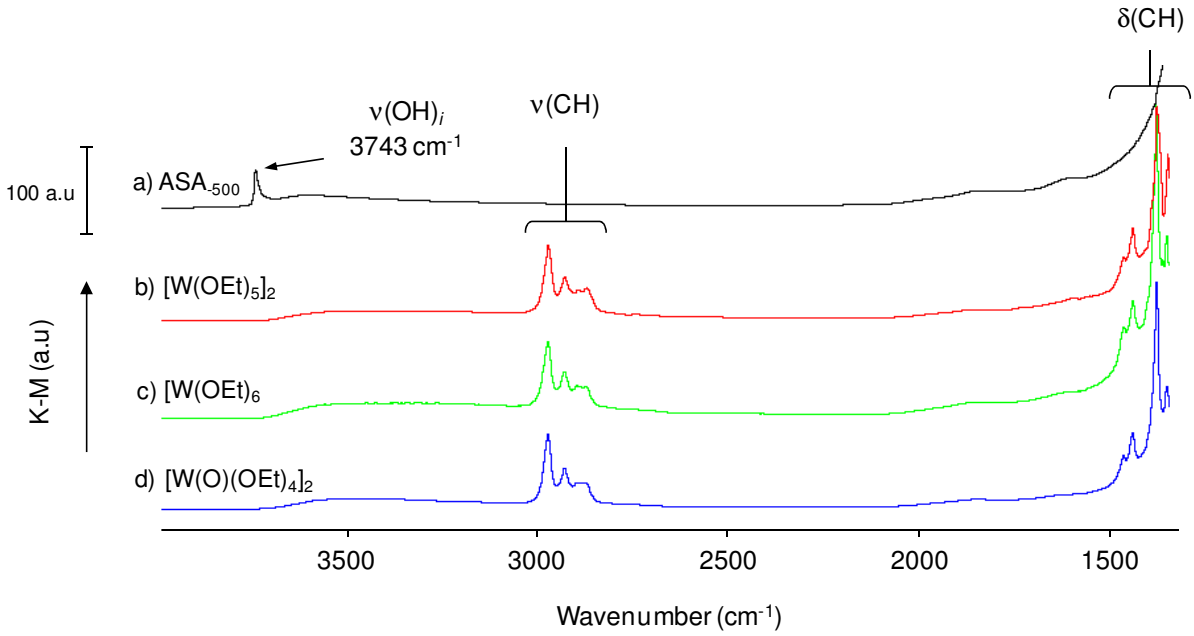

Figure 32: IR spectra (DRIFT) of a) amorphous silica alumina - ASA_{-500} ; and W-based materials supported on ASA_{-500}, prepared with b) $[W(OEt)_5]_2$, c) $W(OEt)_6$, and d) $[W(O)(OEt)_4]_2$.

III.2.b. Characterisation of CSC materials by X-ray photoelectron spectroscopy (XPS)

$[W(OEt)_5]_2$-*G*-0.7/ASA_{-500}, $W(OEt)_6$-*G*-0.7/ASA_{-500} and $[W(O)(OEt)_4]_2$-*G*-0.8/ASA_{-500} were analysed by X-ray Photoelectron Spectroscopy. **Figure 33** shows their W 4f photopeaks, which are very similar. Two doublets with W $4f_{7/2}$ and W $4f_{5/2}$ components are visible. Their principal components W $4f_{7/2}$ are respectively positioned at binding energies (BE) of 36.0 eV and 35.0 eV. The first doublet, positioned at the higher BE, is typical of tungsten (VI) species [Wagner, 1979] and represents about 92 % of the total amount of tungsten visible. The second doublet, which principal component is shifted to lower BE, is assigned to partially reduced tungsten species, reduced *in-situ* upon irradiation by the X-ray beam under the ultra-high vacuum of the apparatus.

In the case of $W(OEt)_6$-*G*-0.7/ASA_{-500} and $[W(O)(OEt)_4]_2$-*G*-0.8/ASA_{-500}, finding a W(VI) environment is consistent with the oxidation state of the initial precursor. In the case of $[W(OEt)_5]_2$-based material, one would expect a W 4f photopeak at lower BE. As far as we know, W(V) has never been assigned to a precise BE. Note that Alov *et al.* and Coulier *et al.* respectively found BE of *ca.* 34.4 eV and *ca.* 33.5 for the W $4f_{7/2}$ component of W(V), respectively in tungsten oxide thin films [Alov, 2005] or in sulphide catalysts [Coulier *et al.* 2002]. Observing a W(VI) environment for $[W(OEt)_5]_2$-0.7/ASA_{-500} may probably be due to the presence

of a dimeric species, where the two tungsten centres are surrounded by six oxygen. The increase of electron density around the metal could explain the shift in binding energy of the photopeak W $4f_{7/2}$ to values typically found for W(VI) species.

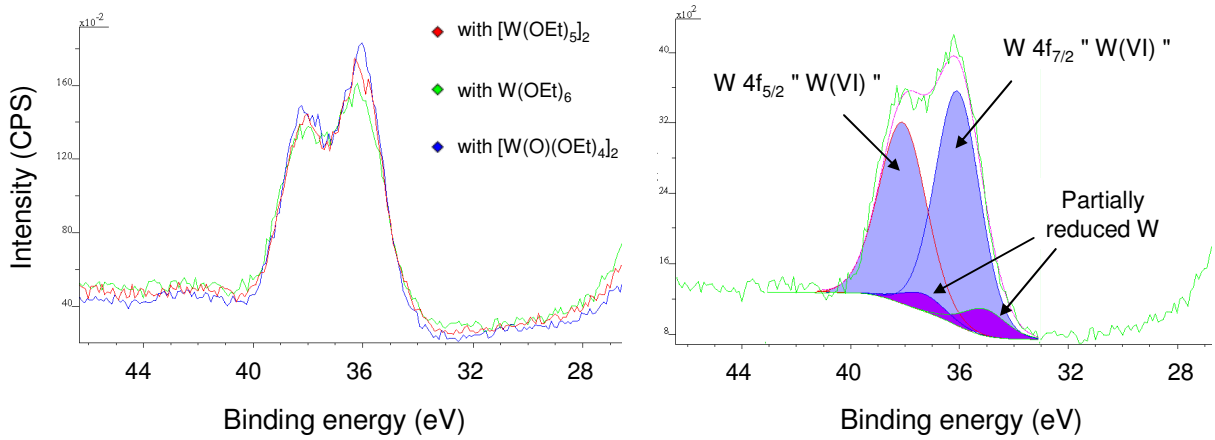

Figure 33: Left: XPS spectra normalised. W 4f contribution of materials prepared by grafting of tungsten on ASA_{-500}. Materials were prepared with $[W(OEt)_5]_2$ (red), $W(OEt)_6$ (green), and $[W(O)(OEt)_4]_2$ (blue). Calibrated *vs.* carbon C 1s at 284.6 eV. Right: decomposition of W 4f photopeak of $W(OEt)_6$ based catalyst.

To conclude, we showed that the deposition of the three different precursors led to catalysts with similar IR and XPS spectra. The surface species found on oxide catalysts appeared to be in a W(VI) environment.

III.3. Characterisation of sulphide catalysts prepared from W(V) or W(VI) precursors

In order to obtain active hydrotreating catalysts, the materials previously impregnated by metallic precursors need to be activated by sulphidation. Sulphidation is the key step to generate the metal sulphides, which represent the active phase in hydrotreating catalysts.

We first tried to carry out the sulphidation of one of the tungsten precursor, to test whether it was possible or not to obtain a 100 % bulk WS_2. Sulphidation of liquid $[W(OEt)_5]_2$ at 600°C under a mixture of 15 $\%_{mol.}$ H_2S/H_2 (see experimental section part II) gives a grey solid which exhibits *ca.* 92 (±5) $\%_{rel.}$ WS_2 with respect to the surface area of W $4f_{7/2}$ and W $4f_{5/2}$ assigned to $W^{(IV)}S_2$. The XPS spectrum (W 4f photopeak) is shown in **Figure 34**.

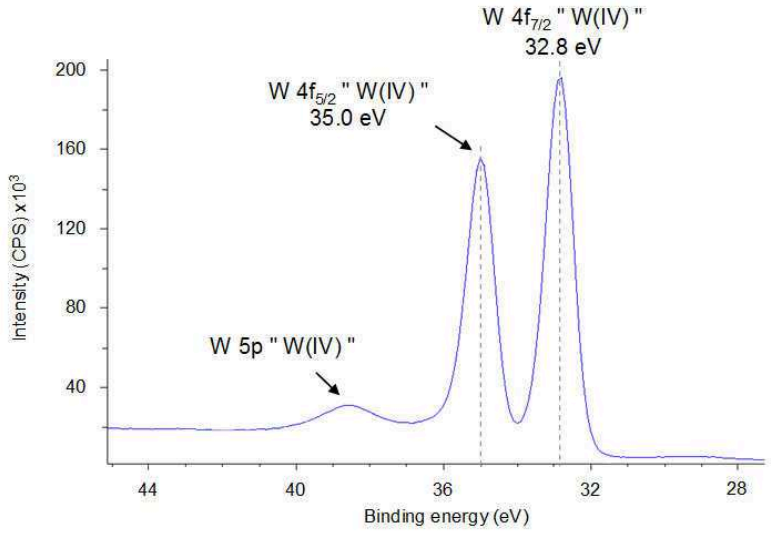

Figure 34: XPS spectra. W 4f photopeak of bulk WS_2 prepared by sulphidation of $[W(OEt)_5]_2$ (details available in experimental section). Calibrated *vs.* C 1s at 284.6 eV.

Sulphidation of the previous materials, prepared by grafting, was performed at 350°C under a mixture of 15 $\%_{mol.}$ H_2S/H_2 as reported in part II. WS_2/ASA catalysts were referred as follows:

- WS_2-*ex.*$[W(OEt)_5]_2$-*G*-0.7/ASA_{-500}
- WS_2-*ex.*$W(OEt)_6$-*G*-0.7/ASA_{-500}
- WS_2-*ex.*$[W(O)(OEt)_4]_2$-*G*-0.8/ASA_{-500}

Figure 35 shows the W 4f photopeaks of the three aforementioned sulphide catalysts, which spectra are similar. Spectral decomposition in W(VI), partially reduced W(V), and W(IV) gave average sulphidation levels of about 71 (± 5).$\%_{rel.}$ WS_2. As mentioned above, sulphidation of $[W(OEt)_5]_2$ at 600°C gives bulk WS_2 with *ca.* 92 (±5) $\%_{rel.}$ WS_2, indicating that the level of sulphidation of the catalysts can somehow be improved. Besides, the same S/W atomic ratio is found for the three catalysts: S/W = 2.3 (at/at).

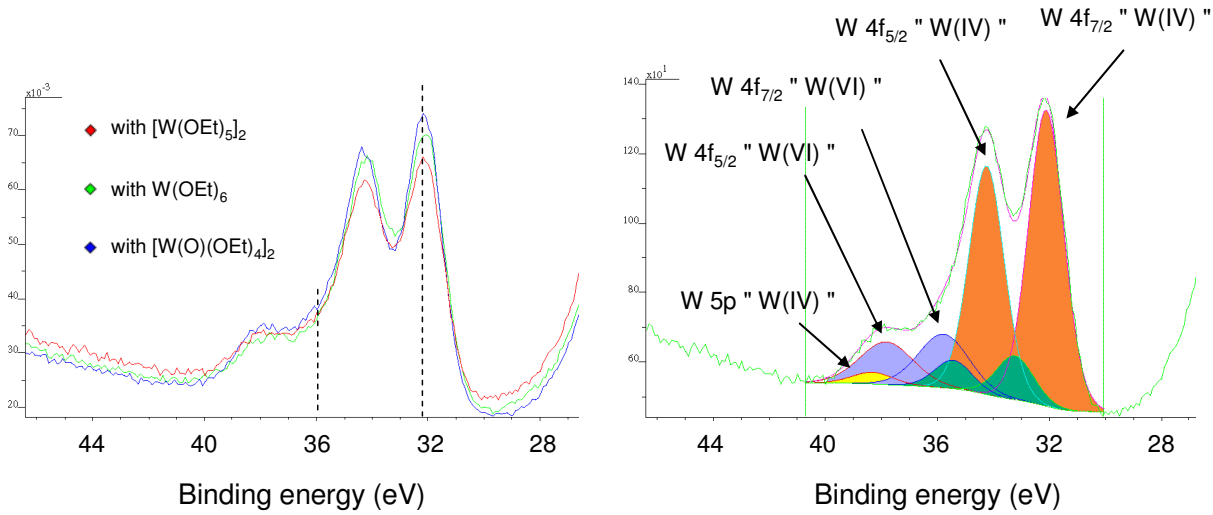

Figure 35: : XPS spectra normalised. W 4f contribution of sulphide catalysts supported on ASA$_{500}$, and prepared with $[W(OEt)_5]_2$ (red), $W(OEt)_6$ (green), and $[W(O)(OEt)_4]_2$ (blue). Calibrated *vs.* carbon C 1s at 284.6 eV. Right: decomposition of W 4f photopeak of $[W(OEt)_5]_2$ based catalyst.

III.4. Benchmarking catalytic activities with conventionally prepared catalysts

Tungsten-based catalysts being known for their high activity in aromatic hydrogenation [Stanislaus and Cooper, 1994; Hensen *et al.,* 2007], the catalytic performances of WS_2/ASA catalysts prepared by deposition of the three different tungsten precursors were tested in hydrogenation of toluene (HYD). The feed was composed of toluene (reactant), cyclohexane (solvent), dimethyldisulphide (sulphiding agent) and aniline. This latter compound is used to inhibit the acidity of the support, and avoid isomerisation of the reactant by the acid sites of the support as explained in the experimental part.

CSC catalysts are compared to conventional WS_2/ASA catalysts, dried or calcined. Conventional materials were prepared by *IWI* of an aqueous solution of ammonium metatungstate, followed by a maturation step of 1 night. Then, after a drying step of 1 night at 120°C, conventional catalysts were referred as "dried". Subsequent calcination under air at 450°C for 2 h gave materials referred as "calcined". These two samples were sulphided at 350°C for 2 h with a 15 $\%_{mol}$. H_2S/H_2 mixture to give respectively the dried and calcined sulphided catalysts. Note that elemental analyses on these materials showed that they exhibit a W-loading of ca 0.5 W/nm².

The intrinsic rate of hydrogenation (or intrinsic HYD rate), expressed in mol(tol)/mol(W)/h, of these catalysts, depending on their tungsten loading (W/nm²) is shown **Figure 36**.

Note that the intrinsic HYD rates activities of these previous catalysts are also compared to three similar catalysts, based on CSC materials prepared by *IWI* of ASA_{-300}.

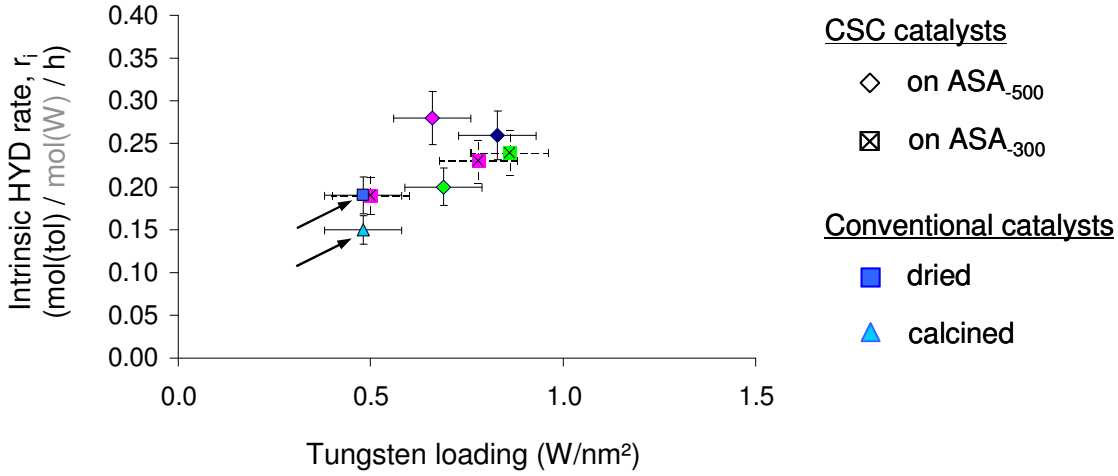

Figure 36: Intrinsic rate of hydrogenation [mol(tol)/mol(W)/h] of catalysts prepared by incipient wetness impregnation (square ⊠) or grafting (diamonds ◇). Precursors used are $W(OEt)_6$ (green), $W(O)(OEt)_4$ (black) and $[W(OEt)_5]_2$ (pink)

Catalysts prepared by the CSC method are active and exhibit HYD rates lying between 0.19 and 0.28 mol(tol)/mol(W)/h and only little difference is found for W(V) and W(VI)-based catalysts, whatever the precursor or the support (*e.g.* ASA_{-300} or ASA_{-500}). Then, although no transmission electron microscopy analyses were undergone on these samples, XPS analyses show that these sulphide phases are, in a first approximation, quite similar (level of sulphidation, intrinsic HYD rates). Besides, conventional catalysts show intrinsic HYD rates (see arrows on **Figure 36**) between 0.15 and 0.19 mol(tol)/mol(W)/h, which is similar or lower than the intrinsic HYD rates observed for CSC WS_2/ASA catalysts. Therefore, these results indicate that the catalysts originating from sulphidation of materials prepared by deposition of a molecular precursor of tungsten on ASA are as active as or even more active than their conventional counterparts, and are thus promising samples.

III.5. Conclusion

In this chapter, we investigated the preparation of non-promoted hydrotreating catalysts from tungsten(V) and tungsten(VI) precursors.

We first characterised three tungsten alkoxides, $[W(OEt)_5]_2$, $W(OEt)_6$ and $[W(O)(OEt)_4]_2$, selected as potential precursors for deposition on ASA. We showed that all the metallic complexes exhibits the characteristic features of alkoxide compounds. Then, we deposited these molecules onto amorphous silica-alumina partially dehydroxylated under high vacuum, and characterised these materials. FT-IR and XPS spectroscopy analyses show no significant differences between the catalysts and are consistent with the formation of grafted tungsten alkoxide surface species. Subsequent treatment with 15 $\%_{mol.}$ H_2S/H_2 yielded three sulphide catalysts, which are hardly possible to differentiate according to XPS analyses. Finally, the catalytic test, *e.g.* hydrogenation of toluene in presence of aniline, shows that all catalysts are active and behave similarly. The comparison with the intrinsic rate of hydrogenation of conventional catalysts reveals that CSC catalysts are as or even more active, given the amount of tungsten loaded on each sample, which is very promising and need to be further studied.

To conclude, we recall that one aim of this PhD work is to study sulphide catalysts, from oxide surface species to WS_2 slabs. To achieve such an investigation, especially *via* a molecular approach, we need a pure and well-characterized tungsten precursor. Therefore, in view of the readily availability of tungsten pentaethoxide $[W(OEt)_5]_2$ in a pure form, present as a dimeric species, we selected this molecular precursor for the rest of the study. For a greater clarity, this precursor will be denoted **$[W(OEt)_5]_2$** in the following chapters.

III.6. References

Alov, N.V., *Journal of Analytical Chemistry* (2005), **60**, 5, 431-435

Bradley, D.C.; Mehrotra, R.C.; Swanwick, J.D. and Wardlaw, W., *Journal of the Chemical Society* (1953), 2025-2030

Bradley, D.C., *Nature,* London (1958), **182**, 1211

Bradley, D.C. International review of science (1972), 5, series I, 65-91, Editions Butterworths, London

Bradley, D.C.; Chisholm, M.H.; Extine, M.W. and Stager, M.E., *Inorganic Chemistry* (1977), **16**, 7, 1794-1801

Bradley, D.C.; Mehrotra, R.C.; Rothwell, I.P. and Singh, A., Alkoxo and aryloxo derivatives of metals (2001), Academic Press, London

Bryan J.C.; Wheeler, D.R.; Clark, D.L.; Huffman, J.C. and Sattelberger, A.P., *Journal of the American Chemical Society* (1991), **113**, 8, 3184–3186

Chisholm, M.H.; Kramer, K.S. and Streib, W.E., *Angewandte Chemie International Edition* (1995), **34**, 8, 891-893

Clegg, W.; Errington, R.J.; Kraxner, P. and Redshaw, C., *Journal of the Chemical Society*, *Dalton Transactions* (1992), **8**, 1431-1438

Cotton, F.A.; DeMarco, D.; Kolthammer, B.W.S. and Walton, R.A., *Inorganic Chemistry* (1981), **20**, 9, 3048-3051

Cotton, F.A.; Schwotzer, W. and Shamshoum, E.S., *Journal of Organometallic Chemistry* (1985), **296**, 1-2, 55-68

Coulier, L.; Kishan, G.; van Veen, J.A.R. and Niemantsverdriet, J.W., *The Journal of Physical Chemistry B* (2002), **106**, 23, 5897-5906

Hensen E.J.M., van der Meer Y., van Veen J.A.R. and Niemantsverdriet J.W., *Applied Catalysis A: General* (2007), **322,** 0, 16-32.

Reagan, W.J. and Brubaker, C.H., *Inorganic Chemistry* (1970), **9**, 4, 827-830.

Stanislaus, A. and Cooper, B.H., *Catalysis Reviews* (1994), **36**, 1, 75-123

Wagner,C.D.; Riggs, W.M.; Davis, L.E.; Moulder, J.F. and Muilenberg, G.E. *Handbook of X-ray photoelectron spectroscopy* (1975), Minnesota

Part IV. Effect of tungsten loading on the nature of surface species obtained after impregnation of $[W(OEt)_5]_2$ on ASA

Outline (part IV)

Outline (part IV) **121**

Introduction **123**

IV.1. Characterisation of CSC materials by X-ray photoelectron spectroscopy (XPS) **123**

IV.2. Characterisation by Infrared spectroscopy (IR) **124**

IV.3. Characterisation by Solid-State NMR spectroscopy (NMR) **126**

IV.4. Insights into the characterisation of surface species **130**

IV.4.a. Deposition of ethanol onto $SiO_{2\text{-}700}$, $Al_2O_{3\text{-}450}$ and $ASA_{\text{-}300}$. 130

IV.4.b. Location of W-containing species 133

IV.4.c. Detailed structure of W-containing species 137

IV.5. Discussion. **141**

IV.5.a. Surface species for coverage below *ca.* 0.8 (± 0.1) W/nm² 141

IV.5.b. Surface species for coverage above *ca.* 0.8 (± 0.1) W/nm² 149

IV.6. Conclusion **150**

IV.7. References **150**

Introduction

In part III, we have shown that CSC catalysts display equal or higher intrinsic hydrogenation rates than conventional catalysts for similar W-loadings ranging from 0.5 to *ca.* 0.9 W/nm². The CSC method, which is thus promising to prepare efficient HYD catalysts, will allow us to investigate in details the preparation of CSC samples step by step, from the oxide phase to the sulphide one and its catalytic activity. In this part IV, we will thus focus on the first step of the preparation of catalysts, *e.g.* the impregnation of the metallo-organic precursor selected in part III : $[W(OEt)_5]_2$. We will investigate the influence of the tungsten loading on the resulting grafted surface species in oxide materials, prior to sulphidation. All CSC samples will be characterised by IR, NMR and XPS spectroscopies. We will investigate in particular how the metal complex is linked to the surface and which species are preferentially formed, as a function of the tungsten coverage (W/nm²).

Four materials with increasing amount of $[W(OEt)_5]_2$ were prepared by incipient wetness impregnation (IWI) on ASA_{-300} having a surface of 228 m²/g. They are referred as follows:

- $[W(OEt)_5]_2$-IWI-0.2/ASA_{-300}, with *ca.* 0.2 (± 0.1) W/nm²
- $[W(OEt)_5]_2$-IWI-0.5/ASA_{-300}, with *ca.* 0.5 (± 0.1) W/nm²
- $[W(OEt)_5]_2$-IWI-0.8/ASA_{-300}, with *ca.* 0.8 (± 0.1) W/nm²
- $[W(OEt)_5]_2$-IWI-1.7/ASA_{-300}, with *ca.* 1.7 (± 0.1) W/nm²

IV.1. Characterisation of CSC materials by X-ray photoelectron spectroscopy (XPS)

XPS spectroscopy analyses were performed to investigate the oxidation state of tungsten surface species. W 4f XPS spectra of three catalysts are shown **Figure 37**; they exhibit a main doublet at 36.0 (±0.1) eV and 38.1 (±0.1) eV associated with W $4f_{7/2}$ and W $4f_{5/2}$ components respectively along with a second one, at lower binding energies (W $4f_{7/2}$: 34.3 ±0.1 eV; W $4f_{5/2}$: 36.4 ±0.1 eV). As described in Part III.2, the two doublets are respectively assigned to tungsten atoms in a W(VI) environment, and to partially reduced tungsten species. As mentioned in chapter III for $[W(OEt)_5]_2$ based catalysts, observation of a W(VI) environment for tungsten surface species is surprising, and could be tentatively ascribed

to W atoms with a coordination sphere containing six oxygen atoms. Reduced tungsten species, as previously mentioned, most likely arise from *in-situ* reduction of W(VI) atoms upon irradiation by the X-ray beam under the ultra-high vacuum of the apparatus.

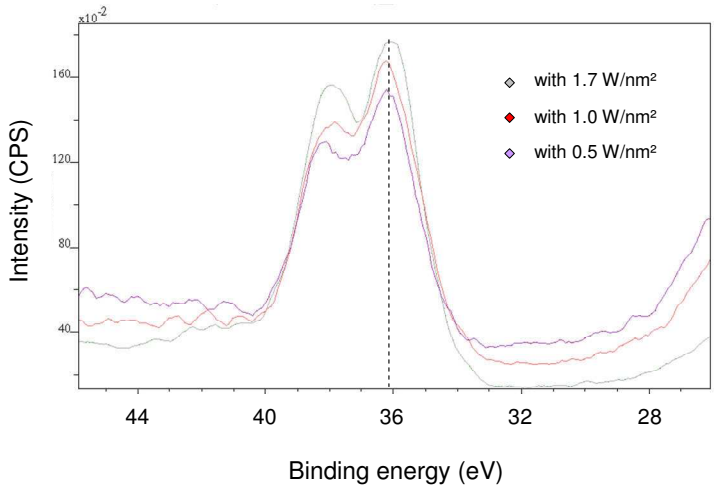

Figure 37: XPS spectra of $[W(OEt)_5]_2$-IWI-/ASA_{-300} catalysts exhibiting 0.5 W/nm², 0.8 W/nm² and 1.7 W/nm². Calibrated *vs.* C 1s at 284.6 eV.

IV.2. Characterisation by Infrared spectroscopy (IR)

When increasing amounts of $[W(OEt)_5]_2$ are impregnated on ASA partially dehydroxylated at 300°C under high vacuum (10^{-5} mbar), the vibration band assigned to isolated silanols [Legrand, 1998, John Wiley & sons Ltd] at 3743 cm^{-1} increasingly disappears by 61 % and 82 % for 0.2 W/nm² and 0.5 W/nm², respectively and vanishes for loading above 0.8 W/nm². While ASA_{-300} contains about 3.2 OH/nm² according to chemical titration with CH_3MgBr (see experimental section), a tungsten loading of 0.8 W/nm² represents *ca.* 0.3 W/OH. Note that a broad band between 3700 and 3300 cm^{-1} associated with bonded OH increases when increasing amounts of precursor are impregnated, in agreement with the presence of more residual silanols interacting with surface organic ligands, probably attached to W. Meanwhile, two groups of bands appear in the region 1800 - 1450 cm^{-1} and 3000 - 2800 cm^{-1}, respectively assigned to δ(CH) and ν(CH) vibrations of the aforementioned ethoxy species. Note that a maximum density of 2 W/nm^2 is expected on the basic of the projected surface area of the molecular complex $[W(OEt)_5]_2$ (*ca.* 1.0 nm²). Overall, the data are consistent with a consumption of isolated silanols ($\nu(OH)_i$ = 3743 cm^{-1}), but not all surface hydroxyls, probably because they

are not all accessible in part because they interact with the complex (presence of shifted OH band interacting *via* van der Waals interaction with organic ligand.

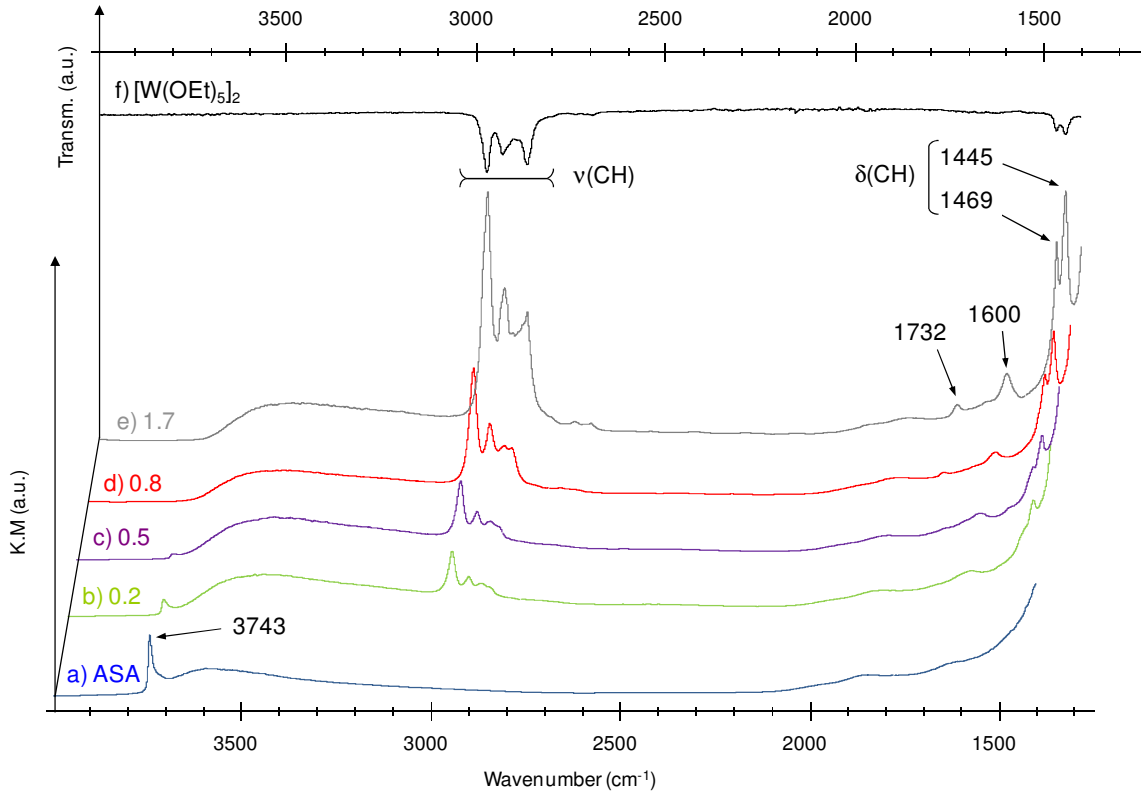

Figure 38: IR spectra. (DRIFT) a) ASA_{-300} and $[W(OEt)_5]_2$-IWI-/ASA_{-300} catalysts: b) 0.2 W/nm²; c) 0.5 W/nm²; d) 0.8 W/nm² and e) 1.7 W/nm². Pure $[W(OEt)_5]_2$ (ATR) is added as reference, f).

Increasing the tungsten loading does not only increase δ(CH) and ν(CH) vibrations intensity, but also leads to the appearance of two additional groups of vibration bands in the 1740-1580 cm^{-1} and 1480-1320 cm^{-1} regions. In the zoomed spectra reported in **Figure 39**, a broad band is present between 1380 cm^{-1} and 1420 cm^{-1} at tungsten loading below 0.5 W/nm². For 0.8 W/nm² a new band appears at 1382 cm^{-1}, which is shifted towards lower wavenumbers as found for the δ(CH) of pure $[W(OEt)_5]_2$, at 1374 cm^{-1}. These observations indicate that at tungsten loading below 0.5 W/nm² one type of surface species is present, while at higher loading, a second type of species, closely related to unperturbed $[W(OEt)_5]_2$ appears.

In addition, two peaks, not present in the starting compound, also appear at *ca.* 1736 cm^{-1} and 1602 cm^{-1} for tungsten loading above 0.5 W/nm². For a loading of 1.7 W/nm², these two peaks are slightly shifted to 1732 cm^{-1} and 1600 cm^{-1}. While their assignment is fully ascertain, one possibility is that the band *ca.* 1732 cm^{-1} is probably a combination band arising from the surface Al-O or Si-O bond. Another possibility is the formation of a putative W=O bond, which

could lead to a harmonic or a combination band in this region. Note that no direct evidence of the presence of W=O bond is found by Raman spectroscopy, because fluorescence has been a major drawback as visible light laser sources have been used so far. Note also the formation of a W=O bond would necessitate the formation of by-products in solution such as alkenes, which have not been observed.

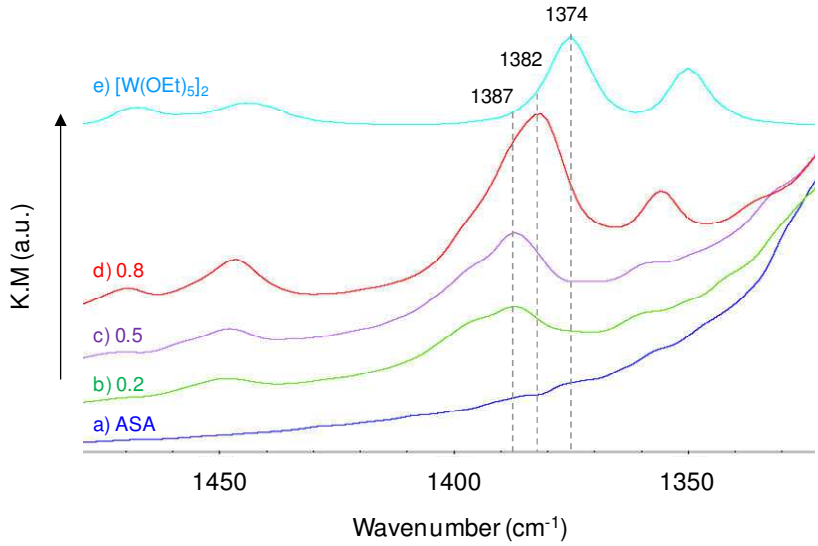

Figure 39: Expanded scale IR spectra of a) ASA_{-300} and $[W(OEt)_5]_2$-IWI-/ASA_{-300} catalysts: b) 0.2 W/nm²; c) 0.5 W/nm² and d) 0.8 W/nm². Pure $[W(OEt)_5]_2$ is added as reference, e).

IV.3. Characterisation by Solid-State NMR spectroscopy (NMR)

The ^{1}H Magic Angle Spinning (MAS) solid-state NMR spectrum of $[W(OEt)_5]_2$-IWI-0.2/ASA_{300}, prepared with *ca.* 0.2 W/nm² (shown **Figure 40**, left, green curve), displays four peaks: these at δ = 5.0 ppm and δ = 3.8 ppm are tentatively attributed to methylene protons CH_2 of two different species, the peak at δ = 1.0 ppm to methyl protons CH_3, and the peak at δ = 1,8 ppm to remaining silanols [Legrand, 1998, John Wiley & sons Ltd; Brunner *et al.*, 1997]. In addition, the ^{13}C Cross-Polarisation (CP) MAS solid-state NMR spectrum (see **Figure 40**, right, green curve) displays three peaks: one at δ = 15 ppm, which corresponds to CH_3 groups and two at δ = 76 ppm and δ = 59 ppm, assigned to two types of OCH_2 groups belonging to different types of ethoxy groups. The former is attributed to ethoxy groups bound to W, while the latter is assigned to ethoxy groups directly bound to the ASA surface.

Examining the NMR spectra of a series of samples with increasing tungsten loadings is very informative. In the ^1H NMR solid-state spectra (**Figure 40-a**), increasing the tungsten loading leads to an increase of the intensity of the peak at δ = 5.0 ppm as well as a shift of the peak at δ = 1.0 ppm to δ = 1.2 ppm. Two pairs of peaks are distinguishable and assigned to different types of ethoxy groups: one at {δ = *5 ppm ;* δ = *1.2 ppm*} and one at {δ = *3.8 ppm ;* δ = *1.0 ppm*} respectively assigned to ethoxy species linked to W and to ethoxy species adsorbed on the ASA surface and linked to either Si or Al. Similarly, the CPMAS ^{13}C solid-state NMR spectrum shows that the broad peak at 76 ppm is shifted to 69 ppm at higher loading, for which it increases and sharpens. Meanwhile, the peak at 15 ppm is shifted to 19 ppm. Furthermore, an additional pair of carbons has a high relative intensity at low loadings at {δ = *59 ppm ;* δ = *15 ppm*}, whose chemical shifts are similar to this observed for ethoxy species adsorbed on aluminosilicates.[Derouane *et al.*, 1978], revealing that such species are preferentially formed at low loadings.

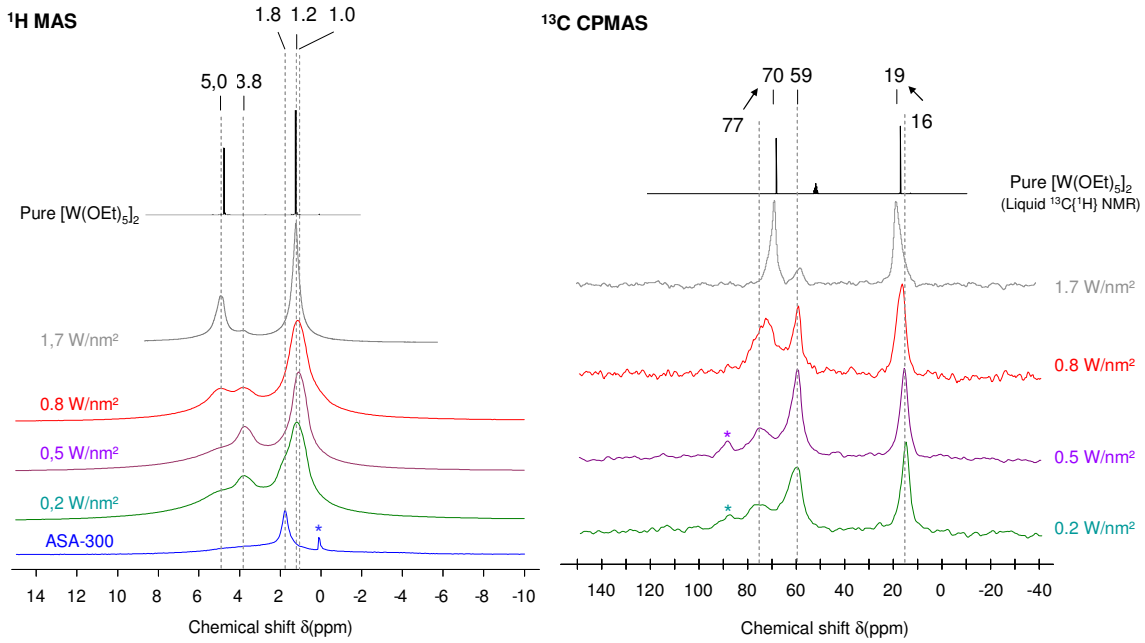

Figure 40: Solid state NMR spectra. ^1H MAS spectra (left) and ^{13}C CPMAS spectra (right) of $[W(OEt)_5]_2/ASA_{-300}$ catalysts exhibiting increasing W/nm². Asterisks denote impurities.

Results of IR analyses described in part IV.2, along with NMR data, reveal that different types of tungsten species are present, depending on the tungsten loading, especially for

loadings above 0.5 - 0.8 W/nm². In order to obtain a more detailed understanding of their associated structure and relative abundance, ^{13}C-labelled samples 20-25% carbon-13 labelled on the methylene carbon, $[W(O\text{-}^{13}CH_2CH_3)_5]_2$ precursor denoted $[W(OEt^*)_5]_2$, were prepared and analyzed by ^{13}C MAS and CPMAS solid-state NMR spectroscopy:

- $[W(OEt^*)_5]_2$-IWI-0.2/ASA_{-300}, with *ca.* 0.2 (± 0.1) W/nm²
- $[W(OEt^*)_5]_2$-IWI-0.5/ASA_{-300}, with *ca.* 0.5 (± 0.1) W/nm²
- $[W(OEt^*)_5]_2$-IWI-0.6/ASA_{-300}, with *ca.* 0.6 (± 0.1) W/nm²
- $[W(OEt^*)_5]_2$-IWI-0.7/ASA_{-300}, with *ca.* 0.7 (± 0.1) W/nm²
- $[W(OEt^*)_5]_2$-IWI-0.9/ASA_{-300}, with *ca.* 0.9 (± 0.1) W/nm²
- $[W(OEt^*)_5]_2$-IWI-2.0+/ASA_{-300}, with more than 2.0 W/nm²

Figure 41 (left) shows the ^{13}C MAS solid-state NMR spectra as a function of the W-loading. For loading of 0.7 W/nm², only three peaks at *ca.* 75, 58 and 14 ppm are visible, which are respectively attributed to [ASA-O-W-O-**C**H_2CH_3], [ASA-O-**C**H_2CH_3] and [-O-CH_2**C**H_3]. Above 0.7 W/nm², sharp peaks appear at 70 ppm and 68 ppm. It is noteworthy that the peak at $\delta \approx 75$ ppm is very broad and is probably due to a large distribution of chemical shift, which can be associated with a species experiencing a broad distribution of chemical environment. On the contrary, above a loading of 0.7 W/nm², narrower peaks appear, consistent with the presence of species with more homogeneous environment and probably associated with mobile species.

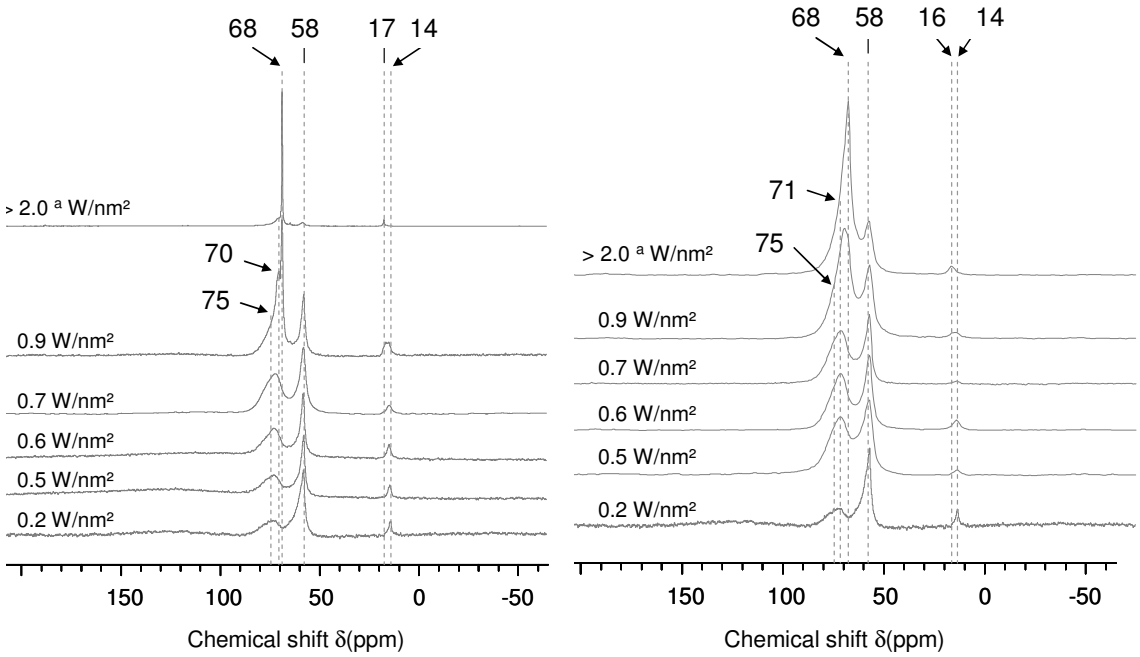

Figure 41: ^{13}C MAS (left) and CPMAS (right) solid-state NMR spectra of ^{13}C labelled catalysts supported on ASA, with increasing W/nm². [a] W loading to be confirmed by elemental analysis.

In fact, these sharp signals disappear on the ^{13}C CPMAS spectra, shown in **Figure 41** (right). Since the efficiency of cross-polarisation (CP) [Pines *et al.*, 1972], associated with the magnetisation transfer between ^{1}H and ^{13}C, is more efficient for strongly bound species (immobile) compared to weakly bound species (physisorbed), it confirms that two types of tungsten species are formed: **grafted** species on the surface for low tungsten loadings (< 0.7 W/nm², corresponding to a W-bound monolayer) as well as more mobile species, **probably physisorbed** on top of the grafted ones for higher loadings (> 0.8 W/nm², corresponding to multilayer).

To strengthen the assignment of ^{1}H and ^{13}C NMR spectra, ^{1}H-^{13}C heteronuclear correlation (HETCOR) NMR experiments were performed. **Figure 42** shows the HETCOR solid-state NMR spectrum of $[W(OEt)_5]_2$-IWI-0.5/$ASA_{-300:}$, with two correlation peaks (δ_H/δ_C) observed at (4.9/75) and (3.8/60) and associated to two types of CH_2, with two long-range correlation peaks at (1.2/75) and (1.2/60) associated with the CH_3 attached to the two types of CH_2, and with another correlation peak at (1.2/17) for the CH_3.

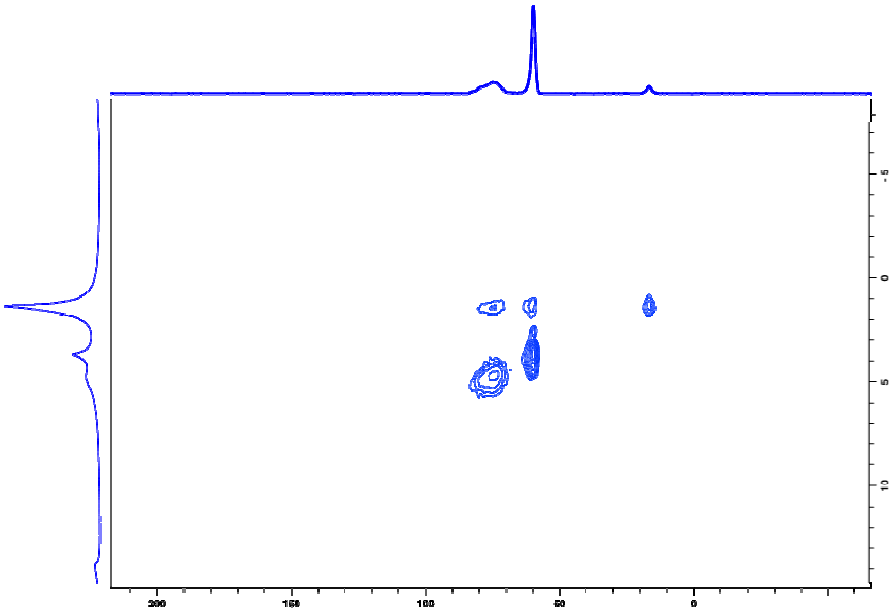

Figure 42: 1D ^{13}C CPMAS solid state NMR spectrum (x-axis), 1D ^{1}H MAS spectrum (y-axis) and contour plot of a ^{1}H-^{13}C HETCOR of $[W(OEt)_5]_2$-IWI-0.5/ASA_{-300}. 1.5k scans, 128 increments, recycling delay of 1 sec, contact time was 1.5 ms. Spinning rate: 10 kHz.

IV.4. Insights into the characterisation of surface species

IV.4.a. Deposition of ethanol onto $SiO_{2\text{-}700}$, $Al_2O_{3\text{-}450}$ and $ASA_{\text{-}300}$.

NMR spectroscopy has revealed that a large amount of surface ethoxides are bound to ASA on the W-containing samples. GC/MS analyses has also shown that less than 0.1 *equiv.* of EtOH / W is released upon grafting of $[W(OEt)_5]_2$, independently of the W loading (0.2 - 1.7 W/nm²). One possible way to form surface ethoxy species is the reaction of EtOH, released upon grafting $[W(OEt)_5]_2$ with surface silanols. This reaction is discussed further later on (p147). The adsorption of alcohols on alumina has been studied for several years, especially for dehydration reactions, that are catalyzed by alumina at high temperatures [Salomon *et al.*, 1967]. EtOH is reported to be strongly adsorbed on alumina [Greenler *et al.*, 1962], especially on the (100) planes hydroxyles of AlOH when calcined at low temperature, and on penta-coordinated Al^{3+} when calcined at temperature higher than 400°C. [Kwak *et al.*, 2011]. Note however that adsorption on Brønsted acid sites (AlOH) or Lewis acid sites (Al^{3+}) is still a matter of debate. [Roy *et al*, 2012] Therefore, ethanol and/or ^{13}C labelled ethanol were contacted to

$SiO_{2\text{-}700}$, $Al_2O_{3\text{-}450}$ and $ASA_{\text{-}300}$ in order to ascertain the proposed reaction pathway and the presence of surface ethoxides.

On $SiO_{2\text{-}700}$, which exhibits *ca.* 0.8 OH/nm², IR spectroscopy analysis (see appendices) highlights that *ca.* 50 % of isolated SiOH are consumed, and shows the characteristic features of ethoxy groups: ν(CH) vibrations between 2983 cm^{-1} and 2881 cm^{-1}, as well as δ(CH) vibrations between 1480 cm^{-1} and 1393 cm^{-1}. Besides, ^1H MAS solid state NMR spectrum, shown in **Figure 43**, reveals four peaks: three are tentatively attributed to adsorbed EtOH ($\delta(CH_2)$ = 3.7 ppm, $\delta(CH_3)$ = 1.0 ppm, δ(OH) = 2.6 ppm) and one to remaining silanols of SiO_2 (δ(OH) *ca.* 1.7 ppm), according to their chemical shift in solution or to literature data [Legrand, 1998, John Wiley & sons Ltd]. The ^{13}C CPMAS NMR spectrum shows two peaks of very low intensity, at 59 ppm and 17 ppm, respectively attributed to CH_2 groups and CH_3 groups of chemisorbed ethoxy groups. These analyses reveal that only a low amount of EtOH is grafted on the silica surface: the major part of ethanol is only physisorbed.

Ethanol was then contacted onto $Al_2O_{3\text{-}450}$, which exhibits *ca.* 3.0 – 3.5 OH/nm² [Rascon *et al.*, 2011]. After impregnation and subsequent washing, $Et{*}OH/Al_2O_{3\text{-}450}$ was analyzed by IR and solid-state NMR. The IR spectra (see appendices) show that *ca.* 61 % of OH are consumed, and shows the characteristic features of ethoxy groups: ν(CH) vibrations between 2967 cm^{-1} and 2869 cm^{-1}, as well as δ(CH) vibrations between 1490 cm^{-1} and 1383 cm^{-1}. Moreover, ^1H MAS solid-state NMR spectrum (**Figure 43**) displays one broad peak at δ = 1.3 ppm and one very broad peak at δ = 3.7 ppm, respectively attributed to CH_3 and CH_2 groups of the ethoxy species strongly adsorbed on alumina. In addition, the ^{13}C CPMAS solid-state NMR spectrum exhibits two peaks at δ = 18 ppm and δ = 58 ppm, associated to the CH_3 and CH_2 groups of the aforementioned ethoxy species. Moreover, ^{27}Al CPMAS solid state NMR shows that a peak of low intensity, tentatively attributed to Al_V species, is visible on the spectrum of the $Et^*OH/Al_2O_{3\text{-}450}$ material which is not observed on pure $Al_2O_{3\text{-}450}$ (see appendices). This result indicate that a restructuration of the surface of alumina, possibly *via* opening of Al-O-Al bridge or the conversion of surface Al_{IV} into Al_V species through the formation of an additional bond with a surface ethoxide. Overall, the reaction of ethanol on alumina leads to strongly adsorbed, probably chemisorbed ethoxy species. Besides, note that traces of ethanol and diethylether (CH_3CH_2-O-CH_2CH_3) were observed in the liquid phase after washing the material (GC/MS analysis), consistent with the fact that: (1) not 100 % of EtOH molecules react with the surface, as observed by IR spectroscopy, (2) EtOH reacts to yield diethylether and water [DeWilde *et al.*, 2013].

EtOH was also contacted onto $ASA_{\text{-}300}$, which exhibits 3.2 OH/nm². First, the aforementioned material was studied directly after impregnation, without any washing step. In

this case, weakly held and strongly adsorbed EtOH molecules could be observed. The IR spectrum of Et*OH/ASA$_{-300}$ (see appendices) highlights characteristic features of ethoxy groups: ν(CH) vibrations between 2983 cm^{-1} and 2881 cm^{-1}, as well as δ(CH) vibrations between 1480 cm^{-1} and 1393 cm^{-1}. Note in particular, the partial consumption of isolated SiOH (35%), and the absence of clear δ(OH) vibration of water expected at *ca.* 1630 cm^{-1}. The ^{1}H MAS solid state NMR spectrum (**Figure 43**) displays three sharp peaks at δ = 1.0 and 3.7 ppm associated to the CH_3 and CH_2 of the ethoxy species strongly adsorbed on ASA, along with a signal at 1.7 ppm attributed to surface silanols. A broad signal is also observed at *ca.* 2.5 ppm, which could be assigned to AlOH and other hydroxyls of ASA, or to OH group of adsorbed ethanol/water. On the ^{13}C MAS solid-state NMR spectrum (see **Figure 44**), two peaks at δ = 14 ppm and δ = 58 ppm are observed and respectively assigned to CH_3 and CH_2 of [ASA-O-CH_2CH_3] surface species.

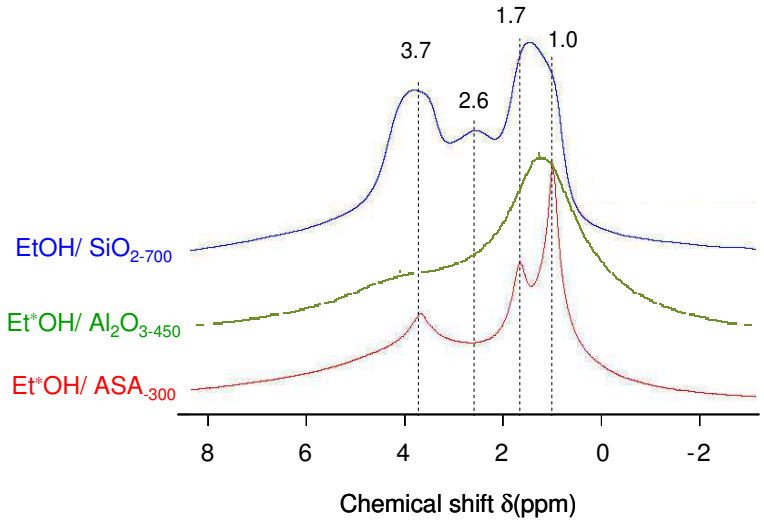

Figure 43: ^{1}H MAS solid-state NMR spectra of EtOH/SiO_{2-700}, Et*OH/Al_2O_{3-450} and Et*OH/ASA$_{-300}$

Furthermore, to ascertain the presence of surface ethoxides, ASA contacted with 1-^{13}C labelled ethanol (Et*OH/ASA$_{-300}$) was washed with cyclohexane and analysed by NMR spectroscopy. No change is observed in the ^{1}H and ^{13}C MAS solid-state NMR spectra {^{1}H-MAS δ = 3.8 ppm and δ = 1.0 ppm; ^{13}C-MAS NMR δ = 58 ppm and δ = 15 ppm}, and only traces of ethanol is found in the solution (GC/MS analysis). These results are in line with a strong interaction (chemisorption) between ethanol and ASA and the formation of surface ethoxy species [ASA-O-CH_2CH_3], linked *via* a Si or an Al atom

Overall, contacting oxide supports with ethanol leads to mainly physisorbed species on silica, and chemisorbed species on alumina and silica-alumina, surface ethoxides, probably linked to the surface *via* a Si or/and an Al atom.

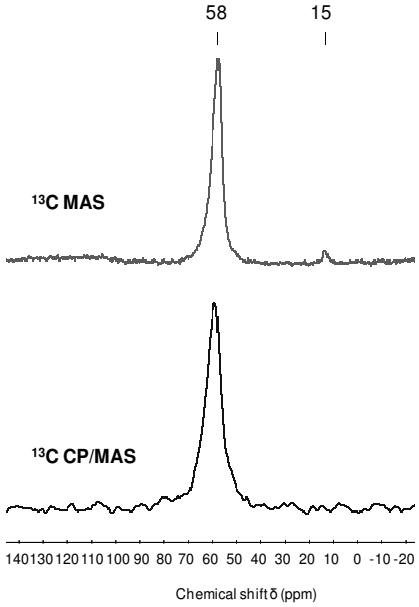

Figure 44: ^{13}C MAS (top right) and ^{13}C CPMAS spectra (bottom right) of ASA_{-300} impregnated with CH_3-$^{13}CH_2$-OH

IV.4.b. Location of W-containing species

In order to probe the location of W species, i.e. whether they are on silica regions, alumina regions or both, the corresponding ^{13}C labelled tungsten materials were prepared by grafting of $[W(OEt^*)_5]_2$ onto $SiO_{2\text{-}700}$ and $Al_2O_{3\text{-}450}$: $[W(OEt^*)_5]_2$-G-0.7/$SiO_{2\text{-}700}$, $[W(OEt^*)_5]_2$-G-0.5/$Al_2O_{3\text{-}450}$ and $[W(OEt^*)_5]_2$-G-0.5/ASA_{-300}, respectively exhibiting 0.7 (±0.1) W/nm², 0.5 (±0.1) W/nm² and 0.5 (±0.1) W/nm²; the results are compared with ASA_{-300}.

IR spectra of the aforementioned materials, shown in **Figure 45**, exhibit the typical features of ethoxy groups: ν(CH) vibrations between 2983 cm^{-1} and 2881 cm^{-1}, as well as δ(CH) vibrations between 1480 cm^{-1} and 1393 cm^{-1}. On silica, 100 % of isolated silanols ($\nu(SiOH)_i$ = 3740 cm^{-1}) are consumed, and residual silanols interacting with surface species are present as evidenced by the broad band between 3700 cm^{-1} and 3300 cm^{-1}. On alumina, $Al_{IV}OH$ (ν(OH) = 3792 cm^{-1}) as well as $Al_{VI}OH$ (ν(OH) = 3770 cm^{-1}) totally disappear and $(Al_{VI})_3OH$ (*ca.* ν(OH) = 3756 cm^{-1}) strongly decreases. However a large amount of residual AlOH is still

observed. Note that on ASA, isolated silanols have totally been consumed, and that residual SiOH are revealed by the broad band between 3700 cm^{-1} and 3300 cm^{-1}. Mass balance analysis shows *ca.* 0.9 W/OH (at/at) for the silica material, and 0.2 W/OH (at/at) for alumina and ASA ones, which means that as previously seen for ASA-based materials, surface hydroxyls are not totally consumed, due either to their lower accessibility or to the steric hindrance of the tungsten precursor.

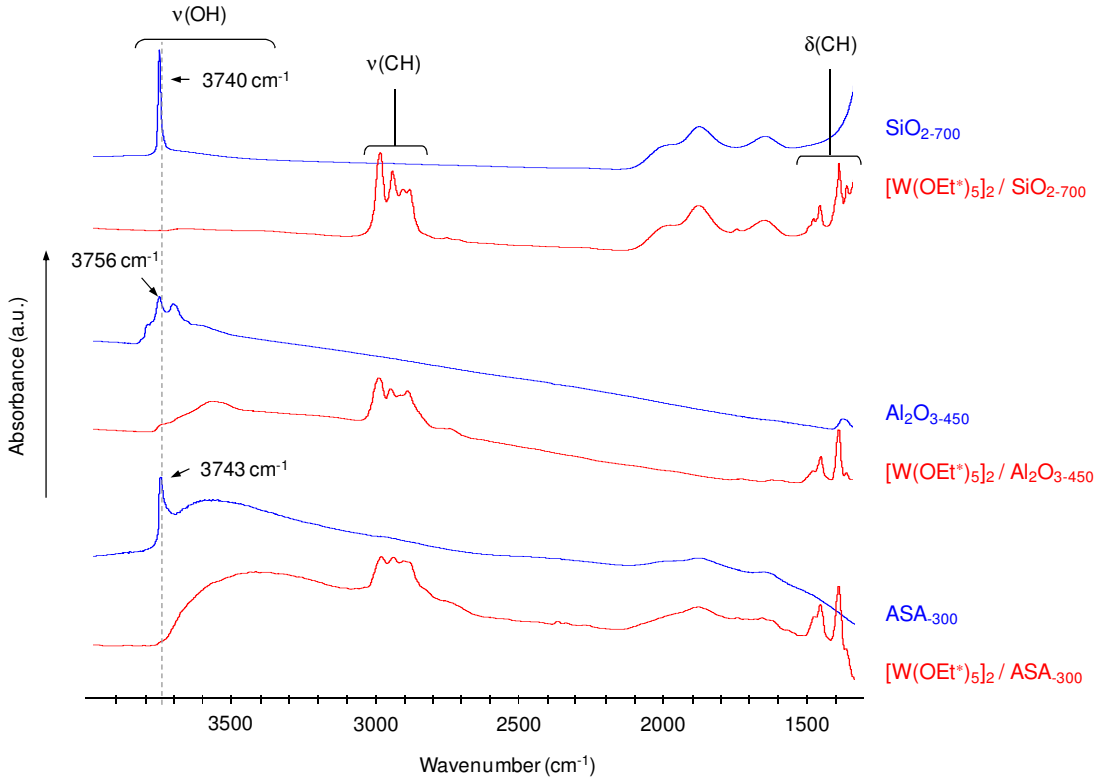

Figure 45: IR spectra (transm.) of $SiO_{2\text{-}700}$, $Al_2O_{3\text{-}450}$ and $ASA_{\text{-}300}$ and corresponding ^{13}C labelled materials

Examining the ^{13}C CPMAS solid-state NMR spectra of these materials confirmed what is observed by IR spectroscopy. On **Figure 46**, All materials, $[W(OEt)_5]_2$ supported on $SiO_{2\text{-}700}$, $Al_2O_{3\text{-}450}$ and $ASA_{\text{-}300}$, exhibit the two peaks at *ca.* $\delta = 72$ ppm and $\delta = 58$ ppm, assigned to $\delta(CH_2)$ of tungsten surface species and surface ethoxides, respectively. Note that these peaks are sharper in the case of the silica support, indicating a narrower distribution of surface species, probably due to weaker interactions between surface species and the support (absence of Lewis acid sites), and to the presence of mainly one type of grafting sites, *e.g.* isolated SiOH. On alumina, the aforementioned peaks are broader than on silica, consistent with the presence of a wider variety of surface species and the possible stronger interactions of species with the

surface, probably with adjacent Al sites. The NMR spectra $[W(OEt^*)_5]_2$ supported on ASA_{-300} exhibits no significant differences of chemical shift with the silica and the alumina ones. Note however that the relative amount of tungsten surface species *vs.* ethoxy surface species, quantified by integration of the $\delta(CH_2)$ peak of tungsten surface species (in the 70-74 ppm region), is lower on alumina (37 %) than on silica-alumina (56 %) than on silica (66 %), at *ca.* the same loading, supporting the aforementioned discussion about EtOH being more easily transferred on alumina or silica-alumina functionalities than on silica's upon grafting. Note however that the signal associated with surface ethoxy on silica is significantly more important than when silica is treated with EtOH, consistent with the assistance of W in the formation of the surface ethoxy species. This species is thus either resulting from the opening of a siloxane bridge either by a grafted surface W species on an adjacent site or by an intramolecular process.

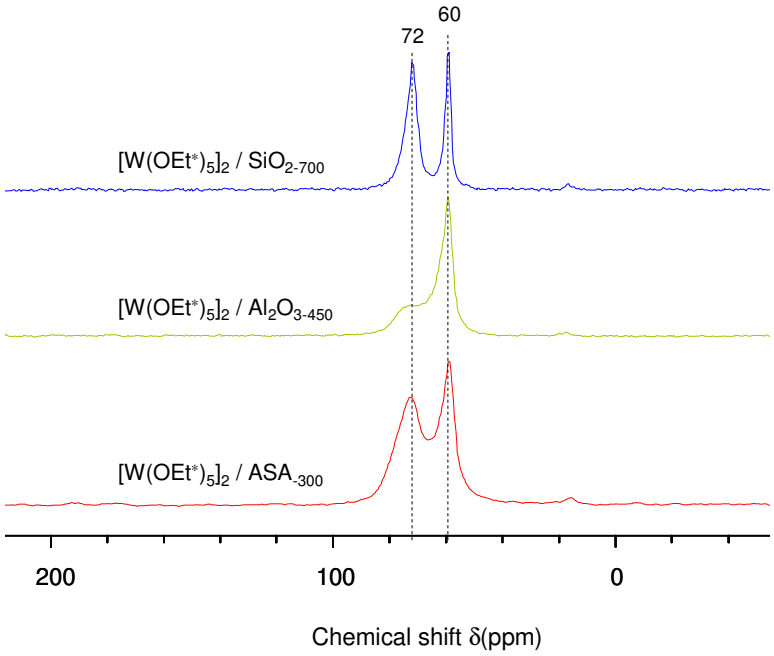

Figure 46: ^{13}C CPMAS Solid-state NMR spectra of ^{13}C labelled materials prepared on SiO_{2-700} (red), Al_2O_{3-450} (green) and ASA_{-300} (blue)

In addition, $[W(OEt^*)_5]_2$ supported on various materials have been analysed by ^{29}Si and ^{27}Al NMR analyses. For $[W(OEt^*)_5]_2$-G-0.7/SiO_{2-700}, the ^{29}Si MAS NMR spectrum is slightly less broad, especially around the Q2/3 sites than the one of pristine SiO_{2-700} (**Figure 47**), which is consistent with the consumption of isolated and germinal surface silanols. For $[W(OEt^*)_5]_2$-G-0.5/Al_2O_{3-450}, the ^{27}Al CPMAS solid-state NMR spectrum (**Figure 48**) displays the two peaks associated with Al_{IV} (70 ppm) and Al_{VI} (11 ppm) sites of alumina, but also an additional one at 39 ppm associated with Al_V sites as previously observed on Et^*OH/Al_2O_{3-450},

suggesting that the surface Al species have been modified upon grafting of the tungsten precursor *via* opening of **Al-O-Al bridges** or the evolution of Al_{IV} into Al_V upon adsorption/chemisorption of ethanol. Finally, for $[W(OEt^*)_5]_2$-G-0.5/ASA_{-300}, no major differences are observed in the ^{29}Si and ^{27}Al solid-state spectrum with respect to these obtain on pristine ASA_{-300} (**Figure 49-a** for ^{29}Si, and **Figure 49-b** for ^{27}Al) showing that ^{29}Si MAS and ^{27}Al CPMAS are not sufficient to reveal modification of the surface species associated with the reaction with M-O-M' bridges (M = Al, Si; M' = Al, Si) or surface hydroxyls.

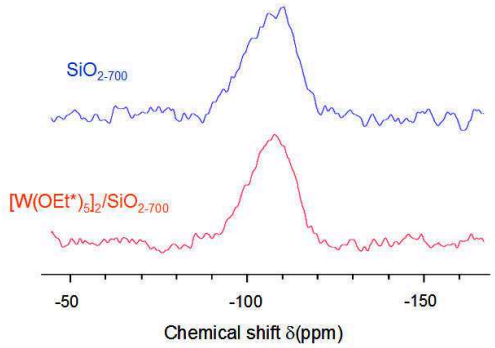

Figure 47: ^{29}Si MAS solid-state NMR of $SiO_{2\text{-}700}$ and $[W(OEt^*)_5]_2$-G-0.7/$SiO_{2\text{-}700}$

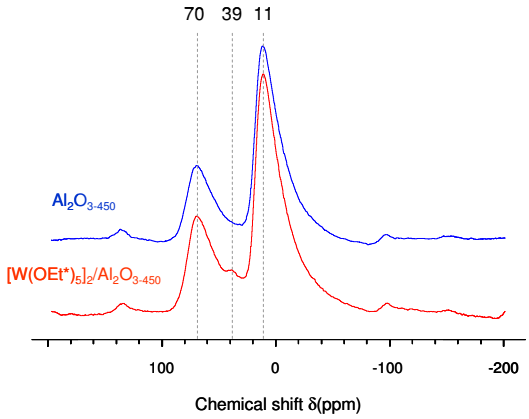

Figure 48: ^{27}Al CPMAS solid-state NMR spectra of $Al_2O_{3\text{-}450}$ and $[W(OEt^*)_5]_2$-G-0.5/$Al_2O_{3\text{-}450}$

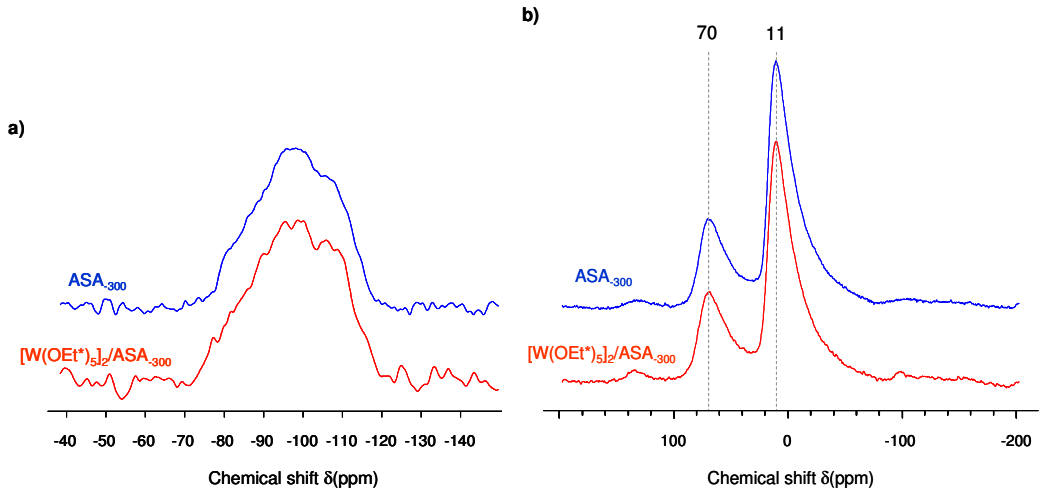

Figure 49: a) ^{29}Si and b) ^{27}Al solid-state NMR spectra of ASA_{-300} and $[W(OEt^*)_5]_2$-G-0.5/ASA_{-300}

IV.4.c. Detailed structure of W-containing species

IV.4.c.1. Decomposition of ^{1}H solid state NMR spectra

To further quantify **surface ethoxides *vs.* ethoxy ligands bound to W**, the ^{1}H MAS solid-state NMR spectra were decomposed for materials with loadings varying between *ca.* 0.2 and 1.7 W/nm² (explanations are detailed in appendices).

First, the ^{1}H spectrum of ASA_{-300} was decomposed with a good fit (sdev = 4.93) with a minimal number of sites: three peaks placed at *ca.* 0.5 ppm, 1.7 ppm and 3.0 ppm (**Figure 50**). The first two peaks are assigned to silanols (SiOH) in different environments, and the last one is tentatively ascribed to aluminols (AlOH), by comparison with literature data on aluminosilicate supports [Brunner *et al.*, 1997; Heeribout *et al.*, 1998; Müller *et al.*, 2000]. The peak mainly attributed to AlOH took into account a ^{1}H {^{27}Al} TRAPDOR experiment performed on the ASA_{-300} sample, in which the peak at *ca.* 3.0 ppm was partly assigned to protons coupled with aluminium atoms. [Crépeau *et al*, 2006] Note that the broad band from about 1 ppm to *ca.* 8 ppm on the ASA_{-300} spectrum could also be assigned to silanol protons in a variety of hydrogen-bonding environments, on the basis of earlier studies on silica gel. [Bronnimann *et al.*, 1988]

For the NMR spectra of the various $[W(OEt)_5]_2$-IWI-/ASA_{-300} materials, besides using the peak of silanols and aluminols described above for ASA_{-300}, additional peaks were introduced to include the signals associated with ethoxides bound to the ASA surface and these bound to tungsten (see **Figure 50**). Each decomposition was performed with several constraints: positions were set with a ± 0.1 ppm uncertainty for most of the peaks, and CH_2/CH_3 ratio for each species was close to 2 / 3. More details are available in the experimental part and appendix A.

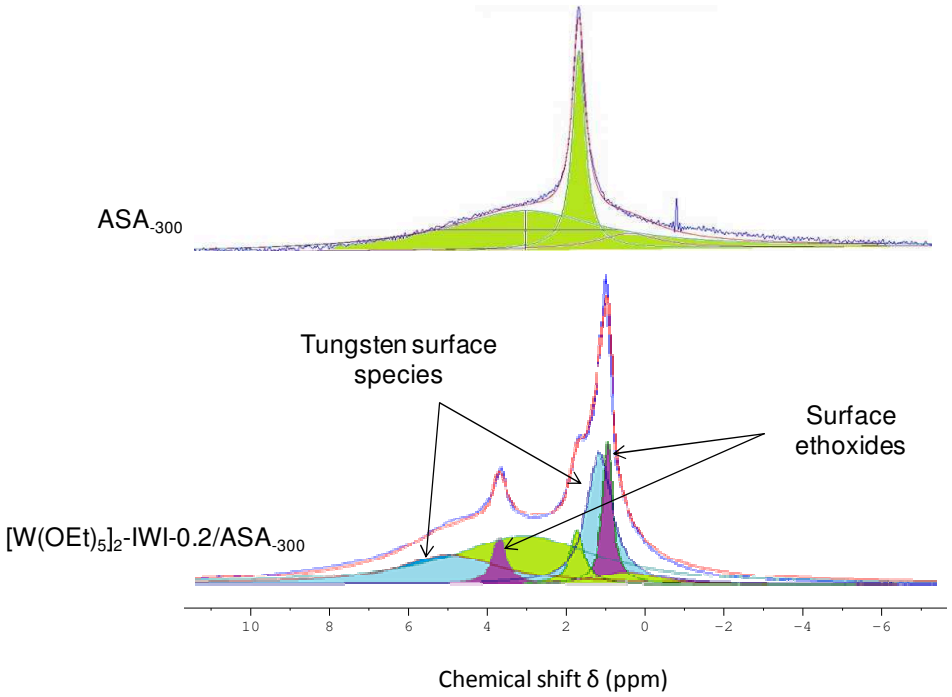

Figure 50: ^{1}H MAS solid state NMR spectra decomposed with dmfit software [Massiot *et al.* 2002]. Top: ASA_{-300} spectrum. Bottom: Catalyst $[W(OEt)_5]_2$-IWI-0.2/ASA_{-300} (*ca.* 0.2 W/nm²). Hydroxyls in green, methylene and methyl protons belonging to ethoxides bound to the ASA surface in purple, methylene and methyl protons bound to W in blue.

The decomposition shows that the **number of ethoxy ligands bound to tungsten** ($\delta(CH_2)$ = 4.9 ppm), **is constant and equal to *ca.* 3.5 ± 0.5** for materials exhibiting tungsten loading **up to 0.8 ± 0.1 W/nm²** (included), and then **increased to *ca.* 4.3 ± 0.5 for higher loading**, as shown **Figure 51**. The data are consistent with the formation of similar (mixture of) surface species at low loadings and with the presence of additional adsorbed unmodified complex $[W(OEt)_5]_2$ at higher loading as previously discussed.

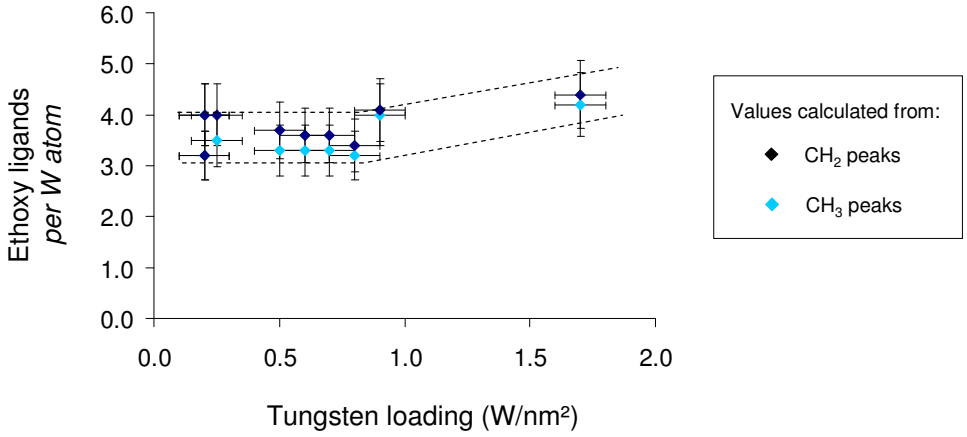

Figure 51: Calculations of the number of ethoxy ligands $[CH_3CH_2\text{-}O]$- linked to a W atom, from ^1H MAS solid-state NMR spectra decomposition.

Moreover, from the decomposition of ^1H-MAS solid-state NMR spectra, the number of -OH groups consumed upon impregnation of $[W(OEt)_5]_2$ can be evaluated, taking into account that the initial amount of hydroxyles is 3.2 OH/nm². OH consumption (OH/nm²) is shown in **Figure 52**.

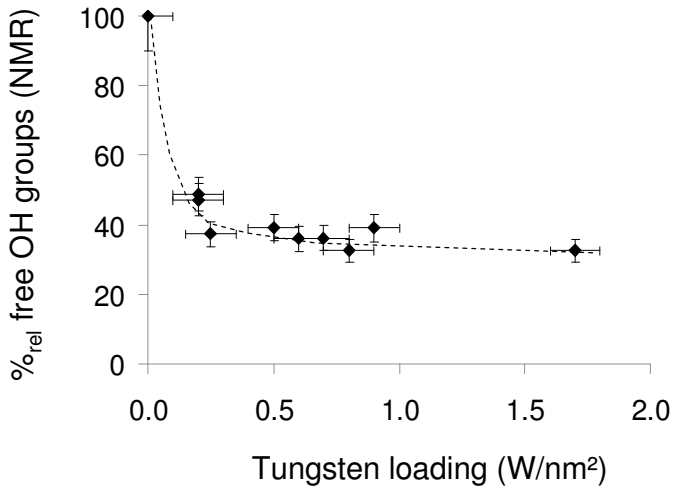

Figure 52: Relative percentage of free OH observed by NMR, depending on the tungsten loading (W/nm²), for $[W(OEt)_5]_2$-IWI-/ASA_{-300} catalysts. Data calculated from ^1H solid-state NMR spectra decomposition.

The $\%_{rel}$ of free OH strongly decreases from 0.2 W/nm² to 0.5 W/nm², and slowly reaches a plateau at higher loading. These results indicate that above W-loading of *ca.* 0.5 to 0.8 W/nm², no more hydroxyls are consumed as previously observed by IR (see part IV.2) and that additional W species must arise from the adsorption of complex, which interact with the first layer of chemisorbed species. The limited amount of hydroxyls that undergo grafting is probably associated with their accessibility combined with to the large size of precursor, which exhibits a large projected area (*ca.* 1.0 nm²), which prevents reaction of all OH groups.

IV.4.c.2. Molecular modelling. From the work of Leydier [Leydier, PhD thesis, Paris, 2012]

Preliminary quantum molecular modelling of the adsorption of the monomeric tungsten(V) pentamethoxide, $W(OMe)_5$, on a model of ASA surface [Chizallet *et al.*, 2009; Chizallet *et al.*, 2010] were previously carried out by density functional theory (DFT) calculations in the PhD thesis of F. Leydier. [2012]. Even if undertaken with a monodentate monomeric complex, this study brings some insights on the interaction of the tungsten molecular precursor with the silica-alumina surface. The calculated reaction energies between a methoxo ligand and various surface hydroxyls vary between -32 and +28 kJ/mol, depending on the type of hydroxyls. The most favourable exchange energies (-32 kJ/mol) was found for an isolated silanol SiOH (**Figure 17-a**). On Si-OH---Al pseudo-bridging silanols (**Figure 17-b**), the energies vary from -22 to -4 kJ/mol. Note that recurrent hydrogen-bondings between a close hydroxyl and one oxygen of the surface complex are observed and that this interaction is stabilizing. More importantly, this computational study shows that W loadings greater than 0.53 W/nm² should lead to disfavoured lateral interactions between methyl groups, which is consistent with the formation of the saturation of the surface at *ca.* 0.7 and 0.8 W/nm² and the formation of additional layer of W species above such loading.

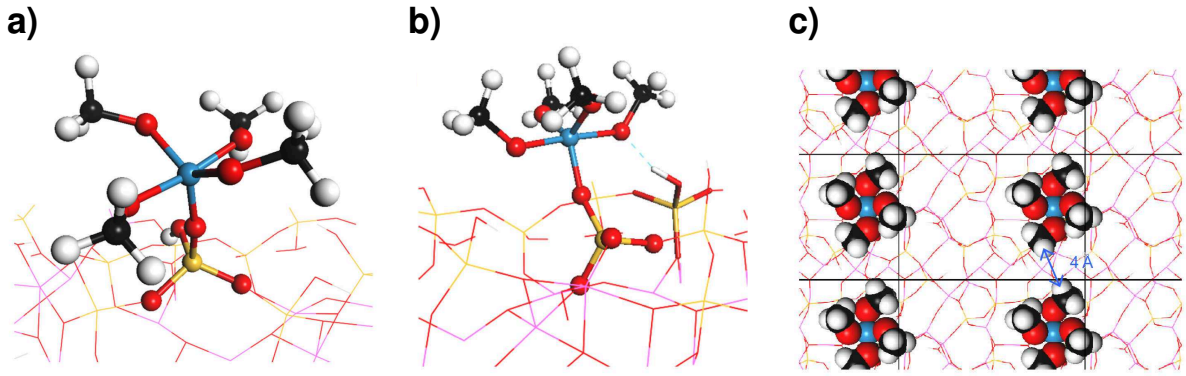

Figure 53: a) b) 3D molecular views of a tungsten surface species [ASA-O-W(OMe)$_4$] resulting from the adsorption of W(OMe)$_5$ on a ASA surface. Two optimal structures obtained by DFT calculations: a) on isolated silanol (SiOH), b) on a Si-OH---Al pseudo-bridging silanol with H-bond. c) Top view of the [ASA-O-W(OMe)$_4$] system corresponding to a coverage of 0.53 W/nm^2 Adapted from [*Leydier, PhD thesis, Paris, 2012]*

IV.5. Discussion.

IV.5.a. Surface species for coverage below *ca.* 0.8 (± 0.1) W/nm²

Al low loading, the results can be summarized as follows:

- Upon deposition of $[W(OEt)_5]_2$ onto silica, alumina, and amorphous silica-alumina, the molecular complex undergo grafting mainly *via* reaction with the surface hydroxyl; less than 0.1 equiv. EtOH is released in the liquid phase, but ethoxy surface species bound directly to ASA are observed. Note that EtOH hardly adsorbs on pure silica samples in the absence of W.
- IR and 1D(2D) solid-state NMR spectroscopies have revealed the presence of two different surface species after deposition of $[W(OEt)_5]_2$ onto silica, alumina and ASA., *e.g.* grafted tungsten ethoxy species and surface ethoxy directly linked to ASA (*via* Si or Al).
- The tungsten surface species are bound to the oxide surface and contain 3.5 (±0.5) remaining ethoxy ligands directly bound to the tungsten centre, thus indicating that tungsten dimers are probably at least bis-grafted on the surface.

- Grafting of $[W(OEt)_5]_2$ on related silica and alumina supports indicate that M-O-M bridges (M = Al, Si) are probably involved in the reaction between the molecular complex and the surface consistent with the formation of surface ethoxy.

On this basis, of the several possible surface species listed in **Table 4**, bipodal (4 ethoxy/W), tripodal (3.5 ethoxy/W) and tetrapodal (3.0 ethoxy/W) are more likely, and they are presumably formed *via* grafting on surface hydroxyl following by opening of adjacent M-O-M' bridges (M = Al, Si; M' = Al, Si).

Table 4: Possible structures for surface species, at low tungsten loading.

Dinuclear species : type of grafting	Structure number	Possible Structure	Ethoxy ligands bound to a W centre
Mono-grafted	I	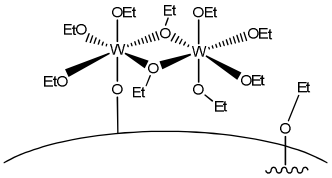	4.5
Mono-grafted	II	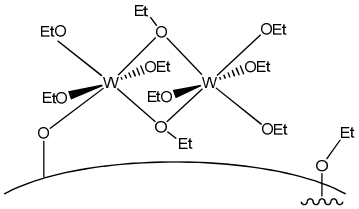	4.5
Mono-grafted	III	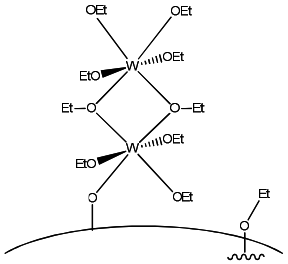	4.5
Mono-grafted	IV	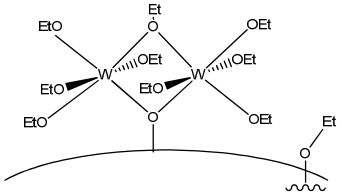	4.5

Bis-grafted	**V**	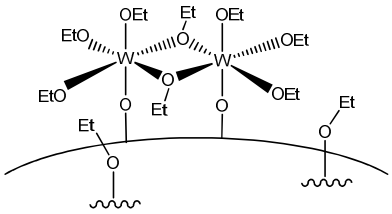	**4.0**
Bis-grafted	**VI**	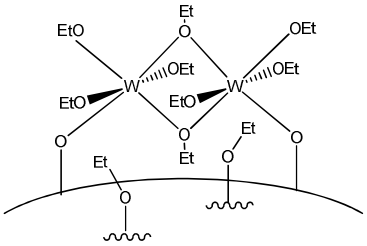	**4.0**
Bis-grafted	**VII**	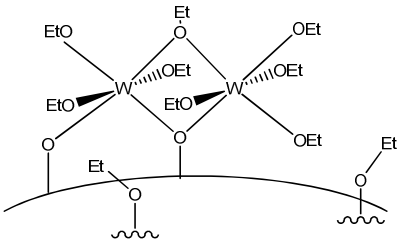	**4.0**
Bis-grafted	**VIII**	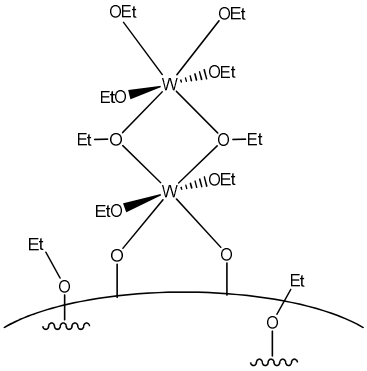	**4.0**
Bis-grafted	**IX**	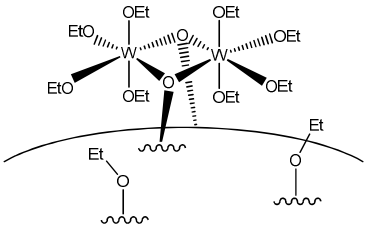	**4.0**

Tris-grafted	**X**	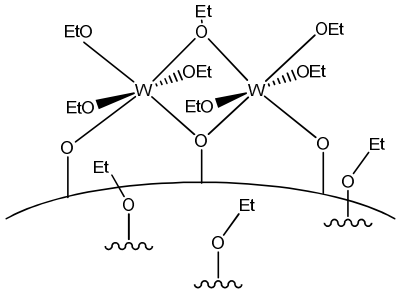	**3.5**
Tris-grafted	**XI**	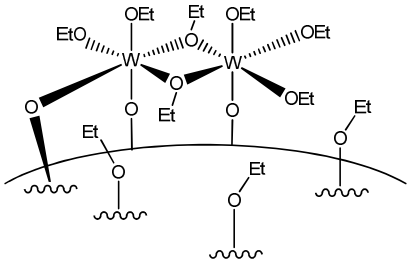	**3.5**
Tris-grafted	**XII**	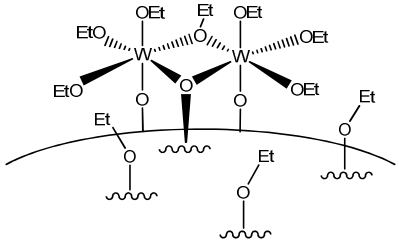	**3.5**
Tris-grafted	**XIII**	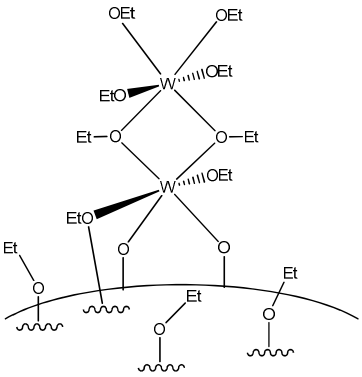	**3.5**
Tetra-grafted	**XIV**	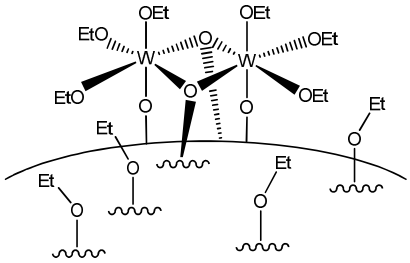	**3.0**

Tetra-grafted	**XV**	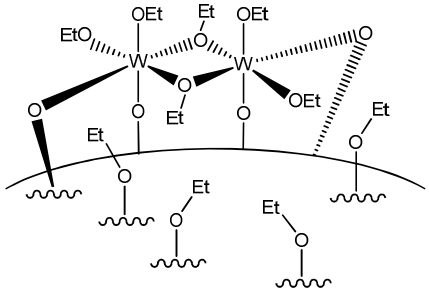	**3.0**
Tetra-grafted	**XVI**	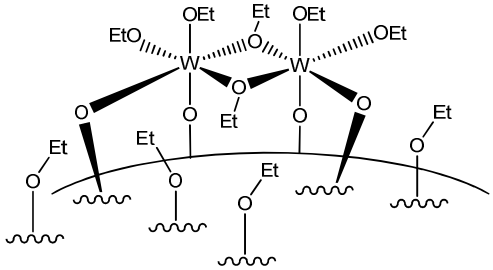	**3.0**
Tetra-grafted	**XVII**	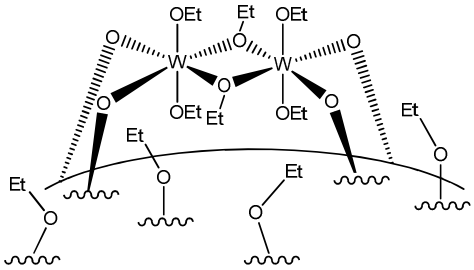	**3.0**
Tetra-grafted	**XVIII**	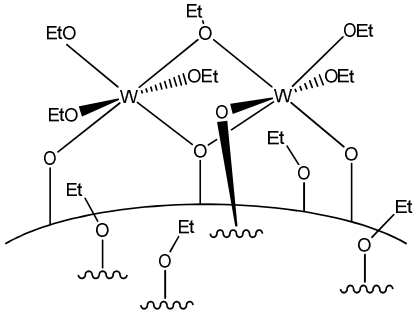	**3.0**

At this point, four families of surface species can be proposed: monografted dinuclear species for structure **I** to **IV**, bis-grafted dinuclear species for structure **V** to **IX**, tris-grafted dinuclear species for structure **X** to **XIII** and finally, tetra-grafted dinuclear ones for structure **XIV** to **XVIII**.

According to the literature, grafting of mononuclear molecular precursors on a support partially dehydroxylated at temperatures lower than 500°C typically yields bis-grafted or tris-grafted metallo-organic complexes. This is, for example, the case for $Ti(NEt_2)_4$,

$Ta(=CH\textit{t}Bu)(CH_2\textit{t}Bu)_3$, $V(=N\textit{t}Bu)(CH_2\textit{t}Bu)_3$, and $Cr(CH_2EMe_3)_4$ with EMe_3 = *t*Bu or $SiMe_3$ [Copéret *et al.*, 2003], which form bis-grafted surface species on partially dehydroxylated silica $SiO_{2\text{-}200}$, which contains 0.86 mmol of $OH.g^{-1}$ or 2.8 $OH.nm^{-1}$. For $ASA_{\text{-}300}$, which contains 3.2 OH/nm^2, a similar behaviour is expected and bis-grafted tungsten centres would be favoured, in particular with dinuclear species, which have a large projected area. Besides, NMR spectra decomposition highlighted *ca.* 3.5 (±0.5) ligands per W atoms, *e.g. ca.* 1.5 (±0.5) $W\text{-}O_{ASA}$ bond with the surface. Assuming that the formation of only dinuclear species (because there are EPR silent and NMR active), structures **V to XVIII** are more likely. However, it is not possible to define how W is grafted to the surface, *i.e.* through grafting *via* terminal or bridging O surface ligands.

Then, to better understand the phenomena involved in the grafting of surface species, we discussed two different reaction mechanisms, presented **Figure 54**.

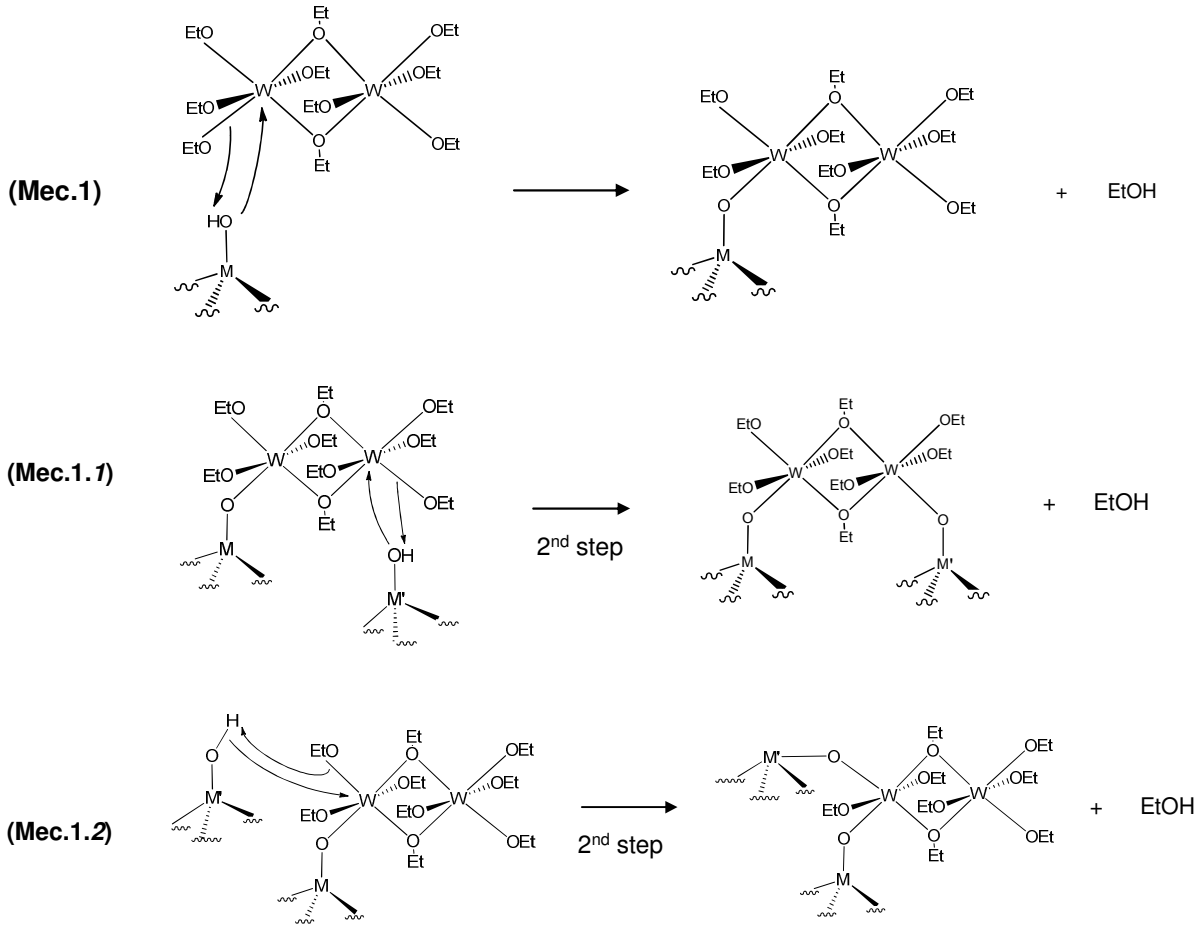

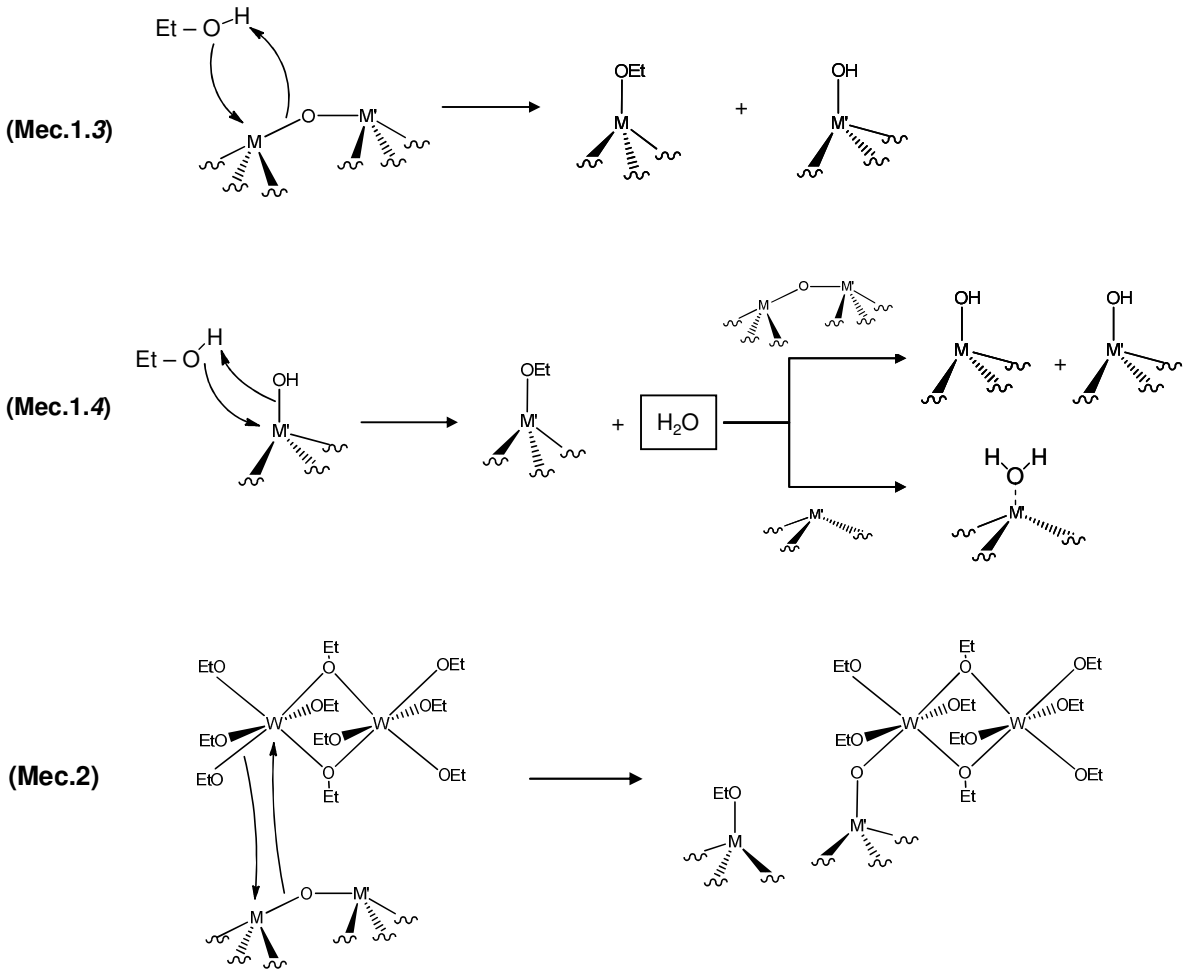

Figure 54: Different mechanisms proposed for reaction between $[W(OEt)_5]_2$ and ASA_{-300} surface functionalities. M and M' stand for Al or Si atoms.

Mechanisms (Mec.1) and (Mec.2) respectively involve grafting of dinuclear species on isolated hydroxyl M-OH; or subsequent opening of adjacent M-O-M' bridge (M = Al, Si; M' = Al, Si) with a W-OEt, which would result in the formation of a ASA-OEt and an additional bond between W and the surface. Note that the grafting reaction can be performed on terminal or on bridging ligands, but grafting *via* terminal ligands are only discussed here for the sake of simplicity.

First, grafting *via* (Mec.1) infers the release of 1 *equiv.* of EtOH per grafted complex. Note also that less than 0.1 *equiv.* of EtOH is released per W upon grafting and that EtOH does not readily react with ASA in the absence of W. Then, considering the large amount of EtO-ASA, the formation of the surface ethoxy must be assisted by tungsten and originates from EtOH as

shown in (Mec.1.*3*) and (Mec.1.*4*) as well as from the reaction of a W-OEt with adjacent M-O-M' bridge as shown in (Mec.2). Water, possibly released upon reaction of EtOH with hydroxyls, can also infer the formation of new hydroxyls, or stay strongly adsorbed on Lewis acid sites. Finally, (Mec. 2) would not lead to a consumption of any surface OH, while (Mec.1) would lead to at least one surface OH consumed by bond formation between the surface and a monografted dinuclear species. **Successive steps** involving (Mec.1) or (Mec.2) **will *in fine* lead to bis, tris and tetra-grafted tungsten centres** as well as numerous surface ethoxy groups. To further illustrate the proposal, (Mec.1.*1*) and (Mec.1.*2*) show the formation of a bis-grafted dinuclear species as a 2nd step of (Mec.1). Note in particular that (Mec.1.*1*) gives a bis-grafted dinuclear species in which the two tungsten centres are monografted, while (Mec.1.*2*) gives a bis-grafted dinuclear species in which only one of the two tungsten centres is linked to the surface, in a bipodal mode. Occurrence of these mechanisms before or after (Mec.2) is also possible.

Finally, we can summarize our propositions (**Table 5**) as follows:

Table 5: Compatibility between our mechanisms and experimental data.

	(Mec.1)	(Mec.2)
Assisted grafting of -OEt species	NO	**YES**
Consumption of surface OH-groups	**YES**	NO
1.5 (± 0.5) bonds W-O_{ASA} bond per W centre	**YES**	**YES**

As shown in **Table 5**, **grafting of $[W(OEt)_5]_2$** cannot involve a single mechanism but likely several ones, by **direct reaction with hydroxyl groups**, and **M-O-M' bridge opening (M = Al, Si; M' = Al, Si).** One ideal grafting pathway would involve the reaction of the dinuclear W molecular species with two M-OH and two adjacent M-O-M' bridge. It would lead to a tetra-grafted W dimer with the concomitant formation of four EtO-ASA surface species (as illustrated by structure **XIV** to **XVIII**).

IV.5.b. Surface species for coverage above *ca.* 0.8 (± 0.1) W/nm²

For tungsten loadings greater than *ca.* 0.8 (± 0.1) W/nm², additional tungsten species are present; they are not directly grafted on the oxide surface, but are adsorbed on previously grafted surface species (multilayer formation); the additional layer of precursors probably interacts with the grafted species *via* W-O(Et)-W bridges or weaker electrostatic interaction. In fact, additional washing with cyclohexane of the material decreases the loading from 1.7 to 1.4 W/nm². Higher coverage/loading probably leads to the formation of additional layers, **more loosely bonded** (**physisorbed**). This is consistent with an increase of the number of EtO ligand bound to W from 3.5 to 4.3 (±0.5) at loading greater than 0.8 W/nm^2, a value closer to the theoretical number of 5 ligands / W expected in $[W(OEt)_5]_2$. In addition, at higher loadings, the new observed species are more mobile according to NMR (sharper signals) and closer to the molecular precursor according to both IR and NMR.

Finally, when **increasing the amount of $[W(OEt)_5]_2$** are deposited, **multilayer** of tungsten species are formed, with **concomitant structural changes**. **W-O(Et)-W bridges** as well as **hydrogen bonds** are supposed to play a role in the stabilisation of the multilayer, more or less strongly bound to the grafted layer of species. One possible sketch of the multilayer is represented in **Figure 55**, which highlights strong interactions (W-O(Et)-W bridges) between tungsten species, as well as weaker ones (dotted arrows), like electrostatic interactions.

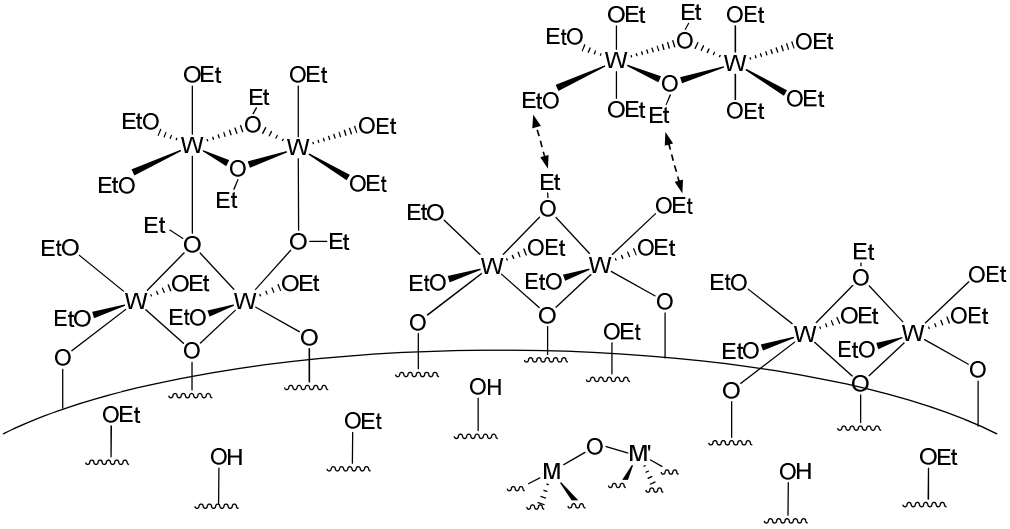

Figure 55: Schematic representation of surface species for high tungsten loadings, where M and M' stand for either Si or Al atoms, and black arrows indicate electrostatic interactions.

IV.6. Conclusion

In this part, we investigated the effect of the tungsten loading on the different surface species of CSC catalysts, especially by XPS, IR, and NMR spectroscopies combined with DFT calculations.

For tungsten loading below 0.8 (±0.1) W/nm², grafted surface W species are formed according to IR spectroscopy, mass balance as well as extensive NMR studies, and their structural features are as follows: the surface W species dinuclear W surface species having an average of 7 ethoxy ligands and being attached by 3 bonds to the surface and surrounded by adjacent ethoxy groups bound directly to the oxide support. They are presumably formed by reaction with the surface hydroxyl and the subsequent grafting takes place *via* reaction with adjacent M-O-M' bridges (M = Al, Si; M' = Al, Si), which leads to the formation of surface ethoxy groups.

For tungsten loading greater than 0.8 (±0.1) W/nm², additional tungsten species results from the adsorption of molecular complexes on top of the aforementioned grafted surface species, which interact more or less strongly *via* either *mu*-bridge ethoxide or electrostatic interactions forming additional layers.

IV.7. References

Bronnimann, C. E.; Zeigler, R. C. and Maciel, G. E., *Journal of the American Chemical Society* (1988), **110**, 2023

Brunner, E., *Catalysis Today* (1997), **38**, 3, 361-376

Chizallet, C. and Raybaud, P. *Angewandte Chemie International Edition* (2009), **48**, 16, 2891-2893

Chizallet, C. and Raybaud, P. *Chem.Phys.Chem*. (2010), **11**, 1, 105-108

Copéret, C.; Chabanas, M.; Petroff Saint-Arroman, R. and Basset, J.M., *Angewandte Chemie International Edition* (2003), **42**, 2, 156-181

Crépeau, G.; Montouillout, V.; Vimont, A.; Mariey, L.; Cseri, T. and Maugé, F., *The Journal of Physical Chemistry B* (2006), **110**, 31, 15172-15185

Derouane, *E.G.*; Nagy, J.B.; Dejaifve, P.; van Hooff, J.H.C.; Spekman, B.P.; Védrine, J.C. and Naccache, C., *Journal of Catalysis* (1978), **53**, 40-55

DeWilde, J.F.; Chiang, H.; Hickman, D.A.; Ho, C.R. and Bhan, A., *ACS catalysis* (2013), **3**, 798-807

Greenler, R.G., *Journal of Chemical Physics* (1962), **37**, 9, 2094-2100

Heeribout, L.; Vincent, R.; Batamack, P.; Dorémieux-Morin, C. and Fraissard, J., *Catalysis letters* (1998), **53**, 1-2, 23-31

Kwak, J.H.; Mei, D.; Peden, C.H.F.; Rousseau, R. and Szanyi, J., *Catalysis Letters* (2011), **141**, 5, 649-655

Legrand, A. P., The Surface Properties of Silicas (1998), Edition John Wiley & Sons Ltd, Chichester

Leydier, F., PhD thesis, Université Pierre et Marie Curie, Paris VI, France (2012)

Massiot, D.; Fayon, F.; Capron, M.; King, I.; Le Calvé, S.; Alonso, B.; Durand, J.O.; Bujoli, B.; Gan, Z. and Hoatson, G. *Magnetic Resonance in Chemistry* (2002), **40** , 70-76

Müller, M.; Harvey, G. and Prins, R., *Microporous and Mesoporous Materials* (2000), **34**, 281-290

Pines, A.; Gibby, M.G. and Waugh, J.S., *Journal of Chemical Physics* (1972), **56**, 1776-1777.

Rascon, F.; Wischert, R. and Copéret, C., *Chemical Science* (2011), **2**, 8, 1449-1456

Roy, S.; Mpourmpakis, G.; Hong, D.Y.; Vlachos, D.G.; Bhan, A. and Gorte, R.J., *ACS Catalysis* (2012), **2**, (9), 1846–1853

Solomon, H.J.; Bliss, H. and Butt, J.B., *Industrial & Engineering Chemistry Fundamentals* (1967), **6**, 3, 325-333

Part V. Evolution of catalysts during sulphidation: from surface species to active WS_2 phases

Outline (part V)

Outline (part V) **155**

Introduction **157**

V.1. Influence of the tungsten loading on conventional and CSC catalysts **157**

V.1.a. Insights into the spreading of oxide species on ASA: the case of conventional materials 158

V.1.b. Characterisation by X-ray photoelectron spectroscopy (XPS) 164

V.1.c. Characterisation by Temperature-programmed reduction (TPR) 167

V.1.d. Characterisation by Transmission electron microscopy (Bright field mode) 171

V.1.e. Characterisation by Scanning transmission electron microscopy (High angle annular dark field) 172

V.1.f. Characterisation by Carbon monoxide adsorption at low temperature (77K), monitored by IR spectroscopy - IR(CO) 175

V.1.g. Catalytic results and discussion 179

V.1.h. Conclusion on the influence of the tungsten loading on the genesis and activity of the active phase of WS_2/ASA catalysts 189

V.2. Influence of the sulphidation temperature on CSC and conventional catalysts **190**

V.2.a. Characterisation by X-ray photoelectron spectroscopy (XPS) 191

V.2.b. Characterisation by Transmission electron microscopy (TEM Bright field mode) 196

V.2.c. Characterisation by Scanning transmission electron microscopy (high angle annular dark field) - STEM-HAADF 199

V.2.d. Characterisation by Carbon monoxide adsorption at low temperature (77K), monitored by IR spectroscopy - IR(CO) 201

V.2.e. Catalytic results and Discussion 203

V.2.f. Conclusion on the influence of the sulphidation temperature on the genesis and activity of the active phase of WS_2/ASA catalysts 210

V.3. References **211**

Introduction

The aim of this chapter is to study the sulphidation and the catalytic properties of materials prepared *via* the controlled surface chemistry (CSC) method, and previously characterised in part IV. They will be compared to conventional catalysts, whether dried or calcined prior to sulphidation. We will investigate for each system the level of sulphidation, the characteristics of the WS_2 slabs (length, stacking number, and 2D morphology) and the catalytic activity in the hydrogenation of toluene. Part V.1 will focus on the influence of the tungsten loading. Indeed, we have seen in part IV that different surface species were observed when the tungsten loading was modified. It is thus interesting to study the influence of each type of species on the genesis of the WS_2 phase. Then, Part V.2 will investigate the influence of the sulphidation temperature in order to get new insights into the evolution of the properties of the active phase, as for example, the amount of WS_2 formed upon sulphidation

V.1. Influence of the tungsten loading on conventional and CSC catalysts

In this part, we will focus on the influence of the tungsten loading on CSC and conventional WS_2/ASA catalysts, where the tungsten loading (W/nm²) is calculated on the basis of elemental analyses and the support surface area (228 m²/g). Moreover, note that conventional materials were prepared by incipient wetness impregnation of an aqueous solution of ammonium metatungstate (polyoxometallate species) on ASA. Drying the material at 120°C gave materials referred as "dried". Subsequent calcination under air at 450°C gave materials referred as "calcined". CSC materials $[W(OEt)_5]_2/ASA_{-300}$ were prepared by incipient wetness impregnation of a cyclohexane solution of $[W(OEt)_5]_2$ onto ASA_{-300}, as reported in the experimental section. Afterwards, CSC and conventional materials underwent sulphidation at 350°C for *ca.* 2 h, with a mixture of H_2/H_2S (15 $\%_{mol.}$ H_2S) at atmospheric pressure, unless otherwise stated.

V.1.a. Insights into the spreading of oxide species on ASA: the case of conventional materials

In part IV, we detailed the case of CSC oxide materials where for W-loadings below 0.8 W/nm², formation of a layer of grafted species occurred. For higher loadings, we observed the formation of a multilayer, composed of more loosely bonded species, chemisorbed or physisorbed onto the layer of grafted tungsten species. With this in mind, we investigate in this first paragraph the possible formation of such layered structures on conventional catalysts, especially in the case of calcined ones for which data are already reported in the literature (see below). According to a simple model where WO_3 species form a close-packed layer of species on the surface (see **Figure 56**), Xie *et al* [Xie and Tang, 1990] estimate the full coverage of a surface (referred as a "*monolayer*") to be *ca.* 0.21 $g_{WO3}/100\ m^2_{support}$. The comparison of this theoretical value with an experimental one collected from XRD data [Liu *et al*., 1985] of WO_3 supported
γ-Al_2O_3 samples revealed that a layer of surface species which correspond to the full coverage of the support was achieved.

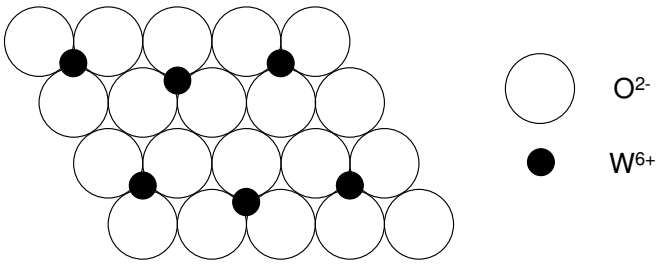

Figure 56: Close-packed "monolayer" for WO_3

A detailed procedure, based on the quantification of residual crystalline compound by XRD [Chung, 1974] is detailed in their paper [Xie and Tang, 1990]. Briefly, the methodology is based on the fact that while no evidence of crystalline phase is detected by XRD when surface species are below a "monolayer" coverage (*e.g.* close-packed species stuck together), crystalline WO_3 is expected to be detected above such a "monolayer". XRD diffractograms of conventional calcined catalysts with 0.5 W/nm², 1.8 W/nm² and 3.7 W/nm² (extrudates were crushed and mixed with α-Al_2O_3) are shown in **Figure 57**.

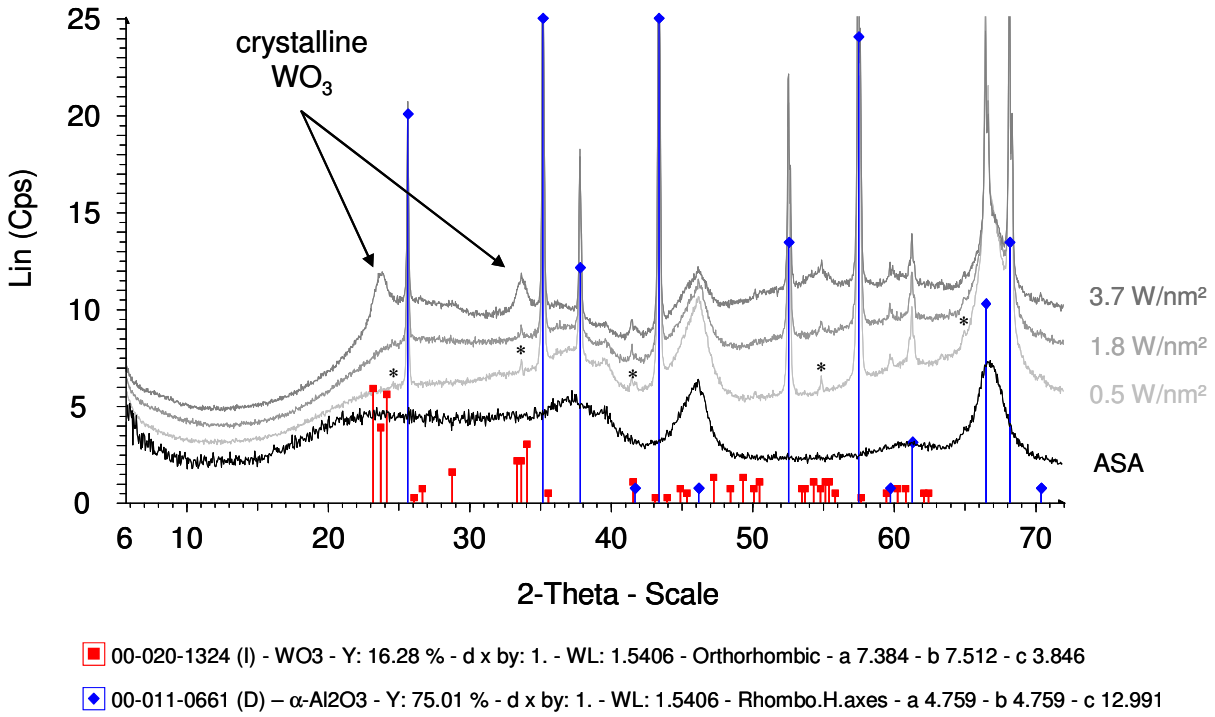

Figure 57: XRD pattern of pristine ASA and conventional calcined catalysts supported on ASA, with increasing W-loadings. α-Al_2O_3 was added to conventional materials for quantification purpose. ∗ indicates diffraction peaks coming from tungsten impurities deposited on of the X-ray tube Cu.

We can see that for tungsten loadings below 1.8 W/nm², no crystalline WO_3 is evidenced, while at 3.7 W/nm², two peaks at *ca.* 2θ = 24° and 2θ = 34° are assigned to crystalline WO_3. Therefore, we assume that for W-loadings ranging from 1.8 W/nm² to 3.7 W/nm², the maximal amount of close-packed species is achieved and that stacking of amorphous WO_3 entities occurs and leads to crystalline WO_3 formation. Our results are in line with literature data where, a "monolayer" coverage of supported WO_3 is reached between 4.1 W/nm² [Yu *et al.*, 2001] and 4.8 W/nm² [Xu *et al.*, 2000] on TiO_2 and between 4.6 W/nm² [van der Vlies, PhD thesis, Zürich, 2002] and 5.4 W/nm² [Xie and Tang, 1990] on γ-Al_2O_3. On Silica, only a layer of species that does not correspond to the full coverage of the support was achieved. It is referred as a "*submonoloayer*" coverage, and is assumed to be *ca.* 0.5 W/nm², from calculations based on the work of Xie et *al.* [1990] and Wang et *al.* [Wang *et al.*, 2003]. Finding a layer of species that

covers the full surface or less than the full surface of a support" was tentatively linked by the authors to thermodynamical aspects, related to the influence of the strength of the bond between the monolayer and the surface on the system entropy. Finally, as our ASA support is composed of 70 $\%_{wt.}$ Al_2O_3, and 30$\%_{wt.}$ SiO_2, this intermediate composition could explain the intermediate threshold between *ca.* 1.8 and 3.7 W/nm² found for a "(sub)monolayer" coverage of WO_3 on ASA.

Finally, finding a threshold between a so-called “(sub)monolayer” and a multilayer to be 0.8 W/nm² for CSC materials, and between 1.8 and 3.7 W/nm² for conventional samples, is not surprising as the projected area of one stoechiometric unit of WO_3 is *ca.* 23 A² [Di gregorio *et al.*, 2004], while the projected area of one $[W(OEt)_5]_2$ dimer is *ca.* 100 A², *e.g.* 50 A² per W. It means that more WO_3 unit than $[W(OEt)_5]_2$ dimers can be packed together to form a “monolayer” of close packed species, *e.g.* that a “(sub)monolayer coverage” is reached more quickly on CSC materials than on conventional calcined ones.

For the sake of clarity, all these results about the different oxide species on CSC and conventional materials, depending on the W-loading, are summarized by schematic representations of each material, as shown on the next pages.

CSC materials are represented in **Figure 58**, where tungsten dinuclear species are illustrated by rectangles. In light pink are represented the tungsten species grafted on the ASA surface, as previously detailed in part IV. Besides, loosely bonded species, forming additional layers deposited onto the grafted one, are shown in pink. The left part of the figure shows a representation of a *side view*, while the right part shows a representation of a *top view*. The former one allows a better understanding of the stacking of the different species, while the latter highlights how the species are dispersed on the surface, on a square of 10 nm long. Note that for more chemical representations, the reader is asked to come back to part IV.

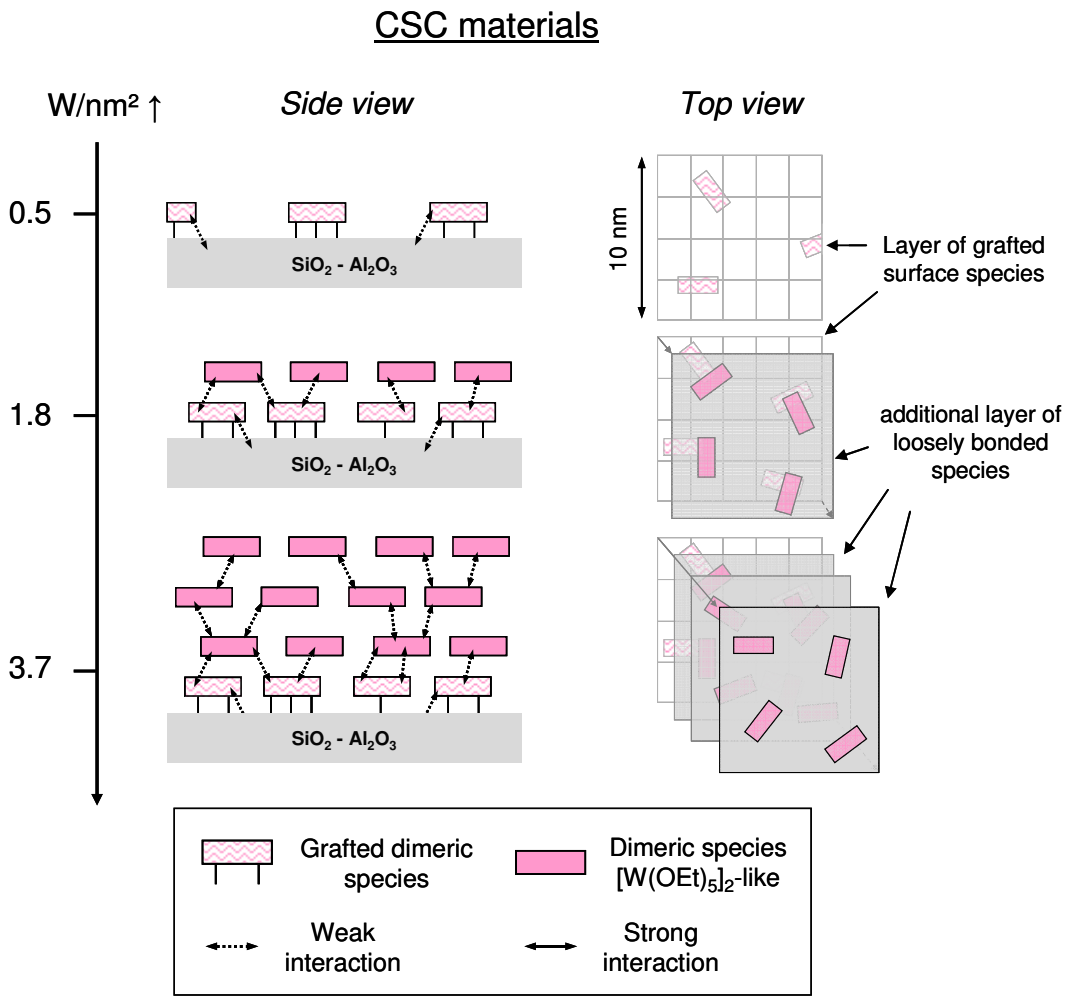

Figure 58: Schematic representation of the surface of CSC materials as a function of the W-loading. Materials were obtained by deposition of $[W(OEt)_5]_2$ onto ASA_{-300}.

The different oxide species found on conventional dried materials are depicted on **Figure 59**. Due to the high number of W in polyoxometallate clusters (12 W), materials with low W-loading exhibit even lower cluster loading on their surface. Note that clusters might be well dispersed, but tungsten atoms found into the clusters are poorly dispersed as linked together inside the cluster structure. Polyoxometallate clusters are linked to the ASA surface by weak interactions (electrostatic type).

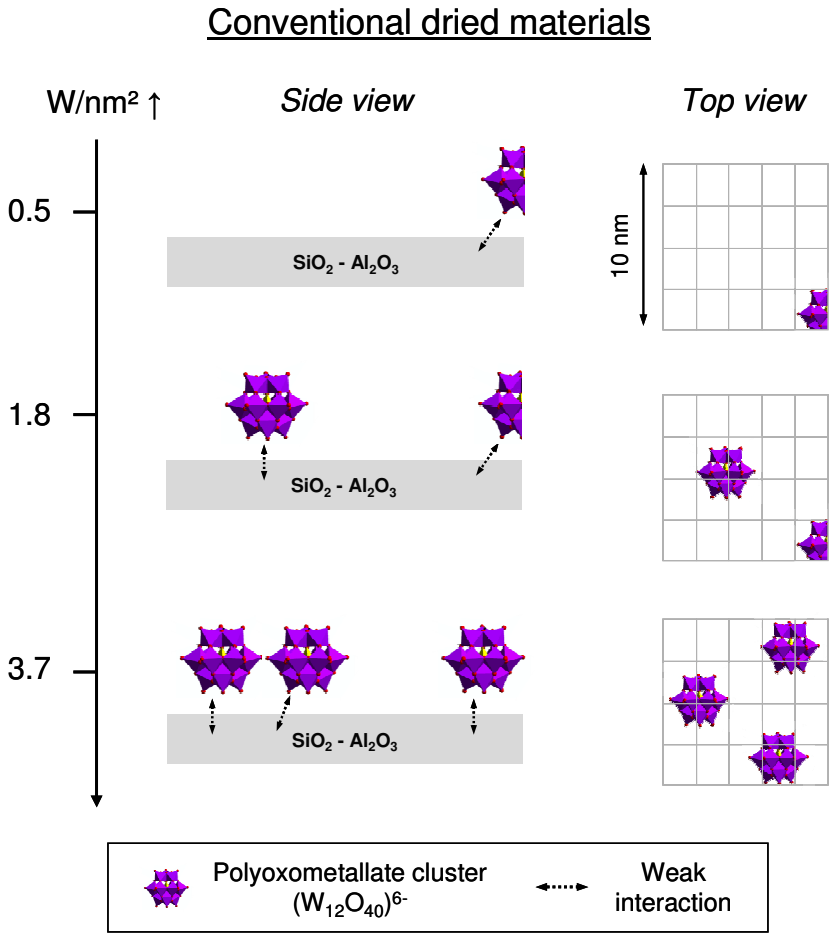

Figure 59: Schematic representation of the surface of conventional dried materials as a function of the W-loading. Materials were obtained by drying impregnated ASA at 120°C for 1 night.

Finally, the different oxide species found on conventional calcined materials are depicted on **Figure 60**. At low loadings, small amorphous WO_3 particles are supposed to be spread onto the ASA surface. Then, increasing the W-loading causes a growth of amorphous WO_3 directed horizontally over the surface, and vertically on top of preformed WO_3 particles. Between 1.8 W/nm² and 3.7 W/nm² in particular, crystalline WO_3 appears, as represented in white and black stripes. It indicates that no more WO_3 can spread onto the ASA surface, *e.g.* that the "(sub)monolayer" is achieved, and that stacking of WO_3 species becomes the main phenomenon. WO_3 is strongly linked to the surface.

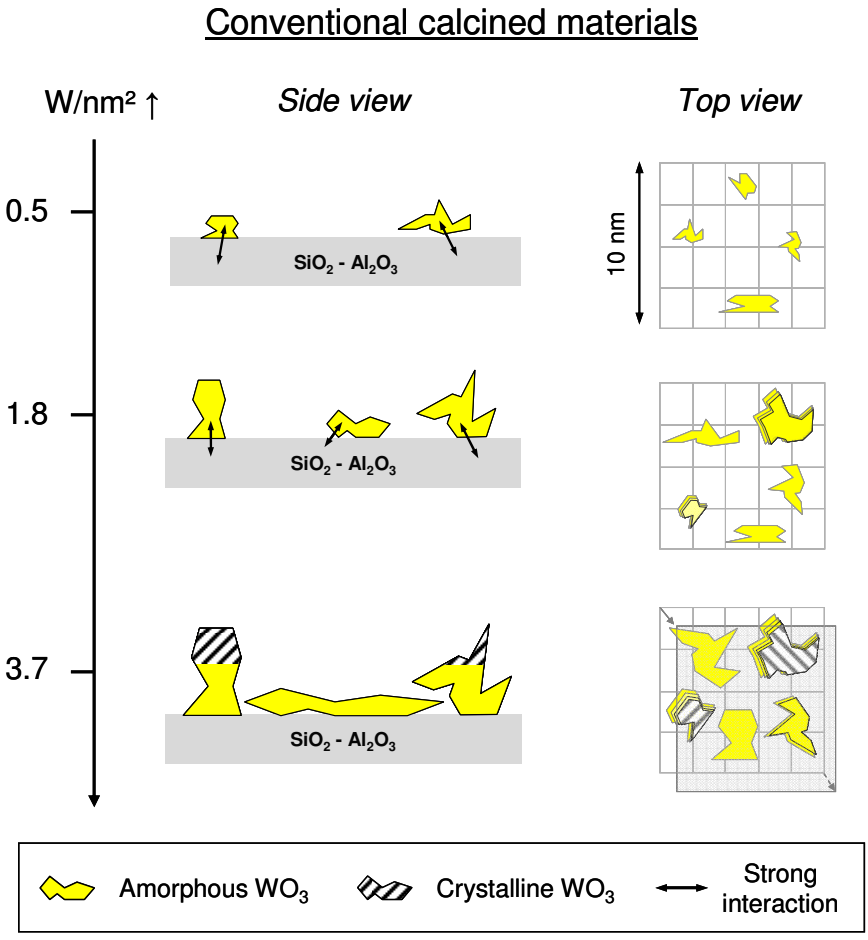

Figure 60: Schematic representation of the surface of conventional calcined materials as a function of the W-loading. Materials were obtained by calcination of a dried material at 450°C, with air, for 2 h

V.1.b. Characterisation by X-ray photoelectron spectroscopy (XPS)

The sulphidation level of CSC and conventional catalysts was studied by XPS, focusing on the decomposition of their W 4f spectrum. The decomposition procedure applied for the whole set of spectra has already been described earlier [Ben Tayeb *et al.*, 2010] and is available in the experimental section, part II. **Figure 61** shows the evolution of the different tungsten phases as well as the S/W atomic ratio in WS_2 slabs, depending on the W loading.

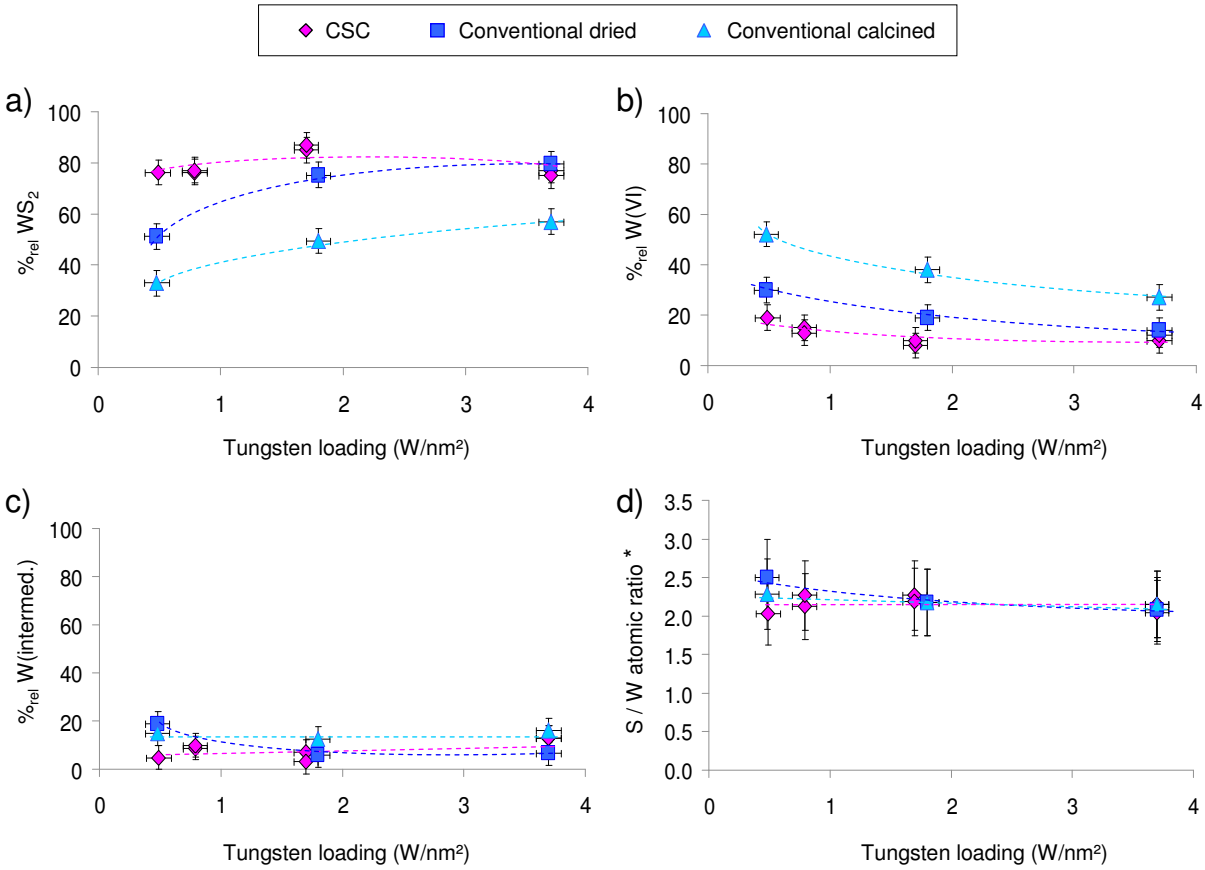

Figure 61: XPS data of CSC and conventional catalysts (dried or calcined) depending on tungsten loading. a) Sulphidation level. b) Relative percentage of non-sulphided W(VI) phase. c) Relative percentage of partially sulphided W(intermed.) phase. d) S/W atomic ratio*, calculated from peak area of W(IV) on W 4f spectra and S(-II) on S 2p spectra.

On **Figure 61-a** we can see that at 0.5 W/nm², the CSC catalyst is sulphided at *ca.* 76 (±5) $\%_{rel,}$ WS_2 while dried and calcined catalysts are only sulphided at 51 (±5) $\%_{rel.}$ WS_2

and 33 (±5) $\%_{rel.}$ WS_2 respectively, which indicates that the CSC catalyst is better sulphided. Note however that the dried catalyst undergo far better sulphidation (higher $\%_{rel.}$ WS_2) than the calcined one, as previously described in the literature.[Reinhoudt *et al.*, 1999] These differences can be explained in terms of reactivity of oxide species. Their sulphidation level is expected to depend either on their "W-O" bond dissociative energy, their interaction with the support, *e.g.* **M-O**-W linkage (M = Al, Si), or on their reducibility, as sulphidation is a reductive process where $W^{(VI)}$ is reduced into $W^{(IV)}$. At low W loadings, all catalysts are covered by well-dispersed species, as revealed by the rather identical W/Al atomic ratio shown in **Table 6.** We recall that for the sake of clarify, examples of CSC and conventional materials' surfaces are illustrated in **Figure 58** to **Figure 60.**

Table 6: W/Al atomic ratio (x100) representing the coverage of tungsten on the ASA. Obtained from XPS analyses

W/nm²	CSC	Dried	Calcined
	W/Al (at/at) x 100		
0.5	1.1	0.8	0.9
1.7	4.8	2.7	2.9
3.7	11.2	5.9	6.1

First, the high level of sulphidation of the CSC materials can be tentatively explained at a more molecular level: “W-OR” bonds in $[W(OEt)_5]_2$ are rather labile and can easily undergo ligand exchange,[Turova, 2002, Kluwer Academic Publishers, London] thus facilitating the reaction between $[W(OEt)_5]_2$-based surface species and H_2S. Then, on conventional catalysts, the energy needed to depolymerise $[WO_4]^{2-}$ tungsten clusters, *e.g.* the energy needed to cleave “W-O” bonds in polyoxometallate, is unknown. We are currently trying to calculate it by molecular modelling, as its comparison with the dissociative energy of the “W-O” bond in $[W(OEt)_5]_2$ could, in a first approximation, allow us to claim which of the oxide species prepared by a CSC or a conventional method undergo more easily “W-O” bond cleavage. Second, WO_3/Al_2O_3 calcined materials are thought to be refractory to sulphidation because of the strong interactions between WO_3 and the surface, assigned to robust Al-O-W linkages in WO_3/Al_2O_3 catalysts. [van der Vlies, PhD thesis, Zürich, 2002] Such metal-support interactions, different on silica and alumina, are often discussed to play an important role in sulphidation. As an example, silica-based materials prepared with conventional precursors more easily undergo sulphidation than alumina ones, as 75 $\%_{rel.}$ *vs.* 50 $\%_{rel.}$ WS_2 are respectively obtained on these supports. [Raybaud and Toulhoat, 2013, Ed. Technip, Paris]. Besides, polyoxometallates species seen on

dried materials are reported to develop weak interaction with oxide supports. [Proust *et al.*, 2012] Differences in metal-support interactions can thus partially explain the better level of sulphidation of dried catalysts. To get further insights into the influence of such interactions, we are currently investigating if the limit observed for the sulphidation level of the CSC catalyst is linked to its M-O-W linkages (M = Al, Si), as grafted dimeric surface species illustrated in chapter IV share more than one bond with the surface, bonds which are not supposed to undergo sulphidation.

For tungsten loadings higher than 0.5 W/nm², higher amounts of tungsten are deposited on the surface, which decrease the distance between WO_x species on conventional catalysts, as illustrated in **Figure 59** and **Figure 60**. It must facilitate sulphidation, considering that migration of closer oxide species upon formation of WS_2 is easier. In particular, CSC catalysts reveal similar level of sulphidation ranging from 76 (±5) $\%_{rel.}$ to 85 (±5) $\%_{rel.}$ WS_2 for tungsten loading between 1.7 and 3.7 W/nm². We could have expected a better sulphidation level of CSC samples, as $[W(OEt)_5]_2$-like species composing the top layers of the multilayer exhibit no interaction with the ASA surface and should behave like pure $[W(OEt)_5]_2$. However, sulphidation of pure $[W(OEt)_5]_2$ at 600°C, H_2S/H_2 (15 $\%_{mol.}$ H_2S) led to bulk WS_2 exhibiting *ca.* 92 (±5) $\%_{rel.}$ WS_2: this is thus not surprising to find that the highest level of sulphidation of W-supported materials prepared with $[W(OEt)_5]_2$ is lower of equal to 92 (±5) $\%_{rel.}$ of the amount of tungsten detected by XPS.

At this point, we have tried to explain the evolution of the $\%_{rel}$ WS_2 observed for CSC and conventional catalysts. Then, we investigated the evolution of $\%_{rel}$ W(VI), presented in **Figure 61-b**, as it is strongly linked to the evolution of $\%_{rel}$ WS_2. The $\%_{rel}$ W(VI) decreases with increasing tungsten loading for all catalysts. At 0.5 W/nm², in the case of the conventional calcined catalysts, the amount of non-sulphided WO_3 is relatively high, confirming that the amorphous oxide phase is very refractory to sulphidation, especially at low tungsten loadings. No clear trend could be found for the amount of intermediate phase $\%_{rel}$ W(intermed.), as shown in **Figure 61-c,** with a value rather constant for all catalysts, at about 8 (±5) $\%_{rel}$. Finally, the S/W atomic ratio of WS_2 slabs stays close to {2.2 ; 2.3} in general, with slightly higher values at low loading.

Finally, we investigated the W/Al atomic ratio (seen by XPS) before and after sulphidation. **Figure 62-a,** shows that this quantity which represents the coverage on the support by tungsten species is lowered upon sulphidation of CSC catalysts. It indicates that sulphidation causes aggregation of the well-dispersed W species (grafted as a monolayer or forming multilayer),

consistent with the formation of more or less stacked WS_2 slabs. On the contrary, **Figure 62-b** and **Figure 62-c,** show that the coverage of ASA by W oxide species of dried and calcined conventional materials does not change upon sulphidation. Besides, values previously reported in **Table 6** show that oxide materials prepared by the CSC method exhibit a better dispersion of tungsten on the surface, except for 0.5 W/nm². After sulphidation, we can see on **Figure 62-d,** that the W/Al atomic ratios are rather similar, whatever the preparation method. We see that the difference between the higher and the lower W/Al atomic ratio for a given loading increases when higher amount of tungsten are impregnated. It reveals that the lower the catalysts loading, the closer the way W spreads on the ASA surface in sulphided samples, whatever the preparation method.

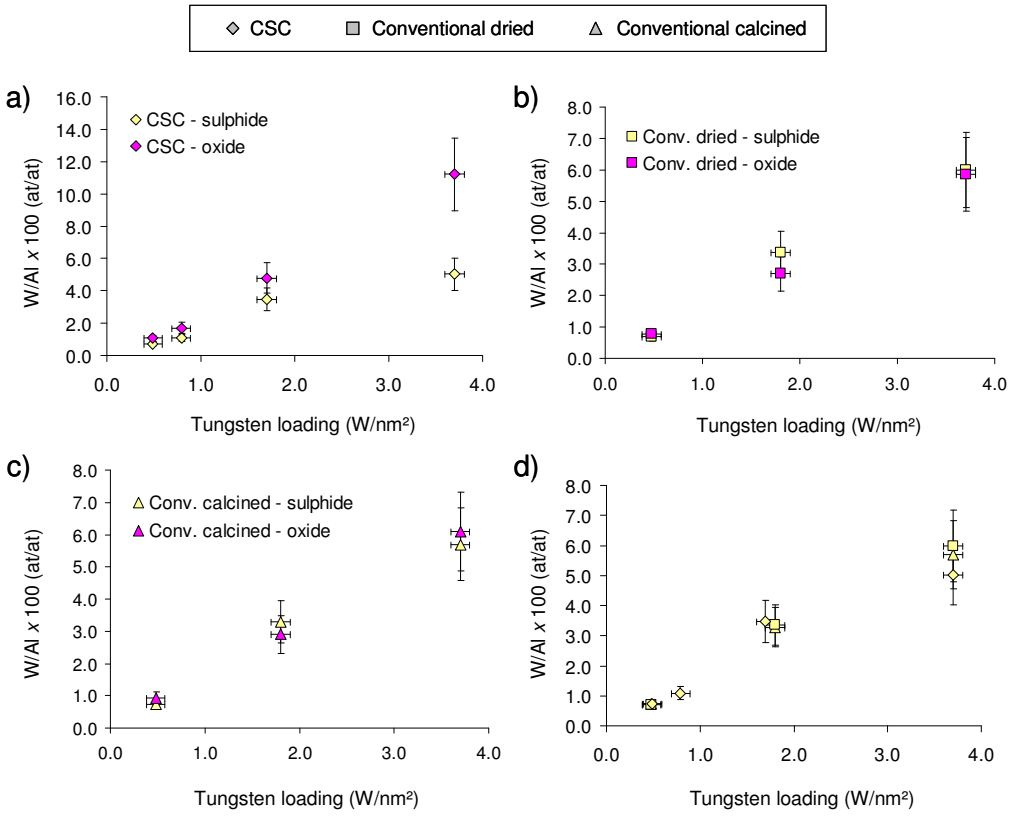

Figure 62: W/Al atomic ratios (x100), obtained from XPS analyses. Comparison between oxide and sulphide materials prepared by a) CSC, b) Conventional dried, and c) Conventional calcined methods. Comparison between sulphided catalysts is depicted in d).

V.1.c. Characterisation by Temperature-programmed reduction (TPR)

We performed TPR experiments on CSC and conventional oxide materials to quantify the reducibility of oxide species deposited on an ASA surface and to identify if it may help to

understand the levels of sulphidation observed in **Figure 61 (part V.1.b)**. TPR patterns of our catalysts, *e.g.* H_2 consumption (mL/min) and temperature (°C) as a function of time are reported in **Figure 63** as well as related H_2 consumptions values, expressed in ml(H_2)/g(W), in **Table 7.** Note that experiments were run from *ca.* 36°C to 1000°C, at 5°C/min, followed by 2 h at 1000°C.

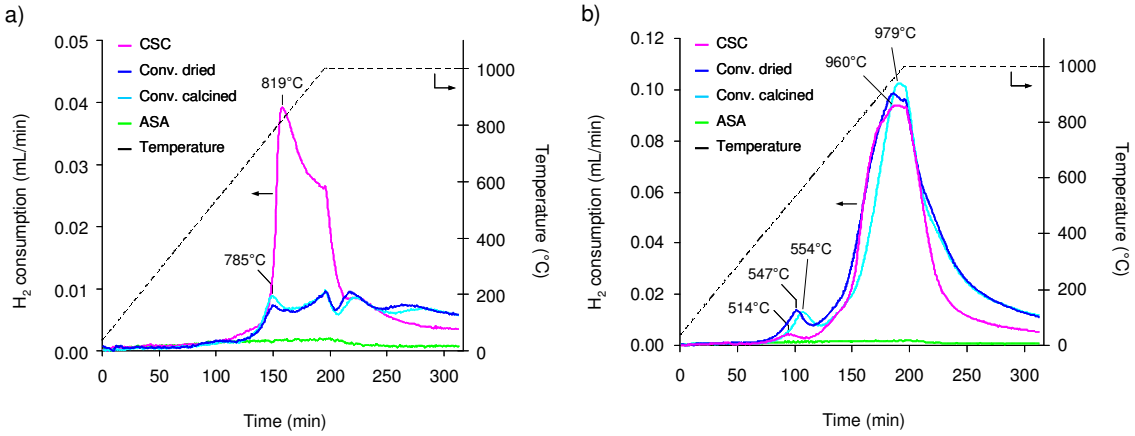

Figure 63: TPR patterns of oxide materials with a) 0.5 W/nm² or b) 1.7-1.8 W/nm². CSC in pink, conventional dried in blue, and conventional calcined catalysts in light blue.

Table 7: H_2 consumption obtained from TPR experiments. STP stands for standard condition of temperature and pressure (273.15 K, 100 kPa)

	H_2 consumption (ml/g(W) (STP))					
	0.5 W/nm²			1.7-1.8 W/nm²		
	CSC	Conv. dried	Conv. calc.	CSC	Conv. dried	Conv. calc.
Total [a]	255	118	121	234	270	245
Std dev.	19	9	9	18	20	18
Theo. value	309	-	371	309	-	371
Ratio exp. / theo. (%)	83	-	33	76	-	66

[a] H_2 consumption from the start to the end of the experiment

First of all, in our conditions the ASA support was found to consume little amount of H_2 (*ca.* 1.4 ml(H_2)/g_{ASA} in standard conditions of temperature, 273.15 K, and pressure, 100 kPa), which has been subtracted from H_2 consumptions obtained for our catalysts and reported hereafter. For catalysts with W-loading of 0.5 W/nm², two reduction peaks are observed below 1000°C: for conventional catalysts, reduction starts at 785 (±24) °C while for CSC ones, reductions starts at 819 (±25) °C. Reduction of conventional species thus begins slightly before molecular species of the CSC material, which seems to indicate an earlier reducibility of

conventional species. However, it has to be balanced against the quantification of the experimental H_2 consumption (from the beginning to the end of the TPR experiment, 313 min) and expected theoretical H_2 consumptions. For estimating the expected theoretical H_2 consumptions, the reduction of $W(OEt)_5$ (for CSC samples) and WO_3 species (for conventional catalysts) were taken into account, in a first approximation. Note that for conventional dried catalysts, this means that we also assume an O/W ratio close to 3 for the W species being reduced. The related equations are shown below:

$$W(OEt)_5 + \frac{5}{2}H_2 \rightarrow W + 5EtOH \qquad \textbf{Eq. 3}$$

$$WO_3 + 3H_2 \rightarrow W + 3H_2O \qquad \textbf{Eq. 4}$$

The corresponding theoretical values are available in **Table 7**. For the CSC sample, 83% of the theoretical amount of H_2 needed to complete reduction is consumed, while only 33% of the theoretical value is found for the calcined sample. Finding values which are below the theoretical ones is not surprising as on the TPR pattern in **Figure 63**, H_2 consumptions are not back to the baseline for the two samples within the time of experiments. Interestingly, more than 2/3 of the CSC surface species are reduced while only 1/3 is reduced for the conventional calcined sample, which indicates that the CSC catalyst is quantitatively more easily reduced, although the reduction temperature starts earlier for conventional catalysts (819°C *vs.* 785°C). This result can partially explain the best sulphidation of CSC species for materials with 0.5 W/nm².

Besides, H_2 consumptions observed for conventional catalysts are found to be identical. As surface species on dried samples (W clusters) and on calcined ones (WO_3 patches) are chemically different, we could have expected a different behaviour toward H_2 (and thus a different reducibility). Moreover, note that we don't know the size of the surface species. These sizes, if different, could influence reduction and thus the quantification of H_2. Therefore, H_2 consumption obtained from TPR experiments cannot explain the XPS results observed on conventional catalysts with 0.5 W/nm² (see part V.1.b).

Then, for tungsten loadings higher than 0.5 W/nm², TPR patterns exhibit two different regions in which reduction peaks are observed for both CSC and conventional materials. Weak reduction peaks are observed at 514°C, 547°C and 554°C respectively for CSC, dried and calcined samples. Then intense peaks are located around 960°C for CSC and dried materials

while situated around 979°C for the calcined sample. The precise assignment of these peaks is not obvious, therefore no further interpretation will be made. However, it is noticeable that reduction peaks for CSC species start at lower or similar temperature than for WO_x species found on conventional samples. Qualitatively, it would indicate an easier sulphidation of CSC species. Besides, looking at the quantification of H_2 consumed upon reduction, CSC materials still exhibit higher level of reduction (76 % of CSC species reduced, as compared with theoretical values) than conventional materials (66 % for the calcined sample). As for samples with 0.5 W/nm², it means that CSC materials are quantitatively more reduced than conventional ones in similar condition. As mentioned before, these results can thus partially explain the better level of sulphidation observed for CSC sample at 1.7 W/nm².

Finally, TPR results found for materials with 0.5 W/nm² and 1.7-1.8 W/nm² are consistent with the observations made from XPS analyses on the sulphidation behaviour of these materials.

First, reducibility of WO_x species has been reported to decrease when their dispersion increases [Thomas *et al.*, 1981; Barton *et al.*, 1998; Macht and Iglesia, 2008], due to stronger interactions with the support (Al_2O_3, ZrO_2). Highly dispersed WO_x supported species are more difficult to reduce. This is coherent with the higher H_2 consumption (expressed per g(W)) for higher loading also explaining the lower level of sulphidation of our catalysts for low W-loadings. Moreover, for low W-loadings, the larger difference in reducibility between $[W(OEt)_5]_2$-based species and conventional ones matched the larger difference of level of sulphidation: 76 (±5) $\%_{rel.}$ *vs.* 51 (±5) $\%_{rel.}$ *vs.* 33 (±5) $\%_{rel.}$ WS_2 respectively for CSC, conventional dried, and calcined samples. For higher W-loadings (as for 1.7-1.8 W/nm²), this difference in reducibility is smaller, which somehow matches the closer $\%_{rel.}$ WS_2 values found between our catalysts: 85 (±5) $\%_{rel.}$ *vs.* 75 (±5) $\%_{rel.}$ *vs.* 49 (±5) $\%_{rel.}$ WS_2 respectively for CSC, conventional dried, and calcined samples.

V.1.d. Characterisation by Transmission electron microscopy (Bright field mode)

Transmission Electron Microscopy (TEM) in Bright Field mode was performed to determine the mean length, L, and mean stacking number, N, of WS_2 slabs. The bar graphs obtained for each catalyst were fitted with a log-normal law. Results are shown **Figure 64.** Bar graphs are available in appendices. For the CSC catalysts, the mean length and stacking number of the WS_2 crystallites are weakly modified by the tungsten loading. In the case of the dried catalysts, only the stacking number increases for increasing amount of tungsten. On the other hand, the length as well the stacking number of the WS_2 slabs of the calcined catalyst increase.

Finally, in the light of the previous results on the sulphidation level of these catalysts, we can say that when increasing the tungsten loading, sulphidation of CSC catalysts has already reached a plateau in terms of $\%_{rel}$ WS_2 (*ca.* 80 ± 5 $\%_{rel}$) and the mean length and stacking of the WS_2 crystallites (L ≈ 3.7 nm, N ≈ 2.8) does not change. In contrast, conventional catalysts, whose sulphidation is not as simple as for CSC catalysts, behave differently: increasing the tungsten loading has a strong effect on the length and the stacking on the WS_2 slabs, which has already been reported for MoS_2 crystallites [Payen *et al.* 1989]. Calcined catalysts are the most sensitive to the tungsten loading upon sulphidation.

TEM in bright field mode, although useful to clearly identify WS_2 crystallites, suffers from a loss of information. As only layered W-S sheets oriented with their (001) basal plane along the electron beam direction are detected, numerous slabs are not considered. In addition, the observation of the W-S sheets lying flat on the support surface is not trivial and would require improving the settings of the apparatus. Considering this, we decided to perform Scanning Transmission Electron Microscopy in High Angle Annular Dark Field mode (STEM-HAADF), a technique which allows a direct map of atomic location to be obtained, with intensities which are dependent on the atomic number Z of the observed atoms.

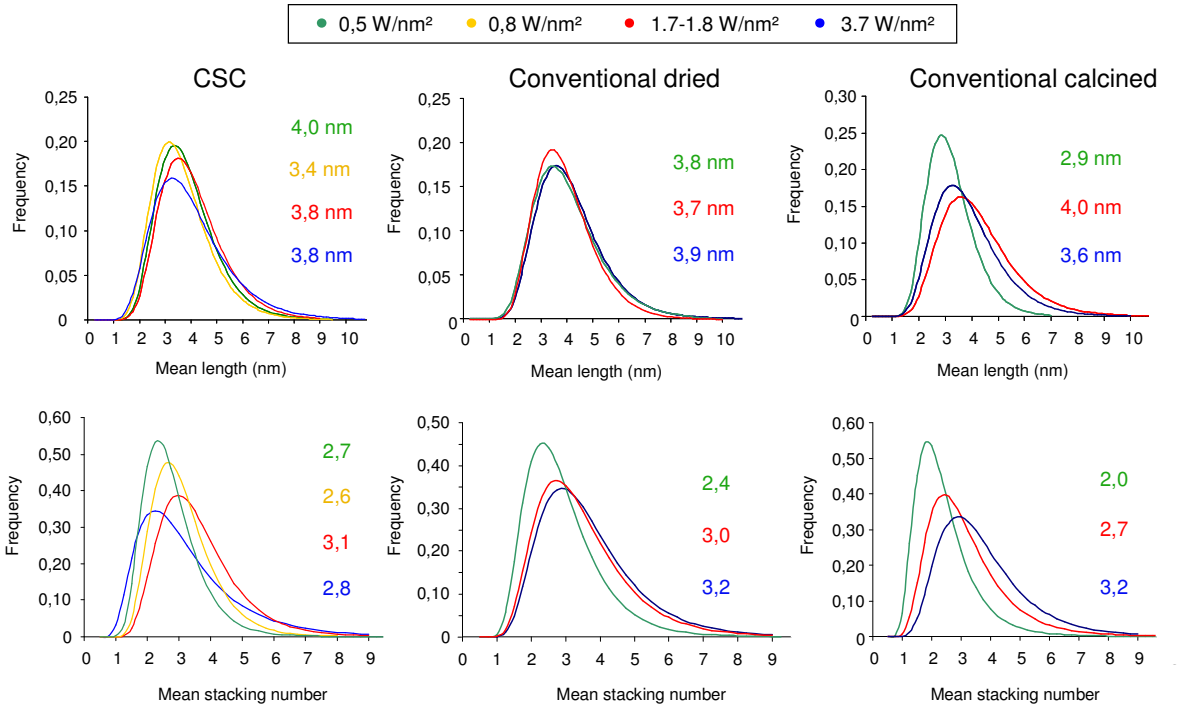

Figure 64: Mean length distribution (a) and mean stacking layer distribution (b) of WS_2 crystallites on WS_2/ASA-300 catalysts when increasing the W loading. Fittings by a Log Normal law.

V.1.e. Characterisation by Scanning transmission electron microscopy (High angle annular dark field)

STEM-HAADF experiments were undertaken by Maria Girleanu at IPCM in Strasbourg through the collaboration between IFPEn and IPCM in Strasbourg. This technique is contrast sensitive, which makes it really interesting to discriminate W from Al or Si. In this case, the contrast is proportional to the square of the atomic number, making possible and easy to identify tungsten. Contrast analysis makes possible to observe WS_2 slabs, either oriented planar of perpendicular to the surface. As a consequence, it allows the direct detection of their 2D morphology. Investigations of the 2D morphology of MS_2 slabs deposited on carbon, and observed by STEM-HAADF, have already been reported in the literature, especially for MoS_2 crystallites supported on carbon [Carlsson *et al.*, 2006, Brorson *et al.*, 2007, Hanssen *et al.*, 2011]. Tungsten sulphide has also be studied through Scanning Tunnelling Microscopy (STM) on model supports as Au(111) surface [Füchtbauer *et al.*, 2006], or on graphite through STEM-HAADF. [Carlsson *et al.*, 2004; Brorson *et al.*, 2007] Here, we decided to analyse catalysts with low tungsten loading, so as to limit the stacking of the WS_2 sheets. Sulphidation

was carried out at 600°C, instead of 350°C, in order to be sure that the slabs were well crystallised. Analyses were performed on WS_2 - supported ASA_{-300} (*ca.* 0.8 W/nm²) and SiO_{2-300} (*ca.* 1.0 W/nm²) CSC catalysts, as well as on conventional calcined catalysts WS_2 - supported ASA (*ca.* 0.5 W/nm²). Calcined catalyst was selected as representative of conventional and industrial catalysts.

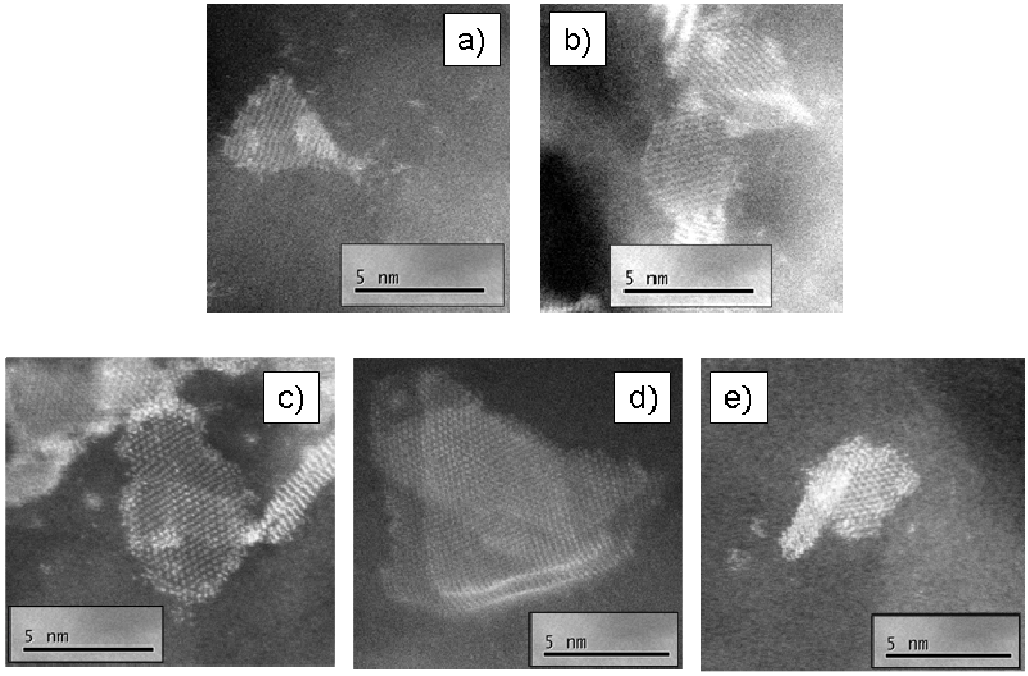

Figure 65: HR STEM-HAADF micrographs of WS_2/ASA catalysts: a) conventional calcined catalyst (0.5 W/nm²). b) CSC catalyst (0.8 W/nm²). Sulphidations of a) and b) were carried out at 600°C, for 2 h, H_2S/H_2 mixture with 15 $\%_{mol.}$ H_2S. c) CSC catalyst (0.8 W/nm²) sulphided at 600°C for 5x6 h, H_2S/H_2 mixture with 15 $\%_{mol.}$ H_2S. d) CSC catalyst (0.5 W/nm²) sulphided at 600°C, 2h, 100% H_2S. e) HR STEM-HAADF micrographs of a CSC WS_2/SiO_{2-300} (1.0 W/nm²), sulphided at 600°C, for 2 h, H_2S/H_2 mixture with 15 $\%_{mol.}$ H_2S.

On **Figure 65**, representing micrographs of planar WS_2 slabs, conventional and CSC catalysts display different 2D morphologies, showing the influence of the two preparation methods. On the conventional catalyst, WS_2 slabs are triangular shaped whereas they are hexagonal shaped on the CSC catalyst, as shown in **Figure 65-a,b**. Similar hexagonal-like morphology was obtained for the CSC catalyst supported on silica (see **Figure 65-e**). While there is a clear difference between the two catalysts, we have not yet fully understood the origin of such morphology differences which may directly be linked to the preparation method and/or

sulphidation conditions. So we first compared the STEM-HAADF results with density functional theory calculations recently undertaken at IFPEN.[Girleanu *et al*., in preparation] In the same spirit as for MoS_2 systems [Schweiger *et al*, 2002], the morphology diagram, shown in **Figure 66**, revealed that the morphology and atomic edge structure depends on the sulfo-reductive conditions. In the sulfo-reductive conditions corresponding to T = 600°C and H_2S/H_2 with 15 $\%_{mol.}$ H_2S, the chemical potential of sulphur of the gas phase, $\Delta\mu_S$, is close to -1.03 eV. The thermodynamically stable morphology as given by the Gibbs-Curie-Wulff laws, is a truncated triangle exhibiting *ca.* 60% M-edge (the ratio of edge lengths being $\frac{L_{W-edge}}{L_{S-edge}} = 1.63$). If one considers sulphiding conditions where H_2S is used as the sole sulfo-reductive agent, the chemical potential of sulphur in the gas phase is close to 0 and the equilibrium morphology should exhibit a higher proportion of W-edge *ca.* 71% ($\frac{L_{W-edge}}{L_{S-edge}} = 2.38$). This theoretical result is qualitatively in line with the STEM observations on conventional catalyst sulphided in 15 $\%_{mol.}$ H_2S/H_2 ; however it differs for CSC catalyst. Therefore, we suspect that the hexagonal 2D morphology observed for CSC catalysts probably arise from another phenomenon (kinetic limitation) induced by the CSC preparation method. At this stage, it has not been possible to pin point the origin of the formation of more hexagonal like slabs *via* the CSC method. However, to check if this phenomenon can be overcome by the sulphidation procedure, we performed a sulphidation of the same CSC catalyst during a longer period of time (30 h) under H_2S/H_2 at 600°C (5 steps of 6 hours, for details see experimental section). STEM-HAADF pictures of this sample revealed large slabs, highly stacked, which made it difficult to find isolated planar ones. The main shape of the slabs resembles more the truncated triangle in closer agreement with the theoretical prediction (see **Figure 65-c**). In addition, a third sulphidation procedure was tested at T = 600°C under pure H_2S (during 2 h): it reveals a similar truncated triangular shape (see **Figure 65-d**), as predicted by DFT calculations for high partial pressure of H_2S.

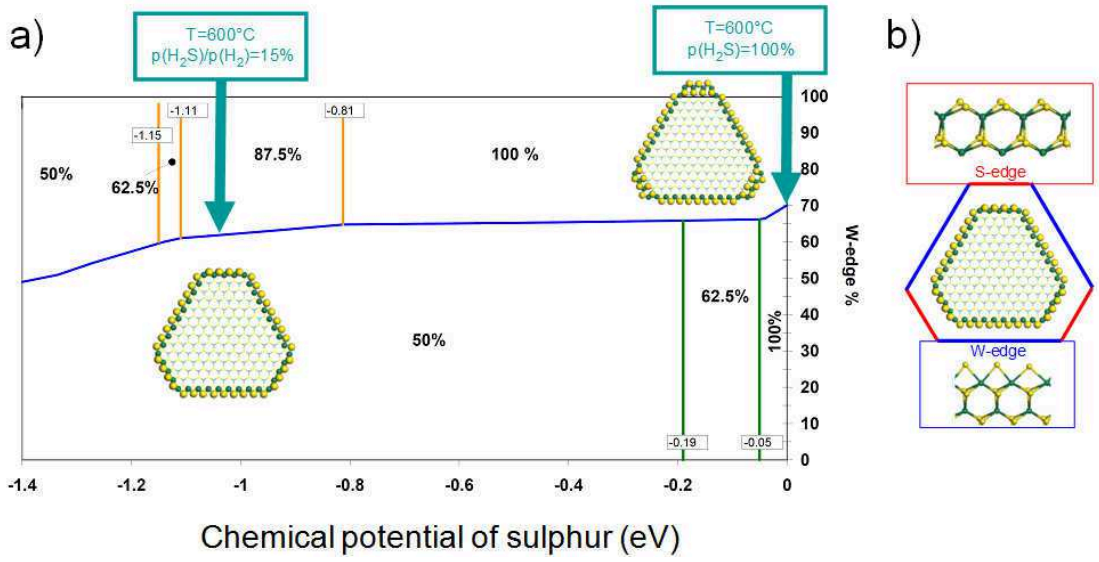

Figure 66: a) Morphology diagram for the WS_2 crystallites as a function of the sulphur chemical potential and the pressure of H_2S, $p(H_2S)/p(H_2)$, at T = 600°C, after reference [Girleanu *et al*, in preparation]. The proportion of W-edge is given by the blue broken line. The S-edge composition in sulphur is reported above the blue line, and the W-edge composition in sulphur is below this line. Sulphur content at the edge is also indicated above. b) Atomic structure of the S-edge and W-edge for the conditions T=600°C and $p(H_2S)/p(H_2)$=15% .

V.1.f. Characterisation by Carbon monoxide adsorption at low temperature (77K), monitored by IR spectroscopy - IR(CO)

CO adsorption at low temperature, monitored by IR spectroscopy, is widely used to characterise the sulphide MoS_2 phase.[Bachelor *et al*, 1984; Peril, 1982; Müller *et al*., 1993; Travert *et al*., 2001; Travert *et al*., 2006] CO behaves as a probe molecule, highlighting acidity of both the support and the active phase. Usually, CO is first adsorbed on the sulphide phase, but due to the low amount of tungsten and the high dispersion of WS_2 slabs on the surface, numerous competitive adsorption sites on the support for carbon monoxide exist.

Figure 67-a shows the IR(CO) spectra, normalised by the amount of W in the samples, and not baseline corrected, of CSC, conventional dried and calcined catalysts, with *ca.* 1.7 W/nm², and a sulphidation temperature of 350°C (H_2S/H_2, 15 $\%_{mol.}$ H_2S). Note that only spectra collected at saturation of the sulphide phase with carbon monoxide are shown (see experimental part for more information).

Similarly, **Figure 67-b** shows the IR(CO) spectra, normalised by the amount of W in the samples, and not baseline corrected, of CSC catalysts with increasing W-loadings (from 0.5 to 1.7 W/nm²), where they are compared to the IR(CO) spectrum of the calcined sample, prepared with 0.5 W/nm². Note that these samples underwent sulphidation at 600°C (H_2S/H_2, 15 $\%_{mol.}$ H_2S) instead of 350°C. Sulphidation at this temperature was realised to get a well formed WS_2 phase, as sulphidation of samples with low W-loadings at 350°C (see part V.1.2) proved to give low relative amounts of WS_2.,Besides, it was the opportunity to analyse two samples previously studied by STEM-HAADF, *e.g.* the CSC catalyst with 0.8 W/nm² and the conventional calcined one with 0.5 W/nm², in order to observe if the IR(CO) signal was different for 2D morphologies that are respectively hexagonal-like or triangular-like. As for **Figure 67-a**, only spectra collected until saturation of the sulphide phase with carbon monoxide are shown.

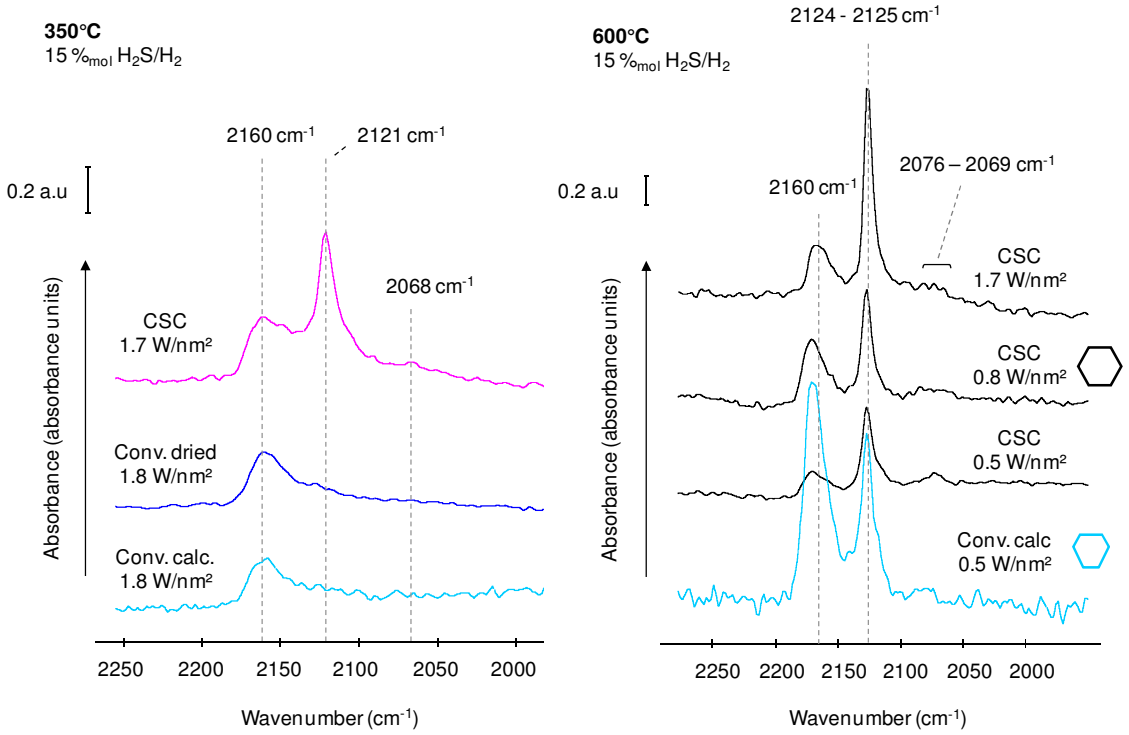

Figure 67: IR(CO) spectra (CO adsorption at 77 K) at saturation of the sulphide phase, resulting from introduction of small doses of CO. Spectra are not baseline corrected, and normalised by the amount of W in the samples. Left) CSC, conventional dried and calcined catalysts sulphided for 2 h (15 $\%_{mol.}$ H_2S/H_2) at 350°C. Tungsten loading: 1.7 W/nm². Right) CSC and conventional calcined catalysts, sulphided at 600°C, in the same sulphidation conditions. CSC catalysts were loaded with 1.7 W/nm², 0.8 W/nm² and 0.5 W/nm². Conventional calcined catalyst was loaded with 0.5 W/nm².

On **Figure 67-a**, CSC catalysts exhibit 3 bands at ν(CO) = 2068 cm^{-1}, ν(CO) = 2121 cm^{-1} and ν(CO) = 2160 cm^{-1}. The two first ones are assigned to CO adsorbed on WS_2 edge sites according to previous works.[Zuo *et al.*, 2004], while the last one is attributed to CO mainly adsorbed Brønsted acid sites of the catalysts. By analogy with IR(CO) data on MoS_2, the two bands attributed to CO adsorbed on WS_2 edge sites are assumed to be assigned to CO interacting with W-edge (2121 cm^{-1}) and S-edge (2068 cm^{-1}) sites respectively. [Travert *et al*, 2001; Travert *et al.*, 2006]. The ν(CO) vibration band at 2121 cm^{-1} exhibit very low intensity on the dried catalyst and is totally absent in the calcined one. Moreover, the ν(CO) vibration band at 2068 cm^{-1} is not visible on the two conventional catalysts.

We are currently investigating what could explain such differences between the catalysts. Several hypotheses can be formulated. Looking at the two major bands, tentatively attributed to CO interacting with W-edge sites and S-edge sites, we could propose that a specific 2D-morphology would be responsible for these signals. Besides, the FWHM of the band at ν = 2121 cm^{-1}, surprisingly very sharp, could highlight very well crystallised edges, on which CO could easily be adsorbed on one type of site, in only one fashion, linear or bent. Conventional catalysts, on which slabs would have more defects on their edges, would exhibit a larger distribution of adsorption sites, shown by a large signal in IR(CO), decreasing dramatically their intensity.

Data collected from integration of the IR(CO) spectra between *ca.* 2140 cm^{-1} and 2050 cm^{-1}, and normalised by the amount of sulphide phase WS_2, are reported in **Table 8**, as expressed in a.u/cm/mol(W)* where a.u stands for absorbance units and where mol(W)* stands for mole of tungsten engaged in the sulphide phase, in the sample.

Table 8: Data collected from IR(CO) analyses of CSC, conventional dried or calcined catalysts, sulphided at 350°C (2 h, 15 $\%_{mol.}$ H_2S/H_2) at 1.7 W/nm^2. a.u stands for absorbance units, and mol(W)* stands for "mole of W engaged in a WS_2 phase in the sample", calculated using $\%_{rel}$ WS_2 (XPS)

350°C 15 $\%_{mol.}$ H_2S/H_2	CSC	Dried	Calcined
a.u / cm / g(cat.) [a]	54	1	0
$\%_{rel}$ WS_2 (XPS)	85	75	50
a.u / cm / g(W)	500	9	0
a.u / cm / mol(W)*	3.2	0.1	0.0

a Calculated with the amount of CO adsorbed at saturation of the sulphide phase, and the mass of the pellet

We can see that the signal area, is much higher for the CSC catalyst compared to the conventional ones. This result means that on the CSC catalyst, interactions between CO and W atoms on the edges of the WS_2 slabs can be stronger, or that there can be more sites readily available for CO interaction.

On **Figure 67-b**, all samples including the conventional one, exhibit a rather narrow band at *ca.* 2124 cm^{-1}, tentatively assigned to CO adsorbed on W-edge sites following the same hypothesis as aforementioned. A rather broad one distinguishable between 2076 cm^{-1} and 2069 cm^{-1}, is tentatively attributed to CO adsorbed on the S-edge sites. However, considering the weak signal/noise ratio, it was difficult to refine the location of this latter vibration band. Besides, the broad band centred at ν(CO) between 2165 cm^{-1} and 2170 cm^{-1} is assigned to CO interacting with Brønsted acid sites.

Finally, for CSC catalysts, independently of the tungsten loading, the signal exhibit the same features, proving that when sulphidation is carried out at 600°C, CO interacts with the same types of sites, whatever the tungsten loading. In particular, the similar shape of the band resulting from CO interaction with W-edge site (≈ 2124 cm^{-1}) of WS_2 slabs could indicate that the sulphide phase of conventional and CSC catalysts are rather identical when sulphided at 600°C, from the point of view of a carbon monoxide molecule, while they are different when sulphided at 350°C. On top of that, as the IR(CO) spectrum of CSC (0.8 W/nm^2) strongly resembles to the one of conventional calcined (0.5 W/nm^2) sample, it means that whatever the 2D morphology (respectively hexagonal, and truncated triangular-like), the frequency of the vibration band of CO adsorbed on W-edge sites is barely changed.

Then, data collected from integration of the IR(CO) spectra between *ca.* 2140 cm^{-1} and 2050 cm^{-1}, and normalised by the amount of sulphide phase WS_2, are reported in **Table 9**, where a.u stands for absorbance units and where mol(W)* stands for mole of tungsten engaged in the sulphide phase, in the sample

Table 9: Data collected from IR(CO) analyses of CSC and conventional catalysts sulphided at 600°C, 2 h, H_2S/H_2 (15 $\%_{mol.}$ H_2S). a.u stands for absorbance units, and mol(W)* stands for "mole of W engaged in a WS_2 phase in the sample", calculated using $\%_{rel}$ WS_2 (XPS)

600°C 15 $\%_{mol.}$ H_2S/H_2	W/nm²			
	CSC			Conv. calc.
	0.5	0.8	1.7	0.5
a.u / cm / g(cat.) [a]	5	13	81	14
$\%_{rel}$ WS_2 (XPS)	78	83	87	81
a.u / cm / g(W)	152	250	750	424
a.u / cm / mol(W)*	1.1	1.6	4.7	2.8

[a] Calculated with the amount of CO adsorbed at saturation of the sulphide phase, and the mass of the pellet

The amount of CO interacting with the sulphide phase increases with the W-loading of CSC catalysts, from 1.0 to 5.0 a.u/cm/mol(W)*. This result means that for CSC samples, when increasing amount of W are deposited and sulphided (600°C), either interactions of CO on W edge sites are stronger, or more edge sites are readily available for CO interaction. Besides, the value found for the conventional catalyst prepared with 0.5 W/nm² is 2.5 times higher than that of its CSC counterpart, which is surprising. This observation could be linked, as aforementioned, to the presence of more edge sites or stronger interactions of CO with edges of WS_2 slabs for the conventional calcined sample.

V.1.g. Catalytic results and discussion

Tungsten-based catalysts being known for their high activity in aromatic hydrogenation [Stanislaus and Cooper, 1994; Hensen *et al.,* 2007], the catalytic performances of the catalysts were tested in hydrogenation of toluene. The feed was composed of toluene (reactant), cyclohexane (solvent), dimethyldisulphide (sulphiding agent) and aniline. This latter compound is used to inhibit the acidity of the support, and avoid isomerisation of the reactant by the acid sites of the support.

Figure 68-a, shows the intrinsic rate of hydrogenation (HYD), $\mathbf{r_i}$, expressed in mole of toluene converted per mole of tungsten per hour, denoted mol(tol)/mol(W)/h, where mol(W) stands for the amount tungsten (in mol) in the sample, calculated from elemental analyses. All these catalysts were sulphided at 350°C (15 $\%_{mol.}$ H_2S/H_2). First, CSC catalysts exhibit a higher intrinsic rate of HYD than conventional catalysts and calcined catalysts are the less active ones.

Second, the HYD rate of CSC catalyst has an optimum at *ca.* 1.7 W/nm². Note that increasing the tungsten loading decreases the HYD rate of conventional catalysts.

Nonetheless, expressing the HYD rate $\mathbf{r_i}$ relative to the amount of tungsten (mol(W)) might not reflect the real activity of the WS_2 slabs, as all W atoms are not sulphided. Therefore, we decided to calculate the rate with respect to W atoms engaged in a WS_2 phase, and to plot the intrinsic rate of HYD expressed by mole of toluene converted per mole of tungsten incorporated in a WS_2 phase per hour, denoted mol(tol)/mol(W)*/h, $\mathbf{r_i'}$, and shown in **Figure 68-b**. The term " mol(W)* " is calculated by multiplying the amount of tungsten in the sample (in mol) by the relative percentage of WS_2 (XPS), obtained for spent catalysts. Note that calculations with data collected from XPS analyses only take into account concentration of tungsten on the surface. However, we considered, in a first approximation, that this so-called HYD rate $\mathbf{r_i'}$ was representative of the catalysts at their steady state. Moreover, as it was not possible to analyse all the spent catalysts, we only performed XPS measurements on specific ones, mainly exhibiting low sulphidation level before test. We found that:

- conventional dried and calcined catalysts with 0.5 W/nm² exhibit 77 (±5) $\%_{rel.}$ WS_2

- the calcined sample prepared with 1.8 W/nm² reveals 78 (±5) $\%_{rel.}$ WS_2

- calcined and CSC spent catalysts with 3.7 W/nm² exhibit respectively 78 (±5) $\%_{rel.}$ WS_2 and 85 (±5) $\%_{rel.}$ WS_2.

Therefore, we can assume that CSC, dried and calcined spent catalysts display average levels of sulphidation of respectively 85 (±5) $\%_{rel.}$ WS_2, 77 (±5) $\%_{rel.}$ WS_2 and 78 (±5) $\%_{rel.}$ WS_2. Finally, **Figure 68-b** shows the intrinsic HYD rate calculated with the aforementioned levels of sulphidation. For the sake of clarity, filled symbols highlight spent catalysts which really underwent XPS analyses. Empty symbols represent hypothetical values based on fresh catalysts' ones.

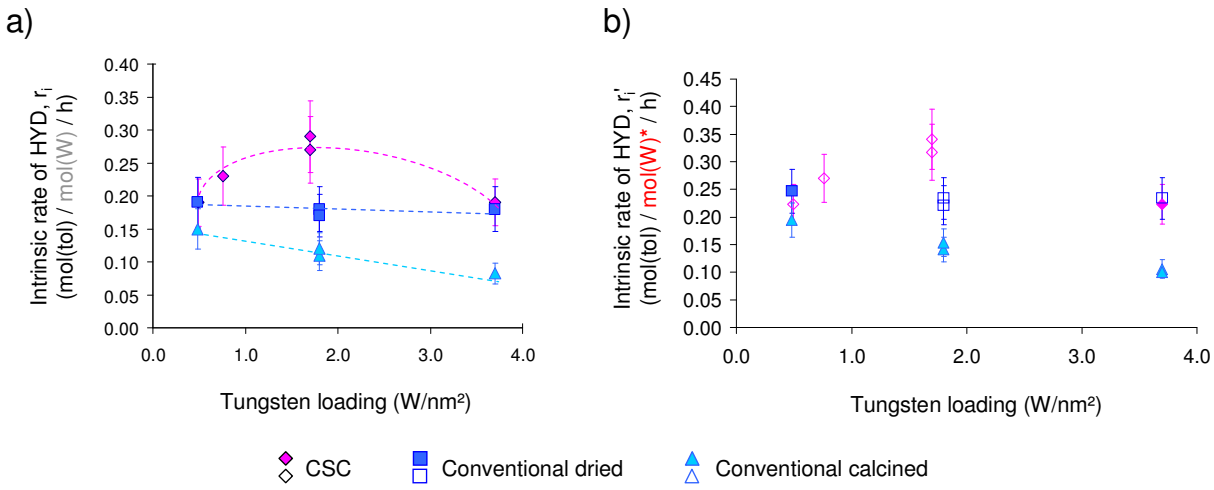

Figure 68: Intrinsic rate of HYD of CSC and conventional catalysts, sulphided at 350°C for 2h with 15 $\%_{mol.}$ H_2S/H_2). a) expressed in mol(tol)/mol(W)/h, where mol(W) is calculated from elemental analyses. b) expressed in mol(tol)/mol(W)*/h, where * stands for mole of W incorporated in a WS_2 phase, calculated using "mol(W)" and the $\%_{rel}$ $WS_2$of spent catalysts (XPS). In b), filled symbols correspond to spent catalysts which underwent XPS analyses. Empty ones correspond to catalysts which $\%_{rel.}$ WS_2 after test has been supposed.

In **Figure 68-b**, the HYD intrinsic rate of CSC and conventional catalysts is very similar to the previous one described in **Figure 68-a**. Indeed, the amount of sulphide phase is supposed not to change for most of the catalysts. On the whole, the main results is that the HYD intrinsic rate of the CSC catalyst is *ca.* 0.33 mol(tol)/mol(W)*/h, which is about 2.2 times higher than the one observed for the conventional calcined catalyst.

Then, we used the mean length and mean stacking number to refine our interpretation of the catalytic activity. For conventional catalysts, we have observed that increasing the tungsten loading led to an increase of the stacking and/or the length of the WS_2 slabs. This last phenomenon causes a decrease of the number of atoms on the edges of the slabs, by increasing the number of atoms belonging to the basal planes. As a consequence, the amount of active sites (which are supposed to be on the edges) decreases: this could be at the origin of the decrease of HYD rates. In the case of the CSC catalysts however, there is no direct explanation justifying the presence of an optimum. Therefore we decided to renormalize the activity by considering the geometrical model of WS_2 slabs initially proposed by Kasztelan *et al*. [Kasztelan *et al*, 1984] This will in particular help us to calculate the number of atoms on the edges.

For a given slab length, the 2D morphology of a crystallite is defined by two parameters, n_M and n_S, standing respectively for the number of M-edge and S-edge atoms, as illustrated in **Figure 69.**

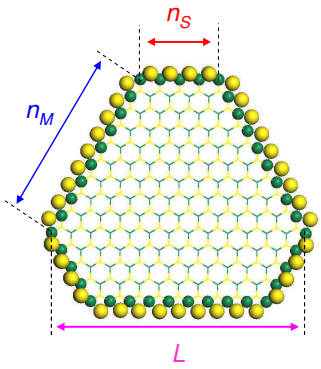

Figure 69: 2D morphology of a WS_2 crystallites defined by the number of W atoms on W-edge (nM) and S-edge (nS). Green balls: tungsten. Yellow balls: sulphur.

As revealed in part V.1.e), conventional catalysts exhibit truncated triangular shaped slabs, with an M-edge proportion of between 60 and 65 atomic% under sulphidation conditions of 600°C with 15 $\%_{mol.}$ H_2S/H_2. Il leads to the following equation:

$$0.60 \leq \frac{n_M}{n_M + n_S} \leq 0.65 \qquad \textbf{Eq. 5}$$

CSC catalysts exhibit rather hexagonal slabs, which means $n_M \approx n_S$.

Moreover, taking into account the mean slab length L, obtained from TEM experiments, we can write the following equation:

$$d(W-W)\times(n_M + n_S) = L \qquad \textbf{Eq. 6}$$

in which d(W – W) ≈ 0.32 nm according to the WS_2 structure.

Moreover, we decided to use the following hypotheses:

(1) M-edge and S-edge sites are HYD active. Indeed, Gandubert *et al* [Gandubert *et al.*, 2008] assign the hydrogenating activity (toluene hydrogenation) of their $CoMoS/Al_2O_3$ catalysts to active sites located on M-edge of crystallites. M-edge sites' HYD activity was also proposed by Moses *et al.*, from their DFT calculations on thiophene hydrogenation by MoS_2 as part of the thiophene HDS reaction. [Moses *et al.*, 2007]. However, involvement of S-edge sites cannot be fully ruled out. Therefore, we also decided to include them as HYD active sites.

(2) corners are also considered as HYD active (their reactivity being not well understood)

(3) every WS_2 slab, on the catalyst surface, can be described by only one geometrical model

(4) in a first approximation, hexagonal model were chosen for CSC catalyst, and truncated triangle model for conventional catalysts, independently of the W loadings. However, note that we do not know the 2D morphology of WS_2 slabs present on spent catalysts, after test. This morphology could be either more triangular or more hexagonal, and could thus influence the results of our activity normalisation.

Then we used the geometrical model, as it was done previously by Gandubert *et al*, [Gandubert, PhD thesis, Lille, 2006] to calculate the number of edge sites (W-edge and S-edge atoms as well as corners sites), relative to the total number of atoms in one slabs. We considered that this amount of edge sites was responsible for the observed HYD rate. **Table 10** summarizes some of the compromises found for the geometrical parameters of each catalyst, depending on the tungsten loading. Best comprises are denoted in bold.

Table 10: Experimental data and Geometrical parameters used for WS_2 slab models of catalysts prepared at 350°C, for 2h with 15 %mol. H_2S/H_2. Bold numbers represent the best comprises found for the catalysts, and used to normalise the intrinsic activity

	W/nm²	Length L from TEM (Å)	Length L' from the model (Å)	n_M	n_S	Number of W in one slab	% W edge [a]	% edge sites [b]	TOF mol(tol)/mol(site)/h
CSC	3.7	38	**38**	**6**	**6**	127	50	28.3	0.79
	1.7	38	**38**	**6**	**6**	127	50	28.3	1.12
	0.8	34	**38**	**6**	**6**	127	50	28.3	0.96
	0.5	40	**38**	**6**	**6**	127	50	28.3	0.79
Conv. dried	3.7	39	**38**	**7**	**5**	127	60	28.5	0.82
	1.8	37	**38**	**7**	**5**	127	60	28.5	0.77
	0.5	38	**38**	**7**	**5**	127	60	28.5	0.87
Conv. calcined	3.7	36	35	7	4	107	67	31.0	0.34
	3.7	36	**38**	**7**	**5**	127	60	28.5	0.35
	1.8	40	**38**	**7**	**5**	127	60	28.5	0.54
	0.5	29	28	5	4	73	56	36.4	0.54
	0.5	29	28	6	3	71	71	37.4	0.52
	0.5	29	**32**	**6**	**4**	92	63	33.0	0.59

[a] Calculated from the number of W atoms on W-edge, relative to the total number of W atoms on edges (W-edge + S-edge)
[b] Calculated from the number of W atoms on W-edge, S-edge and corners, relative to the total number of W atoms in one slab.

Looking at **Table 10** for CSC materials with 1.7 W/nm², for a mean length L ≈ 3.8 nm, the corresponding 2D hexagonal model exhibit $n_M = n_S = 6$, with 50 %W-edge and *ca.* 127 (±1) W per WS_2 slabs. The so-called active sites (or edge sites), *e.g.* W located on corners, W-edge and S-edge, represent *ca.* 28.3 % of the total number of W atom in one CSC slab . For the calcined catalyst with 1.8 W/nm² and a mean length L ≈ 4.0 nm, equations **Eq. 3** and **Eq. 4** gave $\{n_M = 7, n_S = 5\}$, which leads to about 28.5 % of tungsten atoms on edges and corners of the aforementioned calcined catalyst. As a consequence, CSC and conventional calcined catalysts exhibit WS_2 slabs with close amounts of tungsten sites on corners and edges.

Figure 70 shows the intrinsic rate of HYD, expressed in mol(tol)/mol(site)/h, where site stands for "edge sites" (active sites) relative to the total number of atoms in one slab. In other words, this can be considered as a Turnover Frequency (TOF), where the time unit is one hour.

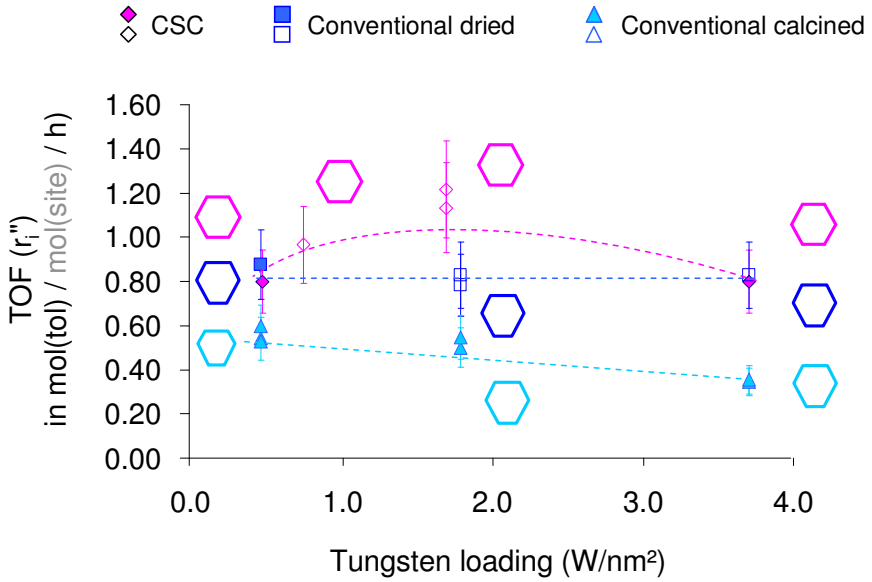

Figure 70: Intrinsic rate of HYD expressed as a TOF, in mol(tol)/mol(site)/h for catalysts sulphided at 350°C, for 2 h, with 15 $\%_{mol.}$ H_2S/H_2. Site stands for active sites, calculated as the number of edge sites (W-edge and S-edge sites and corners) relative to the total number of atoms in one slab.

Conventional dried catalysts exhibit a *quasi* constant TOF at *ca.* 0.82 (±0.13) mol(tol)/mol(site)/h, whatever the tungsten loading. For the calcined samples, the TOF decreases from *ca.* 0.55 (±0.09) to 0.35 (±0.06) mol(tol)/mol(site)/h when the W loading increases, as seen before on **Figure 68-b**. At low as at high W content, TOF of CSC and dried catalysts are similar but in particular, TOF of CSC materials reaches a maximum at *ca.* 1.16 ± 0.19 mol(tol)/mol(site)/h for a W-loading of 1.7 W/nm². This means that the nature of active sites on CSC samples are different for this loading, as it was highlighted by IR(CO) analyses for samples prepared at 350°C.

We performed similar catalytic tests on CSC and conventional calcined samples sulphided at 600°C before test, and exhibiting between 0.5 W/nm² and 1.7-1.8 W/nm². It was the opportunity to study if any difference of activity was observed for the samples on which hexagonal (CSC) or truncated-triangular (conventional) slabs were directly observed by STEM-HAADF before test. Intrinsic HYD rate $\mathbf{r_i}$ expressed in mol(tol)/mol(W)/h is shown in **Figure 71-a**. CSC catalysts prepared at 600°C (15 $\%_{mol.}$ H_2S/H_2) exhibit a HYD rate at least 1.6 times higher than the conventional calcined samples, whatever the W-loading. Moreover,

increasing the W-loading causes a slight decrease of the observed intrinsic HYD rate, for all samples.

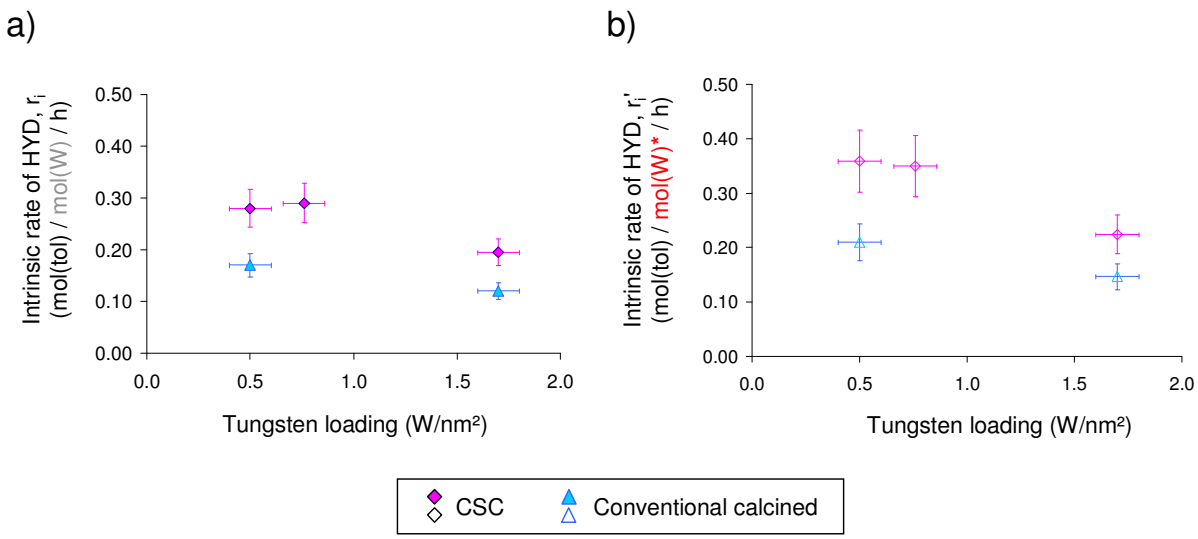

Figure 71: Intrinsic rate of HYD of CSC and conventional calcined catalysts, sulphided at 600°C for 2h with 15 $\%_{mol.}$ H_2S/H_2: a) expressed in mol(tol)/mol(W)/h, where mol(W) is calculated from elemental analyses. b) expressed in mol(tol)/mol(W)*/h, where * stands for mole of W incorporated in a WS_2 phase, calculated using "mol(W)" and the $\%_{rel}$ WS_2 of spent catalysts (XPS). In b), empty symbols correspond to catalysts which $\%_{rel.}$ WS_2 after test has been supposed.

Afterwards, we normalised the intrinsic HYD rate by mole of tungsten sulphided, as previously done for catalysts prepared at 350°C. To do so, XPS analyses were performed prior to catalytic tests, and revealed that the level of sulphidation was lying between 78 and 87 (±5) $\%_{rel.}$ WS_2 for CSC samples while it was ranging from 81 to 82 (±5) $\%_{rel.}$ WS_2 for calcined ones, depending on the W-loading. Spent catalysts did not underwent XPS analyses, but as the amount of WS_2 was rather high for each catalyst before the catalytic test, we supposed that the aforementioned $\%_{rel.}$ WS_2 values could be used to normalise the intrinsic HYD rates, in a first approximation. Results are depicted in **Figure 71-b**. Intrinsic HYD rates follow the same evolution as before normalisation by the amount of WS_2, which is not surprising considering the similar $\%_{rel.}$ WS_2 observed, and finally does not give more information than **Figure 71-a**.

Then, we used the 2D geometrical model to calculate the TOF of these catalysts sulphided at 600°C. The parameters of the 2D models are available in **Table 11.**

Table 11: Experimental data and Geometrical parameters used for WS_2 slab models of catalysts prepared at 600°C, for 2 h with 15 $\%_{mol.}$ H_2S/H_2.

	W/nm²	Length L from TEM (Å)	Length L' from the model (Å)	n_M	n_S	Number of W in one slab	% W edge [a]	% edge sites [b]	TOF mol(tol)/mol(site)/h
CSC	0.5	34	32	6	6	93	50	32.6	0.99
	0.8	34	32	6	6	93	50	32.6	0.97
	0.8	34	38	6	6	127	50	28.3	1.24
	1.7	51	51	6	6	221	50	22.0	1.00
Conv. calc.	0.5	40	38	7	5	127	60	28.5	0.74
	1.8	39	38	7	5	127	60	28.5	0.53

[a] Calculated from the number of W atoms on W-edge, relative to the total number of W atoms on edges (W-edge + S-edge)
[b] Calculated from the number of W atoms on W-edge, S-edge and corners, relative to the total number of W atoms in one slab.

First, there is a significant difference of slab length L between CSC and conventional calcined catalysts. For the CSC catalyst, while the mean value is similar for 0.5 W/nm² and 0.8 W/nm² with *ca.* 3,4 nm (34 Å), it strongly increases to 5.1 nm², highlighting a strong sintering effect. The low values are probably due to grafted surface species which exhibit low mobility upon formation of WS_2 slabs during sulphidation. The highest one found for the 1.7 W/nm² loading probably comes for aggregation of more W centres during sulphidation, due to more mobile species belonging to the layers loosely bonded onto the grafted one. For the calcined sample, the mean slab length is similar with *ca.* 3.9 nm. It is tentatively assigned to the strong interaction of the amorphous WO_3 phase with the surface, which leads to a reduced mobility of W species upon sulphidation.

Second, this difference of slabs length leads to different amount of edge sites on slabs' edges. For CSC catalysts, when increasing the slab length, the relative percentage of edge site decreases, from 32.6 % to 22 % of the number of W atoms in one slab. .For the calcined material, about 28.5 % of edge sites is calculated. These values were used to calculate the TOF.

The TOF, expressed in mol(tol)/mol(site)/h, is shown in **Figure 72**.

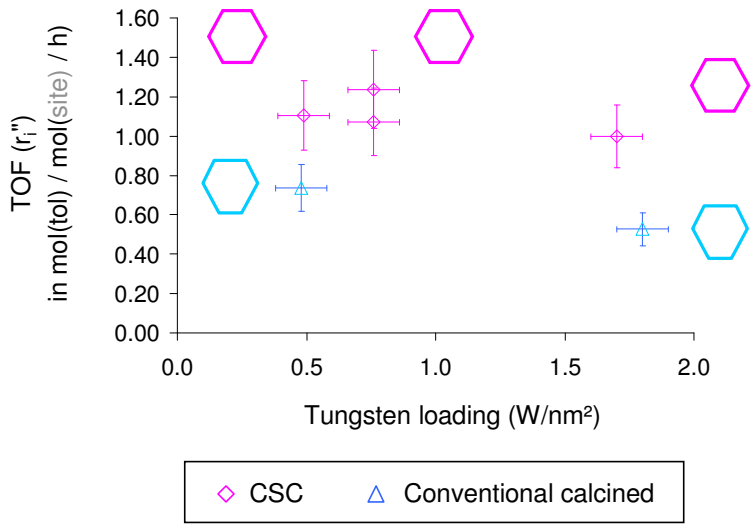

Figure 72: Intrinsic rate of HYD expressed as a TOF, in mol(tol)/mol(site)/h for catalysts sulphided at 600°C for 2 h, 15 $\%_{mol.}$ H_2S/H_2. Site stands for active sites, calculated as the number of edge sites (W-edge and S-edge sites and corners) relative to the total number of atoms in one slab.

The TOF of CSC and conventional calcined catalysts slightly decreases, and no more maximum is observed for the CSC sample with a W-loading 1.7 W/nm², compared to its CSC counterpart sulphided at 350°C. Then, the TOF of conventional catalysts is lower than the one of CSC samples, as previously seen when these materials were sulphided at 350°C.

We tried to refine our interpretation of catalytic results using results obtained by IR(CO) analyses. What is surprising is that quantification results, reported in **Table 8** and **Table 9**, show different amounts of CO interacting with tungsten edge sites, which cannot be directly correlated to the TOF. For catalysts with 0.5 W/nm², sulphided at 600°C, the conventional calcined sample shows 2.9 times more CO interacting with sulphided tungsten edge atoms than its CSC counterpart, while its TOF is *ca.* 1.6 times lower (normalisation of values found in **Table 9** by the corresponding %edge sites of **Table 11**). Similarly, IR(CO) analyses on catalysts with 1.7 W/nm², and sulphided at 350°C (see **Table 8**) reveal that much more CO interacts with edge sites on the CSC sample than on conventional ones. Even if the CSC sample shows a higher TOF, it does not reflect the differences observed in IR(CO) between the dried and the calcined catalysts.

V.1.h. Conclusion on the influence of the tungsten loading on the genesis and activity of the active phase of WS_2/ASA catalysts

To conclude, we prepared well-characterised WS_2-supported ASA catalysts, especially by varying the amount of W deposited. We managed to understand their HYD activity at the molecular level thanks to their sulphidation level obtained by XPS, and with the characteristics of their WS_2 slabs revealed by TEM, geometrical models and IR(CO) analyses. The results of our investigations can be summarized as follows:

(1) The CSC method allows the preparation of well-sulphided catalysts, exhibiting level of sulphidation ranging from 76 to 85 (± 5) $\%_{rel.}$ WS_2 as from 0.5 W/nm² to 3.7 W/nm². These catalysts exhibit higher or similar level of sulphidation than their conventional counterparts. The differences of sulphidation level are partially explained by the reducibility of their oxide surface species, as shown by TPR experiments.

(2) When sulphided at 350°C (15 $\%_{mol.}$ H_2S/H_2), the intrinsic rate of hydrogenation in toluene hydrogenation in presence of aniline is higher for CSC catalysts than for conventional ones, especially compared to their calcined counterparts. The same observation is made when CSC and calcined materials are sulphided at 600°C.

(3) With the help of STEM-HAADF analyses, TEM data, and 2D geometrical model of WS_2 slabs, refinement of catalytic activities allowed the expression of the TOF of our catalysts. The TOF of CSC materials is found to be higher than the conventional ones'.

(4) Geometrical models were based on the average 2D geometry of WS_2 slabs as observed from STEM HAADF analyses and DFT calculations. In this regard, we report for the first time the average 2D-morphology of WS_2 slabs of catalysts supported on industrial support (amorphous silica-alumina or silica): catalysts prepared using conventional precursors exhibits rather truncated triangular slabs. The origin of the formation of more hexagonal like ones *via* the CSC preparation method has not been ruled out yet.

(5) IR(CO) analyses performed on catalysts sulphided at 350°C or 600°C reveal that CO interacts with edge site of WS_2 slabs in a different fashion for CSC and for conventional catalysts. Noteworthy is the observation of a narrow vibration band at $\nu(CO) \approx 2124$ cm^{-1} , assumed to be assigned to CO adsorbed on W-edge atoms. This narrow band, which is not visible on conventional samples sulphided at 350°C, seems to be observed only for catalysts with high level of sulphidation. We were not able to find a

simple link between the quantity of CO interacting with the WS_2 phase of our catalysts and their TOF.

As a consequence, we propose that the higher TOF of CSC catalyst can be attributed to two possible effects. On the one hand, it develops specific nature of edge active sites or specific distribution of edge active sites during catalytic tests. This effect cannot be revealed by IR(CO) but is revealed by STEM highlighting the specific hexagonal morphology before test. This result may imply that the distribution of S-edge/W-edge might also be different within each crystallite during test, thus leading to different TOF. With that respect, this would also mean that S-edge could play a role during toluene hydrogenation. On the other hand, we cannot rule out that different support effects may influence the reactivity itself: this support effect could be inherited from the CSC preparation method itself.

In order to further understand the formation and the reactivity of tungsten sulphide phases, we decided to investigate the influence of the sulphidation temperature, which has been tackled at the end of this part V.1.

V.2. Influence of the sulphidation temperature on CSC and conventional catalysts

In part V.1, we showed that the highest HYD rate was obtained for the CSC catalyst, prepared around 1.7 W/nm². Therefore, we decided to focus on CSC and conventional catalysts prepared at *ca.* 1.7-1.8 W/nm² (*e.g.* ranging from 11 to 13 $\%_{wt.}$ W), and investigate how the sulphidation temperature influences their properties and their catalytic activity in toluene hydrogenation. Part V.2 is thus dedicated to the characterisation of sulphide phases by either XPS, TEM, STEM-HAADF and/or IR(CO) analyses for various sulphidation temperatures ranging from -25°C to 600°C. We will present the intrinsic rate of hydrogenation of our catalysts, and refine catalytic results through the calculation of Turn-Over Frequencies thanks to geometrical models of WS_2 slabs. Parallel with these refinements, influence of peculiar active sites/species (such as CUS or sulfhydryl species M–SH) on observed TOFs will be discussed.

V.2.a. Characterisation by X-ray photoelectron spectroscopy (XPS)

The sulphidation level of CSC and conventional catalysts was studied by decomposition of their W 4f spectrum. Examples of W 4f photopeaks of bulk WS_2, as well as CSC, dried and calcined catalysts (sulphided at 23°C, 2 h, 15% H_2S/H_2) are illustrated in **Figure 73**. Then, the level of sulphidation of CSC, conventional dried and calcined catalysts is reported in **Figure 74**, as the $\%_{rel}$ WS_2 depending on the sulphidation temperature, between -25°C and 600°C (for corresponding W 4f photopeaks, see in appendices).

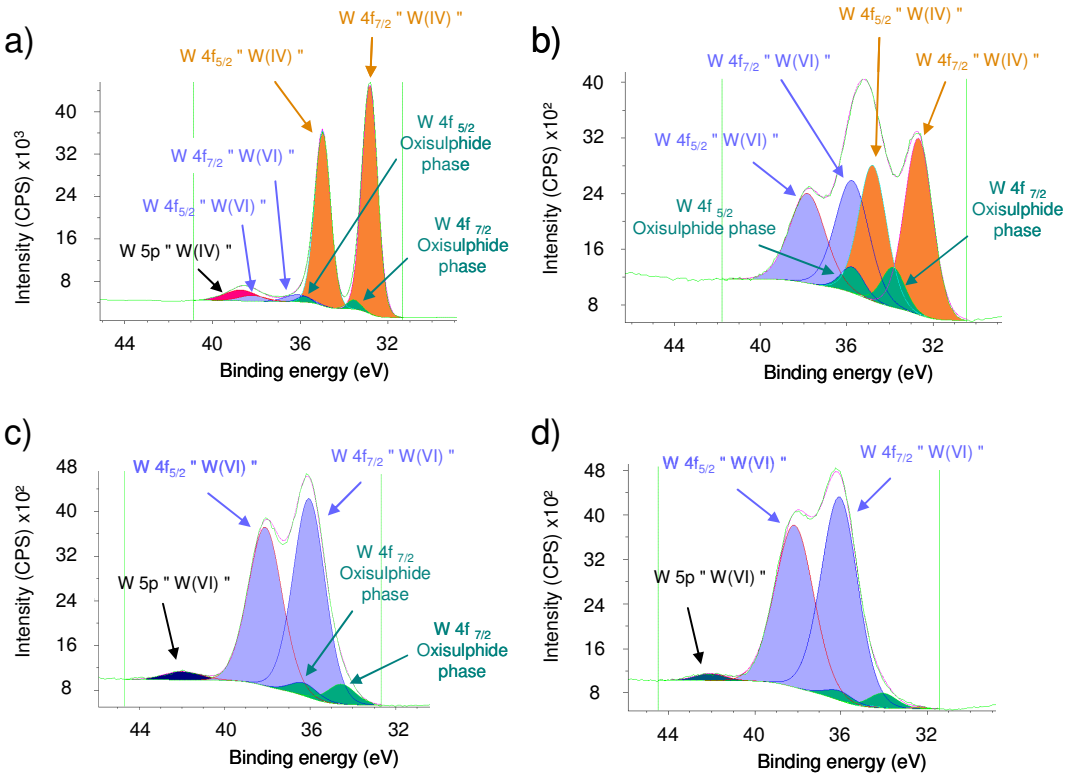

Figure 73: XPS spectra. W 4f photopeak of a) bulk WS_2 coming from sulphidation of $[W(OEt)_5]_2$, b) CSC, c) dried and d) calcined WS_2/ASA catalyst sulphided at 23°C, 2h, 15 $\%_{mol.}$ H_2S/H_2

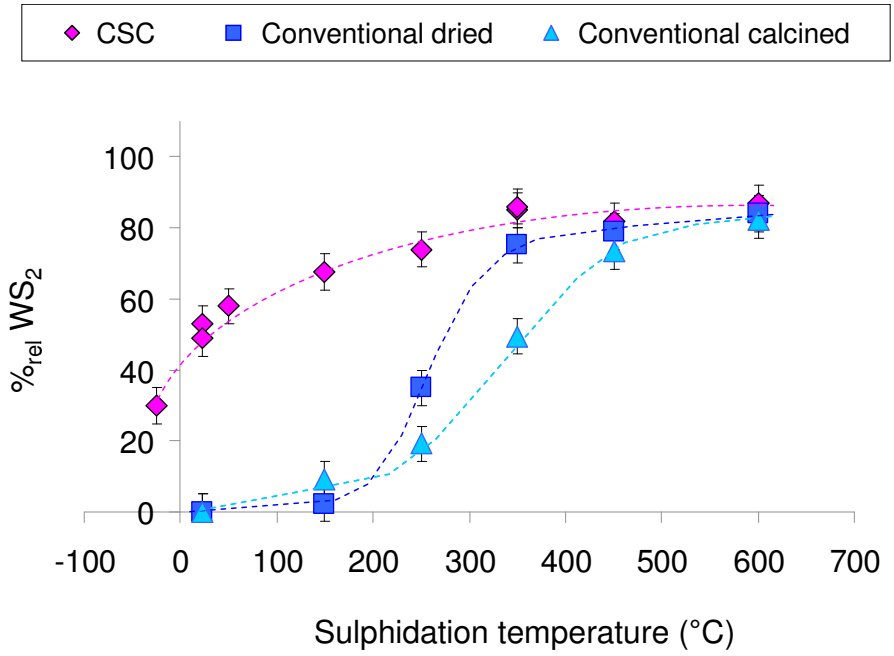

Figure 74: XPS data. Level of sulphidation of CSC and conventional (dried or calcined) catalysts sulphided at different temperatures between 23°C and 600°C (2h, 15 $\%_{mol.}$ H_2S/H_2)

When sulphided at 350°C (2 h, H_2S/H_2 with 15 $\%_{mol.}$ H_2S), which is the conventional temperature used for sulphidation or catalytic tests, the conventional dried catalyst and the CSC catalyst have rather the same level of sulphidation at *ca.* 80 $\%_{rel}$ WS_2, while the calcined one exhibits lower amount of sulphide phase: around 50 $\%_{rel}$ WS_2. For higher sulphidation temperatures, the level of sulphidation of CSC and dried catalysts does not evolve and stays at *ca.* 82 ± 5 $\%_{rel}$ WS_2, while calcined catalyst's one slowly reaches the same plateau, at 600°C. For W-based conventional catalysts, finding a higher level of sulphidation for dried samples compared to calcined ones has previously been reported in the literature by Reinhoudt *et al*. Indeed, they revealed that for NiW/Al_2O_3 catalysts sulphided at 340°C (*ca.* 1 h, H_2S/H_2, ≈ 11 $\%_{mol.}$ H_2S), the amount of sulphide phase was two times lower on calcined materials. [Reinhoudt *et al*. 1998]

More interesting are the results obtained for sulphidation at temperatures lower than 350°C. The curve representing the sulphidation level of conventional NiW catalysts corresponds to the well-known S-shaped curve, as already reported by Breysse *et al*. for conventional NiW/Al_2O_3 catalysts calcined at 500°C [Breysse *et al*., 1988]. In their study, the authors found that the level of sulphidation exhibit an inflexion point located around 300°C, which is close to the inflexion

point (see **Figure 74**) found for our calcined sample at about 350°C. Besides, in order to investigate the support effect between ASA and alumina, we compared the level of sulphidation of our conventional dried sample with another dried one, prepared on γ-Al_2O_3 (1.8 W/nm² also). The latter shows a level of sulphidation of *ca.* 10 $\%_{rel.}$ WS_2 when sulphided at in similar conditions (350°C, 2 h, 15 $\%_{mol.}$ H_2S/H_2) which is more than 7 times lower than the dried catalyst prepared on ASA. The higher level of sulphidation observed on the dried material supported on ASA can be explained by the easier sulphidation of samples prepared on the ASA support developing weaker "support - oxide phase" interactions than alumina.

Moreover, with the use of $[W(OEt)_5]_2$ as W precursor, the S-shaped curve representing the level of sulphidation of CSC catalysts is strongly shifted to lower temperatures, with an inflexion point located at around -25°C. Indeed, we could surprisingly sulphide our CSC materials at room temperature, where about 50 $\%_{rel}$ WS_2 is reached. We were also able to synthesise a WS_2 phase at -25°C, which is as far as we know the first time that W-based catalysts are reported to exhibit tungsten sulphide below 0°C. In the case of conventional catalysts, the first entities of WS_2 appear at *ca.* 150°C but sulphidation begins earlier, with the apparition of a partially sulphided phase (intermediate phase) denoted WO_xS_y. CSC catalysts, however, exhibit sulphidation level far above the ones ever observed for conventional catalysts at this temperature.

In a symmetric way, **Figure 75-a** shows that for CSC catalysts, the amount of non-sulphided W(VI) phase is lower than for conventional ones, as from sulphidation at -25°C. Then the amount of the oxide phase slowly decreases until 150°C. At this temperature, the W(VI) phase of conventional catalysts begins to decrease, more rapidly for dried catalysts than for their calcined counterparts. Finally, *quasi* complete conversion of the oxide phase is achieved after sulphidation at 600°C, with 9 ± 2 $\%_{rel}$ W(VI) remaining.

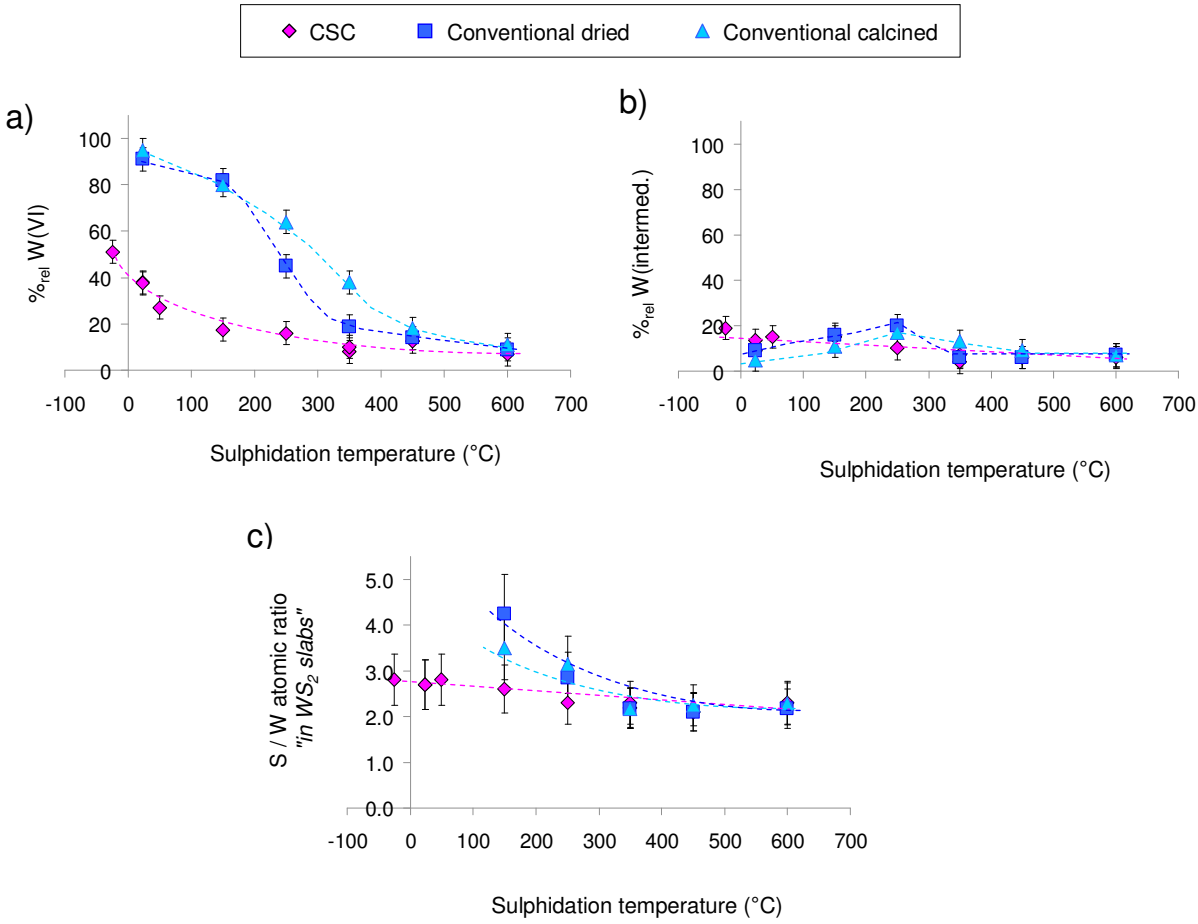

Figure 75: XPS data of CSC and conventional (dried or calcined) catalysts sulphided at different temperatures between 23°C and 600°C (2h, 15 $\%_{mol.}$ H_2S/H_2) a) Relative percentage of non-sulphided W(VI) phase. b) Relative percentage of partially sulphided W(intermed.) phase. c) S/W atomic ratio *"in WS_2 slabs"* calculated from peak area of W(IV) on W 4f spectra and S(-II) on S 2p spectra.

Figure 75-b represents the evolution of the "intermediate phase", coming from the partial sulphidation of the oxide phase. Note that the mechanism of sulphidation is still a matter of debate in the literature, especially the transition from oxide phases to MS_2 (M= W, Mo) *via* oxysulphide species MO_xS_y [Hensen *et al.*, 2007; Payen *et al.*, 1988; van Der Vlies *et al.*, 2002a; Rochet, PhD thesis, Paris, 2011], or *via* MS_3 [Hensen *et al.*, 2007; Payen *et al.*, 1988; Rochet, PhD thesis, Paris, 2011; Sun *et al.*, 2001]. In particular, Rochet, in her study on the sulphidation of calcined Mo/Al_2O_3 materials, revealed that from K-edge Mo-EXAFS spectrum, the intermediate phase formed through sulphidation is better represented by a $\{MoOS_2\}$ model compared to a $\{MoS_3\}$ one. However, this $\{MoOS_2\}$ model, previously proposed by Genuit *et al.*

from EXAFS data [Genuit *et al.*, 2005], contains Mo in a +VI oxidation state, while from her K-edge Mo-XANES spectrum, Rochet finds that Mo is closer to a +IV oxidation state. Moreover, as an unambiguous characterisation of (oxy)sulphide species MoO_xS_y, especially by XPS, has not been achieved so far, every interpretation of experimental data as to be taken with great caution. Back to our study, **Figure 75-b** has allowed to pinpoint that for conventional catalysts, there is a maximal amount of this intermediate phase between 250°C and 300°C, which matches the inflexion point of S-shaped $\%_{rel}$ WS_2 curves. This result is also in line with XPS data of $CoMo/Al_2O_3$ catalysts reported by Gandubert [2006]. Gandubert showed that for sulphide catalysts (H_2S/H_2, 15 $\%_{mol.}$ H_2S) based on dried materials, the inflexion point of the sulphidation level of Mo was around 50°C, a temperature for which the amount of oxysulphide phase was maximal with *ca.* 18 (±5) $\%_{rel.}$ MoO_xS_y. Similarly, she found an inflexion point close to 200°C for calcined samples, concomitant with *ca.* 19 (±5) $\%_{rel.}$ MoO_xS_y. Besides, QEXAFS data reported by A. Rochet [2011] for MoS_2/Al_2O_3 (calcined) catalysts shows that the maximal amount of intermediate phase is reached around 275°C, a temperature which is found to be starting point of MoS_2 apparition, revealing that Mo oxide species needs to be (quasi) fully transformed in $\{MoOS_2\}$ before being changed into MoS_2.

With this in mind, our results are consistent with the literature [Rochet, PhD thesis, Paris, 2011; Gandubert, PhD thesis, Lille, 2006; van Der Vlies, PhD thesis, Zürich, 2002] describing a sulphidation mechanism which proceeds *via* different steps, which are:

- the reduction of tungsten from a +VI to a +V oxidation state, concomitant with the formation of an intermediate phase where sulphur is slowly incorporated in the oxide phase

- the transformation of this partially sulphided oxysulphide phases into WS_2.

Note however that due to their high reactivity, oxide species obtained with the CSC method undergo-sulphidation at lower temperatures than conventional species.

Figure 75-c exhibits the S/W atomic ratio in WS_2 slabs, calculated, in a first approximation, by dividing the relative amount of S(-II) by W(IV) species, respectively obtained from S 2p and W 4f photopeaks decompositions. When the sulphidation temperature increases, this ratio decreases from *ca.* 4.0 to 2.2 for conventional catalysts, and from 2.7 to 2.2 for CSC catalysts. Furthermore, they all exhibit a ratio close to 2.2 when the sulphidation temperature reaches 350°C. These results indicate that for temperatures lower than 350°C, the sulphide phase is not composed of WS_2 slabs with a 1:2 stoichiometry. Different hypotheses could explain such a stoichiometry. First, the 2D morphology of WS_2 slabs, for a given cluster size (*e.g.* number of M-

edge atoms), influences the S/W atomic ratio and can lead to excess or lack of sulphur atoms. For example, Schweiger *et al.* [2002] have shown that for triangular shaped MoS_2 slabs exhibiting 10 Mo atoms on edges, the S/Mo atomic ratio on 100 %S Mo-edge was 2.73, an increases to 3.60 for slabs with 4 Mo-edge atoms. Second, we could expect a decrease of the sulphur coverage on slabs' edges when increasing the temperature. Last but not least, WS_2 slabs genesis could be achieved through the formation of tungsten species supersaturated with sulphur, such as WS_3, as discussed just above. Then, to get further insights into the understanding of the sulphidation of our catalysts, we tried to investigate the decomposition of S 2p spectra of CSC catalysts, but we were not able to find significant results.

Finally, the overall coverages of tungsten on the support's surface are evaluated by XPS. The W/Al and W/Si atomic ratios shown in **Figure 76**, highlight that there is no significant difference between the catalysts, whatever the sulphidation temperature.

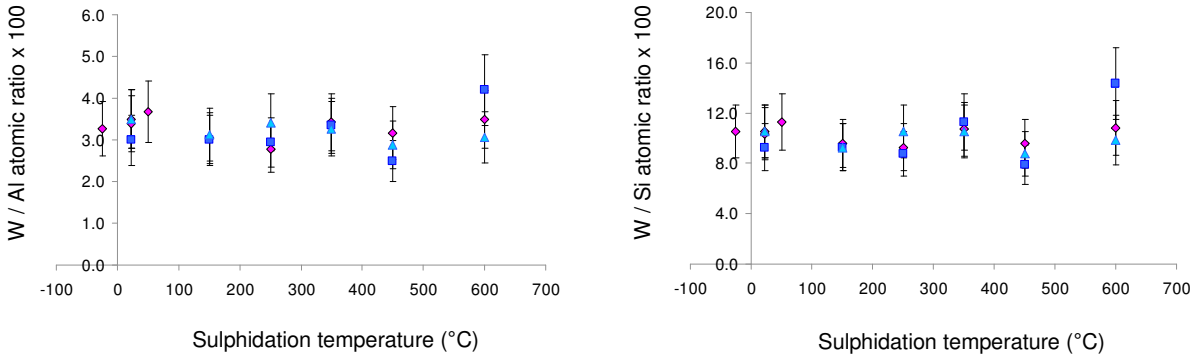

Figure 76: W/Al and W/Si atomic ratios (x100), collected from XPS analyses

V.2.b. Characterisation by Transmission electron microscopy (TEM Bright field mode)

Transmission Electron Microscopy (TEM) in Bright Field mode was performed to determine the mean length, L, and mean stacking number, N, of WS_2 slab, depending on the sulphidation temperature. TEM micrographs of CSC catalysts sulphided at -25°C, 23°C, 350°C and 600°C with a H_2S/H_2 mixture (15 $\%_{mol.}$ H_2S) are shown in **Figure 77**.

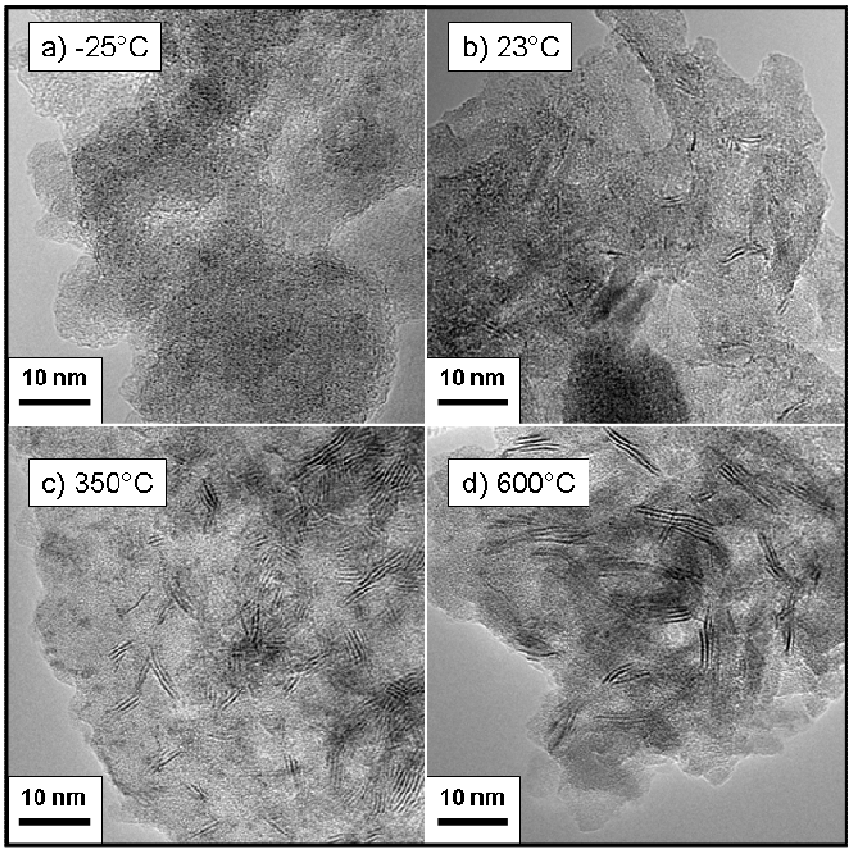

Figure 77: TEM micrographs of CSC catalysts sulphided at a) -25°C, b) 23°C, c) 350°C and d) 600°C. H_2S/H_2 mixture (15 $\%_{mol.}$ H_2S)

These TEM micrographs obviously reveal the growth of WS_2 layers as a function of sulphidation temperature. On TEM micrographs, no WS_2 slabs are observed on the catalyst prepared at -25°C while nanosized spot-like entities (1 nm to 2 nm) are visible. Note that the formation of nanosized particles was reported in the literature for NiW, NiMo and CoMo samples supported on alumina or sili*ca.* They were assigned to non-crystalline W or Mo (oxy)sulphide entities, barely visible in samples sulphided at higher temperatures like 600°C. [Reinhoudt *et al.*, 1998; Kooyman *et al.*, 2001; Okamoto *et al.*, 2009]

Then, mean slabs length and mean stacking number obtained from picture analysis are summarized in **Table 12**, and illustrated by **Figure 78.** Bar graphs are available in appendices.

Table 12: TEM data. Mean length distribution and mean stacking layer distribution of WS_2 crystallites on WS_2/ASA catalysts when increasing the sulphidation temperature. Tungsten loading: *ca.* 1.7 – 1.8 W/nm².

	Sulphidation temperature (°C)	Mean Length L (nm)	Sdt. dev.	Mean stacking number N	Sdt. dev.
CSC	-25	No visible slabs	-	No visible slabs	-
	23	3.2	1.1	2.6	1.2
	150	3.2	1.3	2.4	1.1
	350	3.8	1.3	3.1	1.2
	450	4.2	1.6	3.1	1.4
	600	5.1	2.3	3.5	1.8
Conv. dried	23	No visible slabs	-	No visible slabs	-
	350.0	3.7	1.2	3.0	1.4
	450.0	4.3	1.4	3.3	1.6
	600.0	4.4	1.6	3.6	1.8
Conv. calcined	23	No visible slabs	-	No visible slabs	-
	350	4.0	1.4	2.7	1.3
	450	3.9	1.2	2.9	1.3
	600	4.0	1.2	2.7	1.8

For CSC catalysts and conventional dried catalysts, the mean length of the WS_2 crystallites increases when the sulphidation temperature increases. As shown in **Table 12** and in **Figure 4** between 350°C and 600°C, it respectively varies from *ca.* 3.8 nm to 5.1 nm for the CSC catalyst, and from 3.7 nm to 4.4 nm for its conventional counterpart. In the case of the calcined catalysts, there are no significant changes: L ≈ 4.0 nm. For the stacking number, CSC and conventional dried catalysts exhibit the same behaviour, with a mean stacking between 3.1 and 3.6. As before, the calcined catalyst does not appear to be sensitive to the sintering effect, as N is constant at ca 2.7. This weaker sintering effect observed for the latter sample (calcined) could arise from stronger interactions between oxide surface species and the ASA support, decreasing the mobility of tungsten atoms and thus preventing nucleation of stacked WS_2 slabs. For sulphidation temperature lower than 350°C, only CSC catalysts have been analysed. From 23°C to 150°C, the mean length is barely changed with around 3.2 nm, as for the mean stacking number which ranges from 2.6 to 2.4. In the literature, Glasson [Glasson, PhD thesis, Lyon, 1999] and Baubet [Baubet, PhD thesis, Lyon, 2013], who studied calcined (Co)MoS_2-supported catalysts, showed that the mean length of MoS_2 slabs increases when the sulphidation temperature increases. Concomitantly, they observed that the stacking number barely increases, or could even be stabilised at around 400°C. Their results are thus consistent with ours. Note however that we only considered catalysts with tungsten loading of *ca.* 1.7-1.8 W/nm²

(*e.g. ca.* 11-12 $\%_{wt.}$ W) and catalysts with different tungsten amounts can exhibit WS_2 slabs with different behaviours.

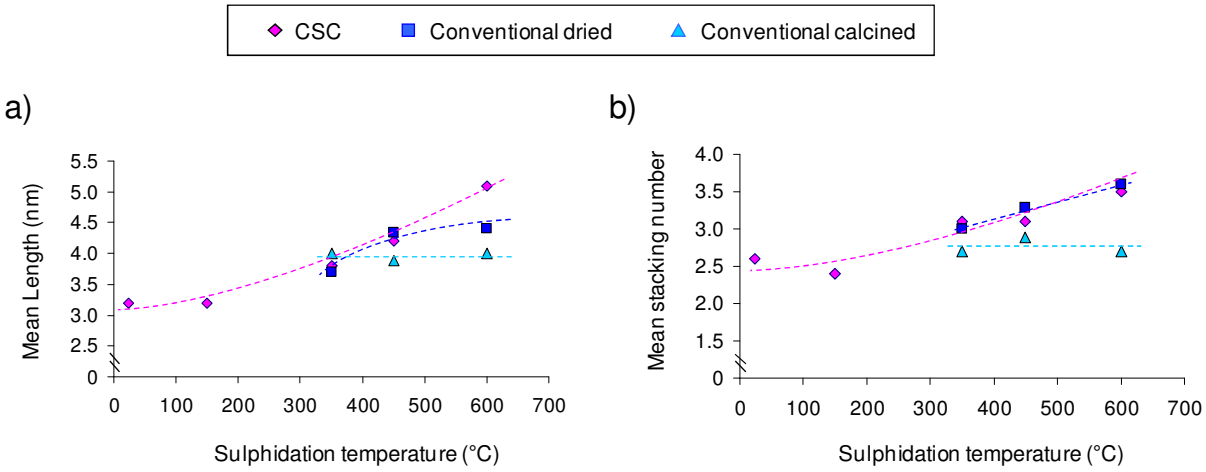

Figure 78: mean length distribution (a) and mean stacking layer distribution (b) of WS_2 crystallites on WS_2/ASA catalysts when increasing the sulphidation temperature. Tungsten loading: *ca.* 1.7 – 1.8 W/nm².

V.2.c. Characterisation by Scanning transmission electron microscopy (high angle annular dark field) - STEM-HAADF

In part V.1.c) we showed that for catalyst sulphided at 600°C, different morphologies could be obtained depending on the preparation method. The CSC method gave rather hexagonal WS_2 slabs, while the conventional method allowed the preparation of truncated triangular ones. However, as sulphidation at 600°C is never used in industrial processes, and that the main part of our study deals with sulphidation and catalytic test performed at 350°C, we carried out STEM-HAADF analyses on samples sulphided at 350°C. As before, we chose a calcined catalyst, exhibiting *ca.* 0.5 W/nm², and a CSC one, loaded with *ca.* 0.8 W/nm². **Figure 79** represents STEM-HAADF micrographs of catalysts sulphided at 350°C and 600°C.

At 350°C, we cannot distinguish a clear morphology, whatever the preparation method. For the CSC catalyst, we can see atomically resolved WS_2 slabs, but stacking effect and difficulties to identify an isolated slab made the 2D shape elucidation almost impossible. Moreover, as in TEM micrographs, STEM-HAADF pictures highlight the presence of nanosized spot-like entities (arrows, on the micrographs), dispersed on the surface. These small entities are much more visible on the conventional catalyst, where it was hard to distinguish WS_2 slabs lying flat on the surface.

At 600°C, hexagonal slabs for the CSC catalyst are formed, whereas a truncated triangular ones for the calcined catalyst. There are still a few nanosized dots on the CSC catalyst surface, not much as before. However, there are far less of these particles on the calcined one, compared with the sulphidation at 350°C.

These analyses have shown that it was difficult to distinguish the 2D morphology of the WS_2 slabs when catalysts are sulphided at 350°C. This is mainly due to the difficulties to find isolated slabs, lying flat on the surface, and not to a low sulphidation level, as slabs "edge-oriented" are visible by STEM and TEM BF. In addition, well-formed slabs exhibiting clear 2D morphology are expected for WS_2 with high degree of crystallinity, supposedly obtained for high sulphidation temperatures (600°C and above). On this purpose, crystallinity of WS_2 slabs is difficult to evaluate. XRD analyses could be performed, but they would only focus on the difference of full width at half height (FWHH) of the stacking peak ($2\theta \approx 14°$) of WS_2, which can suffer from a lack of precision because of the low stacking number of WS_2 slabs observed on our catalysts (3 to 4). Besides, crystalline compounds usually exhibit XPS photopeaks with small FWHH while poorly crystalline ones show broader peaks. As a reference, our as-synthesised WS_2 sample prepared by sulphidation of $[W(OEt)_5]_2$ at 600°C (H_2S/H_2 15 $\%_{mol.}$ H_2S) exhibits a W 4f photopeak where the $W4f_{7/2}$ contribution of W(IV) reveals a FWHH of around 0.82 eV. For the WS_2/ASA catalysts, the main contribution assigned to W(IV) in the W 4f photopeak, *e.g.* W $4f_{7/2}$, is *ca.* 1.53 eV when the materials were sulphided at 23°C and is *ca.* 1.05 eV when the materials were prepared at 600°C. As the FWHH decreases and gets closer to the value found for pure WS_2, we suppose that a better crystallinity of the sulphide phase is reached when sulphided at high temperatures.

Moreover, as the contrast of STEM-HAADF pictures is sensitive to the atomic number, the intense white spot-like entities are attributed to W atoms probably assembled in clusters of different sizes. However, we were not able to figure out if these clusters were the fingerprints of tungsten oxide, and/or partially or fully sulphided tungsten atoms. Moreover, although CSC catalysts have the same level of sulphidation, it is not supposed to influence that much parallel with the sulphidation temperature, the level of sulphidation could influence the presence of these nanosized spot-like entities

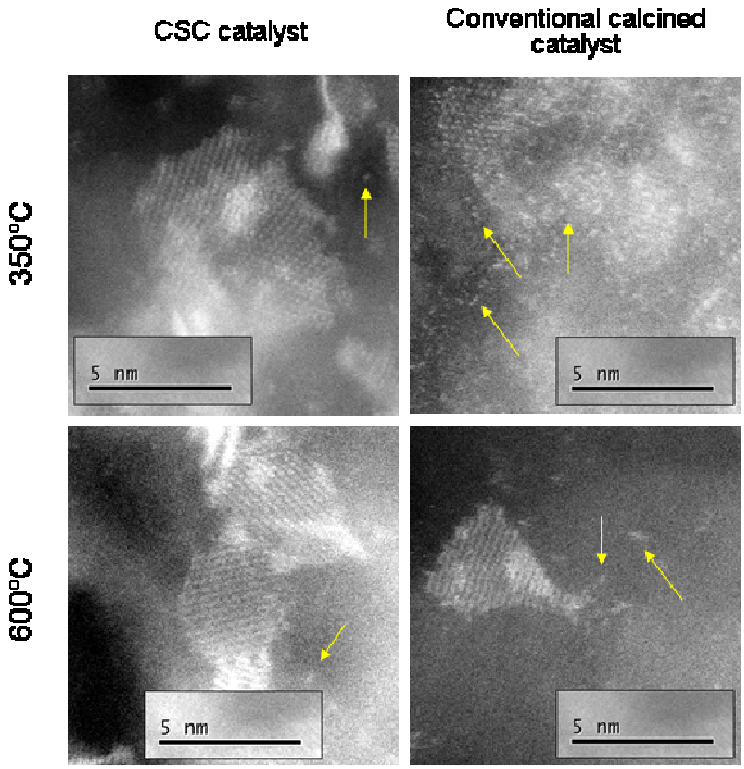

Figure 79: STEM-HAADF micrographs of CSC and conventional dried catalysts sulphided at 350°C and 600°C (H_2S/H_2). Arrows indicate nanosized spot-like entities, supposed to be partially sulphided species (see in the text).

V.2.d. Characterisation by Carbon monoxide adsorption at low temperature (77K), monitored by IR spectroscopy - IR(CO)

IR(CO) analyses were performed on CSC catalysts with 1.7 W/nm², sulphided at 23°C, 350°C and 600°C. Each sulphidation was carried out with a H_2S/H_2 mixture (15 $\%_{mol.}$ H_2S) for 2 h at the desired temperature, followed by a post treatment at 250°C under argon (2 h) to remove any traces of physisorbed H_2S. IR(CO) spectra, normalised by the amount of W in the samples, and not baseline corrected, are shown in **Figure 80.** Note that only spectra collected at saturation of the sulphide phase with carbon monoxide are presented. For sulphidation at 23°C, the catalyst exhibits a broad band between 2170 cm^{-1} and 2080 cm^{-1}, attributed to CO interacting with a partially sulphided phase. Indeed, ν(CO) vibration of carbon monoxide interacting with W atoms exhibiting oxidation states lower than +VI are reported between 2198 cm^{-1} and 2154 cm^{-1} [Yan *et al.*, 1991]. For sulphidation at 350°C, similar features are present, as well as two additional bands: a rather sharp one, positioned at ν(CO) = 2121 cm^{-1},

and a very weak one, close to 2068 cm^{-1}. The sharp band is attributed to a ν(CO) vibration band, assumed to be assigned to CO adsorbed on W-edge atoms, as already discussed in part V.1, while the weak one is attributed to a ν(CO) vibration band, tentatively assigned to CO interacting with S-edge atoms. Presence of the narrow band at ν(CO) = 2121 cm^{-1} for sulphidation at 350°C is due to a better sulphidation of the sample compared to the one prepared at 23°C, probably leading to a reduced distribution of adsorption sites for CO. Then, sulphidation at 600°C gives a sharp band at *ca.* 2124 cm^{-1}, more intense than the one observed for sulphidation at 350°C.

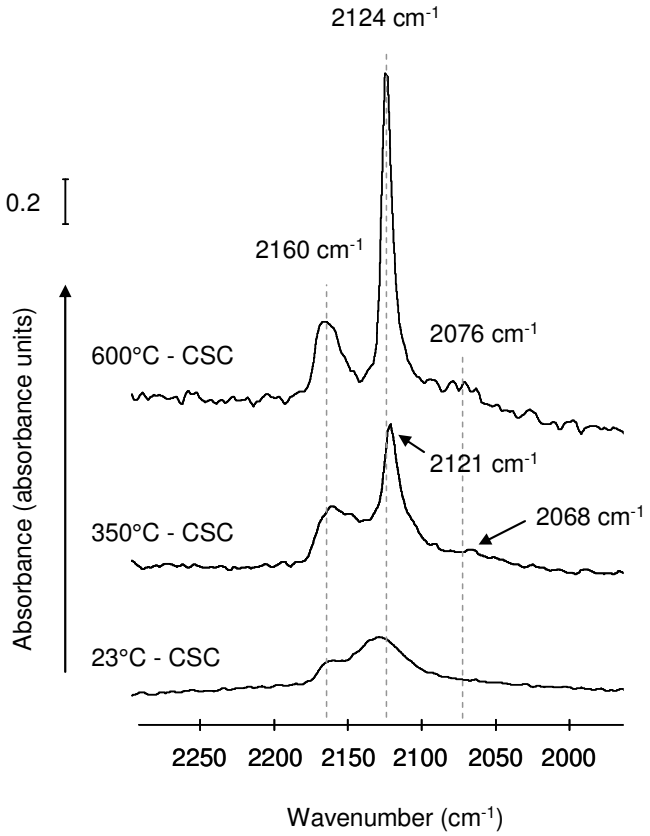

Figure 80: IR(CO) spectra (adsorption at 77 K) of CSC catalysts sulphided at 23°C, 350°C and 600°C, at saturation of the sulphide phase, resulting from introduction of small doses of CO. Spectra are not baseline corrected, and normalised by the amount of W in the samples. Samples were submitted to subsequent post-treatment under argon at 250°C after sulphidation, and before CO adsorption. Tungsten loading: *ca.* 1.7 W/nm².

Quantitative bands' integration reported in **Table 13**, reveals that increasing the sulphidation temperature of the materials leads to a higher amount of CO interacting with the sulphide phase. Normalisation of the CO quantification by the amount of sulphide phase leads

to values spread from 3.2 to 4.7 a.u/cm/mol(W)* where mol(W)* stands for the amount of tungsten (mol) incorporated in the sulphide phase.

Finally, IR(CO) analyses show that sulphidation at low temperatures leads to partially sulphided phases, where tungsten is no more in a +VI oxidation state. Increasing the temperature gives rise to particular sites, with which CO interacts in a peculiar fashion. It leads to a sharp signal at around 2124 ± 3 cm^{-1}, assigned to a narrow distribution of either strong or abundant sites. In the case of the vibration attributed to the interaction between CO and S-edge atoms, the low intensity of the vibration band prevents an accurate quantification from being performed. Moreover, the blue shift observed for the CO stretching vibration, from 2068 cm^{-1} to 2076 cm^{-1} between 350°C and 600°C, could indicate that the interaction between CO and W atoms is stronger when sulphidation is carried out at 350°C, which probably comes from CO interacting with WS_2 slabs which are smaller, or which possibly exhibit a lower amount of adsorption sites.

Table 13: Data collected from IR(CO) analyses of CSC catalysts sulphided at 23°C, 350°C or 600°C (2 h, 15 $\%_{mol.}$ H_2S/H_2). a.u stands for absorbance units, and mol(W)* stands for "mole of W engaged in a WS_2 phase in the sample", calculated using $\%_{rel}$ WS_2 (XPS)

	23°C	350°C	600°C
a.u / cm / g(cat.) [a]	43	54	81
%rel WS2 (XPS)	53	85	87
a.u / cm / g(W)	398	500	750
a.u / cm / mol(W)*	4.1	3.2	4.7

[a] Calculated with the amount of CO adsorbed at saturation of the sulphide phase, and the mass of the pellet

V.2.e. Catalytic results and Discussion

We performed catalytic tests on CSC and conventional catalysts sulphided between 23°C and 600°C. Note that the test, previously described in part V.1) is undertaken at 350°C, increasing the $\%_{rel}$ WS_2 of catalysts sulphided *ex-situ* at temperatures lower than 350°C: the active phase will thus be different from the one we analysed. As a consequence, some spent catalysts were analysed by XPS to get insights into the WS_2 phase which has really catalysed the hydrogenation reaction. Using the same approach as part V.1), we first calculated the HYD rate of catalysts normalised by mole of tungsten in the sample: $\mathbf{r_i}$. , which is shown in **Figure 81**

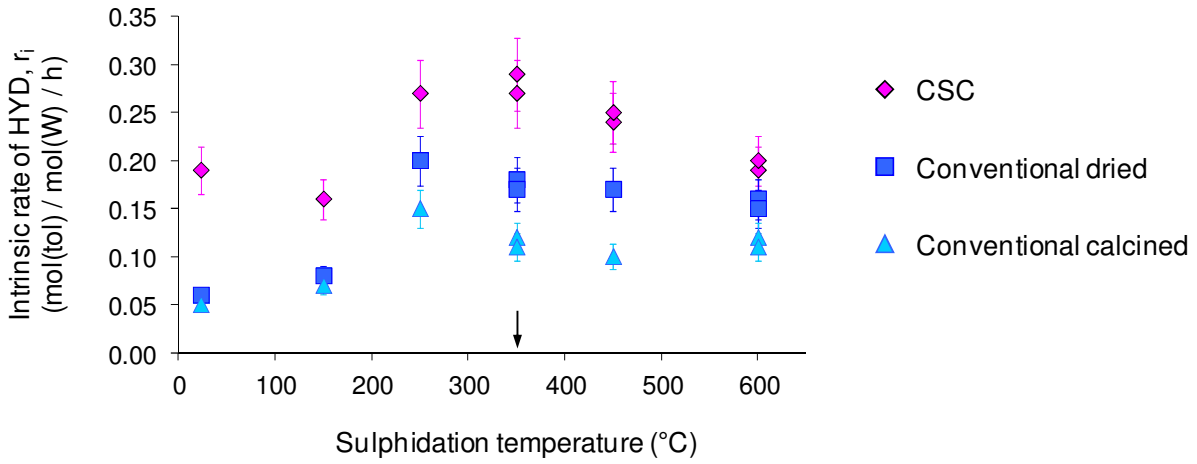

Figure 81: Intrinsic rate of HYD - r_i- of CSC and conventional catalysts sulphided between 23°C and 600°C (*ex-situ* sulphidation, 15 $\%_{mol.}$ H_2S/H_2, before test). r_i is expressed in *mol(tol)/mol(W)/h*, where mol(W) stands for the amount of W (in mol) in the sample

On the whole range of sulphidation temperature, CSC catalysts exhibit higher HYD rates than conventional ones. The HYD rate slowly decreases for temperatures higher than 250°C, no matter what the preparation method. It indicates that sulphidation between 250°C and 350°C is sufficient to provide the best catalytic activity achievable.

To get further insights into the influence of the level of sulphidation of catalysts, we took into account the $\%_{rel}$. WS_2 of spent catalysts. Note that as it was not possible to analyse all the spent catalysts, we only performed XPS measurements on specific ones, exhibiting low sulphidation level before test. We found that:

- CSC and conventional dried catalysts, pre-sulphided at 23°C, previously exhibiting from 50 to 0 $\%_{rel.}$ WS_2, reveal 84 (±5) $\%_{rel.}$ WS_2 after test
- the conventional calcined catalyst, pre-sulphided at 23°C, previously exhibiting no WS_2 phase detected by XPS, exhibits 80 (±5) $\%_{rel.}$ WS_2 after test
- as previously reported in part V.1, the calcined catalyst pre-sulphided at 350°C reveals 78 (±5) $\%_{rel.}$ WS_2 after test

Therefore, we assumed that CSC, dried and calcined spent catalysts display similar average levels of sulphidation after test. Moreover, note that catalysts sulphided at temperatures lower than 250°C where not submitted to a post treatment under argon at 250°C, as post treatment at temperature higher than the pre-sulphidation one could modify the sulphide phase of catalyst.

Finally, the combination of measured $\%_{rel.}$ WS_2 and estimated ones were used to calculate the HYD rate $\mathbf{r_i'}$, expressed in mol(tol)/mol(W)*/h, as shown in **Figure 82**.

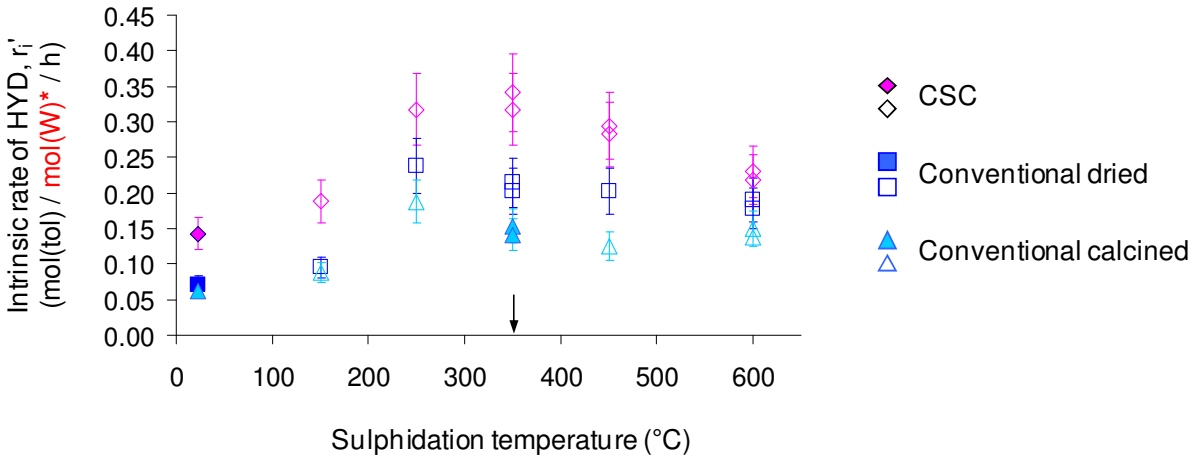

Figure 82: Intrinsic rate of HYD - r_i'- of CSC and conventional catalysts sulphided between 23°C and 600°C (*ex-situ* sulphidation, 15 $\%_{mol.}$ H_2S/H_2, before test). r_i' is expressed in *mol(tol)/mol(W)*/h*, where mol(W)* stand for W engaged in a WS_2 phase, calculated using "mol(W)" (elemental analyses) and the $\%_{rel}$ WS_2 of spent catalysts (XPS). Arrow indicates the temperature at which the test is run: 350°C. Tungsten loading: *ca.* 1.7-1.8 W/nm². Filled symbols correspond to spent catalysts which underwent XPS analyses. Empty ones correspond to catalysts which $\%_{rel.}$ WS_2 after test has been assumed to be similar to catalysts sulphided at 23°C.

As before normalisation by the % rel. WS_2, CSC catalysts exhibit higher HYD rates than conventional ones on the whole range of sulphidation temperature. The HYD rate increases for sulphidation between 23°C and 250°C, and slowly decreases for higher temperatures, no matter what the preparation method. Between 23°C and 250°C, we already demonstrated that there was a deep transformation of the sulphide phase, especially around 250°C - 350°C, which probably explains why the HYD rate increases with the sulphidation temperature. Then for sulphidation temperatures higher than 350°C, the catalytic properties during the reaction were assumed to be stable, because the reaction temperature was equal or lower than that used for the catalyst pre-sulphidation, before test. Therefore, the decreases of activity observed for CSC as well as conventional catalysts is probably attributed to a sintering effect, more important for CSC and dried ones as their HYD rates decrease more rapidly than the calcined ones. This qualitative explanation is consistent with TEM data, reported in part V.2.b) where CSC and conventional dried catalysts exhibited longer WS_2 slabs, with higher stacking numbers

compared to calcined ones, probably due to stronger interactions between the ASA support and amorphous WO_3 species observed on the calcined sample.

In order to take into account this sintering effect, we used the geometrical models presented part V.1.d) to normalise the HYD rate by the number of active edge sites. We calculated models for catalyst sulphided between 350°C and 600°C, using the same hypothesis as before. Note that the slabs length used for the calculation is the length measured for catalysts before test, as TEM measurements have not been run on spent catalysts so far. The best compromises found for geometrical models are presented **Table 14**, in bold letters.

Table 14: Experimental data and Geometrical parameters used for WS_2 slab models of catalysts sulphided at 350°C, 450°C or 600°C, for 2h with 15 $\%_{mol.}$ H_2S/H_2. Bold numbers represent the best comprises found for the catalysts, and used to normalise the intrinsic activity

	W/nm²	Length L from TEM (Å)	Length L' from the model (Å)	n_M	n_S	Number of W in one slab	% W edge [a]	% edge sites [b]	TOF mol(tol)/mol(site)/h
CSC	350	38	38	**6**	**6**	**127**	**50**	**28.3**	**1.16**
	450	42	42	**6**	**6**	**167**	**50**	**25.0**	**1.15**
	600	51	51	**6**	**6**	**221**	**50**	**22.0**	**1.05**
Conv. dried	350	37	38	**7**	**5**	**127**	**60**	**28.5**	**0.73**
	450	43	44	10	4	159	75	26.4	0.80
	450	43	44	**9**	**5**	**163**	**66**	**25.6**	**0.79**
	600	44	44	10	4	159	75	26.4	0.70
	600	44	44	**9**	**5**	**163**	**66**	**25.6**	**0.72**
Conv. calcined	350	40	38	**7**	**5**	**127**	**60**	**28.5**	**0.50**
	450	39	38	**7**	**5**	**127**	**60**	**28.5**	**0.43**
	600	40	38	**7**	**5**	**127**	**60**	**28.5**	**0.49**

Looking at **Table 14** for CSC materials, increasing the slabs length from 3.8 nm (38 Å) to 5.1 nm divides the amount of active sites by *ca.* 1.3 for a hexagonal geometrical model. It directly highlights the loss of active sites due to the sintering effect of WS_2 slabs. For the conventional samples, represented by truncated triangles, the amount of active sites is divided by *ca.* 1.1 for the dried catalyst while it does not change for the conventional calcined one. Finally, CSC materials tend to exhibit less active sites than conventional ones when sulphided at temperatures higher than 350°C.

The corresponding TOFs (r_i"), expressed in mol(tol)/mol(site)/h are shown **Figure 83**.

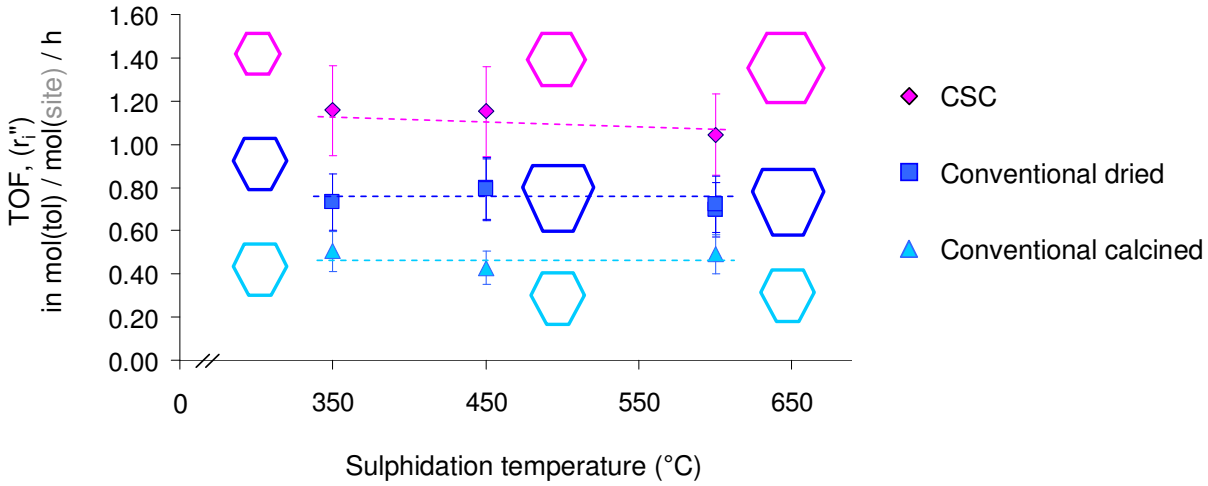

Figure 83: TOF-(r_i'') of CSC and conventional catalysts sulphided between 350°C and 600°C (*ex-situ* sulphidation, 2h 15 $\%_{mol.}$ H_2S/H_2, before test). Expressed in *mol(tol)/mol(site)/h, where mol(site)* stands for the amount of active sites, calculated from the number of tungsten atoms on W-edge, S-edge and corners, relative to the total number of atoms in one slab. Tungsten loading: *ca.* 1.7-1.8 W/nm².

On **Figure 83**, we can see that for each catalyst, the HYD rate r_i'' is rather constant whatever the sulphidation temperature, considering that W atoms on W-edge, S-edge and corner sites are hydrogenation active sites. It means that normalisation of the intrinsic HYD rates by the amount of active sites, calculated with geometrical models, reveals an average TOF for each catalyst. In this case, TOFs of conventional catalysts are still lower than the CSC ones. Supposing that the 2D morphology of CSC catalysts could be more triangular shaped (as truncated triangular slabs reflect the most thermodynamically stable geometry from DFT calculations – see part V.1.e), we tried to calculate similar TOF by using truncated triangular shapes for CSC samples. Results were found to be barely different from the ones discussed just above. Finally, it highlights that, as for catalysts prepared at different tungsten loadings and sulphided at 350°C (H_2S/H_2), another parameter influencing hydrogenation reactions has to be at stake.

One first parameter could be the stacking number, which has been set to 1 in our model. **Figure 78** shows that between 350°C and 600°C, calcined catalysts are less stacked (2.7 - 2.9) than CSC (3.1 - 3.5) and dried ones (3.0 - 3.6). We can thus wonder if each layer of the stacked crystallites exhibits the same HYD activity. In this spirit, several studies have reported structure–activity relationships for sulphide catalysts. Massoth and Muralidhar [Massoth and Muralidhar, 1982] concluded that, for Mo/Al_2O_3 catalysts, all the edge planes of the clusters are HYD active. With their geometrical model, Kasztelan *et al.* [Kasztelan *et al.*, 1984] concluded that HYD are

performed at the edge planes of MoS_2. Later on, Daage and Chianelli [Daage and Chianelli, 1994] proposed the so-called "rim-edge" model (see **Figure 84**) in which HYD is catalyzed exclusively on the top and bottom of edge planes, called *rim sites.*

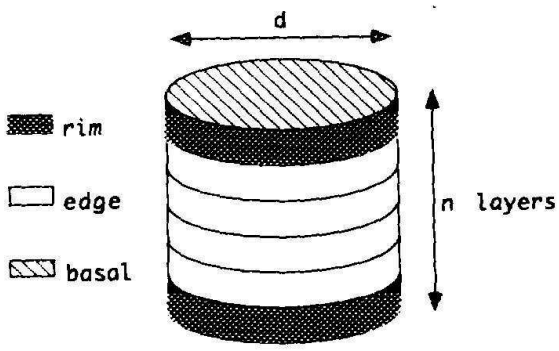

Figure 84: rim-edge model, proposed by Daage and Chianelli [1994]

If we try to draw a parallel with our catalytic results on toluene HYD, and in the spirit of Daage model, WS_2 slabs highly dispersed on the surface, and exhibiting low stacking number (1 or 2) would be more efficient HYD catalysts, as they would maximize their number of rim sites. Note that the same reasoning applies to "brim sites" proposed by Topsøe *et al*. [Topsøe *et al*., 2005], located on the top of monolayered sulphide slabs. However, our results do not match the Daage model as the more hydrogenating catalysts also exhibit the more stacked WS_2 slabs, especially at high sulphidation temperatures. One explanation could be that Daage's model, established for HDS and HYD reaction of dibenzothiophene, is not suitable to describe hydrogenation of toluene. Besides, from TEM experiments and catalytic results, stacking does not seem to influence the toluene HYD for catalysts exhibiting stacking number between *ca.* 2.7 and 3.6.

Besides, a study of Sakashita *et al*. [Sakashita *et al*., 2001] reveals that surface orientation of the support promotes peculiar reactions: MoS_2 crystallites would show higher HYD rates when located on spherical-like alumina exhibiting {111} and {100} planes compared to crystallites located on {100} planes of plate-like alumina planes [Sakashita *et al*., 2001]. Nevertheless, the support used in our study, which is composed of alumina platelets and amorphous silica, is supposed to be stable in the range of temperature we used, and alumina crystallites are not expected to change, therefore not influencing the catalytic activity.

IR(CO) analyses performed on CSC catalysts sulphided at 350°C and 600°C showed that CO was interacting with a large distribution of adsorption sites (on W-edge) at 350°C, and with a narrower one at 600°C: these highly reactive sites probably being the so-called CUS. However,

as the TOF does not seem to be different for these two temperatures, we could suppose that there is little influence of the different adsorption sites, and that CO adsorption has only allowed us to quantify the amount of WS_2 phase.

Then, another parameter can be taken into account to improve our understanding of the catalytic results, which is the presence on sulfhydryl species MSH on WS_2 slabs edges. Indeed, sulfhydryl species, present on slabs edges, take part into the HYD mechanism of toluene, as described by Gandubert *et al*. [2008] and Guernalec *et al*. [Guernalec *et al*, 2004]. From DFT calculations performed at IFPEn (see part V.1.e), WS_2 crystallites modelled in conditions close to our sulphidation conditions (calculations performed at 600°C) revealed that M-edges exhibit a sulphur coverage of 50 %, while S-edges exhibit a sulphur coverage of 87.5 %. Considering in a first approximation that WS_2 and MoS_2 crystallites behave similarly, MSH species could be stabilised either on W-edge of S-edge. Indeed, Prodhomme *et al* [Prodhomme *et al*. 2011] have evidenced by DFT calculations, that for MoS_2 slabs, Mo-edge with 37 %S exhibiting sulphur vacancy (*e.g.* CUS) as well as Mo-edge with 50 %S and 50 %H can be stabilized in relevant HDS conditions. The presence of these two types of sites is expected to favour HDS reactions, as CUS represents readily adsorption sites for sulphided molecule, which can undergo hydrogenation thanks to available H ad-atoms diffusing from neighbouring MSH species. Note that the authors reported that even is the presence of CUS is scarce on Mo-edge, they are abundant on S-edge, which might thus play an important role in hydrodesulphurization reactions.

For toluene hydrogenation in particular, Gandubert *et al*. [2008] have shown that for CoMoS phases, the promoted M-edge with CoMo mixed site provides a stable configuration for toluene adsorption. The stabilisation of adjacent MSH and MH species on the same edge offers a favourable situation for subsequent hydrogenation of toluene, as proposed in the kinetic modelling of Guernalec *et al*. [Guernalec *et al*., 2004; Guernalec *et al*., 2006] With this in mind, the higher activity of CSC catalysts could be tentatively attributed to the hexagonal shape of their crystallites (observed by STEM-HAADF), leading to a more favourable edge structural environment for toluene activation and H_2 activation into MSH and MH species.

Characterisation of such MSH species has already been reported by different authors through analyses of MoS_2 phases by inelastic neutron scattering [Sundberg *et al*., 1991] Raman spectroscopy [Polz *et al*., 1989] or IR spectroscopy [Burrow *et al*., 1989], and correlated with DFT calculations [Prodhomme *et al*., 2011]. Lauritsen *et al.* also reports the characterisation of MSH species by STM studies on MoS_2 phases [Lauritsen *et al*., 2004; Lauritsen *et al*., 2006]. Therefore, performing Raman or IR spectroscopy analyses on catalysts should enable to observe such MSH species on WS_2 phases prepared in this PhD thesis. As another further

perspective to this work, quantifying the amount of sulphur on slabs edge by TPR experiments of WS_2 samples is possible [Raybaud and Toulhoat, 2013, Ed. Technip, Paris]. Breysse *et al.* [Breysse *et al.*, 2002] have summarized the main results found on TPR experiments of sulphide catalysts and they found three peculiar reduction regions on TPR spectra, among which the first one was around 200°C ; the second one between 400°C and 600°C and the last one around 900°C. The two former ones were assigned to sulphur atoms on slabs edges, while the last one was assigned to the total reduction of the sulphide phase. Beside, different groups [Dinter *et al.*, 2009; Afanasiev *et al.*, 2010] proposed that the first peak was caused by reduction of sulphur species (S_2^{2-}) on the M-edge particularly. Regarding these results, TPR experiments performed on our catalysts could probably allow to quantify the amount of sulphur on W-edge as a function of the preparation method. Along with the calculation of the theoretical amount of sulphur atom on W-edge with our geometrical model, it could probably bring complementary insights into the understanding of the sulphur coverage of W-edge, and thus the understanding of the catalytic activity.

V.2.f. Conclusion on the influence of the sulphidation temperature on the genesis and activity of the active phase of WS_2/ASA catalysts

We can summarize our previous findings as follows:

(1) CSC catalysts undergo sulphidation at lower temperatures than conventional ones, due to their high reactivity, already discussed in part V.1. XPS analyses showed that when sulphided at room temperature (which has never reported before, to the best of our knowledge), CSC catalysts exhibit *ca.* 50 $\%_{rel}$ WS_2 when conventional ones show no evidence of WS_2 phase.

(2) IR(CO) analyses showed that for CSC materials sulphided at 23°C, CO was interacting with (oxy)sulphides at wavenumbers higher than expected for well crystallised WS_2. Sulphidation at 600°C totally removes these (oxy)sulphide species. Concomitantly with that, CO was shown to interact with peculiar adsorption sites at $\nu(CO) = 2124 \pm 3$ cm^{-1}, tentatively assigned to W-edge sites, probably being the so-called CUS.

(3) Catalytic activity measurements, together with geometrical model calculations showed that sintering effect at high sulphidation temperature was playing a role in the different HYD TOF observed. W-edge, S-edge and corner sites were taken into account as HYD active sites but another parameter had to be critical to fully explain data collected. Although we have not been able to quantitatively explain the origin of the better TOF of

CSC catalysts, one hypothesis is that it could be linked to the hexagonal morphology of the CSC sample, which present a more favourable edge structure providing a synergy effect between W-edge and S-edge. This synergy effect enhances the H_2 activation into MSH and MH species as well as toluene activation when adsorbed.

At this point, we have described the preparation of catalysts with a molecular approach, from surface species (chapter IV) to the sulphide phase (chapter V). Surface species were characterised depending on the tungsten loading. Then the reactivity of these catalysts was compared with conventional ones', dried or calcined, when sulphided at different tungsten loadings and different sulphidation temperatures.

We showed that CSC catalysts exhibit higher (hydrogenation) TOF than conventional ones, which is promising for the further preparation of promoted samples. Indeed, adding a promoter (Ni, Co) is known to drastically increase the activity of supported MS_2 catalysts (M= W, Mo). With this in mind, we will describe in the next part (chapter VI) the preparation, the characterisation and the catalytic activity of Ni-promoted WS_2 phases.

V.3. References

Afanasiev, P., *Journal of Catalysis* (2010), **269**, 2, 269–280

Bachelier, J.; Tilliette, M.J.; Cornac, M.; Duchet, J.C.; Lavalley, J.C. and Cornet, D., *Bulletin des Sociétés Chimiques Belges* (1984), **93**, 743

Barton, D.G.; Sole, S.L. and Iglesia, E., *Topics in Catalysis* (1998), **6**, 87-99

Baubet, B., PhD thesis, Université Claude Bernard Lyon 1, France (2013)

Ben Tayeb, K.; Lamonier, C.; Lancelot, C.; Fournier, M.; Payen, E.; Bonduelle, A. and Bertoncini, F., *Catalysis Today* (2010), **150**, (3–4), 207-212

Breysse, M.; Cattenot, M.; Decamp, T.; Frety, Roger; Gachet, C.; Lacroix, M.; Leclercq, C.; de Mourgues, L., Portefaix, J.L.; Vrinat, M.; Houari, M.; Grimblot, J.; Kasztelan, S.; Bonnelle, J.P.; Housni, S.; Bachelier, J. and Duchet, J.C., *Catalysis Today* (1988), **4**, 39-55

Breysse, M.; Furimsky, E.; Kasztelan, S.; Lacroix, M. and Perot, G., *Catalysis Reviews, Science and Engineering* (2002), **44**, 4, 651-735

Brorson, M.; Carlsson, A. and Topsøe, H., *Catalysis Today* (2007), **123**, 31-36

Burrow, T.E.; Lazarowych, N.J.; Morris, R.H.; Lane, J. and Richards, R.L., *Polyhedron* (1989), **8**, 1701

Carlsson, A.; Brorson, M. and Topsøe, H., *Journal of Catalysis* (2004), **227**, 2, 530-536

Carlsson, A.; Brorson, M. and Topsøe, H., *Journal of Microscopy* (2006), **223**, 3, 179-181

Chung, F.H., *Journal of Applied Crystallography* (1974), **7**, 526

Daage, M. and Chianelli, R.R., *Journal of Catalysis* (1994), **149**, 414-427

Dinter, N.; Rusanen, M.; Raybaud, P.; Kasztelan, S.; da Silva, P. and Toulhoat, H., *Journal of Catalysis* (2009), **267**, 67-77

Füchtbauer, H.G.; Tuxen, A.K.; Moses, P.G.; Topsøe, H.; Besenbacher, F. and Lauritsen, J.V. Studying the atomic-scale structure of WS_2 nanoclusters, oral communication at MACS VI symposium, Satillieu, France (2013)

Gandubert, A.D., PhD thesis, Université de Lille, France (2006)

Gandubert, A.D.; Krebs, E.; Legens, C.; Costa, D.; Guillaume, D. and Raybaud, P. *Catalysis Today* (2008), **130**, 1, 149–159

Genuit, D.; Bezverkhyy, I. and Afanasiev, P., *Journal of Solid State Chemistry* (2005), **178**, 2759-2765

Girleanu, M.; Alphazan, T.; Boudène, Z.; Raybaud, P.; Gay, A.S.; Ersen, O.; Bonduelle, A. and Legens, C. *in preparation*

Glasson, C.F., PhD Thesis, Université Claude Bernard Lyon 1, France (1999)

Guernalec, N.; Cseri, T.; Raybaud, P.; Geantet C. and Vrinat M., *Catalysis Today* (2004), **98**, 61-66

Guernalec, N.; Geantet, C.; Raybaud, P.; Cseri, T.; Aouine, M. and Vrinat, M., *Oil & Gas Science and Technology – Rev. IFP* (2006), **61**, 4, 515-525

Hansen, L.P.; Ramasse, Q.M.; Kisielowski, C.; Brorson, M.; Johnson, E.; Topsøe, H. and Helveg, S., *Angewandte Chemie International Edition* (2011), **50**, 10153 –10156

Hensen E.J.M., van der Meer Y., van Veen J.A.R. and Niemantsverdriet J.W., *Applied Catalysis A: General* (2007), **322**, 0, 16-32.

Kasztelan, S.; Toulhoat, H.; Grimblot, J. and Bonnelle, J.P., *Bulletin des Sociétés Chimiques Belges* (1984), **93,** 8-9

Kasztelan, S.; Toulhoat, H.; Grimblot, J. and Bonnelle, J. P., *Applied Catalysis* (1984), **13**, 127

Kooyman, P.J.; Hensen, E.J.M.; de Jong, A.M.; Niemantsverdriet, J.W. and van Veen, J.A.R., *Catalysis Letters* (2001), **74**, 1-2, 49-53

Lauritsen, J.V.; Bollinger, M.V.; Laegsgaard, E.; Jacobsen, K.W.; Nørskov, J.K.; Clausen, B.S.; Topsøe, H.; and Besenbacher,F., *Journal of Catalysis* (2004), **221**, 2, 510–522

Lauritsen, J.V. and Besenbacher, F., *Advances in Catalysis* (2006), **50**, 97-147

Liu, Y.J.; Zhao, M.; Guo, Q.L.; Gui, L.L., Xie, Y.C. and Tang, Y.Q., *Acta Chimica Sinica Chinese Edition* (1985), **43**, 728; *Acta Chimica Sinica English Edition* (1985) p313

Macht, J. and Iglesia, E., *Physical Chemistry Chemical Physics* (2008), **10**, 5331-5343

Massoth, F.E. and Muralidhar, G., Proceedings of the Fourth International Conference on the Chemistry and Uses of Molybdenum, Climax Molybdenum Co. (1982), p. 343

Moses, P.G.; Hinnenman, B., Topsøe, H. and Nørskov, J.K. *Journal of Catalysis* (2007), **248**, 8, 188-203

Müller, B.; van Langeveld, A.D.; Moulijn, J.A. and Knözinger, H., *The Journal of Physical Chemistry* (1993), **97**, 9028

Okamoto, Y.; Kato, A.; Usman; Rinaldi, N.; Fujikawa, T.; Koshika, H.; Hiromitsu, I. and Kubota, T., *Journal of Catalysis* (2009), **265**, 2, 216-228

Payen, E.; Kasztelan, S.; Grimblot, J. and Bonnelle, J.P. *Catalysis Today* (1988), **4**, 57-70

Payen, E.; Kasztelan, S.; Houssenbay, S.; Szymanski, R. and Grimblot, J., *The Journal of Physical Chemistry* (1989), **93**, 6501-6506

Peri, J.B., *The Journal of Physical Chemistry* (1982), **86**, 1615-1622

Polz, J.; Zeilinger, H.; Müller, B. and Knözinger, H., *Journal of Catalysis* (1989), **120**, 22-28

Prodhomme, P.Y.; Raybaud, P. and Toulhoat, H. *Journal of Catalysis* (2011), **280**, 178–195

Proust, A.; Matt, B.; Villanneau, R.; Guillemot, G.; Gouzerha, P. and Izzet, G., *Chemical Society Reviews* (2012), **41**, 7605-7622

Raybaud, P. and Toulhoat, H., Catalysis by transition metal sulphides (2013), Editions Technip, Paris

Reinhoudt, H.R.; van Langeveld, A.D.; Kooyman, P.J.; Stockman, R.M.; Prins, R.; Zandbergen, H.W. and Moulijn, J.A., *Journal of Catalysis* (1998), **179**, 2, 443-450

Reinhoudt, H.R.; van der Meer, Y.; van der Kraan, A.M.; van Langeveld, A.D. and Moulijn, J.A., *Fuel Processing Technology* (1999), **61**, 43-54

Rochet, A., PhD thesis, Université Paris Sud (2011)

Sakashita, Y.; Araki, Y. and Shimada, H., *Applied Catalysis A: General* (2001), **215**, 101-110

Schweiger, H.; Raybaud, P. and Toulhoat, H., *Journal of Catalysis* (2002), **212**, 1, 33-38

Stanislaus, A. and Cooper, B.H., *Catalysis Reviews* (1994), **36**, 1, 75-123

Sun, M.; Bürgi, T., Cattaneo, R. and Prins, R., *Journal of Catalysis* (2001), **197**, 172-181

Sundberg, P.; Moyes, R.B. and Tomkinson, J., *Bulletin des Sociétés Chimiques Belges* (1991), **100**, 967

Thomas, R.; de Beer, V. H. J. and Moulijn, J. A., *Bulletin des Sociétés Chimiques Belges* (1981), **90**, 1349

Topsøe, H.; Hinnemann, B.; Nørskov, J.K.; Lauritsen, J.V.; Besenbacher, F.; Hansen, P.L.; Hytoft, G.; Egeberg, R.G. and Knudsen, K.G., *Catalysis Today* (2005), **107-108**, 12-22

Travert, A.; Dujardin, C.; Maugé, F.; Cristol, S.; Paul, J.F.; Payen, E. and Bougeard, D., *Catalysis Today* (2001), **70**, 255-269

Travert, A.; Dujardin, C.; Maugé, F.; Veilly, E.; Cristol, S.; Paul, J.F. and Payen, E. *The Journal of Physical Chemistry B* (2006), **110**, 1261

Turova, N.Y.; Turevskaya, E.P.; Kessler, V.G. and Yanovskaya, M.I., The chemistry of metal alkoxides, N.Y. (2002), Kluwer Academic Publishers, London

van der Vlies, A.J.; Kishan, G.; Niemantsverdriet, J.W., Prins, R. and Weber, T., *The Journal of Physical Chemistry B* (2002), **106**, 3449-3457

van der Vlies, A.J.; Prins, R. and Weber, T., *The Journal of Physical Chemistry B* (2002), **106**, 36, 9277-9285

Wang, Y.; Chena, Q.; Yang, W.; Xie, Z.; Xua, W. and Huang, D., *Applied Catalysis A: General* (2003), **250**, 25-37

Xie, Y.C. and Tang, Y.Q., *Advances in Catalysis* (1990), **37**, 1

Xu, B.; Dong, L.; Fan, Y. and Chen, C., *Journal of Catalysis* (2000), **193**, 88-95

Yan, Y.; Xin, Q.; Jiang, S. and Guo X., Journal of Catalysis (1991), **131**, 234-242

Yu, X.F.; Wu, N.Z.; Huang, H.Z.; Xie, Y.C. and Tang, Y.Q., *Journal of Materials Chemistry* (2001), **11**, 3337–3342

Zuo, D.; Vrinat, M.; Nie, H.; Maugé, F.; Shi, Y.; Lacroix, M. and Li, D., *Catalysis Today* (2004), **93–95**, 1, 751-760

Part VI. Synthesis of supported NiWS phases by the use of $[W(OEt)_5]_2$ and molecular precursors of nickel

Outline (Part VI)

Outline (Part VI) **217**

Introduction **219**

VI.1. Impregnation of Ni-precursors onto ASA-supported alkoxide tungsten species. **221**

VI.1.a. Characterisation of supported NiW species by IR spectroscopy 221

VI.1.b. Characterisation of NiWS sulphide phases by X-ray photoelectron spectroscopy (XPS) 226

VI.1.c. Characterisation of NiWS sulphide phases by Transmission electron microscopy (TEM) 229

VI.1.d. Characterisation of NiWS sulphide phases by STEM-HAADF 230

VI.1.e. Characterisation of NiWS sulphide phases by CO adsorption at low temperature (77K) monitored by IR spectroscopy - IR(CO) 233

VI.1.f. Influence of the Ni content on properties of NiWS phases: the case of $Ni(acac)_2/[W(OEt)_5]_2$/ASA sulphide samples 235

VI.2. Impregnation of Ni-precursors onto a WS_2 phase, prepared at 350°C **238**

VI.2.a. Preparation and characterisation by IR spectroscopy 239

VI.2.b. Characterisation by X-ray photoelectron spectroscopy (XPS) 241

VI.2.c. Characterisation by Transmission electron microscopy (TEM) 242

VI.3. Impregnation of a Ni-precursor onto a WS_2 phase, prepared at 23°C: study of the influence of the Ni content **243**

VI.3.a. Characterisation by X-ray photoelectron spectroscopy (XPS) 244

VI.3.b. Characterisation by Transmission electronic microscopy (TEM) 246

VI.4. Characterisation of spent catalysts **248**

VI.5. Catalytic results **252**

VI.5.a. Benchmarking catalytic activities with conventional samples and industrial references 252

VI.5.b. Influence of the nickel precursor 254

VI.5.c. Influence of the preparation method: deposition of $Ni(acac)_2$ onto supported tungsten species (non sulphided) or onto sulphide ones, prepared at 23°C or 350°C 257

VI.5.d. Influence of the nickel content 259

VI.6. Discussion 262

VI.6.a. Morphology and edge decoration of NiWS crystallites 262

VI.6.b. Optimal parameters for NiWS phases: the balance between the amount of active sites and their intrinsic HYD strength 272

VI.7. Conclusion 278

VI.8. References 279

Introduction

In the previous chapters, we have shown that the CSC approach was suitable to prepare non-promoted WS_2/ASA catalysts exhibiting higher activities than their conventional homologues in hydrogenation of toluene. However, it is well known that non-promoted catalysts are much less efficient than the promoted ones, which typically exhibit higher hydrogenation (HYD) activities by about one order of magnitude. We therefore investigated the preparation of NiWS/ASA catalysts (promoted catalysts) by a CSC method, and compared them to conventional ones.

In part V, we revealed that CSC catalysts prepared by incipient wetness impregnation of $[W(OEt)_5]_2$ onto ASA with 1.7 W/nm² exhibited the highest Turn-Over Frequency (TOF). Then previous studies on NiWS/ASA catalysts realised at IFPEn had previously shown that the highest intrinsic rate of hydrogenation was obtained for Ni/W atomic ratio between 0.2 and 0.3. Therefore, the study will focus first on the preparation of Ni-promoted catalysts *via* CSC with 1.7 W/nm² and an atomic ratio Ni/W of *ca.* 0.2 (at/at).

We investigated *via* CSC the preparation of NiW catalysts by co-impregnation of tungsten and nickel precursors, in a way similar to what is used for the preparation of conventional NiW oxide phases. However, due to the difficulties to find an appropriate solvent for impregnation of both $[W(OEt)_5]_2$ and nickel precursors (Ni-bis-acetylacetonato, $Ni(acac)_2$, or Ni-bis-1-methylcyclopentadienyl, $Ni(1\text{-}MeCp)_2$, or Ni nitrate, $Ni(NO_3)_2$), a successive impregnation approach, with first, an impregnation of tungsten, and then the nickel precursors, was chosen (see **Figure 85**).

As in the literature, previous studies [Okamoto *et al.*, 2005, Okamoto *et al.*, 2009, Maugé *et al.*, 1989; Maugé *et al.*, 1992] had reported the preparation of enhanced HDT catalysts by deposition of the precursor onto a pre-sulphided phases, we decided to investigate the deposition of nickel onto a sulphide phase prepared at 350°C (2 h, 15 $\%_{mol.}$ H_2S/H_2, see **Figure 85**).

Additionally, we investigated the control of the morphology of WS_2 slabs in NiWS catalysts. Indeed, the presence of a promoter (Ni, Co) on crystallites edges is known to promotes their stabilisation and thus to decrease their length. It partly explains why promoted samples usually exhibit smaller slabs than non-promoted ones. As we revealed in part V that sulphidation of non-promoted $[W(OEt)_5]_2$-based samples, at 23°C (15 $\%_{mol.}$ H_2S/H_2), gave small WS_2 slabs (3.2 nm) and numerous nanosized spot-like particles (1 to 2 nm), deposition of nickel on these entities would probably prevent their growth upon additional sulphidation. NiWS samples with smaller

crystallites than conventional NiWS samples would thus be expected. To do so, we studied the deposition of a nickel precursor ($Ni(acac)_2$) onto WS_2 samples sulphided at 23°C, followed by an additional sulphidation at 350°C to anchor the NiWS phase.

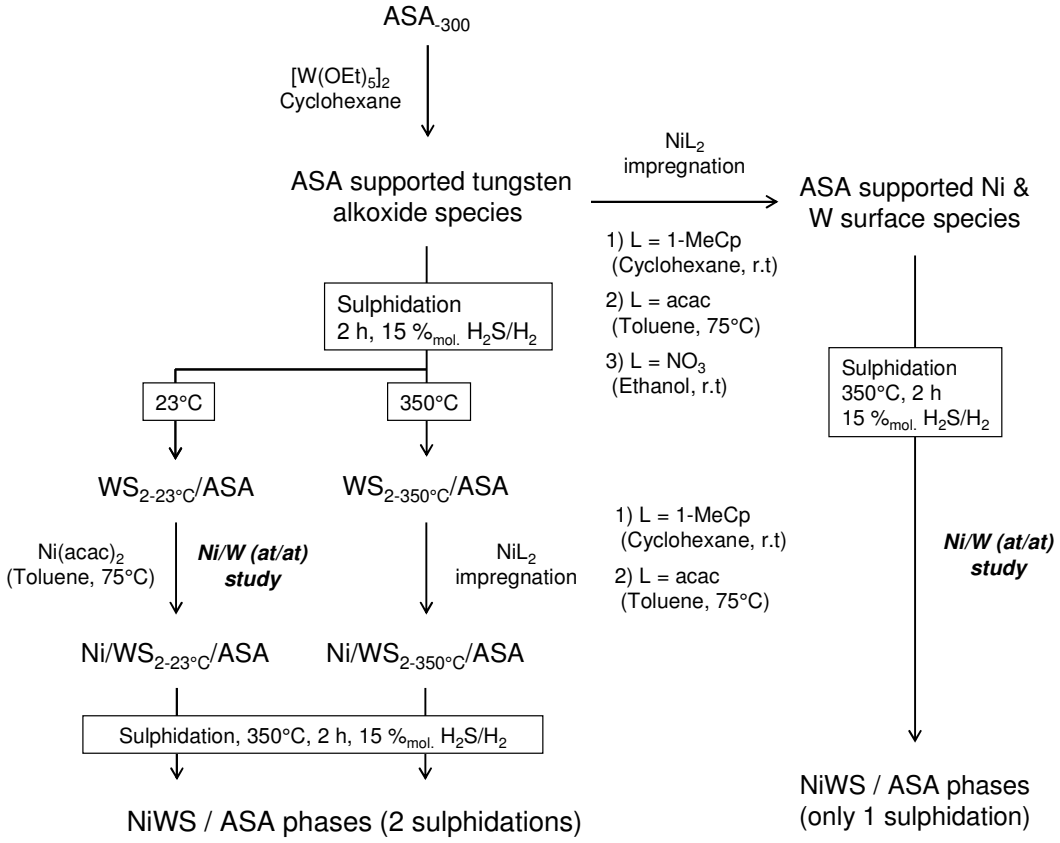

Figure 85: Schematic representation of the different catalyst preparation pathways. r.t. stands for room temperature.

In the same spirit as the studies of Yermakov [Yermakov *et al.*, 1984], Marchand [Marchand *et al.*, 2009] and Gandubert [Gandubert *et al.*, 2008] the effect of the Ni content on the catalytic activity of the NiWS phases was investigated. Samples with different experimental Ni/W atomic ratio were thus prepared, by deposition of $Ni(acac)_2$ onto (1) surface W-species previously obtained by impregnation of $[W(OEt)_5]_2$ on ASA_{-300}, or (2) onto a sulphide phase prepared at 23°C (2 h, 15 %mol. H_2S/H_2). $Ni(acac)_2$ was selected as one of the Ni-precursors because it yielded enhanced HYD activity for NiWS catalysts in preliminary experiments. All results will be compared with benchmark results obtained previously on reference catalysts synthesised at IFPEn. [Raybaud and Toulhoat, 2013, Ed. Technip, Paris]

VI.1. Impregnation of Ni-precursors onto ASA-supported alkoxide tungsten species.

In this part, we report the preparation of various NiWS catalysts by deposition of nickel precursors onto supported tungsten alkoxides species (CSC) or tungsten oxide phases (conventional). The main objective is to investigate the effect of different nickel precursors on the activity of the final NiW phases, before and/or after sulphidation. To do so, IR spectroscopy will help understanding the reactivity of some of the precursors with supported alkoxides. XPS analyses, performed on sulphide sample, will be used to assess the level of sulphidation of tungsten, as well as the formation of the so-called mixed phase "NiWS" which represent the active phase of NiWS catalysts. Note that this study not only deals with CSC materials prepared with molecular precursors of nickel, *e.g.* Ni-bis-acetylacetonato, $Ni(acac)_2$, or Ni-bis-1-methylcyclopentadienyl., $Ni(1\text{-}MeCp)_2$, but also with nickel nitrate ($Ni(NO_3)_2$), commonly used for conventional catalysts, and deposited onto a supported alkoxide W-species (prepared with $[W(OEt)_5]_2$). Besides, we also show characterisation results obtained on catalysts prepared by deposition of $Ni(acac)_2$ onto a conventionally prepared "dried" oxide phase, by impregnation of ammonium metatungstate followed by a subsequent drying step at 120°C.

VI.1.a. Characterisation of supported NiW species by IR spectroscopy

VI.1.a.1. (bis-1-methylcyclopentadienyl) nickel - $Ni(1\text{-}MeCp)_2$ - based material

To evaluate the reactivity of (bis-1-methylcyclopentadienyl) nickel, referred as $Ni(1\text{-}MeCp)_2$, (see **Figure 86**) with surface functionalities of ASA_{-300}, we prepared a supported nickel material (*ca.* 1.0 $\%_{wt.}$, about 0.4 Ni/nm²) by incipient wetness impregnation of $Ni(1\text{-}MeCp)_2$ onto ASA_{-300}.

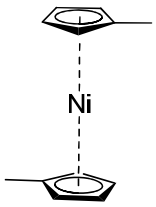

Figure 86: (bis-1-methylcyclopentadienyl) nickel (II) precursor.

The IR spectrum of Ni(1-MeCp)$_2$/ASA$_{-300}$ is shown in **Figure 87**:

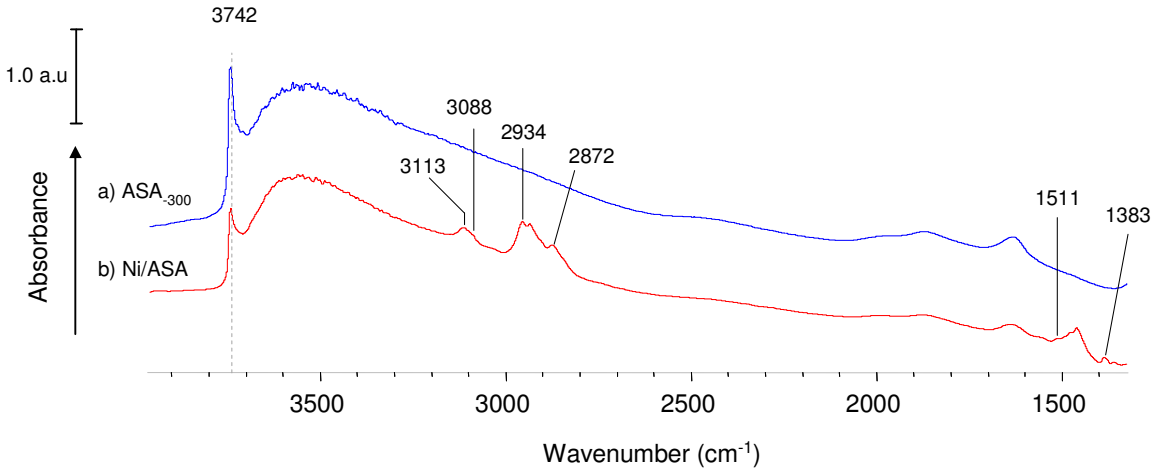

Figure 87: IR spectrum (transm.) of a) ASA$_{-300}$ and b) Ni(1-MeCp)$_2$/ASA$_{-300}$

The IR spectrum reveals a partial disappearance of isolated silanols (ν(OH) = 3742 cm^{-1}, *ca.* 50 % consumed) and the appearance of vibration bands between 3113 and 3088 cm^{-1}, between 2934 and 2872 cm^{-1} as well as between 1511 and 1383 cm^{-1} are respectively assigned to ν(C$_{sp2}$H) and ν(C$_{sp3}$H) stretching vibrations, and δ(CH) vibration of methylcyclopentadienyl rings of the nickel precursor. Ni(1-MeCp)$_2$ is thus not very reactive towards the OH groups of ASA$_{-300}$.

As Ni(1-MeCp)$_2$ is air sensitive, not very stable, even when stored in a glovebox, and not very reactive towards surface hydroxyl functionalities, we investigated the use of another Ni precursor, which contains the more reactive anionic acetyl acetonate ligands, namely (bis-acetylacetonato)nickel, Ni(acac)$_2$ In that case, the corresponding samples have been characterised in much more details as described below.

VII.1.a.2. (bis-acetylacetonato) nickel - Ni(acac)$_2$ - based materials

Ni(acac)$_2$ (**Figure 88**) had to be solubilised in hot toluene before impregnation on ASA$_{-300}$; a solid with *ca.* 0.9 %$_{pds.}$ Ni (about 0.4 Ni/nm²) was obtained.

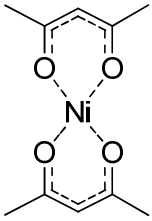

Figure 88: (bis-acetylacetonato) nickel (II) precursor

The IR spectrum of the supported nickel sample, which is shown in **Figure 89**, exhibits the same features as $Ni(acac)_2/\alpha$-Al_2O_3 prepared by Molina *et al.* [Molina *et al.*, 1999] The ν(C=C) stretching vibration at *ca.* 1533 cm^{-1} is in particular attributed by the authors to Hacac species ($C_4H_8O_2$), released from $Ni(acac)_2$ upon reaction with the alumina surface and subsequently interacting with surface Lewis acid site. Besides, note the partial consumption of isolated silanols (ν(OH) = 3742 cm^{-1}, 66 % consumed), resulting from the grafting of the nickel precursor.

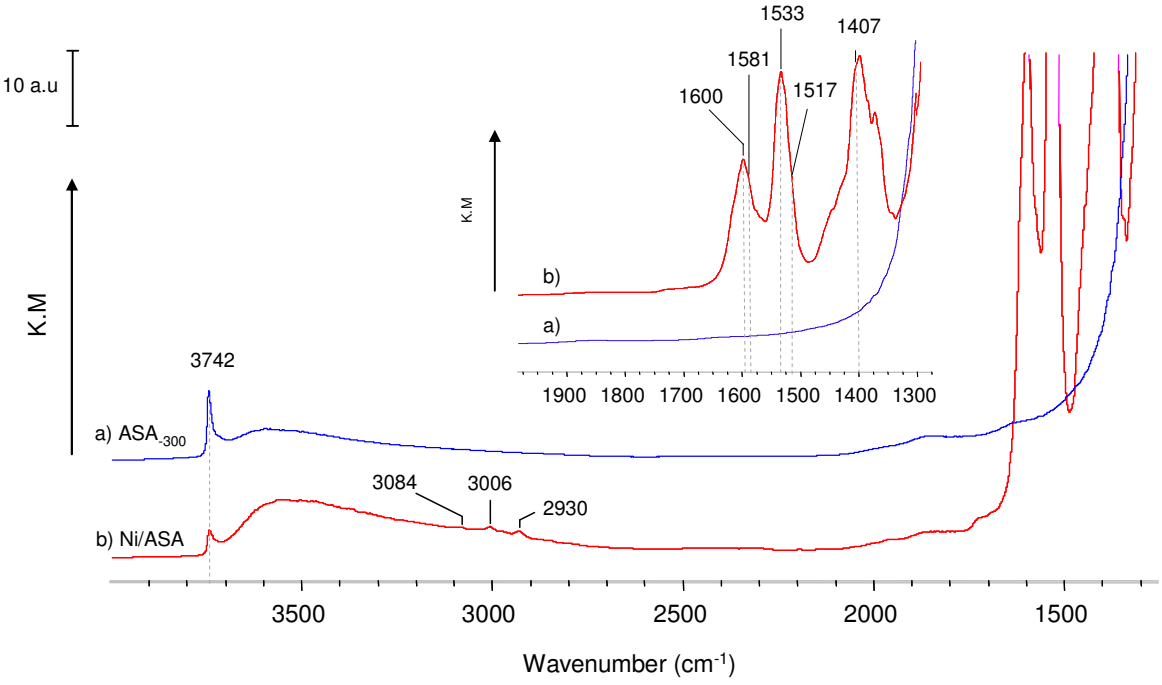

Figure 89: IR spectra (DRIFT) of a) ASA_{-300} and b) $Ni(acac)_2/ASA_{-300}$

For the preparation of supported NiW species, $Ni(acac)_2$ was first solubilised in hot toluene before subsequent impregnation on $[W(OEt)_5]_2$-*IWI*-1.7/ASA_{-300}. IR analysis of the resulting NiW

supported material, shown in **Figure 90-c**, highlights the presence of vibrations bands attributed to different surface species:

- ν(CH) and δ(CH) vibrations bands belonging to tungsten species are respectively observed at *ca.* {2975 – 2873} cm^{-1} and {1470 – 1376} cm^{-1} (reference spectrum: $[W(OEt)_5]_2$-*IWI*-1.7/ASA, **Figure 90-b**)
- ν(CO), ν(C=C) and δ(CH) vibrations bands belonging to nickel species are respectively visible at *ca.* 1600 cm^{-1} and 1517 cm^{-1} as well as 1407 cm-1 (reference spectrum: $Ni(acac)_2/ASA_{-300}$, see **Figure 90-a**)
- ν(CO) = 1533 cm^{-1} and ν(CO) = 1581 cm^{-1} are tentatively assigned to Hacac species, interacting with surface Al^{3+}. [Molina *et al.*, 1999]

Note that the previous IR vibration bands were attributed on the basis of IR analyses of the corresponding samples resulting from the impregnation of $[W(OEt)_5]_2$ (see part IV for details) and $Ni(acac)_2$ separately onto ASA.

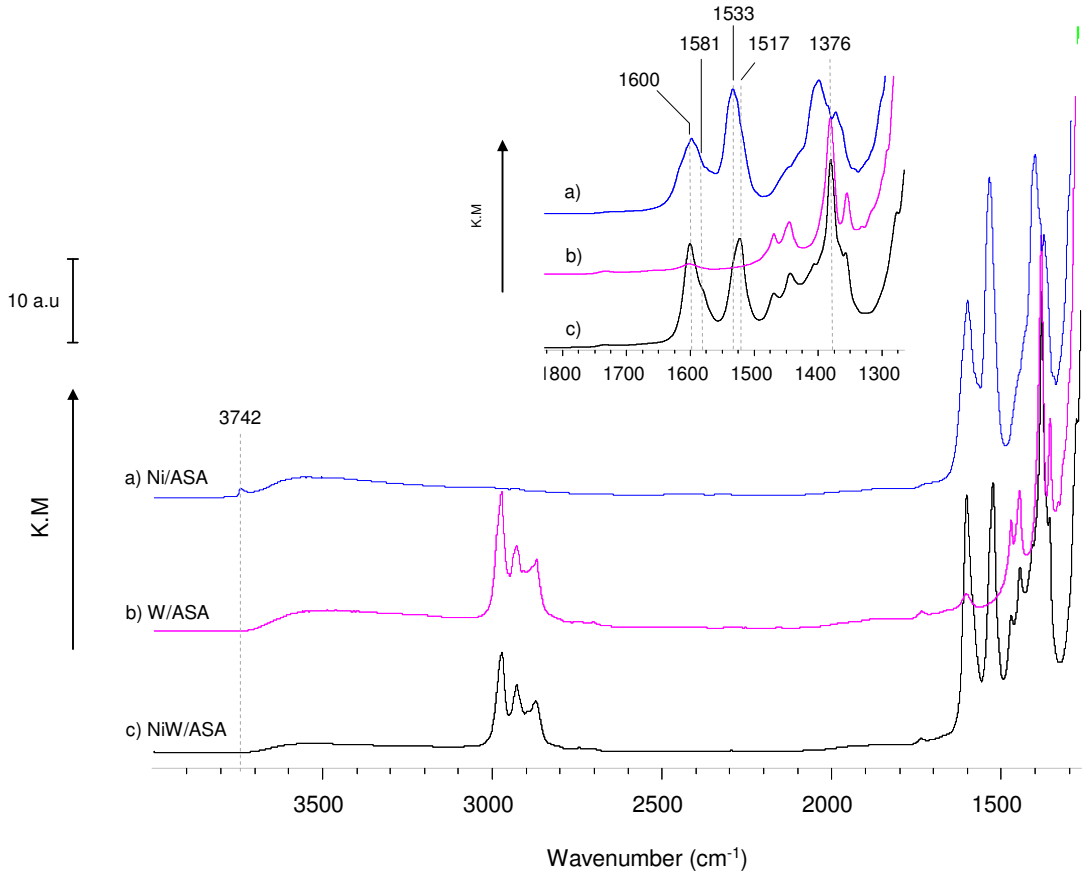

Figure 90: IR spectra of a) $Ni(acac)_2/ASA_{-300}$, b) $[W(OEt)_5]_2$-*IWI*-1.7/ASA_{-300} and c) $Ni(acac)_2$ deposited onto $[W(OEt)_5]_2$-*IWI*-1.7/ASA_{-300}

GC/MS analyses of the liquid phase after impregnation reveal the presence of ethanol and diethylether, while acetyl acetone is not detected. Adsorption of acetyl acetone on the support is also consistent with the work of Salinier *et al.* [Salinier *et al.*, 2009] in which grafting of $Zr(acac)_4$ on silica quantitatively yielded a well-defined monopodal species $(\equiv SiO)Zr(acac)_3$ with Hacac ligands strongly adsorbed on the silica support.

In the same spirit as in part IV, where supported surface W-species' structure was investigated, the structure of Ni and W surface species of the aforementioned supported NiW material is (shortly) discussed. While the reactivity of $Ni(acac)_2$ toward supported surface alkoxide species is unknown, its reaction with titanium alkoxo molecular complexes such as $Ti(OEt)_4$ in toluene is reported to give a $Ni_2Ti_2(acac)_4(OEt)_8$ solid, which crystal structure (XRD) revealed Ti and Ni atoms linked by μ-bridge ethoxy ligands (M-(OEt)-M', with M = Ti, Ni; M' = Ti, Ni). [Kessler *et al.*, 2006] If transposable to tungsten alkoxide complexes, this result would suggest the formation of a compound which formula would be $Ni_2W_2(acac)_4(OEt)_8$, and which structure, inspired from the work of Kessler *et al.*, is illustrated in **Figure 91-a**. As in this PhD, $Ni(acac)_2$ is impregnated on supported alkoxide W-species forming a multilayer ($[W(OEt)_5]_2$-*IWI*-1.7/ASA_{-300} material), the structure of resulting NiW surface species would probably be more complicated to elucidate than the one of species formed in a (more ideal) reaction in liquid phase; it would probably be due to several reactions possible such as (1) acac ligand removed from Ni coordination sphere and reacting with (a) Lewis acid sites of the support, or (b) surface alkoxide W-species (suggested by the release of EtOH in the liquid phase), or (2) reaction of $Ni(acac)_2$ with W-species belonging to the multilayer, that are either rather strongly bonded together (by μ-bridge ethoxy ligand, W-(OEt)-W) or more loosely bonded (by electrostatic interactions). Overall, supported NiW surface species probably contains Ni and W linked by μ-bridge ethoxy ligands, as proposed in **Figure 91-b,c**.

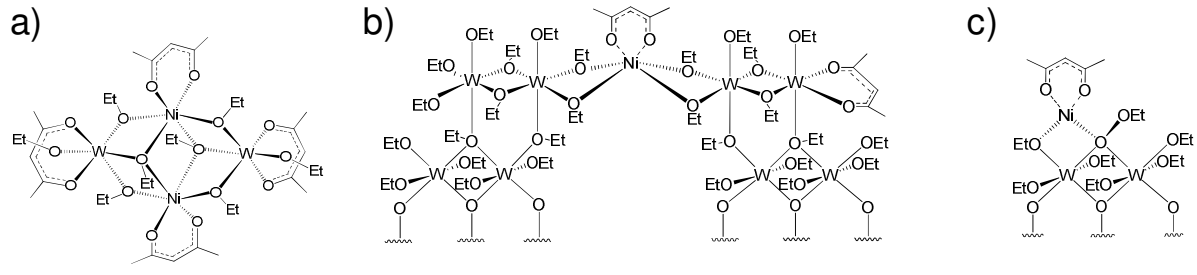

Figure 91: Proposition of structure for a) $Ni_2W_2(acac)_4(OEt)_8$; Surface species containing W and Ni: b) in case of several surrounding surface alkoxide W-species, with acac ligands on Ni or W; c) in case of more isolated surface alkoxide species.

VI.1.b. Characterisation of NiWS sulphide phases by X-ray photoelectron spectroscopy (XPS)

In this part, we show the characterisation of sulphided samples, initially prepared by successive impregnation of first, the W precursor, and then, the Ni one. XPS analyses were run to investigate the level of sulphidation ($\%_{rel.}$ WS_2) as well as the relative percentage of each nickel phases, *e.g.* the NiS phase, the NiO_x phase where Ni is strongly interacting with the ASA support, and finally the mixed phase "NiWS" ($\%_{rel.}$ NiWS), also referred as the promotion degree of the sulphide phase. To evaluate the influence of the CSC method, CSC NiWS phases will be compared to these prepared by conventional approaches.

Conventional dried materials were prepared following the general procedure, *e.g.* incipient wetness impregnation of an aqueous solution of ammonium metatungstate and nickel nitrate on ASA (co-impregnation), followed by a maturation step of 16 h, with subsequent drying at 120°C. Calcined materials were obtained by calcination of the aforementioned dried samples under air, at 450°C for 2 hours. These samples were sulphided at 350°C for 2 h, under a 15 $\%_{mol.}$ H_2S/H_2 mixture.

CSC materials were prepared by impregnation of Ni precursors ($Ni(1\text{-}MeCp)_2$, $Ni(acac)_2$ or $Ni(NO_3)_2$onto $[W(OEt)_5]_2$-IWI-1.7/ASA, and were dried under vacuum (10^{-5} mbar, 2 h). Then, they were sulphided at 350°C for 2 h, under a 15 $\%_{mol.}$ H_2S/H_2 mixture.

Note also the preparation of an additional sample by deposition of $Ni(acac)_2$ onto a conventional catalysts (dried, non-calcined sample referred to as "acac/W(POM)/ASA" where POM stands for polyoxometallate) to investigate the effect of supported W-species (used as support) on the characteristics of the sulphide phase after sulphidation under similar conditions.

For all the catalysts, prepared either by the CSC or conventional methods, tungsten and nickel coverages are calculated on the basis of the support surface area, which is *ca.* 228 m²/g. Tungsten loadings and experimental Ni/W atomic ratio are obtained from elemental analyses, unless otherwise stated.

The whole set of NiW supported materials thus underwent sulphidation at 350°C for 2 h, under a 15 $\%_{mol.}$ H_2S/H_2 mixture. Catalysts are referred as follows:

- NiWS ex. MeCp-*IWI*-0.2/$[W(OEt)_5]_2$-1.6/ASA_{-300} with 1.6 (±0.1) W/nm² and Ni/W ≈ 0.21
- NiWS ex. acac-*IWI*-0.2/$[W(OEt)_5]_2$-1.6/ASA_{-300} with 1.6 (±0.1) W/nm² and Ni/W = 0.21
- NiWS ex. NO_3-*IWI*-0.3/$[W(OEt)_5]_2$-1.5/ASA_{-300} with 1.5 (±0.1) W/nm² and Ni/W = 0.30

- NiWS / ASA ex conventional dried, with 1.8 (±0.1) W/nm² and Ni/W = 0.22
- NiWS / ASA ex conventional calcined, with 1.8 (±0.1) W/nm² and Ni/W = 0.22
- NiWS ex. acac-*IWI*-0.2/W(POM)-1.8/ASA, with 1.8 (±0.1) W/nm² and Ni/W = 0.22

Data obtained by decomposition of the W 4f, and Ni 2p photopeaks are summarized in **Table 15**. Note that decomposition of Ni 2p photopeaks has already been reported in previous studies [Guichard *et al.*, 2008]. An example of Ni 2p decomposition is shown in **Figure 92**.

Table 15: XPS data, obtained by decomposition of W 4f and Ni 2p photopeaks of NiWS/ASA catalysts. CSC ones were prepared by deposition of $Ni(acac)_2$ or $Ni(1\text{-}MeCp)_2$ or $Ni(NO_3)_2$onto $[W(OEt)_5]_2$-*IWI*-1.7/ASA_{-300}. Conventional ones were prepared by co-impregnation of $Ni(NO_3)_2$ and ammonium metatungstate. Additional sample prepared by impregnation of $Ni(acac)_2$ on a conventional dried W-oxide phase. Sulphidations *ex-situ* were carried out at 350°C, for 2 h, under a 15 $\%_{mol.}$ H_2S/H_2 mixture.

		$\%_{rel.}$ WS_2	$\%_{rel.}$ W(VI)	$\%_{rel.}$ W(intermed.)	W/Al at. ratio (x100)
CSC	*ex.* $Ni(acac)_2$	71	11	18	2.5
	ex. $Ni(1\text{-}MeCp)_2$	73	12	15	2.6
	ex. $Ni(NO_3)_2$	73	16	12	3.3
Conventional dried		73	12	15	2.7
Conventional calcined		56	24	20	3.0
ex. acac/W(POM)		69	15	16	2.7

		$\%_{rel.}$ NiWS	NiWS site / nm²	$(Ni/W)^a_{slab}$
CSC	*ex.* $Ni(acac)_2$	80	0.27 ± 0.04	0.33 ± 0.04
	ex. $Ni(1\text{-}MeCp)_2$	53	0.17 ± 0.03	0.25 ± 0.03
	ex. $Ni(NO_3)_2$	63	0.29 ± 0.04	0.23 ± 0.03
Conventional dried		66	0.26 ± 0.04	0.30 ± 0.03
Conventional calcined		57	0.23 ± 0.04	0.30 ± 0.03
ex. acac/W(POM)		7	0.03 ± 0.01	0.05 ± 0.01

[a] $(Ni/W)_{slab}$ is calculated using NiWS and WS_2 quantification results from XPS experiments.

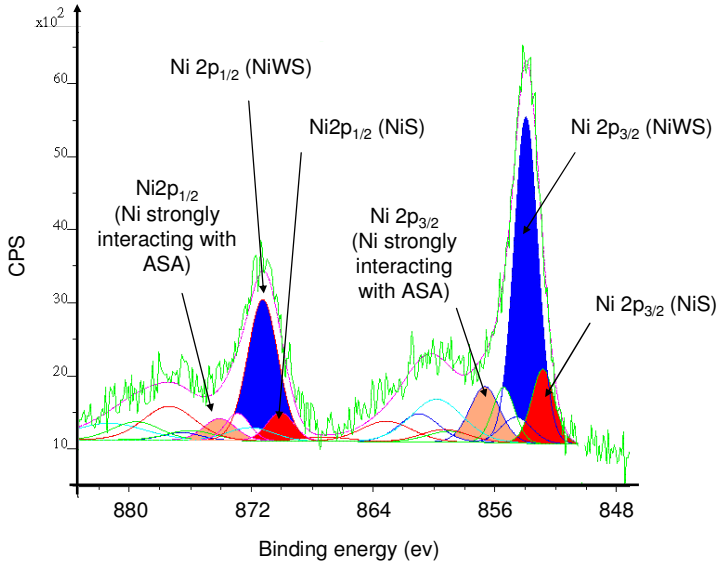

Figure 92: XPS spectrum. Ni 2p photopeak decomposition with 3 contributions: NiWS, NiS and Ni interacting with ASA, also referred as NiO_x. Additional peaks are satellites of the different Ni $2p_{3/2}$ and Ni $2p_{1/2}$ contributions. Calibration *vs.* C 1s at 284.6 eV.

Table 15 reveals that CSC catalysts exhibit similar levels of sulphidation ranging from 71 (±5) to 73 (±5) $\%_{rel.}$ WS_2, which is about 10 % lower than for the non-promoted WS_2/ASA catalysts prepared in part V. The relative amounts of W(VI) and intermediate phase W(V) are not significantly different from each other. The surface coverages of tungsten, as detected by XPS (W/Al), are also similar, except for the sample prepared with $Ni(NO_3)_2$ which exhibit a higher surface coverage of tungsten. Then, compared to the sample prepared with $Ni(1\text{-}MeCp)_2$, **the amount of active phases**, also called mixed phases "NiWS", are higher for catalysts prepared with $Ni(acac)_2$ and $Ni(NO_3)_2$, and lead to *ca.* 0.27 (±0.04) NiWS site/nm² and 0.29 (±0.04) NiWS site/nm² respectively. Note also that "NiWS site/nm²" stands for the amount of mixed site per nm², calculated in a first approximation by multiplying the nickel coverage Ni/nm² (elemental analyses) by the $\%_{rel.}$ NiWS (XPS). Only *ca.* 0.17 (± 0.03) NiWS sites/nm² are found for the $Ni(1\text{-}MeCp)_2$-based catalyst. Besides, catalysts were also compared with respect to their **nickel-to-tungsten atomic ratio in NiWS nanocrystallites**, denoted $\mathbf{(Ni/W)_{slab}}$. These data represent the amount of Ni incorporated in a mixed phase "NiWS", at a crystallite scale, and correspond experimentally to the amount of Ni engaged in a mixed phase "NiWS", divided by the amount of W in a WS_2 phase. In the table, sulphide slabs of the $Ni(acac)_2$-based catalyst are characterised by a higher $(Ni/W)_{slab}$ ratio, which is *ca.* 0.33 (± 0.04), while values ranging from 0.23 to 0.25 (± 0.03) are found when $Ni(NO_3)_2$ or $Ni(1\text{-}MeCp)_2$ are used as Ni precursors.

The improved incorporation of Ni in a mixed phase "NiWS" when using $Ni(acac)_2$ can be tentatively explained by the presence of well-dispersed Ni and W species on the surface, promoting an intimate contact between Ni atoms with W ones.

For conventional catalysts, the same trend as for non-promoted conventional ones is found: dried catalysts show higher level of sulphidation ($\%_{rel.}$ WS_2) and exhibit lower amount of W(VI) phase than their calcined counterparts, while their tungsten surface coverage of tungsten, detected by XPS, is similar. However, the amounts of NiWS site/nm² are not really affected by calcination of the sample, with 0.26 (± 0.04) NiWS site/nm² and 0.23 (± 0.04) NiWS site/nm² for the dried and the calcined samples respectively. A similar trend is observed for the nickel-to-tungsten ratio in tungsten sulphide slabs: $(Ni/W)_{slab}$ = 0.30 (± 0.03) for calcined and dried catalysts.

Note that the sample prepared by deposition of $Ni(acac)_2$ onto a conventionally prepared oxide phase (dried sample, earlier referred as W(POM)) exhibit a level of sulphidation close to that of CSC samples, but its promotion degree ($\%_{rel.}$ NiWS) is extremely low: the NiWS phase is thus barely present on this sample, in favour of the formation of a undesirable NiS phase.

Comparison of CSC and conventional catalyst show that their sulphide phase is similar in terms of sulphidation (close $\%_{rel.}$ WS_2, W/Al atomic ratio), except for the calcined sample, which undergo sulphidation in a lesser extent. While incorporation of nickel into the WS_2 phase (NiWS site.nm²) is rather similar for conventional catalysts and CSC ones prepared from $Ni(acac)_2$, and $Ni(NO_3)_2$, the sample prepared with $Ni(1\text{-}MeCp)_2$ reveals a lower amount of NiWS sites. Besides, deposition of $Ni(acac)_2$ onto W(POM) is finally the preparation which leads to the lower amount of NiWS sites.

VI.1.c. Characterisation of NiWS sulphide phases by Transmission electron microscopy (TEM)

TEM analyses were also performed to evaluate the average length and stacking number of WS_2 crystallites of NiWS catalyst. Analyses were performed on catalysts prepared by CSC ($Ni(acac)_2$ based sample only) or conventional approaches. The results, summarized in **Table 16**, reveal that the mean length of sulphide slabs (L) and their mean stacking number (N) is similar whatever the preparation method used, with L ≈ {3.6 - 3.7} nm and N ≈ 3.1. These results are similar to non-promoted WS_2 /ASA catalysts ones (see part V.1).

Table 16: Mean slabs length and mean slabs stacking number of NiWS/ASA catalysts with *ca.* {1.7 - 1.8} W/nm², Ni/W ≈ 0.2 (at/at)

	Mean slabs length L (nm)	Std dev.	Mean slabs stacking number N (nm)	Std dev.
CSC *ex.* $Ni(acac)_2$	3.7	1.1	3.1	1.4
Conventional dried	3.6	1.1	3.1	1.4
Conventional calcined	3.5	1.2	3.1	1.6

VI.1.d. Characterisation of NiWS sulphide phases by STEM-HAADF

We performed STEM-HAADF analyses on conventional calcined catalysts in order to: (1) identify the 2D morphology of the promoted WS_2 slabs, and (2) investigate the location of Ni atoms on the edges of the slabs, in the spirit of the previous work of Deepak *et al.* [Deepak *et al.*, 2011] on Co doped MS_2 (M = W, Mo) nanowire catalysts supported on Al_2O_3 .

First, we investigate the 2D morphology of WS_2 crystallites on a calcined catalyst with low tungsten loading, *e.g.* 0.5 (±0.1) W/nm², exhibiting a Ni/W atomic ratio of 0.19, after sulphidation at 600°C for 2 h with a H_2S/H_2 mixture (15 $\%_{mol.}$ H_2S). In the case of non-promoted WS_2 catalysts, STEM-HAADF micrograph of a calcined sample (see part V.1.e) shows a predominantly triangular shape of the metal sulphide phase. In contrast, **Figure 93** highlights a truncated hexagonal shape in the case of the addition of Ni promoter atoms. The images thus reveal a modification on the slab shape within the substitution of W atoms by Ni ones: a clear morphological change from a triangle to a roughly hexagonal shape was observed for the WS_2 slabs supported on amorphous silica-alumina, which is correlated to the presence of Ni promoter atoms.

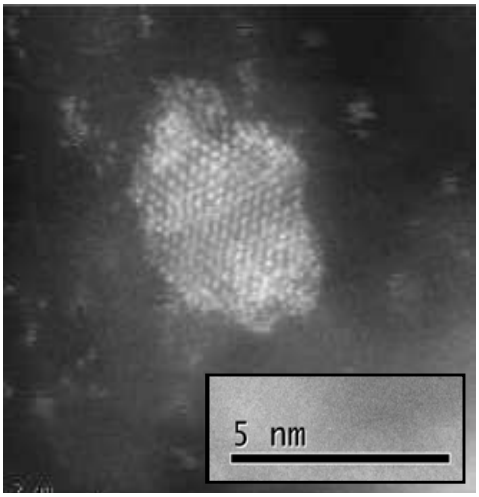

Figure 93: STEM-HAADF micrograph of a Ni-promoted WS_2 slabs, supported on ASA. Catalyst: NiWS/ASA with 0.5 W/nm², Ni/W ≈ 0.2 (at/at), prepared by a conventional method, calcined, and sulphided *ex-situ* at 600°c for 2 h under a mixture of H_2S/H_2. [from Girleanu *et al.*, *in preparation*].

In the same spirit as in part V.1.e for unpromoted WS_2 phases, DFT calculations were carried out to understand this phenomenon [Girleanu *et al.*, *in preparation*]. Considering the Ni-promoted WS_2 nanocrystallite, a combined effect of the promoter and the sulphur coverage on the edge energy is expected. As observed for the Ni promoted MoS_2 system [Schweiger *et al.*, 2002] Ni reveals peculiar effect on WS_2: the edge energy of the Ni promoted edges is significantly lower than the non-promoted one (**Figure 94**). This energy gain is induced by the substitution of some W atoms by Ni atoms at the edges as illustrated in **Figure 95**. This effect obviously depends on the type of edge: the S-edge energy decreases more significantly than the W-edge energy. For $\Delta\mu_S =$ -1.03 eV which corresponds to the sulphidation conditions used here (15 $\%_{mol.}$ H_2S/H_2 mixture and T = 600°C), the decoration of the W-edge by Ni is less favoured than the S-edge: **Figure 95** shows that the S-edge exhibits a Ni/W edge ratio close to 1/2 whereas it is close to 1/3 on the W-edge. This also implies that the $\frac{L_{W-edge}}{L_{S-edge}}$ decreases to 1.1: the W-edge length diminishes to the profit of the S-edge. The NiWS nanocristallite morphology is expected to become more hexagonal with respect to the previous WS_2 morphology as revealed by STEM.

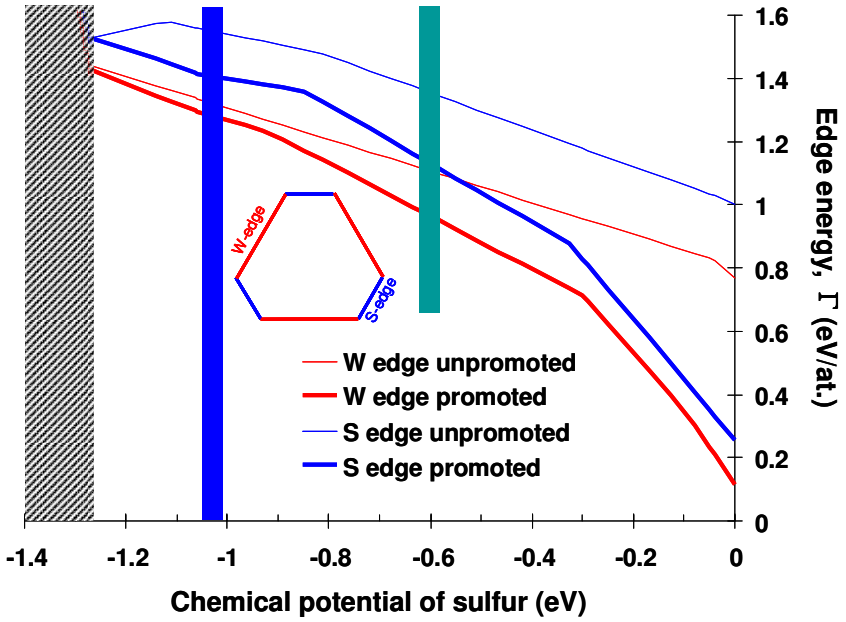

Figure 94: Evolution of the energy of the W-edge and S-edge as a function of the chemical potential of Sulphur in the experimental conditions. The vertical bars correspond to the three sulphiding conditions discussed in the main text (including our experimental ones). The dashed region represents the segregation domain of Ni

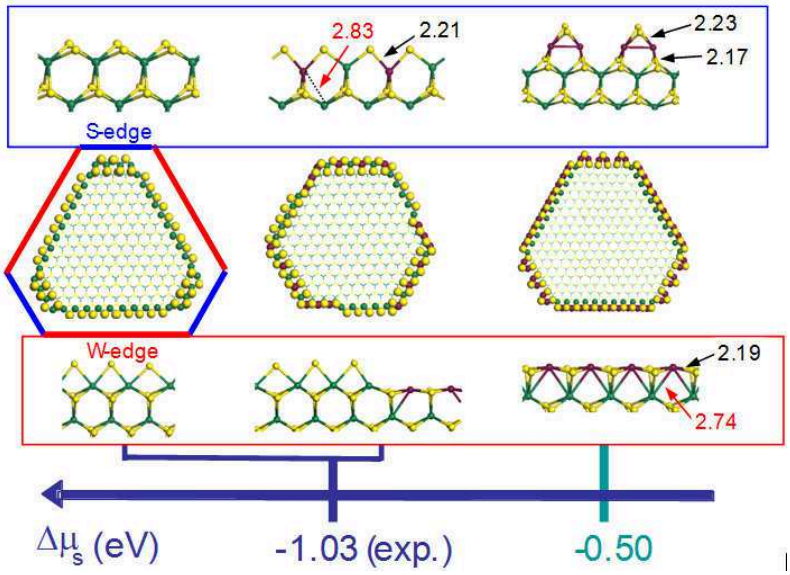

Figure 95: Molecular structure of the non-promoted WS_2 and NiWS nanocrystallites as a function of chemical potential of sulphur and the corresponding local edge structure. Ni-S (black) and Ni-W (red) distances are reported in Å. Note that the size used for representing the crystallite models are about 45 Å, *i.e.* close to the one observed by STEM and reported in Figure 93

Furthermore, the local coordination of W atoms is modified by the presence of neighbouring Ni atoms. In particular, the coordination number of W atoms located on the S-edge decreases to 4. On the W-edge, the W atom located in close vicinity of Ni has a coordination number to 5. The Ni atoms are mainly 4-fold coordinated. It must be underlined that the optimized Ni-S distances (2.19-2.23 Å) and Ni-W (2.74-2.85 Å) distances are in good agreement with former EXAFS data reported on NiWS catalyst supported either on carbon [Louwers *et al.*, 1993] or on silica-alumina. [van der Meer *et al.*, 2004; Kelly *et al.*, 2009] Moreover, as discussed by Kelly *et al.* [2009] the coordination number of Ni-atoms is found to be close to 4 with either a tetrahedral environment on the S-edge or a square planar one on the M-edge and on the S-edge depending on the chemical potential value (**Figure 95**). Similar Ni environment have been reported for NiWS [Sun *et al.*, 2004] and for NiMoS system. [Schweiger *et al.*, 2002, Raybaud *et al.*, 2000]

It can be added that according to **Figure 95**, different sulphidation conditions (higher chemical potential of sulphur, of about -0.50 eV), also lead to a similar morphological trend with a higher Ni/W ratio at both edges.

VI.1.e. Characterisation of NiWS sulphide phases by CO adsorption at low temperature (77K) monitored by IR spectroscopy - IR(CO)

CO adsorption at low temperatures, monitored by IR spectroscopy (transmission mode), was performed on the CSC NiWS/ASA catalyst prepared with $Ni(acac)_2$, and on conventional NiWS/ASA catalysts, dried or calcined, sulphided at 350°C (2 h, H_2S/H_2 mixture with 15 $\%_{mol.}$ H_2S). Note that as from the beginning of our study, a post treatment of 2 h at 250°C under argon is performed right after sulphidation in order to remove any traces of physisorbed H_2S.

IR(CO) spectra are shown in **Figure 96.** As in part V, only spectra collected at saturation of the sulphide phase with carbon monoxide are presented. Band attribution and data obtained from spectra analysis are summarized in **Table 17**. Attributions were based on the work of Zuo *et al.* [Zuo *et al.*, 2004] on alumina supported NiWS sulphide phases (400°C, 10% H_2S/H_2), conventionally prepared by calcination at 450°C of alumina supported NiW species, obtained by co-impregnation of nickel nitrate and ammonium metatungstate. CO stretching vibrations were assigned as follows: $\nu(CO)_{NiWS}$ at 2134 cm^{-1} and 2080 cm^{-1}, $\nu(CO)_{NiS}$ at 2100 cm^{-1} and $\nu(CO)_{WS2}$ at 2121 cm^{-1} and 2065 cm^{-1}. The CSC catalysts exhibit a spectrum where signals of CO interacting with NiWS and NiS are clearly visible, alongside with an additional shoulder attributed to CO interaction with WS_2. Besides, the broad peak observed for the calcined

catalyst only allows the clear assignment of CO interacting with NiWS. The broad tail situated at lower wavenumbers can be attributed to peaks of CO interacting with NiS and WS_2. Then, considering the broad peak obtained for the dried NiWS/ASA catalyst, interpretation must be taken cautiously. However, we can still highlight that CO interacting with a NiWS phase is observed at *ca.* 2136 cm^{-1}, in line with the results obtained for the other catalysts.

Further quantification of the amount of CO adsorbed, normalised by the number of W atom engaged in a WS_2 phase, reveals that the sulphide phase of the calcined catalyst adsorb about 3.4 times more CO than the dried one, and 1.6 times more CO than its CSC counterparts. These results are surprising as the previous IR(CO) analyses performed on unpromoted catalysts (see parts V.1.f.) show that the sulphide phase of the calcined one was barely interacting with CO. As a conclusion, the sulphide phase of CSC, conventional dried and conventional calcined NiWS/ASA catalysts are different in view of these IR(CO) analyses.

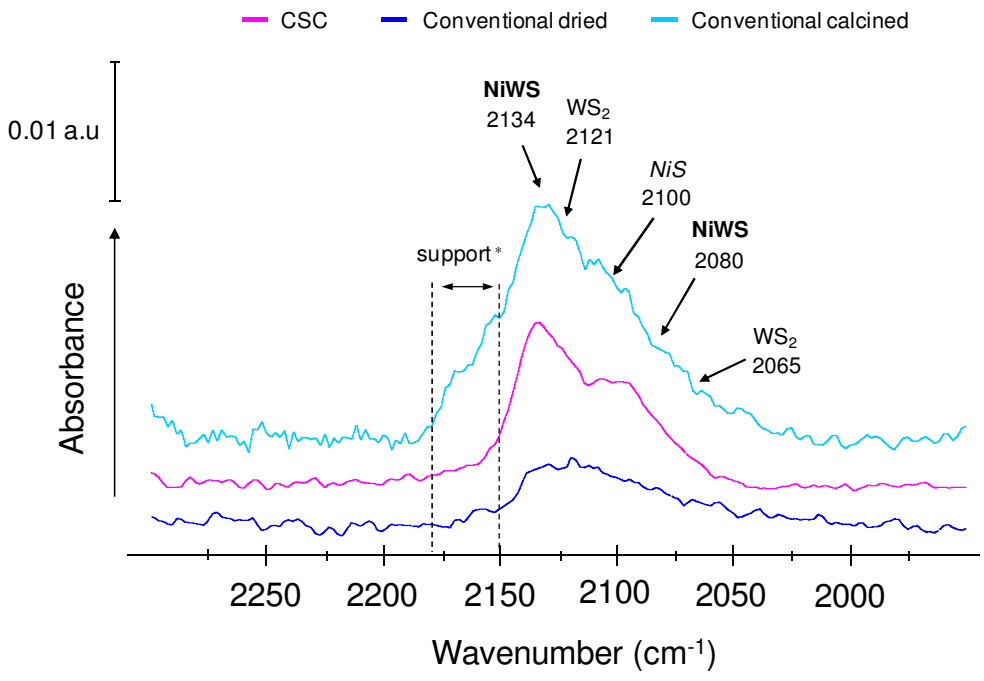

Figure 96: Infrared spectra of CO adsorbed at low temperature, IR(CO), on sulphided CSC (pink), conventional dried (blue) and calcined (light blue) NiWS/ASA catalysts. W-loading is *ca.* 1.7 W/nm². Sulphidations *ex-situ* were carried out at 350°C, 2 h, under a H_2S/H_2 mixture (15 $\%_{mol.}$ H_2S), before CO adsorption. * stand for interaction of CO with Lewis and/or Brønsted acid sites

Table 17: Data collected from IR(CO) spectra analyses. mol(W)* stands for "mole of W engaged in a WS_2 phase, calculated using $\%_{rel}$ WS_2 (XPS)

	ν(CO) interacting with					Integration [a]
	NiWS	NiS	WS_2	NiWS	WS_2	(a.u / cm / mol(W)*)
CSC	2134	2100	2121	2080	2065	3.1
Conv. dried	2131	2100	2120	2080	-	1.5
Conv. calcined	2136	2100	2124	-	-	5.1

[a] Integration is calculated with the total amount of CO adsorbed at saturation of the sulphide phase, and the mass of the pellet

VI.1.f. Influence of the Ni content on properties of NiWS phases: the case of $Ni(acac)_2/[W(OEt)_5]_2$/ASA sulphide samples

As previous characterisations of NiWS/ASA catalysts revealed that the CSC ones prepared with $Ni(acac)_2$ exhibited the highest amount of NiWS site/nm², and that preliminary catalytic tests revealed they were highly active, we decided to study the influence of the Ni/W atomic ratio on the promotion of the sulphide slabs using this Ni precursor. Therefore, we prepared 3 catalysts with increasing Ni content, *e.g.* increasing experimental Ni/W atomic ratios, by deposition of $Ni(acac)_2$ onto a CSC material: $[W(OEt)_5]_2$-*IWI*-1.7/ASA_{-300}.

Catalysts are referred as follows:

- NiW ex. acac-*IWI*-0.2/$[W(OEt)_5]_2$-1.6/ASA_{-300} with 1.6 W/nm² and Ni/W = 0.21
- NiW ex. acac-*IWI*-0.4/$[W(OEt)_5]_2$-1.5/ASA_{-300} with 1.5 W/nm² and Ni/W = 0.44
- NiW ex. acac-*IWI*-1.0/$[W(OEt)_5]_2$-1.5/ASA_{-300} with 1.5 W/nm² and Ni/W = 1.00

Note that the initial W-loading was 1.7 W/nm², but elemental analyses on the final materials revealed W-loading going from 1.6 to 1.5 W/nm² respectively. These lower $\%_{wt.}$ W amounts are attributed to the leaching of tungsten species during impregnation (extraction by toluene), even if performed with only a slight excess of solution with respect to pore volume. Indeed, we showed in part IV that at 1.7 W/nm², the CSC catalyst is covered by a multilayer of surface species *e.g.* a layer of species grafted on the surface; the additional layers are likely loosely bonded species, and can therefore be removed by additional step involving solvents.

VI.1.f.1. Characterisation by X-ray photoelectron spectroscopy (XPS)

The aforementioned catalysts underwent sulphidation at 350°C for 2 h, under a mixture of H_2S/H_2 (15 $\%_{mol.}$ H_2S), to give the 3 NiWS/ASA catalysts referred as:

- NiW**S** ex. acac-*IWI*-0.2/$[W(OEt)_5]_2$-1.6/ASA_{-300} with 1.6 W/nm² and Ni/W = 0.21
- NiW**S** ex. acac-*IWI*-0.4/$[W(OEt)_5]_2$-1.5/ASA_{-300} with 1.5 W/nm² and Ni/W = 0.44
- NiW**S** ex. acac-*IWI*-1.0/$[W(OEt)_5]_2$-1.5/ASA_{-300} with 1.5 W/nm² and Ni/W = 1.00

The catalysts were analysed by XPS. Data are summarized in **Table 18.** Note that independently of the Ni/W atomic ratio, the level of sulphidation is *ca.* 69 ± 2 $\%_{rel.}$ WS_2. The relative amount of W(VI) phase and partially sulphided phase (Wintermed.) as well as the tungsten coverage on the surface is more or less constant.

Table 18: XPS data, obtained by decomposition of W 4f and Ni 2p photopeaks of CSC NiWS/ASA catalysts prepared by deposition of $Ni(acac)_2$ onto $[W(OEt)_5]_2$-*IWI*-1.7/ASA_{-300} with W-loadings between 1.5 W/nm² and 1.6 W/nm², and Ni/W atomic ratio between 0.21 and 1.00. Sulphidations *ex-situ* were carried out at 350°C for 2 h, under a mixture of H_2S/H_2 (15 $\%_{mol.}$ H_2S).

W/nm²	Ni/W (at/at)	%rel. WS_2	%rel. W(VI)	%rel. W(intermed.)	W/Al at. ratio (x100)
1.6	0.21	71	11	18	2.5
1.5	0.44	67	13	20	2.2
1.5	1.00	69	13	18	2.4

W/nm²	Ni/W (at/at)	%rel. NiWS	NiWS site / nm²	$(Ni/W)^a_{slab}$
1.6	0.21	80	0.27 ± 0.04	0.33 ± 0.04
1.5	0.44	52	0.35 ± 0.05	0.57 ± 0.06
1.5	1.00	27	0.41 ± 0.06	0.50 ± 0.06

[a] $(Ni/W)_{slab}$ is calculated using NiWS and WS_2 quantification results from XPS experiments.

Figure 97 shows the evolution of the effective content of Ni ($\%_{wt.}$) in NiWS, NiS and NiO_x phases, where NiO_x stands for Ni strongly interacting with ASA, as a function of the experimental Ni/W ratio. The formation of NiS develops almost linearly when increasing the Ni/W ratio, while the amount of NiWS phase starts by increasing before reaching a plateau between Ni/W atomic ratios of *ca.* 0.6 to 0.7. These results are found to be similar to the ones reported for NiWS/ASA catalysts when prepared with higher W (thus Ni) content, *e.g.* 23-25 $\%_{wt.}$ W [Raybaud and Toulhoat, 2013, Ed. Technip, Paris, p255]. Besides, the effective content of NiO_x linearly increases. Finally, quantification of NiWS site/nm² (see **Table 18**) reveals that the sample with Ni/W = 1.00 (at/at) contains more Ni inserted in a mixed NiWS phase, thus more

potentially active sites. Note however that due to the high amount of nickel in the sample, a slight variation of $\%_{rel.}$ NiWS causes a rather important variation of NiWS/nm², possibly increasing the experimental error in our calculation. Nonetheless, it is still clear that the more Ni precursor is added, the more NiWS sites are formed, as previously reported for $NiMoS/Al_2O_3$ catalysts by Marchand *et al.* [2009]. Concomitant with the NiWS site/nm² increase, the nickel-to-tungsten ratio in sulphide crystallites (referred as $(Ni/W)_{slab}$) increases and reaches a maximum located between 0.57 (±0.06) and 0.50 (±0.06) for Ni/W ≥ 0.44 (at/at). Within the experimental error, it indicates that a maximal amount of Ni decorating the crystallites edges can be reached, due to a complete substitution of tungsten edge atoms by nickel ones, for a given 2D morphology and slabs length. Combining the 2D morphology of NiWS crystallites modelled by DFT calculations (part VI.1.d) and an average slab length of 35 Å (TEM analyses of these samples, sulphided at 350°C with 15% $_{mol.}$ H_2S/H_2, are discussed in the next part: VI.1.f.2) crystallites are fully decorated for $(Ni/W)_{slab}$ values of about 0.44. The experimental value, lying between 0.57 and 0.50, is thus compatible with the theoretical one, obtained with geometrical model combining DFT and TEM data. These models will be detailed in part VI.6. Note also that experimental values are compatible with the ones reported by Marchand *et al.* through DFT calculations and experimental results obtained on (Co)NiMoS supported phases $((Co)Ni/Mo)_{slab}$ ranging from 0.42 to 0.52 for crystallites of about 3.2 nm). [Marchand *et al.*, 2009]

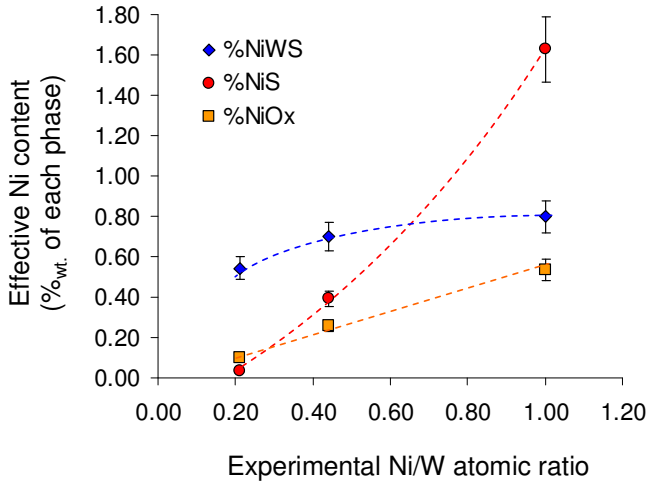

Figure 97: XPS data. Effective content of Ni in the different Ni phases: mixed phase NiWS, NiS and Ni strongly interacting with ASA (referred as NiO_x). NiWS/ASA catalysts prepared by deposition of $Ni(acac)_2$ onto $[W(OEt)_5]_2$-*IWI*-1.7/ASA_{-300} with W-loadings between 1.5 W/nm² and 1.6 W/nm², and Ni/W atomic ratio between 0.21 and 1.00. Sulphidations *ex-situ* were carried out at 350°C for 2 h, under a mixture of H_2S/H_2 (15 $\%_{mol.}$ H_2S).

VI.1.f.2. Characterisation by Transmission electron microscopy (TEM)

TEM analyses were performed on the 3 previous catalysts, and the results are shown in **Table 19**. While there are no large differences between the mean slabs length values, the slabs length slightly decreases from 3.7 nm to 3.3 nm when increasing the Ni/W atomic ratio. The stacking number is *quasi* steady with an average of about 2.9 crystallites stacked together, for all catalysts. These results are in line with the work of Zuo *et al* on $NiWS/Al_2O_3$ catalysts (*ca.* 3.2 W/nm², calcined at 450°C, before sulphidation at 400°C, 10 % H_2S/H_2), who reported a decrease of the slabs length, from 4.1 to 3.8 nm, respectively for Ni/W = 0.20 and Ni/W = 0.69 (at/at).[Zuo *et al.*, 2004] Moreover, considering a similar 2D morphology for NiWS crystallites of the 3 aforementioned samples, the decrease of the slabs length, observed when increasing the experimental Ni/W atomic ratio, infers an increase of the $(Ni/W)_{slab}$, ratio from *ca.* 0.40 to 0.48. This is in line with XPS results reported in part VI.1.f.1 which revealed a maximum lying between 0.50 and 0.57 (±0.06).

Table 19: Mean slabs length and mean slabs stacking number of NiWS/ASA catalysts prepared by deposition of $Ni(acac)_2$ onto $[W(OEt)_5]_2$-*IWI*-1.7/ASA_{-300} with *ca.* {1.5 - 1.6} W/nm² and Ni/W atomic ratio varying from 0.21 to 1.00 (at/at). Sulphidations *ex-situ* were carried out at 350°C for 2 h, under a mixture of H_2S/H_2.

W/nm²	Ni/W (at/at)	Mean slabs length L (nm)	Std dev.	Mean slabs stacking number N (nm)	Std dev.
1.6	0.21	3.7	1.1	3.1	1.4
1.5	0.44	3.5	1.2	2.7	1.1
1.5	1.00	3.3	1.1	2.9	1.3

VI.2. Impregnation of Ni-precursors onto a WS_2 phase, prepared at 350°C

In this part, we focus our study on the deposition of $Ni(acac)_2$ and $Ni(1\text{-}MeCp)_2$ directly on sulphided tungsten materials. This preparation method has already been described in the literature for different metals and different sulphide materials. For example, $Co(acac)_2$ was impregnated on MoS_2/Al_2O_3 catalyst [Roukoss *et al.*, CRC 2009], and $Ni(C_3H_5)_4$ was impregnated on WS_2/SiO_2 [Yermakov *et al.*, 1984, while $Co(CO)_3NO$ was deposited on MoS_2 catalysts supported on SiO_2 by chemical vapour deposition [Okamoto *et al.*, 2005, Okamoto *et al.*, 2009] or Al_2O_3 [Maugé *et al.*, 1989; Maugé *et al.*, 1992]. Note that catalysts prepared with this preparation method have revealed improved catalytic activities in thiophene

hydrodesulphurization compared to conventional deposition procedures using co-impregnation of aqueous solution containing cobalt (nickel) salt alongside with tungsten (molybdenum) precursors.

VI.2.a. Preparation and characterisation by IR spectroscopy

In this part, $Ni(1\text{-}MeCp)_2$ and $Ni(acac)_2$ were used to prepare NiWS/ASA catalysts where Ni precursors were deposited onto preformed sulphide phases. For each catalyst, the nickel precursor is deposited by incipient wetness impregnation (cyclohexane solution of $Ni(1\text{-}MeCp)_2$ or hot toluene solution of $Ni(acac)_2$, see experimental part) on a WS_2-1.7/ASA material, **previously sulphided at 350°C** for 2 h with a H_2S/H_2 mixture (15 $\%_{mol.}$ H_2S). After evacuation under vacuum, the solid is submitted to sulphidation a second time using the same conditions to give the final NiWS/ASA material. Catalysts are referred as follows:

- NiWS ex. MeCp-*IWI*-0.2/$WS_{2\_350°C}$-1.7/ASA_{-300} with 1.7 W/nm² and Ni/W = 0.20
- NiWS ex. acac-*IWI*-0.2/$WS_{2\_350°C}$-1.7/ASA_{-300} with 1.7 W/nm² and Ni/W = 0.20

Note that 0.2 refers to the Ni/W atomic ratio, and 1.7 refers to the W-loading, as stated in the previous chapters. On these samples the tungsten content is based on elemental analyses, while the nickel content used for calculations is based on the amount of precursor weighted in the impregnation solution, as no Ni elemental analyses have been obtained so far.

The catalyst prepared with $Ni(acac)_2$ has been studied by IR spectroscopy (transmission), before and after impregnation, as well as after subsequent sulphidation at 350°C. Besides, note that these two samples were analysed after dilution in low specific surface area α-alumina (< 10 m²/g) to improve the analysis quality (higher IR transparency of the sample pellet) without significantly adding surface OH groups. For reference, **Figure 98-a** shows the spectrum of the $WS_{2\_350°C}$/ASA catalyst, used as a support for the impregnation. Very low intensity ν(CH) vibrations between 2988 cm^{-1} and 2886 cm^{-1} as well as δ(CH) vibrations around 1448 cm^{-1} and 1400 cm^{-1}, tentatively attributed to traces of remaining tungsten surface species or remaining surface ethoxides. Traces of isolated silanols (ν(OH) = 3743 cm^{-1}) are visible, as well as physisorbed H_2O which probably comes from sample pollution before analysis. After impregnation, the IR spectrum, shown in **Figure 98-b**, exhibits the typical features of pure $Ni(acac)_2$ with ν(C=C) at 1520 cm^{-1}, ν(C=O) at 1607 cm^{-1} and 1595 cm^{-1} and δ(CH) between

1406 cm^{-1} and 1367 cm^{-1}. In addition, the ν(C=O) at 1533 cm^{-1} is attributed to Hacac in interaction with the surface. As discussed before, traces of isolated silanols are observed. We can thus say that after deposition of $Ni(acac)_2$ on WS_2/ASA, IR spectroscopy reveals that the nickel molecular precursor is in interaction with the ASA surface, but no feature of any direct interaction with WS_2 has been observed. After subsequent sulphidation, the IR spectrum, shown in **Figure 98-c**, illustrates that the ν(OH) vibration of isolated silanols are slightly more intense. Presence of small amount of these hydroxyls upon sulphidation reveals that if there are M-O-W linkages (M=Si, Al) between sulphide slabs and the surface, not 100 % of isolated silanols $SiOH_i$ are involved. Besides, no more IR bands attributed to acetylacetonato ligands of $Ni(acac)_2$ are visible, which means that the nickel precursor has been transformed, and that Ni belongs to either in NiWS, NiS or NiO_x phases.

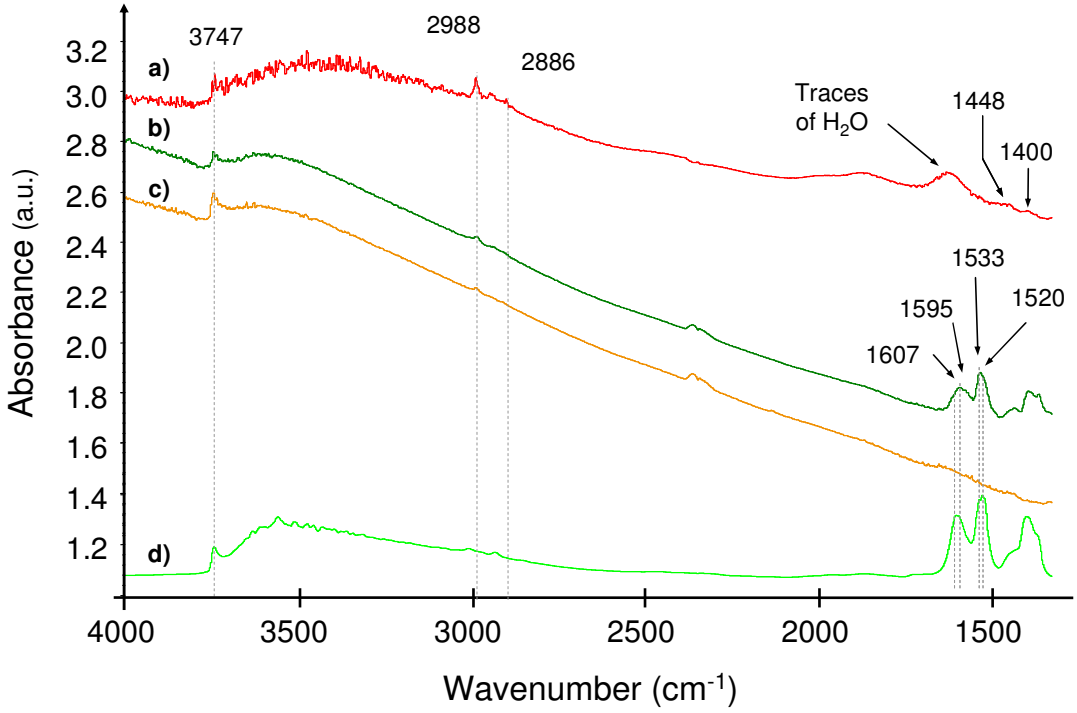

Figure 98: IR spectra of a) $WS_{2\_350°C}$-1.7/ASA_{-300}, b) $Ni(acac)_2$ deposited onto $WS_{2\_350°C}$-1.7/ASA_{-300}, c) NiWS ex.acac-*IWI*-0.2/$WS_{2-350°C}$-1.7/ASA_{-300} and d) $Ni(acac)_2$/ASA_{-300} as a reference spectrum.

VI.2.b. Characterisation by X-ray photoelectron spectroscopy (XPS)

Data collected from XPS analyses of the two NiWS catalysts are shown in **Table 20**. Similar level of sulphidation (*ca.* 84 $\%_{rel.}$ WS_2) is found for both samples. Note that these values match the highest $\%_{rel.}$ WS_2 found for non-promoted WS_2/ASA samples, in part V.2 (*e.g.* 85 (±5) $\%_{rel.}$ WS_2 for a sulphidation at 350°C), which is not surprising as the WS_2 phase has been generated by the pre-sulphidation step (350°C) before impregnation of the Ni precursor. In addition, their relative amount of W(VI) and partially sulphided phase (Wintermed.) do not exhibit large differences. The tungsten surface coverage is similar, with values typically lying within the ones found for NiWS/ASA catalysts prepared by deposition of the nickel precursor directly onto the tungsten surface species, as shown in **Table 15.**

Table 20: XPS data, obtained by decomposition of W 4f and Ni 2p photopeaks of NiWS ex. MeCp-*IWI*-0.2/$WS_{2\_350°C}$-1.7/ASA_{-300} and NiWS ex. acac-*IWI*-0.2/$WS_{2\_350°C}$-1.7/ASA_{-300}. Sulphidation carried out at 350°C, for 2 h with a H_2S/H_2 mixture (15 $\%_{mol.}$ H_2S)

		$\%_{rel.}$ WS_2	$\%_{rel.}$ W(VI)	$\%_{rel.}$ W(intermed.)	W/Al at. ratio (x100)
CSC	*ex.* $Ni(acac)_2$	84	7	9	2.8
	ex. $Ni(1\text{-}MeCp)_2$	83	10	7	3

		$\%_{rel.}$ NiWS	NiWS site / nm²	$(Ni/W)^a_{slab}$
CSC	*ex.* $Ni(acac)_2$	45	0.15 ± 0.02	0.17 ± 0.02
	ex. $Ni(1\text{-}MeCp)_2$	44	0.15 ± 0.02	0.17 ± 0.02

[a] $(Ni/W)_{slab}$ is calculated using NiWS and WS_2 quantification results from XPS experiments.

For both catalysts, the relative amount of NiWS phase is analogous and leads to *ca.* 0.15 ± 0.02 NiWS site/nm² for each catalyst. The nickel-to-tungsten atomic ratio in NiWS slabs, $(Ni/W)_{slab}$, is also similar: $(Ni/W)_{slab}$ = 0.17.

VI.2.c. Characterisation by Transmission electron microscopy (TEM)

TEM experiments have only been performed on the sample prepared with $Ni(acac)_2$. The analysis reveals that the mean slabs length is *ca.* 4.0 nm and that the mean stacking number is *ca.* 3.4. These values are slightly higher than the ones found for the catalysts previously analysed (see **Table 16** and **Table 19**).

As explained in part VI.1.d, the edge energy of the Ni promoted edges is significantly lower than the non-promoted ones, which should stabilise edges with less edge atoms, *e.g.* leading to smaller slabs. This effect should preferentially occur if Ni and W precursors are added simultaneously such as during co-impregnation and if they undergo sulphidation simultaneously. However, NiWS catalysts analysed in this part were prepared by deposition of Ni onto a pre-formed WS_2 phase (350°C, 2 h, 15 %mol. H_2S/H_2). Without the promoter, crystallites of the pre-formed WS_2 phase exhibit a longer mean slabs length. We suspect that the subsequent deposition of Ni followed by sulphidation at 350°C (2 h, 15 $\%_{mol.}$ H_2S/H_2) does not influence the length of WS_2 crystallites, which have been settled down at the pre-sulphidation step of the W precursor.

Then, observing longer and more stacked slabs after several sulphidations can possibly indicate that only one *ex-situ* sulphidation of 2 h at 350°C with a 15 $\%_{mol.}$ H_2S/H_2 mixture is not sufficient to stabilize the slabs length and stacking. This assumption would suggest that any interpretation of catalytic activity using the slabs length and stacking number obtained on fresh catalysts has to be taken cautiously. Indeed, it would be more accurate to perform XPS and TEM analyses on spent catalysts, and interpret data to get the amount of sulphided and promoted phase, as well as mean length and stacking number of slabs. In our study of NiWS/ASA catalysts with W-loadings between 1.7 and 1.8 W/nm², XPS analyses were performed on spent catalysts but no exhaustive TEM analyses were conducted. However, TEM analyses of fresh and spent NiWS/ASA catalysts prepared by CSC or conventional methods, and which contain *ca.* 3.5 W/nm², with Ni/W = 0.2 (at/at), revealed that the slabs length and stacking number observed on spent catalysts were little higher than on fresh ones. In particular, length and stacking number of slabs showed to be less than 10 % higher on spent catalysts, compared to fresh ones. Therefore, we decided not to perform TEM analyses on spent catalysts, assuming that less than 10 % of variation was lying within the uncertainty of the analyses.

VI.3. Impregnation of a Ni-precursor onto a WS_2 phase, prepared at 23°C: study of the influence of the Ni content

In this part, we try to control the morphology and in particular, the length of the WS_2 crystallites by taking advantage of a low sulphidation temperature used on CSC catalyst. Previously, we have shown that sulphidation of 23°C (part V.2) enabled to trigger off little sulphided particles which size was lower or equal to 3.2 nm on CSC catalysts (at least for the corresponding amount of pre-sulphided WS_2 crystallites). We decided to incorporate nickel at this stage, in order to block the growth of future WS_2 slabs using the edge stabilisation provided by Ni addition on WS_2 crystallite edge (as quantified by DFT).

We study the influence of the Ni loading of catalysts prepared by deposition of $Ni(acac)_2$ onto a sulphided material, **prepared at 23°C** (2 h, 15 $\%_{mol.}$ H_2S/H_2). Indeed, we showed in part V that sulphidation of the CSC material $[W(OEt)_5]_2$-*IWI*-1.7/ASA_{-300}, at room temperature in these conditions gives a WS_2/ASA catalyst which exhibits *ca.* 50 $\%_{rel.}$ WS_2, with small WS_2 crystallites of about 3.2 nm along with several nanosized spot-like entities (1 nm to 2 nm). *Via* deposition of nickel onto such a material, we suppose that we could obtain:

- smaller sulphide slabs compared to the previously analysed NiWS catalysts. Indeed, promoted catalysts are known to be covered by smaller slabs than their unpromoted counterparts [Baubet, PhD thesis, Lyon, 2013]. This is due to a "promoter effect" which reduces the size of MS_2 crystallites (M = Mo, W) by diminishing their edge energy. We thus tried to deposit Ni on the small slabs and nanosized entities found on the WS_2/ASA catalyst sulphided at 23°C to prepared promoted slabs for which growth would be somehow limited by the promoter, even at low Ni/W atomic ratio, as illustrated in **Figure 99.**
- a better promotion of the sulphide phase, as sulphidation of tungsten at 23°C is incomplete. Indeed, sulphide species (WO_xS_y or WS_2) are supposed not to be well organized (few WS_2 slabs visible, presence of nanosized spot-like entities) or crystallised, and Ni could also be incorporated in the WS_2 matrix more easily.

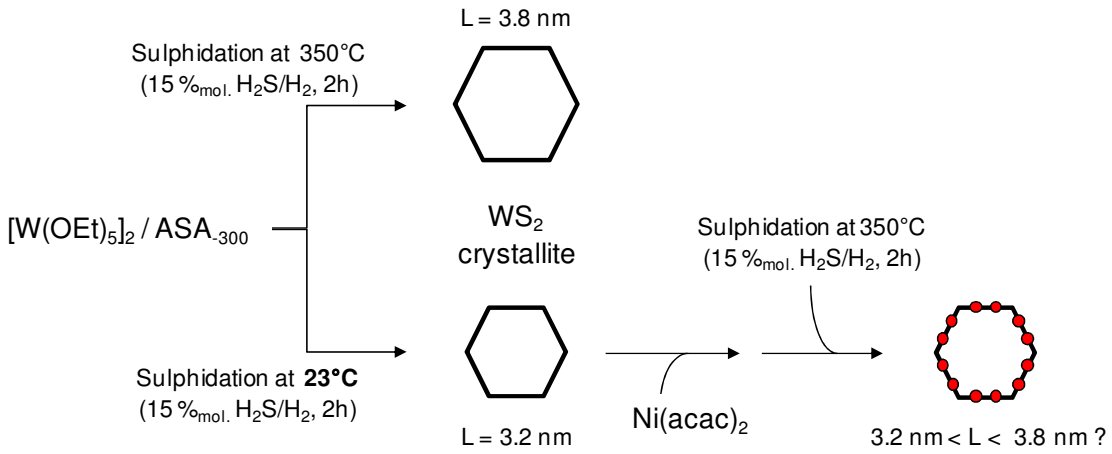

Figure 99: Schematic representation of the expected edge effect of Ni on WS_2 crystallites (T_{sulph} = 23°C) by the Ni promoter. Hexagons stand for WS2 crystallites. Red balls stand for Ni atoms.

VI.3.a. Characterisation by X-ray photoelectron spectroscopy (XPS)

3 catalysts were prepared with increasing Ni/W atomic ratios, by impregnation of $Ni(acac)_2$ (in hot toluene) on a sulphide phase originating from sulphidation of $W(OEt)_5]_2$-*IWI*-1.7/ASA_{-300} at 23°C (2 h, 15 $\%_{mol.}$ H_2S/H_2). Catalysts are referred as follows:

- NiWS ex. acac-*IWI*-0.2/$WS_{2\_23°C}$-1.6/ASA_{-300} with 1.6 W/nm² and Ni/W = 0.24
- NiWS ex. acac-*IWI*-0.5/$WS_{2\_23°C}$-1.6/ASA_{-300} with 1.6 W/nm² and Ni/W = 0.44 [(a)]
- NiWS ex. acac-*IWI*-0.9/$WS_{2\_23°C}$-1.5/ASA_{-300} with 1.5 W/nm² and Ni/W = 0.85

where [(a)] refers to a sample for which the Ni content is based on the amount of Ni added in the impregnation solution, and needs to be confirmed by elemental analyses.

XPS data are summarized in **Table 21**. These catalysts exhibit levels of sulphidation ranging from 74 (±5) to 78 (±5) $\%_{rel.}$ WS_2, which is slightly higher than the sample prepared by deposition of $Ni(acac)_2$ on supported alkoxides, with 71 (±5) $\%_{rel.}$ WS_2 (see part VI.1.b). In addition, they are slightly lower than the level of sulphidation of the sample prepared by addition of $Ni(acac)_2$ on $WS_{2\text{-}350°C}$/ASA, *e.g.* 84 (±5) $\%_{rel}$ WS_2 (see part. VI.2.b.). Besides their relative amount of W(VI) and partially sulphided phase (Wintermed.) do not show large differences. The tungsten surface coverage (W/Al) is similar, with values slightly greater than that found for NiWS/ASA catalysts prepared by deposition of the nickel precursor directly onto the supported

alkoxides species (see **Table 15**). It indicates that W is slightly more dispersed on the ASA surface for these catalysts, which probably originates from the high tungsten coverage of the surface, observed on supported alkoxides materials, in part V.1.b. The well-dispersed tungsten phase, which is not sulphided after pre-sulphidation at 23°C (*ca.* 40 $\%_{rel.}$ from XPS analyses in part V.2.a), can thus gently spread over the ASA surface upon the second sulphidation step (subsequently performed after Ni addition).

Table 21: XPS data, obtained by decomposition of W 4f and Ni 2p photopeaks of CSC NiWS/ASA catalysts prepared by deposition of $Ni(acac)_2$ onto $WS_{2\_23°C}$-1.7/ASA_{-300} , pre-sulphided at 23°C. With W-loadings between 1.5 W/nm² and 1.6 W/nm², and Ni/W atomic ratio between 0.24 and 0.85. Sulphidations *ex-situ* were carried out at 350°C for 2 h, under a mixture of H_2S/H_2.

W/nm²	Ni/W (at/at)	%rel. WS_2	%rel. W(VI)	%rel. W(intermed.)	W/Al at. ratio (x100)
1.6	0.24	78	11	11	2.8
1.6 [a]	0.44 [a]	74	11	15	2.9
1.5	0.85	75	13	12	3.1

[a] To be confirmed by elemental analyses

W/nm²	Ni/W (at/at)	%rel. NiWS	NiWS site / nm²	$(Ni/W)^b_{slab}$
1.6	0.24	53	0.21 ± 0.03	0.27 ± 0.03
1.6 [a]	0.44 [a]	41	0.30 ± 0.05	0.41 ± 0.05
1.5	0.85	10	0.13 ± 0.02	0.16 ± 0.02

[a] To be confirmed by elemental analyses
[b] $(Ni/W)_{slab}$ is calculated using NiWS and WS_2 quantification results from XPS experiments.

Figure 100 shows the evolution of the effective Ni content in NiWS, NiS and NiO_x phases. The formation of NiS and NiOx (Ni strongly interacting with the ASA support) phases develop almost linearly when increasing the experimental Ni/W ratio. On the contrary, when increasing this Ni/W atomic ratio, the amount of NiWS phase increases before reaching a maximum for an experimental Ni/W atomic ratio of 0.4 - 0.5, and then decreases. Then the quantification of NiWS site/nm² reveals that the catalyst prepared with Ni/W = 0.44 exhibits the highest amount of NiWS site/nm², estimated to be 0.30 NiWS site/nm². The $(Ni/W)_{slab}$ follows the same trends as the amount of NiWS sites: when increasing the Ni/W atomic ratio, $(Ni/W)_{slab}$ increases from 0.27 to 0.41 and then decreases until reaching *ca.* 0.16. Finding a decrease of the amount of the NiWS phase at high Ni content can be tentatively explain as follows: when deposited on a sulphide phase, whatever the pre-sulphidation temperature, the Ni precursor hardly react with the sulphide phase, and is poorly dispersed on the surface; subsequent sulphidation promotes the incorporation of Ni in a mixed phase "NiWS", concomitantly with the formation of non

negligible amount of NiS and NiOx phases. For low Ni content, the formation of unwanted Ni phases is not predominant. However, at high Ni contents, when higher amount of poorly dispersed nickel precursor is deposited, incorporation of Ni into a mixed phase is harder, thus promoting the formation of undesirable NiS (predominantly) and NiOx phases.

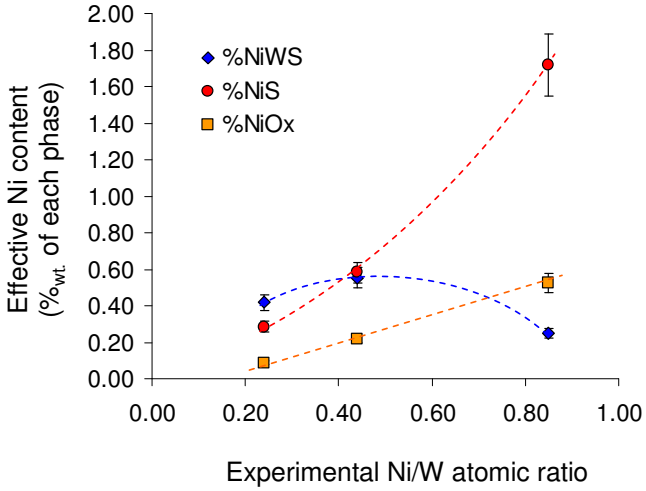

Figure 100: XPS data. Effective content of Ni in the different Ni phases: mixed phase NiWS, NiS and Ni strongly interacting with ASA (referred as NiO_x). NiWS/ASA catalysts prepared by deposition of $Ni(acac)_2$ onto $WS_{2\_23°C}$-1.7/ASA_{-300}, pre-sulphided at 23°C. With W-loadings between 1.5 W/nm² and 1.6

VI.3.b. Characterisation by Transmission electronic microscopy (TEM)

TEM analyses were performed and data are summarized in **Table 22**. The mean slabs length of the catalyst prepared with Ni/W = 0.24 (at/at) is *ca.* 3.5 nm. This value hardly changes upon increasing the Ni/W atomic ratio. The same trend is observed for the stacking number of WS_2 crystallites, which is close to 2.8, whatever the Ni/W ratio. The mean length and mean stacking layer distributions, obtained with the bar graphs of each catalyst (see appendices), subsequently fitted with a log-normal law, are shown in **Figure 101**. As they are *quasi* identical, we can assume that the length and stacking number distribution are similar for all catalysts.

Note that one objective of this study is to identify if adding nickel on pre-formed small WS_2 crystallites could limit their growth upon sulphidation. The starting $WS_{2\_23°C}$-1.7/ASA_{-300} material used as "support" exhibits slabs length of *ca.* 3.2 nm. Then, with all the previous TEM analyses on CSC NiWS/ASA catalysts, the average value of WS_2 slabs length is *ca.* 3.6 nm, which is similar to the values found here. It means that the length of NiWS crystallites is not significantly

different when samples, sulphided at 350°C, are initially prepared by successive impregnation of $Ni(acac)_2$ on either supported alkoxide species or on sulphide ones, prepared at 23°C. However, note that this preparation method enables the preparation of smaller slabs than when a sulphide material prepared at 350°C is used as a support (3.5 nm *vs.* 4.0 nm).

Table 22: Mean slabs length and mean slabs stacking number of NiWS/ASA catalysts prepared by deposition of $Ni(acac)_2$ onto $WS_{2\_23°C}$-1.7/ASA_{-300} pre-sulphided at 23°C.with W-loadings between 1.5 W/nm² and 1.6 W/nm², and Ni/W atomic ratio between 0.24 and 0.85. Sulphidations *ex-situ* were carried out at 350°C for 2 h, under a mixture of H_2S/H_2.

W/nm²	Ni/W (at/at)	Mean slabs length L (nm)	Std dev.	Mean slabs stacking number N (nm)	Std dev.
1.6	0.24	3.5	1.2	2.8	1.3
1.6 [a]	0.44 [a]	3.6	1.1	3.0	1.5
1.5	0.85	3.7	1.2	2.8	1.3

[a] Elemental analyses are underway

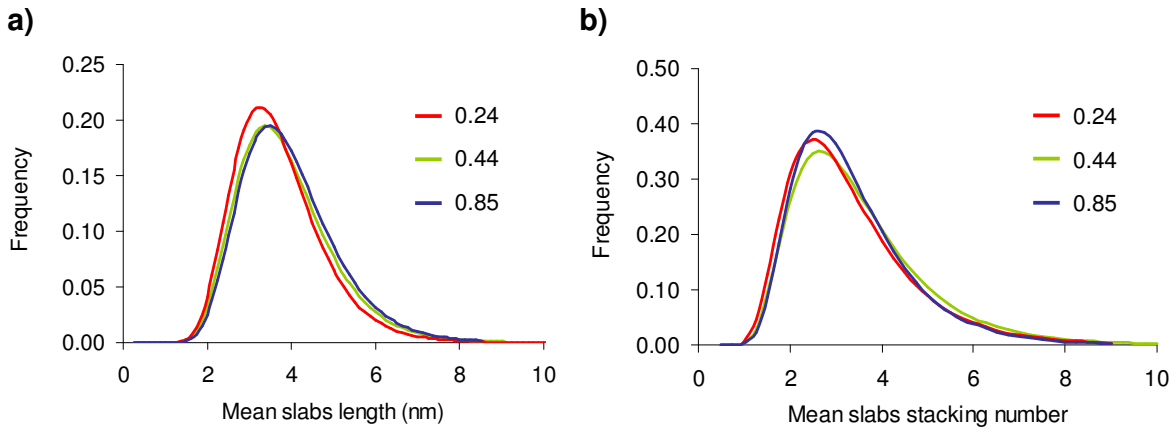

Figure 101: Mean length distribution (a) and mean slabs stacking layer distribution (b) of WS_2 crystallites of NiWS/ASA catalysts prepared by deposition of $Ni(acac)_2$ onto $WS_{2\_23°C}$-1.7/ASA_{-300} pre-sulphided at 23°C.with W-loadings between 1.5 W/nm² and 1.6 W/nm², and Ni/W atomic ratio of 0.24, 0.44 and 0.85. Sulphidations *ex-situ* were carried out at 350°C for 2 h, under a mixture of H_2S/H_2.

VI.4. Characterisation of spent catalysts

In order to interpret the catalytic results, it is more accurate to use data collected from analyses of spent catalysts, especially XPS ones. Therefore, XPS analyses was carried out on catalysts recovered after toluene hydrogenation in the presence of aniline (vide infra, part VII.5). This part only discusses the characterisation of the sulphide phase. XPS data were obtained by decomposition of W 4f and Ni 2p photopeaks. The results are summarized in **Table 23**.

After catalytic tests, all CSC catalysts prepared by deposition of nickel onto supported alkoxide species exhibit nearly the same level of sulphidation, comprised between 72 $\%_{rel.}$ WS_2 and 81 $\%_{rel.}$ WS_2. Conventional catalysts show a similar amount of sulphide phase, with 77 $\%_{rel.}$ and 74 $\%_{rel.}$ WS_2 for the dried and the calcined ones, respectively. These values are not significantly different from fresh catalysts for the conventional dried sample, as for CSC catalysts prepared with experimental Ni/W atomic ratios of 0.2. However, for Ni/W = 0.44 (at/at) or Ni/W = 1.00, levels of sulphidation are significantly improved during the catalytic test, by conversion of both W(VI) and the intermediate phase W(V) into WS_2. The sample prepared by deposition of Ni onto a sulphide material, *e.g.* $WS_{2\_350°C}$, exhibits the same $\%_{rel.}$ WS_2 before and after test, at *ca.* 85 $\%_{rel.}$ WS_2.

Regarding the tungsten coverage on the ASA surface (W/Al at/at), it is, in average, slightly decreased but the differences with fresh samples are not really significant.

More interesting, NiWS, NiS and NiO_x phases can be strongly impacted by the catalyst and its experimental Ni/W atomic ratio. Indeed, the promotion level, *e.g.* the amount on nickel incorporated in a mixed phase "NiWS" ($\%_{rel.}$ NiWS) decreases from 80 $\%_{rel.}$ to 65 $\%_{rel.}$ for the CSC catalysts prepared by impregnation of $Ni(acac)_2$ onto $[W(OEt)_5]_2$/ASA with Ni/W = 0.2 (at/at), before and after test. This decrease takes place in favour of the formation of a NiS phase which relative amount increases from 5 $\%_{rel.}$ to 26 $\%_{rel.}$ A similar but weaker phenomenon is observed for the conventional dried material, which loses 14 $\%_{rel.}$ of NiWS. For these samples, it seems like the sulphidation occurring during the catalytic test lower the amount of Ni incorporated into a "NiWS" phase. On the contrary, two catalysts show significantly improved level of promotion, with an increase of 13 $\%_{rel.}$ and 18 $\%_{rel.}$ respectively for the CSC catalyst prepared with $Ni(1\text{-}MeCp)_2$, and for the catalyst prepared by impregnation of $Ni(acac)_2$ onto a $W_{(POM)}$/ASA support (*e.g.* a conventional dried oxide phase). This nickel migration between the different phases occurs at the expense of the NiS one. It means that in these last two cases, the sulphidation taking place during the test favours the transfer of nickel

atoms from NiS particles to WS_2 slabs. The other catalysts that were tested exhibit no significant changes.

Moreover, the comparison of the amount of NiWS site/nm² (see **Figure 102**) on fresh and spent catalysts shows that NiWS catalysts mainly exhibit lower amounts of NiWS site per nm² after the catalytic test, except for the samples prepared by deposition of $Ni(1\text{-}CpMe)_2$ on the CSC material (supported alkoxide species) and the catalyst prepared by impregnation of $Ni(acac)_2$ onto $W_{(POM)}$/ASA. For these two catalysts, the number of NiWS site/nm² after test is respectively 0.32 and 0.10 site/nm². For the other ones, we find between 0.17 and 0.33 NiWS sites per nm².

Similar results are obtained when plotting the Ni-to-W atomic ratio in NiWS crystallites (see **Figure 103**): all NiWS/ASA catalysts display lower $(Ni/W)_{slab}$ values except for the two specific ones detailed just above. Finally, we see that after the HYD test, all the Ni-to-W atomic ratio in NiWS crystallites are lying between 0.12 and *ca.* 0.40, values respectively found for $Ni(acac)_2$-0.2/$W_{(POM)}$/ASA and $Ni(acac)_2$/$[W(OEt)_5]_2$/ASA with Ni/W between 0.44 and 1.00 at/at.

Finally, note that analyses of spent catalysts initially prepared by deposition of $Ni(acac)_2$ on a sulphide material prepared at 23°C are underway.

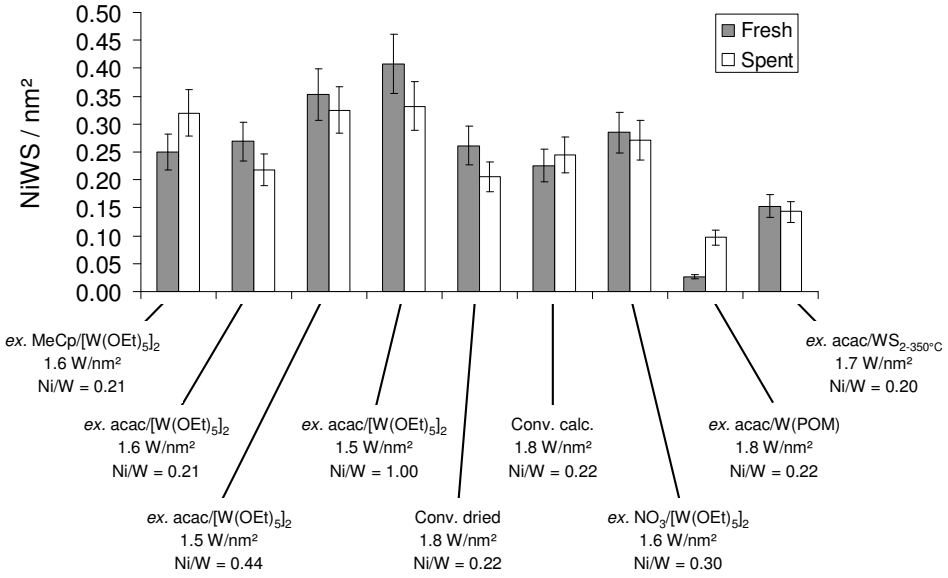

Figure 102: Comparison of the amount of mixed site per nm² for NiWS catalysts before (fresh) and after (spent) toluene hydrogenation. Data obtained from calculations based on NiWS (XPS) and Ni (elemental analyses) quantification.

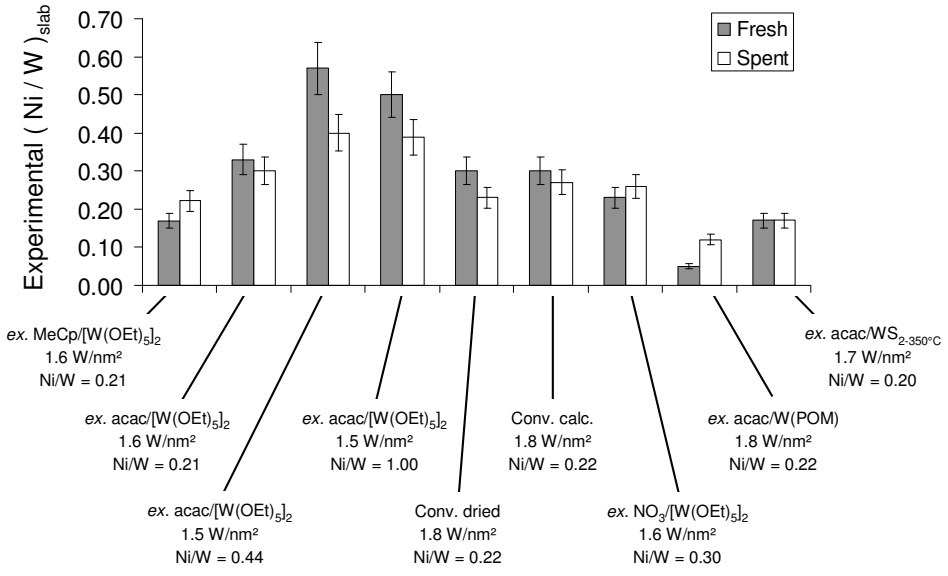

Figure 103: Comparison of the experimental Ni-to-W atomic ratio in NiWS crystallites for NiWS catalysts before (fresh) and after (spent) toluene hydrogenation. Data obtained from calculations based on NiWS and WS_2 quantification (XPS)

	ex. $Ni(1\text{-}MeCp)_2/[W(OEt)_5]_2$		*ex.* $Ni(acac)_2/[W(OEt)_5]_2$		*ex.* $Ni(acac)_2/[W(OEt)_5]_2$		*ex.* $Ni(acac)_2/[W(OEt)_5]_2$	
W/nm²	1.6		1.6		1.5		1.5	
Ni/W	0.20		0.21		0.44		1.00	
Fresh *vs.* Spent	Fresh	*Spent*	Fresh	*Spent*	Fresh	*Spent*	Fresh	*Spent*
$\%_{rel.}$ WS_2 (± 5%)	73	72	71	74	67	81	69	78
$\%_{rel.}$ W(VI)	12	11	11	9	13	10	13	8
$\%_{rel.}$ W(V)	15	17	18	17	20	9	18	14
W/Al (x100)	2.6	2.6	2.5	2.3	2.2	2.0	2.4	2.2
$\%_{rel.}$ NiWS (± 10%)	53	66	80	65	52	48	27	22
$\%_{rel.}$ NiS	29	20	5	26	29	35	55	54
$\%_{rel.}$ NiO_x	18	14	15	9	19	17	18	24
NiWS site / nm²	0.17	**0.22**	0.27	**0.22**	0.35	**0.33**	0.41	**0.33**
$(Ni/W)^a_{slab}$	0.25	**0.32**	0.33	**0.30**	0.57	**0.40**	0.50	**0.39**

	Conventional dried		Conventional calcined		*ex.* $Ni(NO_3)_2/[W(OEt)_5]_2$		*ex.* $Ni(acac)_2/W_{(POM)}$		*ex.* $Ni(acac)_2/WS_{2\_350°C}$	
W/nm²	1.8		1.8		1.5		1.8		1.7	
Ni/W	0.22		0.22		0.30		0.22		0.20	
Fresh *vs.* Spent	Fresh	*Spent*	Fresh	*Spent*	Fresh	*Spent*	Fresh	*Spent*	Fresh	*Spent*
$\%_{rel.}$ WS_2 (± 5%)	73	77	56	74	73	76	69	74	84	85
$\%_{rel.}$ W(VI)	12	12	24	13	16	8	15	16	7	8
$\%_{rel.}$ W(V)	15	11	20	13	11	16	16	10	9	7
W/Al (x100)	2.7	2.7	3.0	3.1	3.3	2.9	2.7	2.9	2.8	2.7
$\%_{rel.}$ NiWS (± 10%)	66	52	57	62	62	59	7	25	45	42
$\%_{rel.}$ NiS	29	32	33	22	24	25	71	51	41	42
$\%_{rel.}$ NiO_x	5	16	10	16	14	16	22	24	14	16
NiWS site / nm²	0.26	**0.21**	0.23	**0.25**	0.28	**0.27**	0.03	**0.10**	0.17	**0.17**
$(Ni/W)^a_{slab}$	0.30	**0.23**	0.30	**0.27**	0.23	**0.26**	0.05	**0.12**	0.15	**0.14**

[a] Calculated using NiWS and WS_2 quantification results from XPS experiments.

Table 23: XPS data, obtained by decomposition of W 4f and Ni 2p photopeaks of CSC and conventional NiWS/ASA catalysts before (fresh) and after toluene hydrogenation (spent). W-loadings: 1.5 W/nm² to 1.8 W/nm². Ni/W atomic ratio: 0.20 and 1.00. Sulphidations *ex-situ* were carried out at 350°C for 2 h, under a mixture of H_2S/H_2 with 15 $\%_{mol.}$ H_2S.

VI.5. Catalytic results

VI.5.a. Benchmarking catalytic activities with conventional samples and industrial references

The NiWS/ASA catalysts were tested in toluene hydrogenation in presence of aniline, in order to evaluate their HYD activity and determine if the CSC method improves the preparation of more active NiWS phases by comparison with conventional catalysts. As mentioned in part V through the discussion about catalytic activities of non-promoted catalysts, interpreting catalytic results with XPS data collected from analyses of spent samples is more accurate than using XPS data obtained on fresh catalysts. Some of the results presented in this part come thus from calculations with data collected from XPS analyses of spent materials, when necessary (see **Table 23**). Note however that we used TEM results obtained on fresh samples, as we previously assume that mean slabs length and stacking number are, in a first approximation, not significantly changed by the test.

First, preliminary tests were performed to evaluate the catalytic potential of five catalysts:

(1) a CSC catalyst prepared by deposition of $Ni(acac)_2$ onto $[W(OEt)_5]_2$/ASA: 1.7 W/nm², *e.g.* 12.9 $\%_{wt.}$ WO_3 and Ni/W = 0.21 at/at, *e.g.* 0.9 $\%_{wt.}$ NiO

(2) a conventional dried catalyst with 1.8 W/nm², *e.g.* 14.4 $\%_{wt.}$ WO_3 and Ni/W = 0.22, *e.g.* 1.0 $\%_{wt.}$ NiO

(3) a similar conventional calcined catalyst

(4) an industrial NiWS/ASA sample, with *ca.* 27.0 $\%_{wt.}$ WO_3 (*e.g.* 4.4 W/nm²) and *ca.* 3.5 $\%_{wt.}$ NiO (*e.g.* Ni/W = 0.4)

Note that CSC and conventional samples underwent pre-sulphidation *ex-situ* (350°C, 2 h, 15 $\%_{mol.}$ H_2S/H_2) prior to the test, while industrial catalysts were not.

The weight flow rate of toluene converted, expressed by gram of toluene converted per gram of catalyst per hour (g(tol)/g(cat)/h) is shown in **Figure 104**. The CSC sample is *ca.* 1.5 times more active than the industrial NiW one, while it contains at least 2.0 times less WO_3 *equiv.* This results shows that the CSC method is really promising as it provides NiWS/ASA

catalysts more active than the industrial reference, while lower W loaded (by 40 $\%_{wt.}$) can be used.

Comparison of conventionally prepared NiWS/ASA catalysts, dried or calcined, reveals that both samples are not significantly different, and 30% less active than the CSC sample.

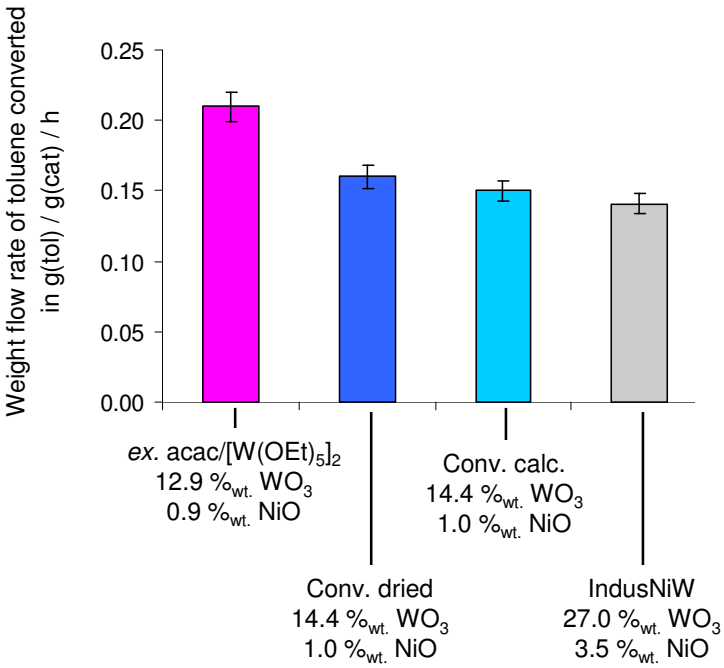

Figure 104: Weight flow rate of toluene converted by different Ni promoted catalysts, with different WO_3 and NiO loadings. Expressed in g(tol)/g(cat)/h. No *ex-situ* sulphidation for industrial catalysts. *Ex-situ* sulphidations of CSC and conventional catalysts were carried out at 350°C, for 2 h, in a 15 $\%_{mol.}$ H_2S/H_2 mixture, prior to HYD tests.

To get further insight into the intrinsic activity of these catalysts, the rate of hydrogenation, expressed in mole of toluene converted per mole of tungsten per hour (mol(tol)/mol(W)/h) is reported in **Figure 105**. Given the tungsten loading of each sample, the CSC catalyst displays the more active sites, expressed by W atoms. Its intrinsic rate of HYD is *ca.* 4.0 times higher that the industrial counterpart (IndusNiW), and the comparison between the intrinsic HYD rate of the CSC and conventional dried or calcined materials (prepared with similar amount of W and Ni) reveals the CSC NiWS phase is more efficient in hydrogenation.

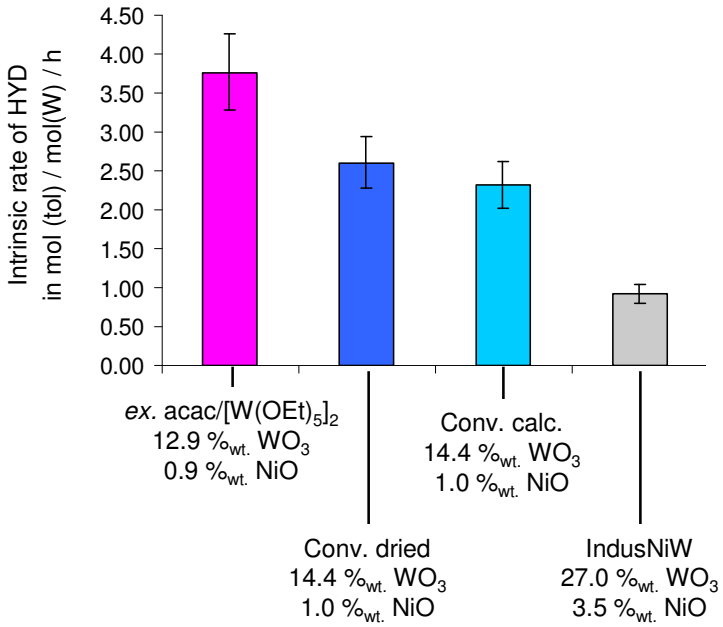

Figure 105: Intrinsic HYD rate of different Ni promoted catalysts, with different WO_3 and NiO loadings. Expressed in mol(tol)/mol(W)/h. No *ex-situ* sulphidation for industrial catalysts. *Ex-situ* sulphidations of CSC and conventional catalysts were carried out at 350°C, for 2 h, in a 15 $\%_{mol.}$ H_2S/H_2 mixture prior to HYD tests.

Therefore, even if not normalised by the amount of sulphide phase on each catalyst, these results reveal an improvement of activity (g(tol)/g(cat)/h) and intrinsic HYD rate (mol(tol)/mol(W)/h) brought by the use of a molecular approach in the preparation of NiWS/ASA catalysts.

VI.5.b. Influence of the nickel precursor

Then, we evaluated the performances of CSC and conventional NiWS/ASA catalysts, prepared with different Ni-precursors, which characterisation is described in part VI.1. All these catalysts exhibit similar W-loading (1.5 to 1.8 W/nm²) and Ni content (Ni/W = 0.21 to 0.30), and underwent sulphidation under the same conditions as described before: 15 $\%_{mol.}$ H_2S/H_2 mixture at 350°C for 2 h. **Figure 106** shows the weight flow rate of toluene converted by these catalysts, expressed in g(tol)/g(cat)/h.

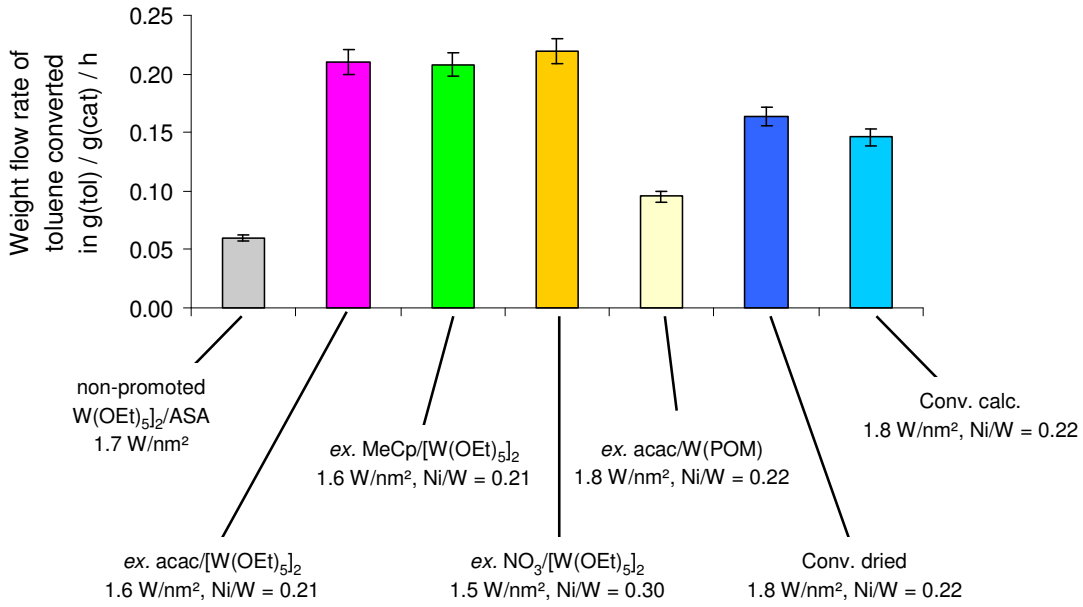

Figure 106: Weight flow rate of toluene converted [g(tol)/g(cat)/h] by different (Ni)WS_2/ASA catalysts, prepared with either $Ni(acac)_2$, $Ni(1\text{-}MeCp)_2$ or $Ni(NO_3)_2$. CSC samples are compared with conventional dried and calcined ones. W-loading ranging from 1.5 to 1.8 W/nm². Ni/W (at/at) ranging from 0.21 to 0.30. Sulphidations *ex-situ* were carried out at 350°C, for 2 h, in a 15 $\%_{mol.}$ H_2S/H_2 mixture prior to HYD tests.

First, the less active NiWS/ASA catalyst, prepared by deposition of $Ni(acac)_2$ on a conventional dried tungsten phase [$W_{(POM)}$], is 1.6 times more hydrogenating than the non-promoted WS_2/ASA sample (0.10 *vs.* 0.06 g(tol)/g(cat)/h), which highlights the crucial role of the promoter to improve hydrogenation reactions, as described for various transition metal sulphide by the volcano curve of Guernalec *et al.*, correlating sulphur-metal bond energies and intrinsic catalytic activities in toluene hydrogenation. [Guernalec *et al.*, 2006; Guernalec *et al.*, 2011] No significant difference is observed between sulphide materials prepare by deposition of $Ni(acac)_2$, $Ni(1\text{-}MeCp)_2$ and $Ni(NO_3)_2$ on supported alkoxide species (CSC): they are the most active samples, with about 0.21 (±0.01) g(tol)/g(cat)/h. Moreover, the comparison between conventional and CSC catalysts reveals that the three aforementioned CSC samples are at least 30 % more active than conventional samples. These latter are, however, more active than the sample prepared by deposition of $Ni(acac)_2$ on conventional dried tungsten phase denoted $W_{(POM)}$. In addition, note that compared to the calcined sample, the slightly higher activity found of the dried sample is not really significant.

The HYD activity of CSC samples thus seems not to depend on the nickel precursor, when deposited on supported alkoxides species. However, it is important to stress that deposition of

$Ni(acac)_2$ on a pre-formed conventional dried oxide phase ($W_{(POM)}$) do not enhance the activity, which highlight the strong role of the tungsten surface species (dispersion on the surface and reactivity toward Ni-precursors) on which promoters are deposited when samples are prepared by successive impregnation.

The intrinsic HYD rate of the previous catalysts is depicted in **Figure 107**. Results are similar to the previous ones found for the weight flow rate of toluene converted. The CSC method allows the preparation of samples exhibiting the highest intrinsic HYD rates (ranging from 3.51 to 3.77 (±0.49) mol(tol)/mol(W)/h), probably due to their high amount of mixed phase NiWS, as revealed by XPS on spent catalysts. In particular, when catalysts are prepared by deposition of $Ni(acac)_2$ onto a conventional tungsten oxide phase (dried), *e.g.* $W_{(POM)}$/ASA, their intrinsic HYD rate is two times lower than when prepared by deposition of a Ni-precursor on supported tungsten alkoxide species, which is correlated with the lower amount of NiWS sites observed on the former sample: 0.10 site/nm² *vs.* 0.22 site/nm². However, intrinsic HYD rates of the best CSC samples are *ca.* 30% higher than that of conventionally prepared catalysts, while they reveal similar amount of NiWS sites (0.21 to 0.25 (±0.4) NiWS site/nm²): as a consequence, another parameter such as the $(Ni/W)_{slab}$ ratio must influence the activity and the nature of active site(s). This ratio is slightly higher for CSC samples (between 0.26 and 0.32) than for conventional ones (0.23 to 0.27), which signifies that more Ni atoms have substituted W ones, and probably have formed more *mixed sites* on edges (Ni in close vicinity to W at the edge). Note also that the slabs length also plays a role, especially in the 2D morphology of crystallites and in the repartition of *mixed sites* on edges, which will be discussed later on in the discussion (part VI.6), together with the influence of the $(Ni/W)_{slab}$ parameter.

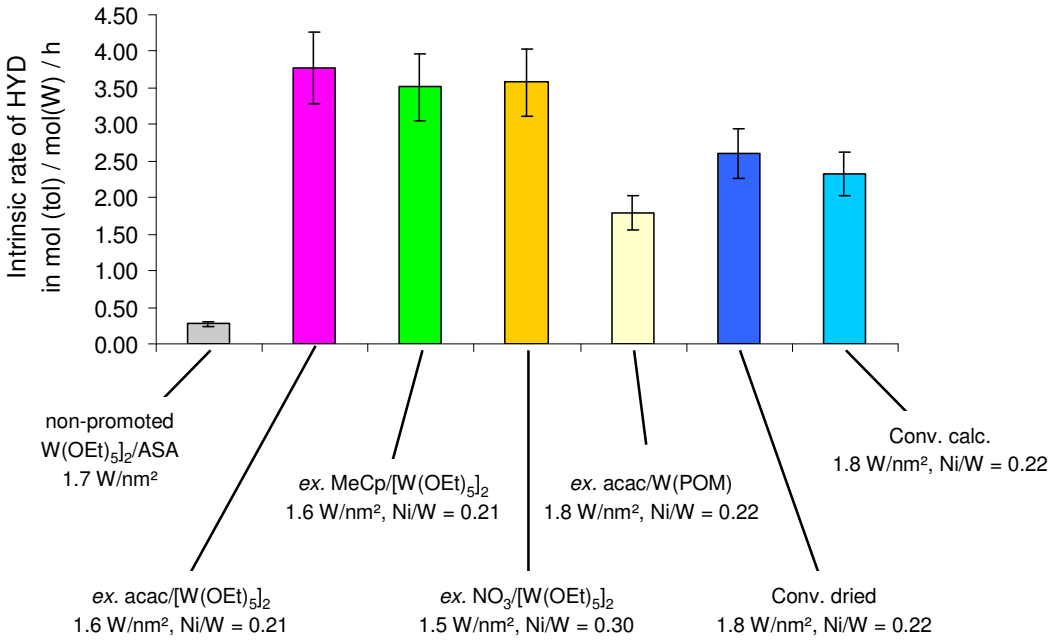

Figure 107: Intrinsic HYD rate of different (Ni)WS_2/ASA catalysts, expressed in mol(tol)/mol(W)/h. NiWS/ASA samples prepared with either $Ni(acac)_2$, $Ni(1\text{-}MeCp)_2$ or $Ni(NO_3)_2$. CSC samples are compared with conventional dried and calcined ones. W-loading ranging from 1.5 to 1.8 W/nm². Ni/W (at/at) ranging from 0.21 to 0.30. Sulphidations *ex-situ* were carried out at 350°C, for 2 h, in a 15 $\%_{mol.}$ H_2S/H_2 mixture prior to HYD tests

VI.5.c. Influence of the preparation method: deposition of $Ni(acac)_2$ onto supported tungsten species (non sulphided) or onto sulphide ones, prepared at 23°C or 350°C

Then, the activity of NiWS/ASA catalysts, prepared by deposition of the nickel precursor on to a sulphide phase (prepared at either 23°C or 350°C, 2 h , 15 $\%_{mol.}$ H_2S/H_2) was compared to the activity of CSC samples ex. $Ni(acac)_2$, referred as *ex.* acac/$[W(OEt)_5]_2$ (considered to be one of the most active CSC sample) and conventional catalysts. The weight flow rate of toluene converted is shown in **Figure 108.**

Deposition of a nickel precursor onto a sulphide material, prepared at 350°C or 23°C, allows the synthesis of catalysts exhibiting different activities. Indeed, the catalyst prepared with a material sulphided at 23°C (referred as *ex.* acac/$WS_{2\text{-}23°C}$) converts 1.8 times more toluene than its CSC counterpart obtained on a sulphide phase prepared at 350°C (denoted *ex.* acac/$WS_{2\text{-}350°C}$). Besides, no significant activity difference is found between the catalysts for

which the nickel is impregnated directly onto CSC surface alkoxide species (*ex.* acac/$[W(OEt)_5]_2$), or onto a CSC sulphide phase, prepared à 23°C: they convert between 0.20 and 0.21 (±0.01) g(tol)/g(cat)/h, which is more than 30 % higher than conventionally prepared samples.

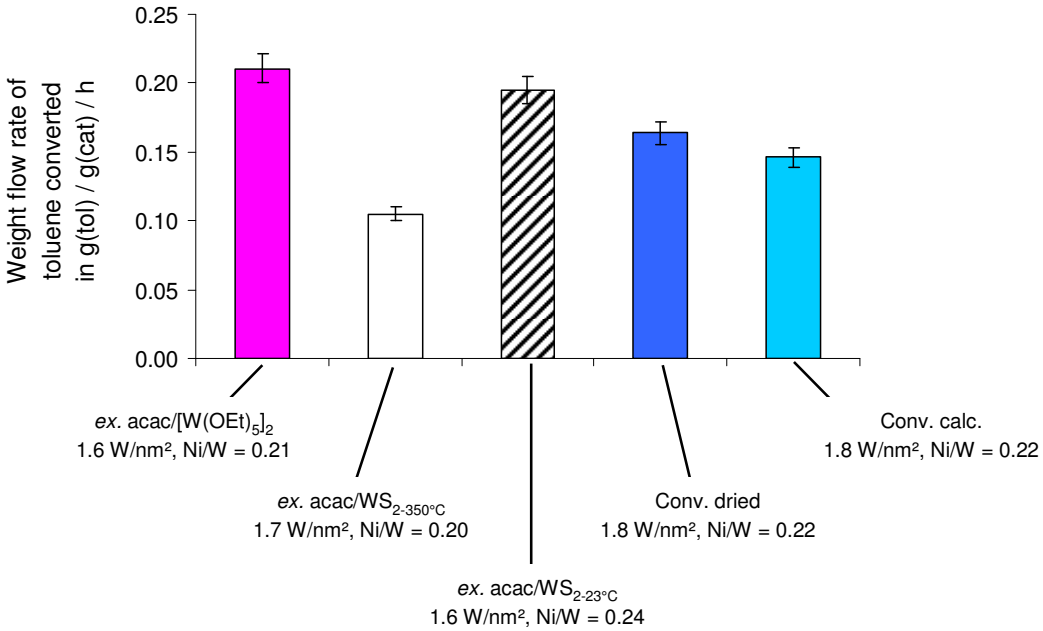

Figure 108: Weight flow rate of toluene converted [g(tol)/g(cat)/h] by different Ni promoted catalysts, prepared with either $Ni(acac)_2$ deposited onto supported tungsten alkoxide species, or deposited onto sulphide phases prepared at either 350°C or 23°C (2 h , 15 $\%_{mol.}$ H_2S/H_2). CSC samples are compared with conventional dried and calcined ones. W-loading ranging from 1.6 to 1.8 W/nm². Ni/W (at/at) ranging from 0.20 to 0.24. Sulphidations *ex-situ* were carried out at 350°C, for 2 h, in a 15 $\%_{mol.}$ H_2S/H_2 mixture prior to HYD tests

Then, we investigated the influence of the preparation method on the intrinsic HYD rate of these catalysts (see **Figure 109**). Conclusions are similar to the ones previously found for the weight flow rate of toluene converted. The most important is that preparation of a CSC samples by deposition of $Ni(acac)_2$ onto a sulphide material prepared at 23°C, subsequently followed by a sulphidation at 350°C, gives a NiWS/ASA catalyst exhibiting an intrinsic HYD rate as high as the one observed for sample prepared by impregnation of the Ni-precursor directly onto supported alkoxide species, which is higher than that of conventionally prepared samples. These results will be discussed later on, in part VI.6.

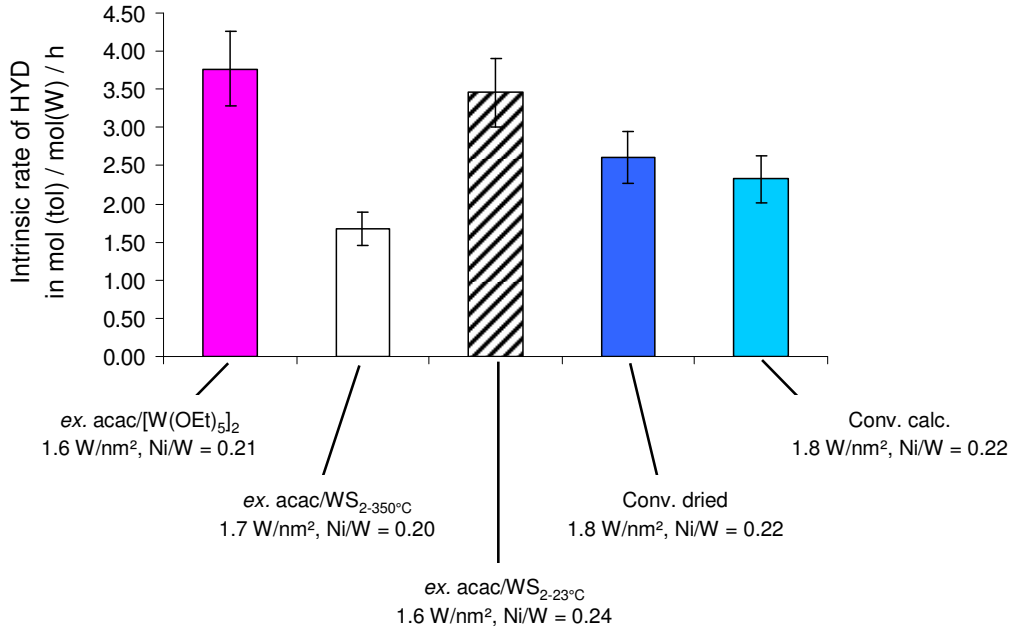

Figure 109: Intrinsic HYD rate [mol(tol)/mol(W)/h] of different Ni promoted catalysts, prepared with either $Ni(acac)_2$ deposited onto supported tungsten alkoxide species, or deposited onto sulphide phases prepared at either 350°C or 23°C (2 h , 15 $\%_{mol.}$ H_2S/H_2). CSC samples are compared with conventional dried and calcined ones. W-loading ranging from 1.6 to 1.8 W/nm². Ni/W (at/at) ranging from 0.20 to 0.24. Sulphidations *ex-situ* were carried out at 350°C, for 2 h, in a 15 $\%_{mol.}$ H_2S/H_2 mixture prior to HYD tests

VI.5.d. Influence of the nickel content

Then, the intrinsic HYD rate of NiWS/ASA catalysts (1.5 to 1.6 W/nm²) was investigated as a function of their Ni content. They were prepared by deposition of Ni-precursors either on supported alkoxide species, or on a sulphide material previously prepared at 23°C for 2 h with a 15 $\%_{mol.}$ H_2S/H_2 mixture. **Figure 110** reveals that for these samples, the ones prepared on supported surface alkoxide W-species (*ex.* acac/$[W(OEt)_5]_2$) exhibit an intrinsic HYD rate which decreases for Ni/W atomic ratio higher than 0.44: from 3.77 to 1.49 mol(tol)/mol(W)/h. This trend is found to be similar to the one observed for conventional calcined NiWS/ASA (4.3 W/nm²) exhibiting increasing amount of Ni [Raybaud and Toulhoat, 2013, Ed. Technip, Paris, p255]. However, the Ni/W atomic ratio after which the intrinsic HYD rate of these conventional catalysts decreases is lower, at about 0.30 (at/at). On the contrary, catalytic results found for catalysts prepared onto a sulphide phase prepared at 23°C (*ex.* acac/$WS_{2\_23°C}$) follow a different trend:

increasing the amount of nickel slightly increases the intrinsic HYD rate which seems to reach a plateau between 3.9 and 4.0 mol(tol)/mol(W)/h. Finally, as the experimental error is close to 0.5 for the most active materials, we can assume that the highest intrinsic rate of HYD achievable for catalysts with *ca.* 1.6 (± 0.1) W/nm² lies between 3.7 and 4.0 mole of toluene converted per mole of tungsten per hour. For catalysts with greater W-loading, this intrinsic rate is lowered to *ca.* 1.5 mol(tol)/mol(W)/h.

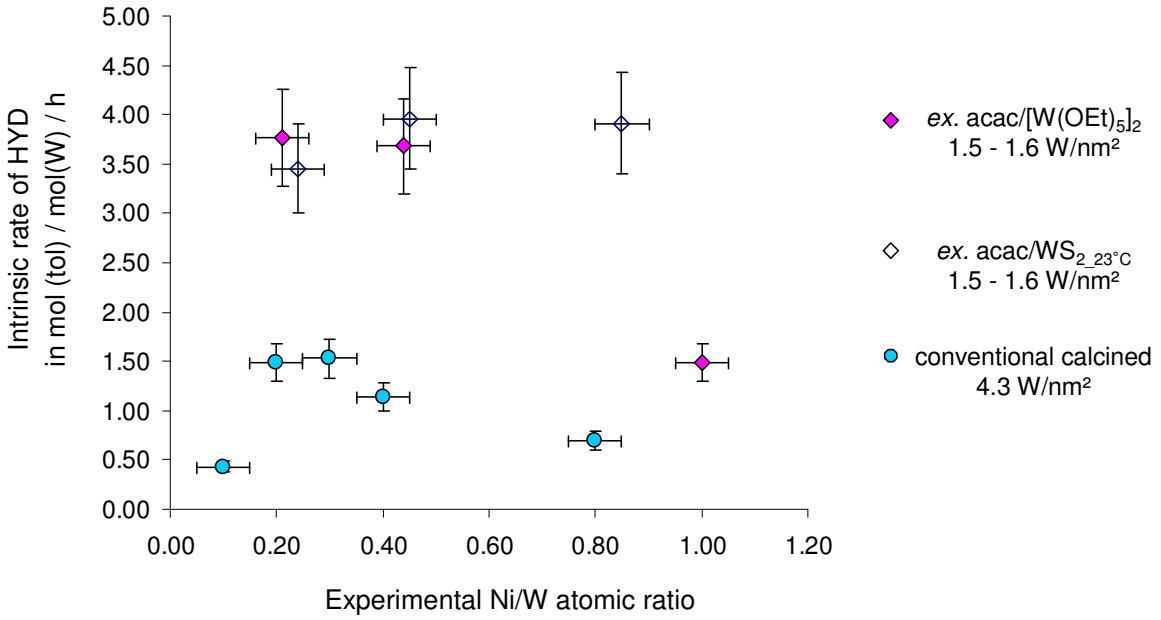

Figure 110: Intrinsic HYD rate of CSC NiWS/ASA catalysts depending on their Ni/W experimental atomic ratio. Catalysts (diamonds) were prepared by deposition of $Ni(acac)_2$ onto supported W species (non sulphided) or sulphided ones (23°C, 2 h, 15 $\%_{mol.}$ H_2S/H_2), with W-loading between 1.5 and 1.6 W/nm². HYD rates of conventional catalysts (4.3 W/nm², circles) were obtained from ref. [Raybaud and Toulhoat, 2013, Ed. Technip, Paris, p255]. *Ex-situ* sulphidations were carried out at 350°C for 2 h, under a mixture of 15 $\%_{mol}$ H_2S/H_2, prior to HYD tests

Then, we investigated the effect of the amount of Ni engaged in a mixed phase "NiWS" (active phase) on the weight flow rate of toluene converted by our catalysts. **Figure 111** shows the weight flow rate of toluene converted, in g(tol)/g(cat)/h, as a function of the effective Ni content in a NiWS phase ($\%_{wt.}$). Note that the effective Ni content is calculated by multiplying the Ni content (elemental analyses) by the relative amount of NiWS phase ($\%_{rel.}$ NiWS) detected by XPS on spent catalysts. The activity increases rather linearly when the amount of Ni incorporated in a mixed phase "NiWS" increases. Note in particular, the striking decrease of

activity observed for the CSC sample with Ni/W = 1.00 (at/at), which is probably due to the presence of numerous NiS particles, which is supported by the high amount of NiS phase detected by XPS (*ca.* 54%$_{rel.}$, see **Table 23**). The NiS phase could cover the active NiWS phase, thus lowering the amount of NiWS phase detected by XPS, or preventing toluene to react with active sites (low accessibility), thus decrease the HYD activity.

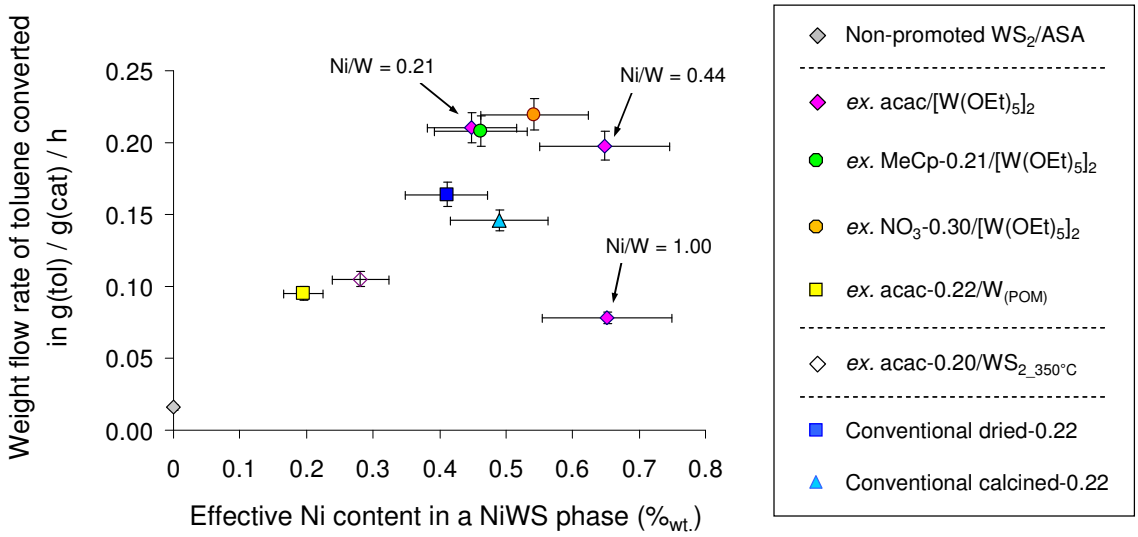

Figure 111: Weight flow rate of toluene converted [g(tol)/g(cat)/h] for NiWS/ASA catalyst prepared by CSC or conventional method, as a function of the effective Ni content in a NiWS phase (%$_{wt.}$). Catalysts exhibit between 1.5 to 1.8 W/nm², with experimental Ni/W atomic ratio between 0.20 and 1.00. *Ex-situ* sulphidations were carried out at 350°C for 2 h, under a mixture of 15 %$_{mol.}$ H_2SH_2S/H_2 prior to HYD tests

In the next part, we will discuss these results and tentatively explain them by the combination of 2D geometrical models, XPS and TEM data, together with the help of DFT calculations.

VI.6. Discussion

VI.6.a. Morphology and edge decoration of NiWS crystallites

In this part, we define the 2D morphology of NiWS crystallites in the same spirit as in part V, *e.g.* with a geometrical model taking into account TEM data (mean slabs length) and DFT calculations. DFT modelling, reported earlier in this study, revealed that the 2D morphology of WS_2 crystallites was changed upon addition of the Ni promoter: the M-edge length, $L_{W\text{-}edge}$, is diminished, in favour of the S-edge length, $L_{S\text{-}edge}$, as summarized in **Table 24**

Table 24: Morphology parameter of W-edge and S-edge for our experimental conditions: -1.03 eV

$\Delta\mu_s$ (eV)	$\left[\frac{L_{W-edge}}{L_{S-edge}}\right]_{non\ promoted}$	$\left[\frac{L_{W-edge}}{L_{S-edge}}\right]_{promoted}$
-1.03	1.63	1.12

The morphology diagram of NiWS crystallites obtained by DFT modelling is shown in **Figure 112**.

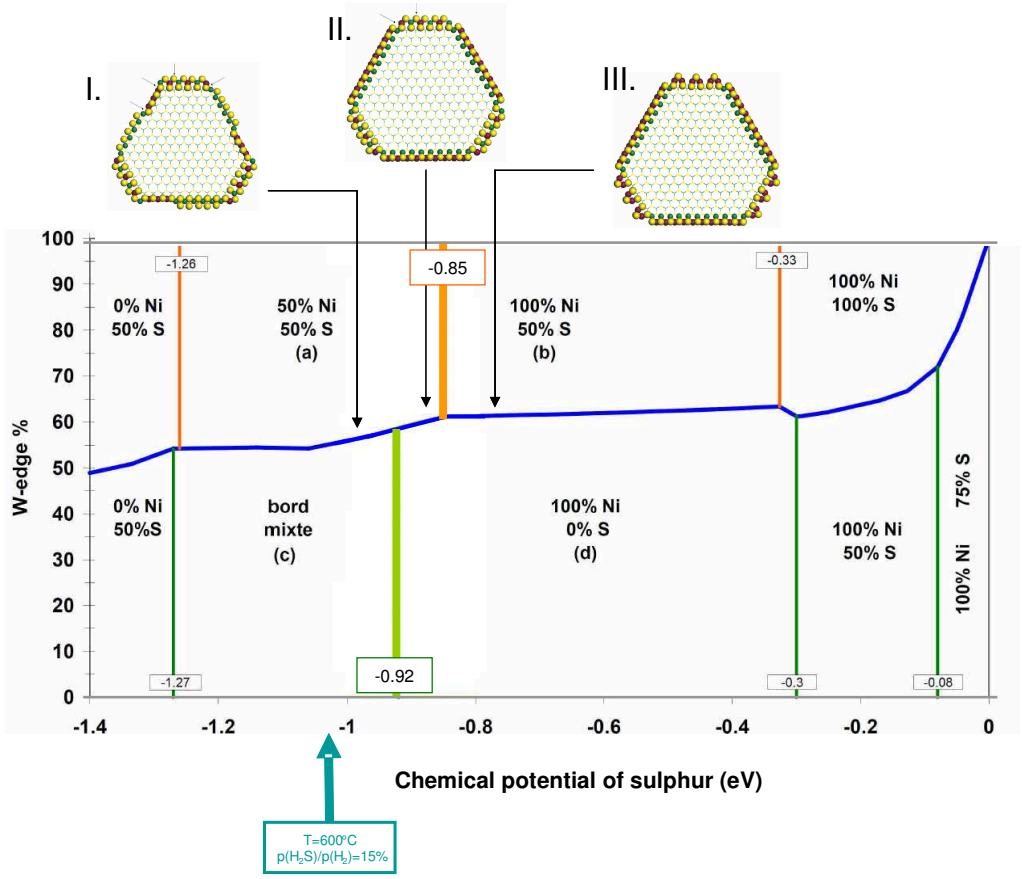

Figure 112: Morphology diagram of NiWS crystallites as a function of the chemical potential and $p(H_2S)p(H_2)$ at T=650 K (377°C) [Girleanu *et al.*, *in preparation*]. The proportion (percentage) of W-edge is given by the blue broken line. The S-edge compositions are above the blue line, and the W-edge compositions are below this line. Ni repartition on either W-edge or S-edge in also reported. The green arrow emphasizes our experimental conditions: $\Delta\mu_S$ = -1.03 eV

In our experimental conditions ($\Delta\mu_S$ = -1.03 eV), **Figure 112** highlights that crystallites tend to be deformed hexagons, with about 55 % of W-edge. As in part V, the 2D morphology of a crystallite is defined by the two parameters n_M and n_S, which respectively stands for the number of M-edge and S-edge atoms. Therefore, considering a slight fluctuation around $\Delta\mu_S$ = -1.03 eV, and for a given slab length, the 2D morphology follows the equation

$$0.55 \leq \frac{n_M}{n_M + n_S} \leq 0.60 \qquad \textbf{Eq. 7}$$

Note that no STEM HAADF experiments were performed on CSC catalysts, contrary to conventional calcined ones. As a consequence, we assume that the 2D morphology of CSC NiWS crystallites is similar to that of conventional samples. Note that this hypothesis, about crystallites observed on CSC samples following DFT calculations, has not been taken into account for non-promoted samples. Indeed, STEM-HAADF pictures revealed that crystallites observed on non-promoted CSC WS_2/ASA catalysts were much more hexagonal shaped that predicted, while the 2D morphology of WS_2 slabs observed on conventionally prepared samples matched the predictions.

Besides, **Figure 112** also shows the stability domain of 3 relevant NiWS crystallite structures, while only one structure is expected to be stabilized in our experimental conditions (T = 350°C, $p(H_2S)/p(H_2) \approx 15\ \%_{mol.} \Leftrightarrow \Delta\mu_S = -1.03$ eV). However, as boundaries between each structure are rather close (-0.92 eV and -0.85 eV) and assuming a slight fluctuation in sulphiding conditions $\Delta\mu_S = -1.03$ eV, we assume that the 3 structures can probably be stabilized. These 3 NiWS crystallites exhibit $n_M = 8$ and $n_S = 4$, concomitantly with:

1) Ni substituting 50 % of the W atoms on S-edge, along with 25 % of the W atoms on W-edge, as shown **Figure 113-I.** This structure is the one expected with our experimental conditions.
2) Ni substituting 50 % of the W atoms on S-edge, along with 100 % of the W atoms on W-edge, as shown in **Figure 113-II.**
3) Ni substituting 100 % of the W atoms on S-edge and W-edge, as shown in **Figure 113-III.**

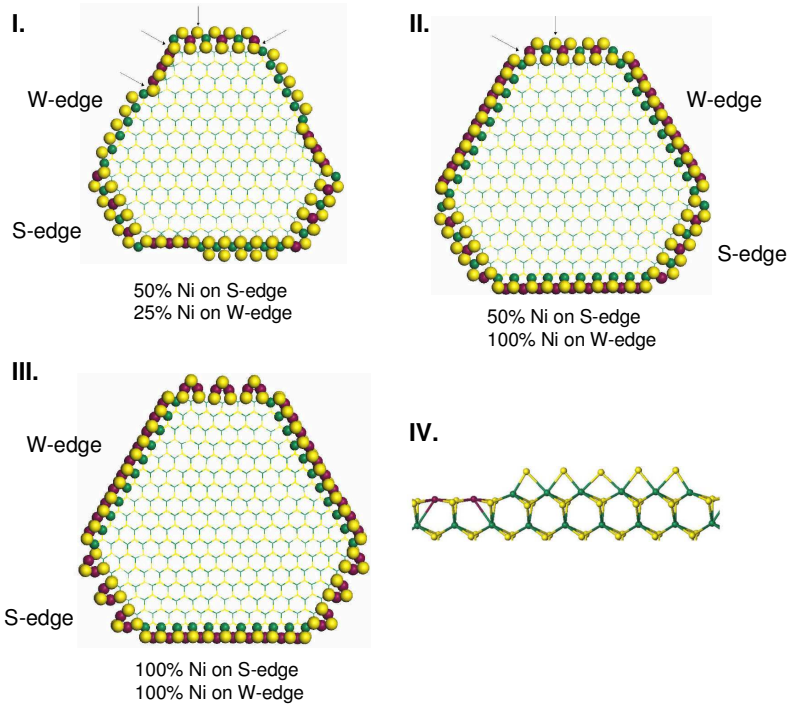

Figure 113: NiWS crystallites with n_M=8, n_S=4. Mixed sites (if present) are indicated by arrows; I. Partially decorated on S-edge and W-edge; II. Partially decorated on S-edge and fully decorated on W-edge and III. Fully decorated on S-edge and W-edge; IV. W-edge of structure I. Green balls: tungsten. Red balls: nickel, Yellow balls: sulphur [Girleanu *et al., in preparation*]

Note that configuration **I.** is the only one where *mixed sites* "NiWS" are located on W-edges (*mixed sites* representing, as previously stated, Ni atoms in close vicinity to W ones at the edge); this peculiar configuration is supposed to represent the active site of HYD and HDS reactions. It is noteworthy that the W-edge exhibits neither Ni.W.Ni.W nor Ni.Ni.W.W pairings. The only stable form with Ni on W-edge reveals edges with 6 tungsten atoms followed by 2 nickel ones (*e.g.* 25% Ni on W-edge), as shown in **Figure 113-IV.** (note that Ni atoms on corners are not included in the count of Ni on edges). This behaviour of Ni toward W in NiWS phases is not common, as Ni or Co are reported to stabilize Mo-edges with Ni.Ni.Mo.Mo pairing or Co.Co.Mo.Mo and Co.Mo.Co.Mo pairings in NiMoS and CoMoS crystallites, respectively. [Krebs *et al.*, 2008; Krebs *et al.*, 2009].

Then, in order to investigate how Ni atoms decorate WS_2 slabs, *e.g.* in which extent Ni atoms can replace W ones on edges (either W-edge or S-edge), we calculated, with the help of geometrical models, the **nickel-to-tungsten substitution ratio (atomic) on crystallites edges**

and corners, denoted $\mathbf{X_{subst.}}$. This parameter refers to the amount of nickel atoms which have substituted W ones on edges and/or corners. It is calculated with the following equation inspired from previous works of the literature [Marchand *et al.*, 2009; Baubet, PhD thesis, Lyon, 2013; Gandubert, PhD thesis, Lille, 2006]

$$X_{subst} = \frac{\left(\frac{Ni}{W}\right)_{slab}}{1+\left(\frac{Ni}{W}\right)_{slab}} \times \frac{(number\ of\ M\ atoms)_{total}}{(number\ of\ M\ atoms)_{edges+corners}} \qquad \textbf{Eq. 8}$$

where $(Ni/W)_{slab.}$, is obtained by XPS and experimentally corresponding to the amount of Ni in a NiWS phase divided by the amount of W in a WS_2 phase; and where (number of M atoms) stands for either the total number of metal atoms in a crystallite, or the number of metal atoms on edges and corners only.

Calculations are based on 2D geometrical models simulated with slabs lengths obtained by TEM analyses of the following NiWS/ASA catalysts prepared:

1) by deposition of $Ni(acac)_2$ onto $[W(OEt)_5]_2$/ASA, referred as *ex.* acac-***(Ni/W)***/$[W(OEt)_5]_2$, for Ni/W atomic ratio of 0.21, 0.44 and 1.00 (at/at)
2) by deposition of $Ni(acac)_2$ onto a sulphide phase, prepared at 350°C, referred as *ex.* acac/$WS_{2\text{-}350°C}$
3) by a conventional method, samples being dried or calcined

First, we studied the theoretical $(Ni/W)_{slab}$ parameter in order to find for which value every W atoms on edges would be substituted by Ni ones. In other words, we focused on the highest $(Ni/W)_{slab}$ for which the atomic Ni-to-W substitution ratio on edges and corners (X_{subst}) is 100 %. Calculations are summarized in appendix F (**Table F.a**). 100% of W atoms on edges and corners are found to be substituted by Ni ones for $(Ni/W)_{slab}$ higher than 0.36, given the slab length and %W-edge. Conversely, experimental $(Ni/W)_{slab}$ values obtained by XPS analyses of spent catalysts were used to calculate Ni-to-W substitution ratio on edges and corners, for our catalysts. Results are summarized in **Table F.b** (see appendix F). Calculations which match **Eq. 7** at best are illustrated in **Figure 114**. For the sake of comparison, theoretical data points (appendix F, **Table F.a**) are also depicted in the same figure. Data corresponding to the catalysts that have been analysed are highlighted by arrows.

Then, for given slabs lengths, corresponding geometrical models are in line with partial or total substitution of W by Ni on edges and corners. On top of that, this result correlates well with

experimental XPS data where the highest Ni-to-W atomic ratio in sulphide crystallites of spent catalysts is 0.40 (see part VI.4). Several geometrical models are thus compatible with our catalysts: either a **hexagonal model** with $n_M = n_S = 5$ or **deformed hexagonal models** from $\{n_M = 6; n_S = 4\}$ to $\{n_M = 8; n_S = 5\}$, depending on the slabs length.

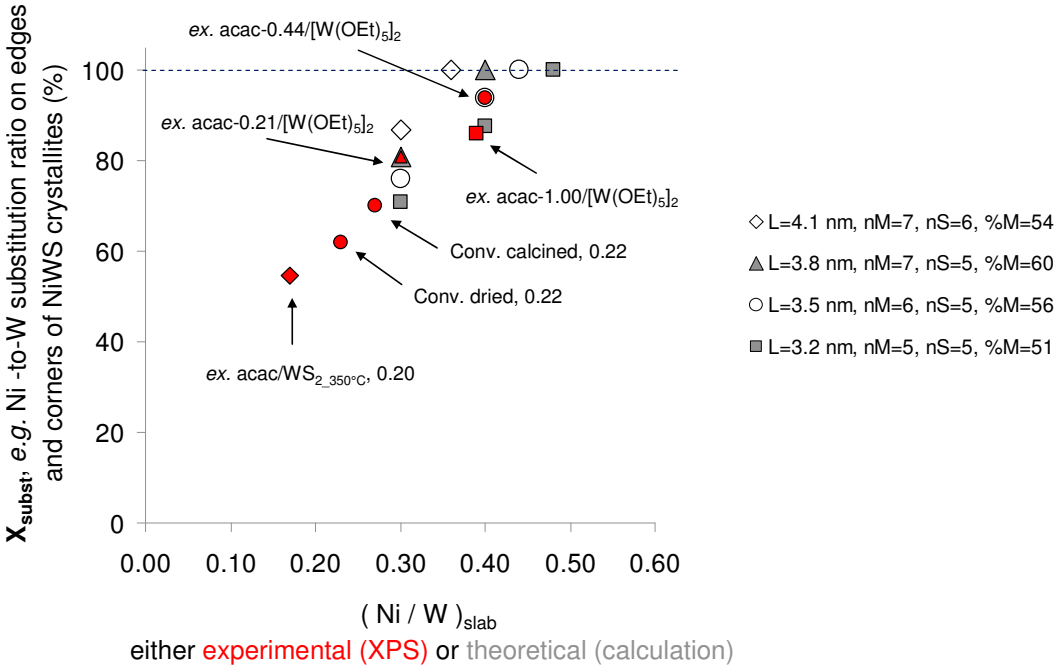

Figure 114: Theoretical and experimental atomic Ni-to-W substitution ratio on edges and corners ($X_{subst.}$) as a function of $(Ni/W)_{slab}$ (*e.g.* Ni-to-W atomic ratio in NiWS crystallites). Theoretical values are calculated from 2D geometrical models along with TEM data. Experimental ones (red symbol and arrows) are calculated from 2D geometrical models along with TEM and XPS data (spent catalysts). Only data that match conditions of Eq. 7 are depicted.

However, location of Ni on W-edge or on S-edge of NiWS crystallites present on our different samples has not been ruled out yet. In order to investigate this peculiar location of Ni on edges, we used the relative distribution of Ni on W-edge and S-edge obtained for each of the 3 stable crystallites (for example: 50 %Ni on S-edge, 25 %Ni on W-edge for structure I., see **Figure 113** or **Figure 112**) to calculate theoretical values of $(Ni/W)_{slab}$, referred as $(Ni/W)_{slab\_theo}$, and theoretical values of the atomic Ni-to-W substitution ratio on edges and corners, denoted X_{subst_theo}. Indeed, for a fixed 2D geometrical model, a unique couple $\{(Ni/W)_{slab}\ ; X_{subst}\}$ is observed for a fixed repartition of Ni on W-edge and S-edge.

The following formulas were used:

(1) to calculate the number of Ni atoms substituting W ones on edges:

$$Ni_{edges} = \%Ni_{W-edge} \times (number\ of\ M\ atoms)_{W-edge} + \%Ni_{S-edge} \times (number\ of\ M\ atoms)_{S-edge} \quad \textbf{Eq. 9}$$

where $\%Ni_{W\text{-}edge}$ and $\%Ni_{S\text{-}edge}$ stand for the relative% of Ni on W-edge and S-edge respectively, and where $(number\ of\ M\ atoms)_{W\text{-}edge}$ and $(number\ of\ M\ atoms)_{S\text{-}edge}$ stand for the number on metal atoms on W-edge and S-edge respectively.

(2) to calculate the number of W atoms not substituted by Ni ones:

$$(number\ of\ W\ atoms)_{total} = (number\ of\ M\ atoms)_{total} - Ni_{edges+corners} \quad \textbf{Eq. 10}$$

where $(number\ of\ W\ atoms)_{total}$ stands for the total number of tungsten atoms in a crystallite, and where $(number\ of\ M\ atoms)_{total}$ stands for the total number of metal atoms in a crystallite. Note that considering the presence of one Ni atom on each corner of the 3 relevant NiWS crystallites, we assume, in a first approximation, that in each case, corner atoms are Ni atoms. The total amount of Ni atoms is thus $Ni_{edges+corners} = Ni_{edges} + 6$.

(3) to calculate the $(Ni/W)_{slab\_theo}$ atomic ratio:

$$\left(\frac{Ni}{W}\right)_{slab\_theo} = \frac{\dfrac{Ni_{edges+corners}}{(number\ of\ W\ atoms)_{total}}}{1 - \dfrac{Ni_{edges+corners}}{(number\ of\ W\ atoms)_{total}}} \quad \textbf{Eq. 11}$$

where $Ni_{edges+corners}$ and $(number\ of\ W\ atoms)_{total}$ are as described above.

(4) to calculate the theoretical atomic Ni-to-W substitution ratio on edges and corners, X_{subst_theo}:

$$X_{subst\_theo} = \frac{Ni_{edges+corners}}{(number\ of\ M\ atoms)_{edges+corners}} \quad \textbf{Eq. 12}$$

where Ni_{edge} is as described above, and where $(number\ of\ M\ atoms)_{edge+corners}$ stands for the number of metal atoms on edges and corners of a crystallite.

Results of our calculations are summarized in **Table 25**.

Table 25: NiWS crystallites data obtained from calculations based on geometrical models and theoretical values of %Ni on S-edge and %Ni on W-edge, obtained by DFT modelling

Length L from TEM (Å)	Length L' from the model (Å)	*nM*	*nS*	%Ni on S-edge	%Ni on W-edge	$(Ni/W)_{slab\_theo}$	X_{subst_theo} (%)
40	41	8	5	100	100	0.37	100
				50	100	0.30	85
				50	25	0.14	44
		7	6	100	100	0.36	100
				50	100	0.27	81
				50	25	0.14	48
37	38	8	4	100	100	0.41	100
				50	100	0.34	88
				50	25	0.15	44
		7	5	100	100	0.40	100
				50	100	0.31	83
				50	25	0.15	46
35 - 36	35	6	5	100	100	0.44	100
				50	100	0.33	82
				50	25	0.17	48
		7	4	100	100	0.45	100
				50	100	0.37	86
				50	25	0.16	45
33	32	6	4	100	100	0.49	100
				50	100	0.39	80
				50	25	0.16	50
		5	5	100	100	0.48	100
				50	100	0.35	85
				50	25	0.19	47

Table 25 highlights that for the crystallite structure supposed to be the more stable according to DFT in our experimental conditions (50 %Ni on S-edge and 25 %Ni on W-edge), between 45 % and 50 % of W atoms are substituted by Ni ones on edges and corners, given the different slab lengths. More generally, **Figure 115** illustrates all values found in **Table 25**, *e.g.* X_{subst_theo} as a function of the $(Ni/W)_{slab\_theo}$, calculated for different slab lengths.

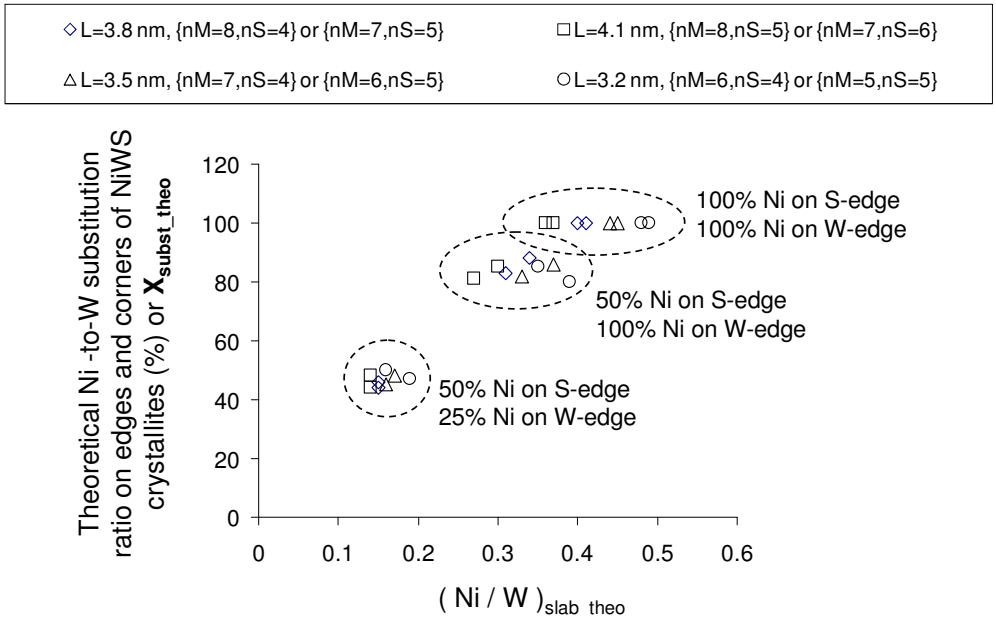

Figure 115: Theoretical Ni-to-W substitution ratio as a function of the theoretical Ni-to-W atomic ratio in NiWS crystallites $(Ni/W)_{slab\_theo}$. Calculated with DFT data and slabs length, between 3.2 nm and 4.1 nm, with the help of geometrical models

Figure 115 highlights 3 different regions, one for each of the 3 types of NiWS crystallite structures (described in **Figure 113**), depending on the location of nickel on W-edge and S-edge. Crystallites with partially decorated edges reveal theoretical $(Ni/W)_{slab\_theo}$ between 0.14 and 0.19, while crystallites with partially decorated S-edge but fully decorated W-edge show $(Ni/W)_{slab\_theo}$ between 0.27 and 0.39. Fully decorated crystallites exhibit $(Ni/W)_{slab\_theo}$ spread from 0.36 and 0.49.

Then, the comparison between the aforementioned theoretical values (**Figure 115**) and the experimental ones found for our catalysts (**Figure 114**) is represented in **Figure 116**. The points obtained from experimental results or DFT calculations and located in the same areas highlights that theoretical and experimental data can be correlated with the use of geometrical models. The figure also reveals that for CSC catalysts, when the nickel precursor is deposited onto a CSC sulphide material (350°C), a Ni coverage of 25 % on W-edge and 50 % on S-edge probably occurs. When the nickel is impregnated onto CSC surface alkoxide species (*e.g.* $[W(OEt)_5]_2$/ASA), the crystallite structure tends to be fully decorated on the W-edge and partially decorated on S-edge (50%). It thus seems possible to **control the location of Ni atoms substituting W ones** by **modifying the material** on which the promoter is impregnated, *e.g.* **a non sulphided, or a sulphide one** prepared at 350°C. Then, note that these samples,

for which $(Ni/W)_{slab}$ is lower than 0.30, exhibit experimental Ni/W atomic ratio close to 0.20 (at/at). Increasing the amount of nickel up to Ni/W = 1.00 is found to give Ni saturated W-edge and S-edge, *e.g.* fully decorated crystallites with $(Ni/W)_{slab}$ around 0.40. Besides, it is hard to draw conclusions from data obtained on conventional catalysts but results suggest that their crystallites are half decorated on S-edge, with Ni coverages on W-edge comprised between 25 % and 100 %. However, as every NiWS samples are covered by a distribution of NiWS crystallites, exhibiting more or less Ni atoms substituting W ones, data obtained by XPS (as well as TEM) analyses are averaged and have to be interpreted with caution, considering the experimental accuracy.

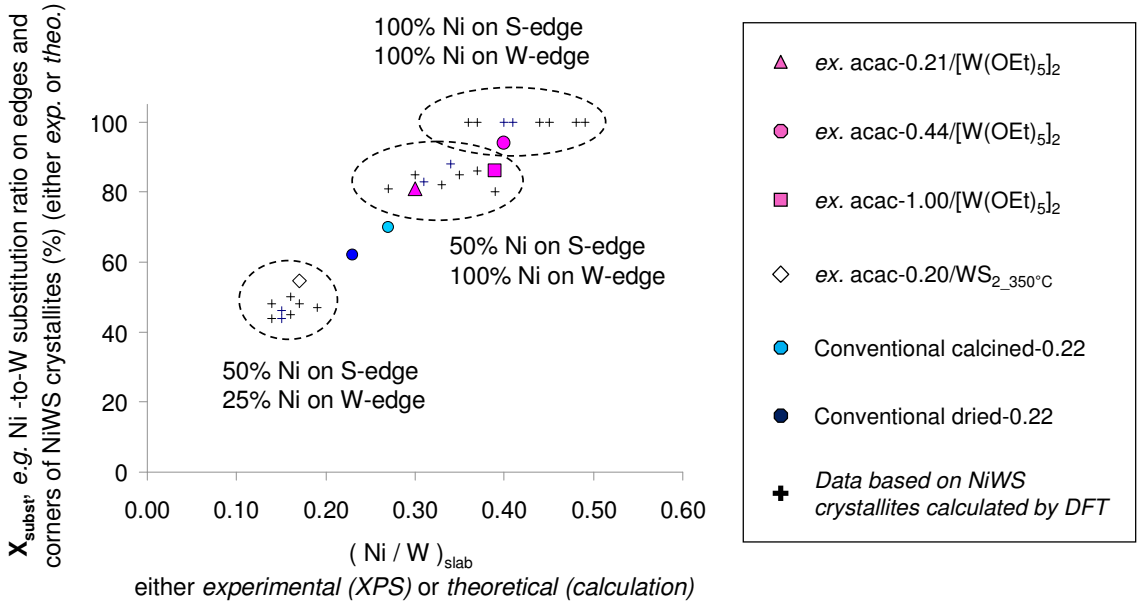

Figure 116: X_{subst} (*e.g.* atomic Ni-to-W substitution ratio in NiWS crystallites) as a function of $(Ni/W)_{slab}$: comparison between data obtained by analyses of (spent) catalysts (XPS, TEM) and data obtained by calculation based on DFT modelling data, together with the help of geometrical models. Catalysts exhibit between 1.5 and 1.8 W/nm², with experimental Ni/W atomic ratio between 0.20 and 1.00 (at/at). *Ex-situ* sulphidations were carried out at 350°C for 2 h, under a mixture of 15 $\%_{mol.}$ H_2S/H_2, prior to the HYD tests

VI.6.b. Optimal parameters for NiWS phases: the balance between the amount of active sites and their intrinsic HYD strength

Depending on the targeted experimental Ni-to-W atomic ratio Ni/W, NiWS crystallites of conventional and CSC catalysts exhibit different values of $(Ni/W)_{slabs}$, which thus lead to different nickel environments on the W-edge and S-edge of the crystallites. These differences are linked to the presence or not of *mixed active sites* which can partly explain catalytic activities presented in part VI.5.

First, we evaluated the hydrogenating potential of our samples by investigating the weight flow rate of toluene converted. Samples prepared by a molecular approach appear to be promising hydrogenating catalysts. Indeed, they proved to be as active as or more active than industrial references containing higher amounts of Ni and W (NiWS phases supported on ASA). To deepen one's understanding of this better HYD behaviour, the study of corresponding intrinsic HYD rates has been undertaken, revealing that deposition of a nickel precursor (*e.g.* $Ni(acac)_2$, $Ni(1\text{-}MeCp)_2$ and $Ni(NO_3)_2$) onto supported tungsten alkoxide species (*e.g.* a $[W(OEt)_5]_2$-1.7/ASA material) leads to the highest intrinsic HYD rates achieved in this study, probably due to the higher amount of NiWS phase, concomitantly with an optimal Ni-to-W atomic ratio in NiWS crystallites $(Ni/W)_{slab}$, spread from 0.26 and 0.32. Such $(Ni/W)_{slab}$ values give about 80 % of Ni substituting W atoms on crystallites edges (for a mean slabs length L ≈ 3.8 nm), which leads to sulphide slabs exhibiting 50 %Ni on S-edge, and 100 %Ni on W-edge.

Then deposition of $Ni(acac)_2$ onto sulphide material, prepared at 23°C lead to NiWS phases with activities similar to the ones of the more active catalysts. This can be partly due to their similar slabs length (*ca.* 3.6 nm), and to the high amount of CSC surface species still remaining on the support after sulphidation at 23°C (*ca.* 40 $\%_{rel}$ W(VI)), which probably enable, together with Ni surface species, the formation of more NiWS sites upon sulphidation at 350°C, thus leading to highly active NiWS crystallites). Moreover, although we are still missing analyses on this spent catalyst, characterisation of the fresh sample shows a $(Ni/W)_{slab}$ value close to 0.27, which is located in the region for which NiWS crystallites exhibit 50 %Ni on S-edge, and 100 %Ni on W-edge. This repartition of Ni is similar to that of the previous CSC NiWS samples prepared on CSC surface alkoxide species. On the contrary, deposition on $Ni(acac)_2$ onto $WS_{2\_350°C}$/ASA gives NiWS catalysts at least two times less active than deposition onto $WS_{2\_23°C}$. This result is thus tentatively linked to the different repartition of Ni on edges after subsequent sulphidation of both samples at 350°C. A nickel repartition of 50 %Ni on S-edge and 25 %Ni on

W-edge, obtained for the sample *ex.* acac/$WS_{2\text{-}350°C}$ would thus be less favourable than a repartition of 50 %Ni on S-edge and 100% Ni on W-edge.

Besides, the investigation of the influence of the Ni content revealed different trends between CSC samples, prepared by deposition of the Ni precursor onto surface alkoxide species or a tungsten sulphide phase (prepared at 23°C). For the latter NiWS/ASA catalysts, increasing the experimental Ni/W ratio from 0.24 to 0.85 (at/at) slightly increases intrinsic HYD rates while a strong drop is observed for the former sample, when Ni/W is higher than 0.44 (at/at) (see **Figure 110**). As XPS analyses of spent NiWS catalysts *ex. acac*/$WS_{2\_23°C}$ have not been performed yet, the next interpretation is based on the previous result obtained for the sample prepared by deposition of Ni onto $WS_{2\_\mathbf{350°C}}$/ASA, although they are not similar. We suppose that the drop of HYD activity is linked to a different decoration of crystallites' W-edge and S-edge. Indeed, samples which underwent deposition of Ni onto a sulphide material exhibit a lower Ni-to-W substitution ratio on edges and corners (X_{subst}) than for samples which underwent deposition of Ni directly on a tungsten oxide phase. As increasing the Ni content was found to increase the aforementioned substitution ratio in crystallites (see **Figure 116**), it means that for a given Ni content, catalysts prepared by **deposition of Ni onto the WS_2 sulphide material** would have **lower Ni-to-W substitution ratios on edges and corners**, than their counterpart prepared by deposition of Ni on surface tungsten species. On top of that, fully decorated crystallites are expected for high Ni content. The strong decrease of activity observed on $Ni(acac)_2$-1.00/$[W(OEt)_5]_2$/ASA can be explained by two effects. First, as in this case, NiWS crystallites do not contain *mixed edge sites* (Ni in close vicinity to W at the edge, see **Figure 113**, structure **III.**), they are suspected to be less active (or inactive) because of the presence of fully decorated crystallites. As proposed for NiMoS or CoMoS [Gandubert *et al.*, 2008; Krebs *et al.*, 2009; Marchand *et al.*, 2009], the simultaneous presence of Ni close to W atoms at the edge should be optimal for activity, whereas the sole presence of Ni atoms at the edges would be less favourable. The reason for that was given by the presence of Ni Lewis site and W-SH groups mandatory to promote the hydrogenation of toluene. A second effect must also be underlined: for high Ni content, high amounts of NiS phase are observed, and thus can somehow hinder of the accessibility to HYD active sites located on crystallites' edges.

Hence, reaching high intrinsic HYD rates is expected for optimal edge decoration of NiWS crystallites. We previously showed that the parameter $(Ni/W)_{slab}$ could be modified by the preparation method, or by the amount of Ni added to the catalyst (*e.g.* experimental Ni/W atomic ratio). However, as the Ni-to-W atomic ratio in crystallites $(Ni/W)_{slab}$ is linked to the

Ni-to-W substitution ratio on edges and corners (X_{subst}), it modifies the amount of NiWS mixed site, as shown in **Figure 117**. This figure clearly shows that the amount of NiWS sites per nm² increases as $(Ni/W)_{slab}$ increases, knowing that this latter parameter ranges from 0.10 and 0.40 for spent catalysts which underwent XPS analyses. With this relationship, we can discuss **Figure 111** which shows the weight flow rate of toluene converted (g(tol)/g(cat)/h) as a function of the effective Ni content in a NiWS phase. The linear increase of the amount of toluene converted can be explained by the increase of Ni decorating NiWS crystallites, probably on both W-edge and S-edge as seen on **Figure 116**. Then, the dramatic drop of weight flow rate observed at high Ni content in NiWS crystallites can be related to $(Ni/W)_{slab}$ values close to 0.39, which are correlated with the stabilization of fully decorated crystallites, suspected to be less active as explained before. The high activity observed for samples with intermediate Ni content in a NiWS phase is thus due to an intermediate amount of NiWS sites, as well as an optimal promoter decoration on W-edge and S-edge (reported earlier in this study to be close to 50 % decorated S-edge and 100 % decorated W-edge crystallites). Finally, the **optimal edge decoration** for NiWS crystallites is achieved for nickel-to-tungsten atomic ratio in crystallites **$(Ni/W)_{slab}$ comprised between 0.23 and 0.39 (at/at)**, corresponding to NiWS sites concentration comprised **between 0.22 and 0.33 (±0.05) NiWS sites/nm²**.

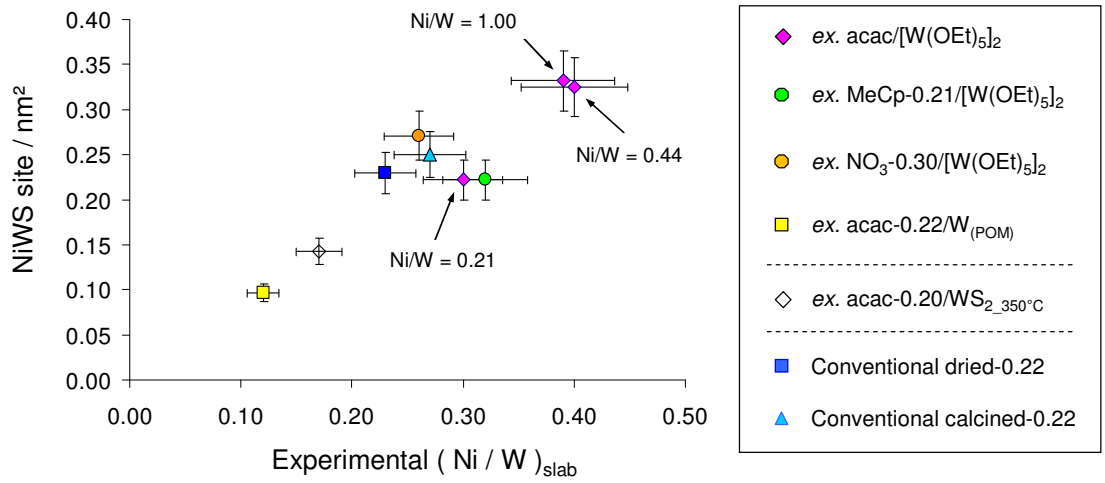

Figure 117: Relationship between the amount of NiWS site per nm² and the experimental Ni-to-W atomic ratio in NiWS crystallites $(Ni/W)_{slab}$

At this point, we have shown that only the presence of an optimal amount of NiWS active sites allows NiWS/ASA catalysts to reach high HYD rates. Concomitantly with that, we also showed that samples supposed to exhibit the highest number of *mixed sites* (*e.g.* with a Ni

repartition of 25% Ni on W-edge and 50 %Ni on S-edge) are less active than samples with lower amount of mixed sites (observed with the following repartition of Ni: 100 %Ni on W-edge, 50 %Ni on S-edge). The **strength of active sites** was thus investigated, by plotting the intrinsic HYD rate expressed by mole of toluene converted by mole of Ni incorporated in a NiWS phase, per hour (referred as mol(tol)/mol(Ni)*/h where mol(Ni)* stands for the amount of Ni incorporated in a NiWS phase). Note that these results, presented in **Figure 118**, take into account XPS data obtained on spent catalysts.

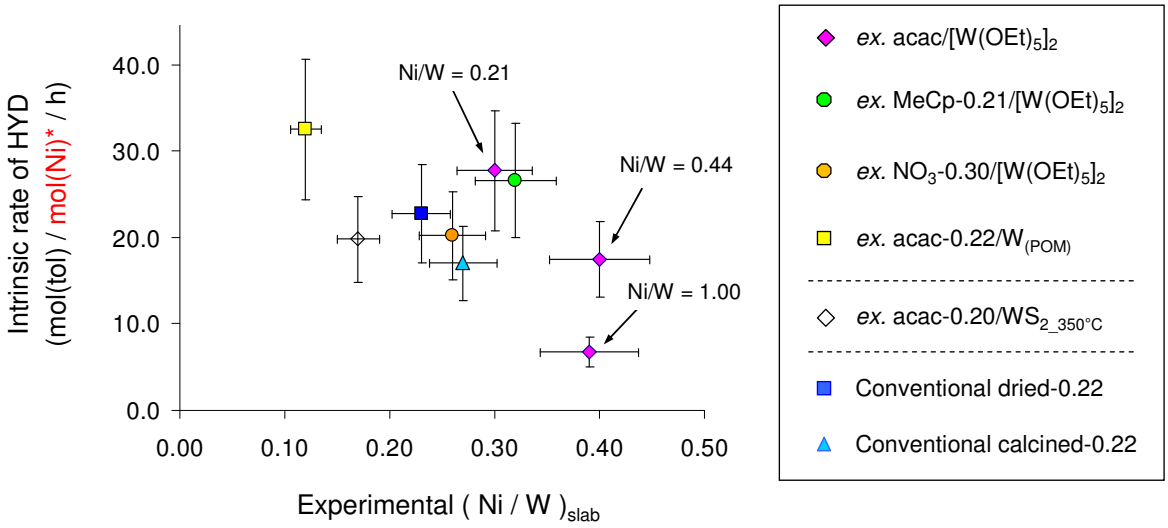

Figure 118: Intrinsic HYD rate of NiWS/ASA catalysts prepared by CSC or conventional method. Expressed in mol(tol)/mol(Ni)*/h, as a function of the Ni-to-W atomic ratio in NiWS crystallites $(Ni/W)_{slab}$, quantified by XPS. Mol(Ni)* stands for the amount (mole) on Ni incorporated in a NiWS phase. Catalysts exhibit between 1.5 and 1.8 W/nm², with experimental Ni/W atomic ratio between 0.20 and 1.00 (at/at). *Ex-situ* sulphidations were carried out at 350°C for 2 h, under a mixture of 15 $\%_{mol.}$ H_2S/H_2, prior to the HYD tests

When the experimental $(Ni/W)_{slab}$ ratio increases, the intrinsic HYD rate decreases. This observation is consistent with the work of Marchand *et al.* [2009] on $NiMoS/Al_2O_3$ catalysts and Costa *et al.* on additived-impregnated dried $CoMoS/Al_2O_3$ catalysts. [Costa *et al.*, 2013] It means that for low $(Ni/W)_{slab}$ values, NiWS sites are rather **isolated** (low amount of NiWS sites, dispersed on crystallites edges) **but are highly active**. On the contrary, for higher values of $(Ni/W)_{slab}$, the amount of NiWS sites increases (concomitantly with the Ni coverage of edges) while their intrinsic HYD rate decreases. In average, the highest intrinsic HYD rates are thus observed for $(Ni/W)_{slab}$ ranging from 0.12 and 0.32. These results, concomitantly with the previous ones on the repartition of Ni on edges, imply that **when Ni only partially decorates**

W-edge and S-edge (50% Ni on S-edge, 25% Ni on W-edge), NiWS sites tend to be **intrinsically more hydrogenating** than when Ni fully decorates NiWS crystallites, *e.g.* for $(Ni/W)_{slab}$ values close or higher than 0.39, as illustrated in **Figure 119**.

In **Figure 119**, taking the example of NiWS crystallites obtained by DFT modelling (with n_M = 8 and n_S = 4), the structure stabilized at low $(Ni/W)_{slab}$ exhibit 0.30 *mixed sites* by edge sites (*e.g.* 15 mixed site over 45 edge atoms, corners included). On the contrary, the structure assumed to be stabilized for $(Ni/W)_{slab}$ values of about 0.40 exhibits no mixed sites. It thus confirms the key role of *mixed site* in HYD reactions, as previously reported by Gandubert *et al.* [2008] for CoMoS phases. In addition, as for all NiWS/ASA samples the amount of edge sites is relatively close (from 26.6 % to 32.6 % of the total number of atoms in a crystallite, given its length) the influence of the location of mixed sites (on W-edge or S-edge) is assumed not to be significant. HYD reactions are supposed to depend on the existence of activated intermediates generated on both edges: H atoms (hydride or sulfhydryls) and adsorbed toluene or toluene hydrogenated derivatives. This synergy effect between the two edges was also underlined for non promoted WS_2 systems investigated in Part V. Note finally that as far as we know, probing the strength of mixed sites located on edge, or corners, is barely possible.

Finally, a compromise of all our results lead to an **optimal nickel-to-tungsten atomic ratio in crystallites** $(Ni/W)_{slab}$ belonging to the interval **{0.23 - 0.32}**. This final result means that catalysts prepared with an **experimental Ni/W atomic ratio** between **0.20 and 0.30 (at/at)** provide NiWS phases with optimised Ni-promoted crystallites, which is supported by previous work of the literature [Raybaud and Toulhoat, 2013, Ed. Technip, Paris, p255]

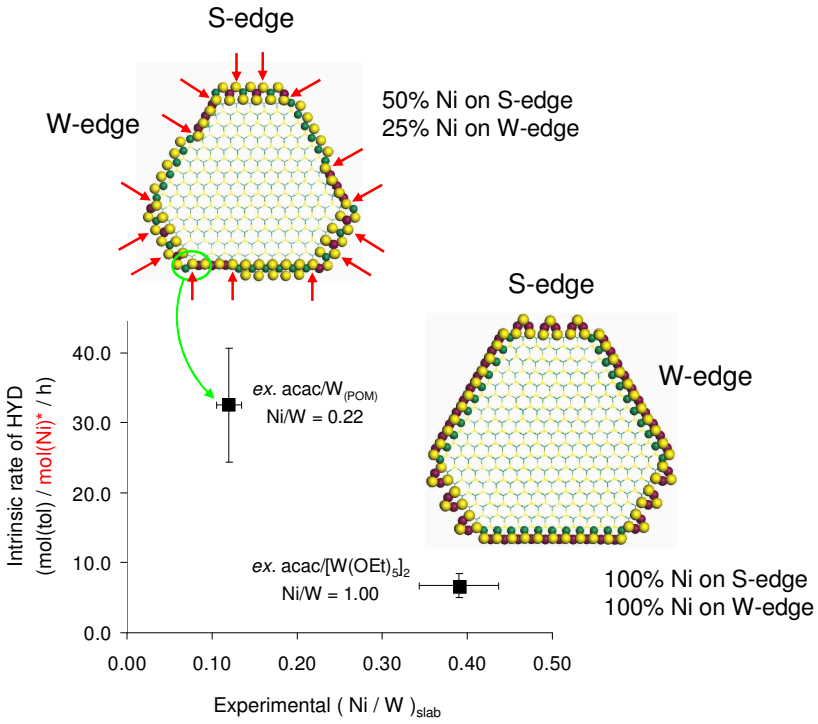

Figure 119: Illustration of the strength of NiWS active sites: *mixed sites (red arrows)* found on NiWS crystallites with 25 %Ni on W-edge and 50 %Ni on S-edge *vs.* fully decorated NiWS crystallites. Green balls: tungsten. Red balls: nickel, Yellow balls: sulphur. Mol(Ni)* stands for the amount (mole) on Ni incorporated in a NiWS phase.

Comparison between catalytic activities of previous CSC catalysts (*ex.* acac/$[W(OEt)_5]_2$) and conventional dried or calcined NiWS/ASA ones is now discussed. Conventional samples exhibit intermediate Ni-to-W atomic ratio in crystallites $(Ni/W)_{slab}$, of respectively 0.23 and 0.27 (at/at), which would lead to intermediate Ni decoration of W-edge and S-edge, and thus to the presence of *mixed sites* providing the expected HYD activity. However, the balance between the amount of NiWS sites and their strength (intrinsic HYD rate) is supposed not to be as optimal as that of CSC samples, which exhibit similar $(Ni/W)_{slab}$ values but higher intrinsic HYD rates. Note that all these interpretations do not take into account the slabs stacking, which is, however, not supposed to have a significant influence as TEM analyses reveal only slight differences between the samples.

VI.7. Conclusion

The aim of this part was to study NiWS/ASA catalysts prepared by a molecular approach, with different Ni-precursors and different impregnation strategies. Through XPS and TEM analyses on catalysts before and after catalytic tests, as well as with the help of 2D geometrical models and DFT modelling, we demonstrated that:

(1) the HYD activity of NiWS/ASA catalysts is linked to the presence of mixed sites (Ni atoms in close vicinity to W ones, at the edge)

(2) the strength (intrinsic HYD rate) of these mixed sites is higher when they are isolated on crystallites edges. This strength decreases when the Ni content on edges increases.

(3) finding the right balance between the amount of NiWS sites and their strength is the key parameter to reach high intrinsic HYD rates. This balance is strongly correlated with the Ni repartition on W-edge and S-edge.

We investigated the influence of different Ni-precursors on the level of sulphidation as well as the amount of active phase formed on NiWS samples, concomitantly with the consequences on their HYD activity. We found strong similarities between conventional NiWS/ASA samples (prepared by co-impregnation of ammonium metatungstate and nickel nitrate) and CSC material obtained by impregnation of bis-acetylacetonato nickel ($Ni(acac)_2$) or nickel nitrate on supported surface alkoxide W-species. The activity of CSC samples in toluene hydrogenation were found to be *ca.* 30 % higher, which is tentatively assigned to the reactivity of CSC tungsten surface species toward Ni precursors upon deposition. This increase of activity can be related to a more intimate contact between Ni and W atoms, which promotes the formation of NiWS crystallites with an optimal balance between the amount and the strength of active sites.

The influence of the preparation method was also investigated by impregnation of Ni-precursors on ASA-supported alkoxide species or on a CSC sulphide material (prepared at either 350°C or 23°C). Deposition of nickel onto supported surface alkoxide tungsten species or sulphide ones prepared at 23°C (2 h, 15 $\%_{mol.}$ H_2S/H_2) leads to high intrinsic HYD activities, correlated with the optimal balance observed between the presence of mixed sites and their strength. More interestingly, we propose that impregnation of the nickel precursor on supported surface alkoxide W-species is in favour of the formation of NiWS crystallites exhibiting highly Ni-decorated edges (either 100 %Ni on W-edge and 50 or 100 %Ni on S-edge), while impregnation of the nickel precursor on a sulphide material prepared at 350°C (same sulphiding

conditions) leads to crystallites' structure partially decorated, with 25% Ni on W-edge and 50 %Ni on S-edge, less optimal for HYD reactions.

The study of the influence of the Ni content reveals an optimal promoter-to-tungsten ratio in crystallites $(Ni/W)_{slab}$ located in between 0.23 and 0.32 (at/at). This ratio, experimentally found by XPS analyses of spent catalysts, is achieved when samples are initially prepared with experimental Ni/W atomic ratio in between 0.20 and 0.30.

Finally, the preparation of NiWS/ASA catalysts *via* a molecular approach is found to be very promising from an industrial point of view. CSC samples are at least more than 50 % more active than their industrial NiWS/ASA counterpart, while they exhibit at least 2 times less W atoms.

VI.8. References

Baubet, B., PhD thesis, Université Claude Bernard Lyon 1, France (2013)

Costa, V.; Guichard, B.; Digne, M.; Legens, C.; Lecour, P.; Marchand, K.; Raybaud, P.; Krebs, E. and Geantet, C., *Catalysis Science & Technology* (2013), **3**, 140

Deepak, F.L.; Esparza, R.; Borges, B.; Lopez-Lozano, X. and Jose-Yacaman, M., *ACS Catalysis* (2011), **1**, 5, 537-543

Gandubert, A.D., PhD thesis, Université de Lille, France (2006)

Gandubert, A.D.; Krebs, E.; Legens, C.; Costa, D.; Guillaume, D. and Raybaud, P. *Catalysis Today* (2008), **130**, 1, 149–159

Guernalec, N.; Geantet, C.; Raybaud, P; Aouine, M. and Vrinat, M. *Oil & Gas Science and Technology – Rev. IFP* (2006), **61**, 4, 515-525

Guernalec, N.; Geantet, C.; Cseri, T.; Vrinat, M.; Toulhoat, H. and Raybaud, P. *Dalton Transactions* (2010), **39**, 8420– 8422

Guichard, B.; Roy-Auberger, M.; Devers, E.; Legens, C. and Raybaud, P., *Catalysis Today* (2008), **130**, 1, 97-108.

Kelly, S.D.; Yang, N.; Mickelson, G.E.; Greenlay, N.; Karapetrova, E.; Sinkler, W. and Bare, S.R., *Journal of Catalysis* (2009), **263**, 1, 16-33

Kessler, V.G.; Spijksma, G.I.; Seisenbaeva, G.A.; Håkansson, S.; Blank, D.H.A. and Bouwmeester, H.J.M., *Journal of Sol-Gel Science and Technology* (2006), **40**,163-179

Krebs, E.; Daudin, A. and Raybaud, P., *Oil & Gas Science and Technology – Rev. IFP* (2009), **64**, 6, 707-718

Krebs, E.; Silvi, B. and Raybaud, P. *Catalysis Today* (2008), **130**, 1, 160-169

Louwers, S.P.A. and Prins, R. *Journal of Catalysis* (1993), **139**, 2, 525-539

Marchand, K.; Legens, C.; Guillaume, D.; and Raybaud, P., *Oil & Gas Science and Technology – Rev. IFP* (2009), **64**, 6, 719-730

Maugé, F.; Vallet, A.; Bachelier, J.; Duchet, J.C. and Lavalley, J.C., *Catalysis Letters* (1989), **2**, 1, 57-61

Maugé, F. and Lavalley, J.C., *Journal of Catalysis* (1992), **137**, 69-76

Molina, R.; Centeno, M.A.; and Poncelet, G., *The Journal of Physical Chemistry B* (1999), **103**, 6036-6046

Okamoto, Y.; Kato, A.; Usman, Sato, K.; Hiromitsu, I. and Kubota, T. *Journal of Catalysis* (2005), **233**, 1, 16-25

Okamoto, Y.; Kato, A.; Usman; Rinaldi, N.; Fujikawa, T.; Koshika, H.; Hiromitsu, I. and Kubota, T., *Journal of Catalysis* (2009), **265**, 2, 216-228

Raybaud, P. and Toulhoat, H., Catalysis by transition metal sulphides (2013), chapt. 2.3.2, p247, Editions Technip, Paris

Raybaud, P. and Toulhoat, H., Catalysis by transition metal sulphides (2013), chapt. 2.3.2.2, Editions Technip, Paris

Raybaud, P.; Hafner, J.; Kresse, G.; Kasztelan, S. and Toulhoat, H., *Journal of Catalysis* (2000), **190**, 1, 128-143

Roukoss, C.; Laurenti, D.; Devers, E.; Marchand, K.; Massin, L. and Vrinat, M., *Comptes Rendus Chimie* (2009), **12**, 6-7, 683, 691

Salinier, V.; Corker, J.M.; Lefebvre, F.; Bayard, F.; Dufaud, V. and Basset, J.M., *Advanced Synthesis & Catalysis* (2009), **351**, 2155-2167

Schweiger, H.; Raybaud, P. and Toulhoat, H., *Journal of Catalysis* (2002), **212**, 1, 33-38

Schweiger, H.; Raybaud, P.; Kresse, G. and Toulhoat, H., *Journal of Catalysis* (2002), **207**, 1, 76-87

Sun, M.; Nelson, A.E. and Adjaye, J., *Journal of Catalysis* (2004), **226**, 1, 41, 53

van der Meer, Y.; Hensen, E.J.M.; van Veen, J.A.R. and van der Kraan, A.M., *Journal of Catalysis* (2004), **228**, 2, 433, 446

Yermakov, Y.I.; Startsev, A.N. and Burmistrov, V.A., *Applied Catalysis* (1984), **11**, 1, 1-13

Zuo, D.; Vrinat, M.; Nie, H.; Maugé, F.; Shi, Y.; Lacroix, M. and Li, D., *Catalysis Today* (2004), **93-95**, 1, 751-760

Part VII. General conclusion and perspectives

VII.1. General conclusion

The aim of this thesis was to improve and understand at a molecular level the sulphidation of tungsten-based hydrotreating catalysts, whether promoted or not by Ni. It required the control and the understanding of each step of the catalyst preparation; and we have decided to approach the problem through **"controlled surface chemistry"** (CSC). In particular, we chose to control the density and the distribution of metal sites (W or Ni/W) through the grafting of well-defined molecular precursors (W and Ni/W) onto partially dehydroxylated amorphous silica-alumina with a given density of reactive sites (3.2 OH/nm^2), and to thereafter carry out the sulphidation step in a controlled way (controlled growth of WS_2 from well-defined isolated W sites under a 15 $\%_{mol.}$ H_2S/H_2 mixture, at 350°C). Each step was evaluated by means of multiple characterisation techniques such as infrared (IR), nuclear magnetic resonance (NMR) and X-ray photoelectron (XPS) spectroscopies as well as transmission electron microscopy (TEM).

The **"controlled surface chemistry"** (CSC) concept had been widely used for the preparation of highly active single-site catalysts, in particular for reactions such as alkene metathesis, hydrogenation or polymerization ; it usually referred to as Surface Organometallic Chemistry since organometallics are used. This concept has also been applied to control the growth of supported metallic nanoparticles, and few examples have discussed its use to the preparation of hydrotreating catalysts. In fact, the literature survey has revealed that preparation of supported surface species with metallo-organic precursors (small mono or bimetallic metal centre(s) linked to a wide variety of ligands, typically allyl) could be used to improve the sulphidation of W-based catalysts, to increase the amount of active phase of promoted NiWS/ASA catalysts, *e.g.* the so-called mixed phase "NiWS" and to increase the catalytic activities of such catalysts in HDS or HYD reactions.

In this work, tungsten molecular complexes with reactive anionic ligands towards surface hydroxyl functionalities of the ASA support had to be selected. In the view of promising preliminary results obtained at IFPEn, tungsten alkoxides were selected, more specifically,

tungsten (V) and tungsten (VI) alkoxide precursors, either monomeric of dimeric, such as $[W^{(V)}(OEt)_5]_2$, $W^{(VI)}(OEt)_6$ or $[W^{(VI)}(=O)(OEt)_4]_2$.

First, a series of ASA-supported alkoxide W-species were prepared by impregnation of the aforementioned W alkoxide precursors on partially dehydroxylated ASA (typically at 300 °C) and characterised by IR and NMR spectroscopies. The corresponding sulphide materials were then obtained by sulphidation (2 h, 15 $\%_{mol.}$ H_2S/H_2, 350°C) and subsequently characterised by XPS (materials referred to as "CSC" samples). Independently of the structure of the molecular precursor and its oxidation state, similar final materials are obtained with high levels of sulphidation (71$\%_{rel.}$ to 72 $\%_{rel.}$ WS_2) and good catalytic performances in toluene hydrogenation in the presence of aniline. In fact, their catalytic performances are either similar or greater than the benchmark catalysts prepared by the conventional approach (*e.g.* impregnation of an aqueous solution of ammonium metatungstate on ASA, followed by a drying step, and a calcination one if needed).

In view of this promising results and the commercial availability of $[W(OEt)_5]_2$ in a pure form, the effect of metal loading (W/nm²) and of preparation methods, on the structure of the surface species at each step, and the activity of the resulting sulphide phases in the hydrogenation of toluene in the presence of aniline, was evaluated.

Combined mass balance analysis, extensive IR, and solid-state NMR analyses on materials prepared by impregnation of $[W(OEt)_5]_2$ on ASA partially dehydroxylated at 300°C as well as computational studies show that:

(1) at low loading (below 0.8 (±0.1) W/nm²), grafting of $[W(OEt)_5]_2$ leads to the formation of dinuclear species, having an average of 7 remaining ethoxy ligands, and being attached by 3 bonds to the ASA surface (see **Figure 120**). The multiple grafting is accompanied by the formation of ethoxy groups linked to the ASA surface, a process probably assisted by W. The grafting of $[W(OEt)_5]_2$ onto ASA has been rationalised and involves the reaction of alkoxy ligands of $[W(OEt)_5]_2$ (terminal or bridging) with surface hydroxyls as well as with M-O-M' bridges (M = Al, Si; M' = Al, Si). In addition, the resulting ethanol evolved during the grafting process probably further reacts with M-O-M' bridges. Despite all these evidences, a precise location of surface species on silica or alumina parts of the ASA support has not been possible.

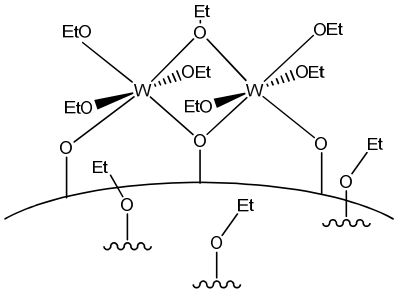

Figure 120: Example of tungsten surface species probable found on non-sulphided $[W(OEt)_5]_2$-based material

(2) For tungsten loading greater than 0.8 (±0.1) W/nm², the additional tungsten species are adsorbed more or less strongly on top of the grafted W surface species *via* either μ-bridge ethoxide or electrostatic interactions, making an overlayer of W molecular species according to detailed NMR and IR spectroscopic analysis (see **Figure 121**).

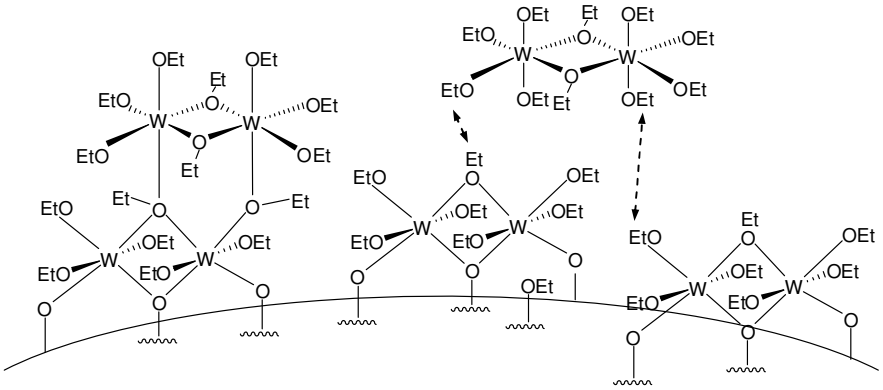

Figure 121: Example of a multilayer formed by alkoxide W-species. Arrows stand for electrostatic interactions

Upon sulphidation under standard conditions (350°C, 2 h, 15 $\%_{mol.}$ H_2S/H_2), the CSC catalysts display greater or similar amount of WS_2 phase (level of sulphidation up to 85 (±5) $\%_{rel.}$ WS_2) than conventional catalysts according to XPS, whatever the W-loading. According to X-ray diffraction and temperature-programmed reduction (TPR) experiments, the genesis of different amount of WS_2 phases probably results from the different chemical nature of tungsten surface species (*e.g.* dinuclear species, tungsten clusters, or patches of tungsten oxide), their dispersion on the surface, and their interactions with the ASA support, which likely influence their sulphidation. These different surface species are illustrated in **Figure 122.**

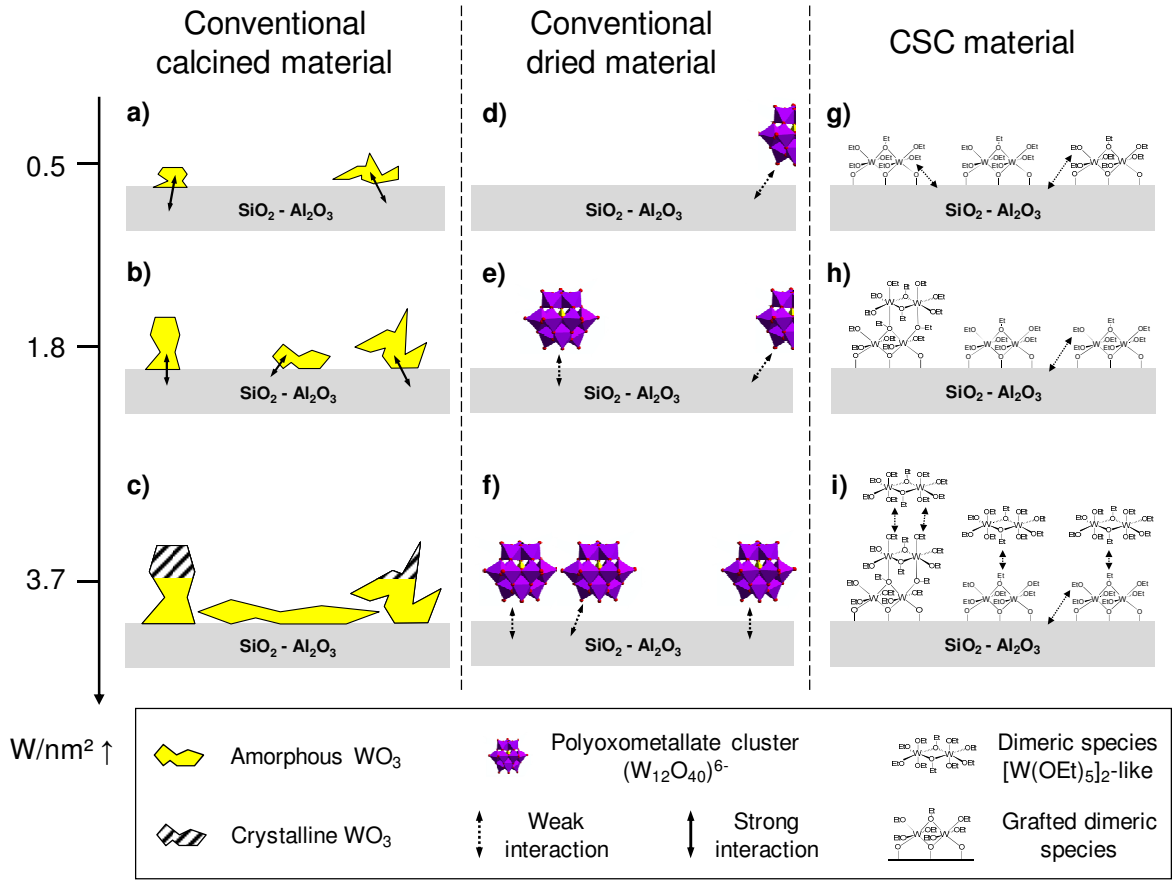

Figure 122: Schematic representation of surface W-species observed for increasing W-loadings on CSC and conventional dried and calcined catalysts

At 0.5 W/nm² in particular, CSC samples undergo sulphidation in a larger extent than their conventional counterparts (76 $\%_{rel}$. WS_2 *vs.* 33 $\%_{rel}$ WS_2 for the calcined sample). While their surface coverages are similar in terms of W/Al atomic ratios and therefore cannot explain the differences between the various preparation methods, it is likely that their reducibility/sulphidation depends strongly on the strength and the nature of the interaction between W and its ligands (supports *vs.* O-network in HPA, *vs.* O-network in an oxide layer), making a larger difference between the conventional calcined oxide phases and supported alkoxide species. In addition, the higher levels of sulphidation observed for greater W-loadings (up to 85 $\%_{rel.}$ WS_2 for CSC samples with a W content greater than 0.5 W/nm²) is assigned to: (1) the greater proximity between surface W sites, which could facilitate sulphidation through an easier migration of surface species and (2) to the presence of weakly adsorbed and more mobile W species in the multilayer of the CSC samples. Note also that the enhanced reactivity

of these CSC surface species towards sulphidation probably originates from their similarities to the starting molecular complex, which is readily converted in bulk WS_2 under similar conditions. On the contrary, for conventional materials and specifically in the case on the calcined one, formation of stacked species is concomitant with the appearance of crystalline WO_3, an oxide phase known to be refractory to sulphidation, thus explaining the lower level of sulphidation of calcined samples.

The stronger modification of mean slabs length and stacking number occurs for sulphide phases originating from calcined materials as revealed by TEM: mean slab length and mean stacking number increase when greater amounts of tungsten are used. Noteworthy, STEM-HAADF experiments show for the first time clear evidence that the 2D morphology of WS_2 slabs on conventional non-promoted catalysts supported on oxide (ASA, as a relevant industrial support) is close to a truncated triangle, for sulphidation carried out at 600°C (2 h, 15 $\%_{mol.}$ H_2S/H_2).

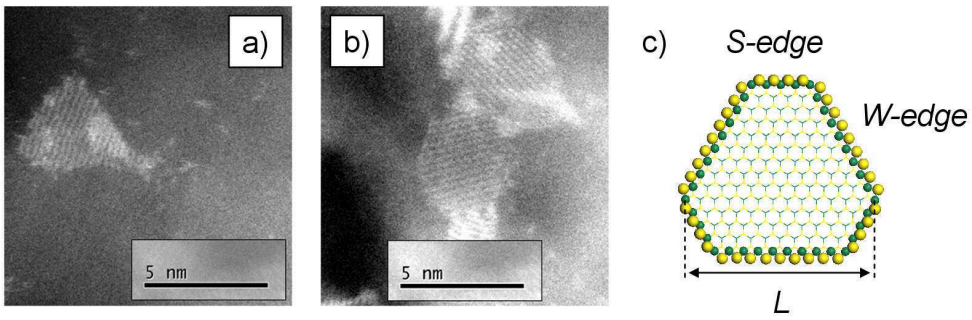

Figure 123: STEM-HAADF micrograph of isolated WS_2 slabs found on sulphide catalysts prepared by: a) a conventional calcined method; b) a molecular approach. Experimental conditions: 600°C, 2 h, 15 $\%_{mol.}$ H_2S/H_2. c) Crystallite structure stabilised in the corresponding experimental conditions, as obtained by DFT calculations

This result, shown in **Figure 123-a**, is in line with what has been found on model catalysts, based on WS_2 deposited onto graphite or gold surfaces. The 2D morphology also matches what has been predicted from DFT calculations, *e.g.* a 2D morphology exhibiting a ratio between the W-edge length and the S-edge length, $\frac{L_{W-edge}}{L_{S-edge}}$, close to *ca.* 1.6. [Girleanu *et al.*, *in preparation*]

In the case of CSC catalysts (600°C for 2 h, H_2S/H_2 15 $\%_{mol.}$ H_2S), the 2D morphology is more hexagonal (**Figure 123-b**). While the origin of this peculiar morphology is not clear yet, one hypothesis is that the CSC method induces the formation and the stabilisation of a kinetic form of WS_2 slabs, with a less triangular shaped 2D morphology than the thermodynamically stable one found for calcined samples.

Catalytic activity in toluene hydrogenation have also been evaluated by taking into account the amount of sulphide phase detected by XPS analyses on spent catalysts, in order to express activity per surface (active) sites. With the help of TEM data, DFT calculations and geometrical models, Turn-Over Frequencies (TOF) can be evaluated and expressed in mole of toluene converted per mole of tungsten on edge and corners per hour, assuming that W atoms on W-edge, S-edge and corners are active hydrogenation sites. CSC materials are typically more active than conventional ones, especially for a W-loading of 1.7 W/nm². Even if not totally understood, TOF differences likely originate from different amounts of active sites such as the so-called CUS (Coordinatively Unsaturated Sites), but it can also results from the presence of different type of active sites. In fact, IR(CO) analyses (recorded a low temperature, *ca.* 77K), are consistent with the presence of different sulphide phases on CSC and conventional sulphide samples, when sulphidation is performed at 350°C: CO strongly interacts with the sulphide phase of CSC samples, while much lower or even no interaction is observed for conventional materials. Noteworthy, this strong interaction of CO with WS_2 is highlighted by a sharp band at $\nu(CO) = 2121 \pm 3\ cm^{-1}$, tentatively attributed to a CO interaction with W-edge of WS_2 crystallites. However, further work is necessary to ascertain the IR signature of CO interacting with a WS_2 sulphide phase and quantify the amount of CO interacting with the surface sites.

Another important parameter has been to study the effect of the sulphidation temperatures in order to obtain more information about the genesis of the sulphide phase, With the most promising systems (W-loading close to 1.7 W/nm²), XPS has shown that the level of sulphidation follows an S-shaped curve as a function of the sulphidation temperature for all samples (see **Figure 124**). The inflection point, however, depends greatly on the preparation methods.

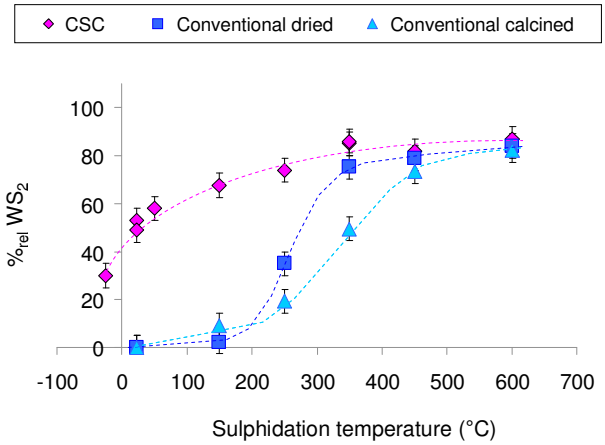

Figure 124: Level of sulphidation of CSC and conventional (dried or calcined) catalysts sulphided at different temperatures between 23°C and 600°C (2 h, 15 $\%_{mol.}$ H_2S/H_2). W-loading: 1.7 - 1.8 W/nm²

The CSC materials undergo sulphidation at much lower temperatures, well below 200 °C, than the conventional catalysts. The sulphide phases formed on CSC and dried materials suffer from significant sintering according to TEM, compared to the calcined sample (vide supra), probably because of the weaker interactions between the support and the more mobile surface species. Note that STEM-HAADF could not clearly distinguish 2D morphology of WS_2 crystallites when sulphidation is performed at 350°C. Higher temperatures such as 600°C would thus be a requirement for the observation of clear 2D morphologies, indicating that WS_2 slabs are not well crystallised at lower temperature.

Catalytic performances in toluene hydrogenation are also influenced by the length of WS_2 crystallites. The CSC catalysts are intrinsically more active catalysts, based on TOF calculated from the geometrical models, DFT modelling, TEM and XPS data, with *ca.* 2.0 mole of toluene converted per mole of edge sites and corner per hour. Such improved intrinsic activity could be linked to the hexagonal morphology of their WS_2 crystallites with an edge structure providing a synergy effect between W- and S-edge. This synergy effect possibly enhances the H_2 activation into MSH and MH species as well as toluene activation when adsorbed on edges.

Overall, the preparation of non-promoted catalysts *via* a molecular approach has allowed a better understanding of the genesis of the sulphide phase through the detailed characterisation of surface species at each step (prior and post-sulphidation). It has also provided WS_2/ASA catalysts with improved sulphidation level and with WS_2 crystallites exhibiting enhanced intrinsic HYD rates in toluene hydrogenation in the presence of aniline (see **Figure 125**).

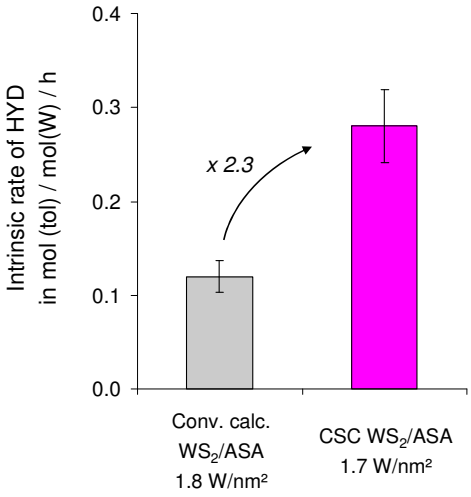

Figure 125: Intrinsic HYD rate of conventional calcined (1.8 W/nm²) and CSC (1.7 W/nm²) WS_2/ASA catalysts, sulphided at 350°C (2 h, 15 $\%_{mol.}$ H_2S/H_2). Expressed in mol(tol)/mol(W)/h

Ni-promoted catalysts, known to be more active, were also prepared *via* the CSC approach. Ni-promoted samples were targeted with a W-loading of *ca.* 1.7 (±0.1) W/nm², a W content found to be optimal for CSC samples. Different Ni-precursors, for instance bis-acetylacetonato nickel, $Ni(acac)_2$, bis-1-methylcyclopentadienyl nickel, $Ni(1\text{-}MeCp)_2$, and nickel nitrate, $Ni(NO_3)_2$, were impregnated on ASA supported tungsten alkoxide species, with a nickel content corresponding to Ni/W ≈ 0.2 (at/at), considered to be optimal for HYD reactions. For $Ni(acac)_2$ in particular, such a preparation method have probably promoted the formation of rather well-dispersed nickel and tungsten species where Ni and W are in close vicinity, since alkoxide/acac ligand can readily bridge two metal centres. Upon sulphidation, these surface species, while not fully characterised, generate NiWS crystallites with high amount (up to 80 (±10) $\%_{rel.}$ NiWS) of Ni incorporated in a NiWS *mixed phase,* which is considered to be very important for the catalytic reaction. Given tungsten and nickel contents of all samples, XPS analyses of spent catalysts show that the amount of active sites is strongly influenced by the nature of tungsten surface species on which the nickel precursor was deposited: the amount of NiWS sites per nm² is improved from 0.10 (±0.02) NiWS site/nm² (Ni deposited on a conventional dried oxide phase) to 0.33 (±0.04) NiWS site/nm², if Ni is impregnated on supported surface alkoxide W-species (CSC material).

Characterisation by TEM has revealed that no significant difference of slab length and stacking number is observed as a function of the preparation method (CSC *vs.* conventional). Noteworthy, STEM-HAADF analyses performed on conventional calcined samples (0.5 W/nm², Ni/W ≈ 0.2) reveal that the 2D morphology of promoted sulphide crystallites is more hexagonal

than the non-promoted ones', as proposed/rationalised by DFT calculations. [Girleanu *et al.*, *in preparation*] These calculations highlighted the presence of Ni lowers the edge energy of S-edge in a greater extent than of that of W-edge: the ratio $\frac{L_{W-edge}}{L_{S-edge}}$ is thus decreased to 1.1.

The nickel precursor was found to have no influence on the catalytic properties of CSC NiWS/ASA samples, which are found to be more active that conventionally prepared samples.

Results can be rationalized in the same spirit as for non-promoted samples, by combining DFT modelling, TEM data and geometrical models, together with XPS data. From DFT modelling studies, 3 relevant NiWS crystallites are possibly stabilised under conditions close to the experimental ones (see **Figure 126**):

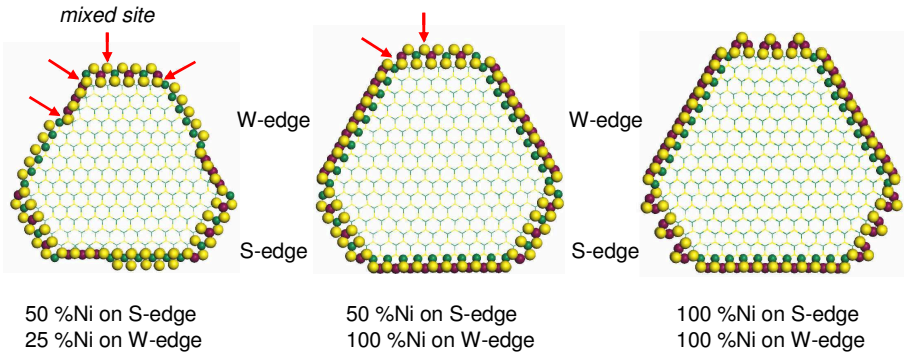

Figure 126: DFT modelling. NiWS crystallites possibly stabilised in conditions close to the experimental ones (350°C, 15 $\%_{mol.}$ H_2S/H_2)

By calculating to which extent Ni substitutes W on crystallites' edges and corners, the CSC approach is found to promote different repartitions of Ni on edges. Indeed, NiWS/ASA samples prepared by impregnation of the nickel precursor onto a CSC sulphide material, prepared at 350°C (2 h, 15 $\%_{mol.}$ H_2S/H_2) exhibit crystallites with partially decorated edge: 25 %Ni on W-edge and 50 %Ni on S-edge, while, these, obtained by deposition of $Ni(acac)_2$ onto supported alkoxide species show crystallites with fully decorated W-edge (100 %Ni) and partially decorated S-edge (50 %Ni). Such differences thus infer different amounts of *mixed sites* (Ni in close vicinity of W) on edges. As these sites are involved in HYD reactions, controlling **their amount would be an important parameter,** which needs to be studied in more details.

In fact, when increasing the Ni/W atomic ratio, XPS analyses show that the amount of NiWS phase increases, concomitantly with the appearance of higher and higher amount of undesirable nickel sulphide phase NiS. Increasing the Ni-to-W atomic ratio in crystallites, $(Ni/W)_{slab}$, infers an increase of the amount of active phase, concomitant with an activity improvement. Noteworthy is the dramatic decrease of activity observed for high Ni contents in the sample (Ni/W ≈ 1.0 at/at), which is tentatively assigned to the greater amount of NiS phase, probably covering NiWS crystallites, thus lowering their activity. Finally, an optimal amount of active phase is achieved for NiWS/ASA catalysts (either CSC or conventional) with $(Ni/W)_{slab}$ between 0.23 and 0.39 (at/at).

However, the amount of active site is not the only important parameter: the strength of *mixed site* also plays a role in the catalytic activity of NiWS phases. Indeed, looking at the intrinsic hydrogenation rate, expressed by mole of toluene converted by mole on Ni incorporated in a NiWS phase per hour, reveals that isolated active sites, found for low values of $(Ni/W)_{slab}$, are intrinsically more active. In particular, when Ni only partially decorates W-edge and S-edge (50% Ni on S-edge, 25% Ni on W-edge), NiWS sites are intrinsically more hydrogenating than when Ni fully decorated NiWS crystallites. Finally, high catalytic activities are strongly linked to the balance the amount of active sites and their strength: a rather good compromise is obtained for nickel-to-tungsten atomic ratio in crystallites $(Ni/W)_{slab}$ between **0.23 and 0.32**. Such values are obtained by preparation of NiWS/ASA catalysts with an experimental Ni/W atomic ratio between **0.20 and 0.30 (at/at).**

To conclude on the promising catalytic performances of CSC samples, the best NiWS/ASA catalyst is compared to a calcined NiWS/ASA sample, used as an industrial reference (see **Figure 127**). The CSC sample (1.7 W/nm², Ni/W ≈ 0.2 at/at) appears to be about 4 times more hydrogenating than the reference industrial catalyst (4.4 W/nm², Ni/W ≈ 0.4 at/at).

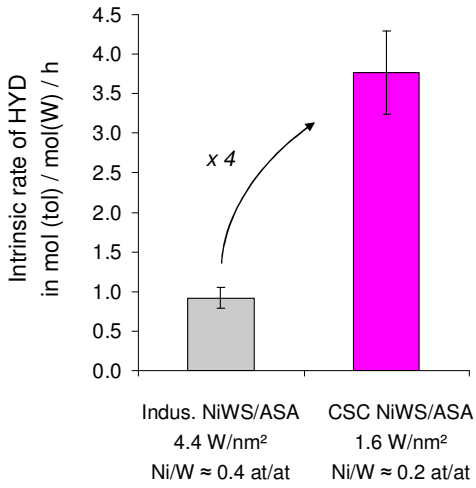

Figure 127: Intrinsic HYD rate reference and CSC Ni promoted catalysts, with different W and Ni loadings. Expressed in mol(tol)/mol(W)/h

Overall, the CSC approach has also lead to the improvement of the performances of Ni-promoted catalysts, which display faster rate in hydrogenation than conventional catalysts considered as industrial references. Their greater performances are tentatively explained by the right balance between the strength and the amount of NiWS active sites.

VII.2. Perspectives

Concerning surface chemistry, the structure of surface alkoxide species, revealed by NMR and IR analyses, has to be refined by complementary spectroscopic techniques such as EXAFS or High Resolution Ultrafast MAS NMR [Roussey *et al.*, 2011] combined with MultiQuantum MAS NMR experiments (MQ-MAS) and computational approaches. [Chizallet and Raybaud, 2009; Chizallet and Raybaud, 2010] Such methods would allow having a more detailed structure analysis of the first coordination sphere and the environment of W surfaces species. In addition, it should be possible to evaluate the location of ASA-supported W-surface species, whether on silica, alumina, or both, through Dynamic Nuclear Polarisation Surface Enhanced NMR spectroscopy (DNP SENS) [Lesage *et al.*, 2010], which could interrogate the special proximity of protons of the surface species with ^{27}Al or ^{29}Si.

Concerning tungsten sulphide phases, we have shown that improving the levels of sulphidation of tungsten was possible. For non-promoted samples, 87 (±5) $\%_{rel.}$ WS_2 was reached according to XPS, for catalysts prepared *via* CSC using $[W(OEt)_5]_2$ as a molecular precursor. An interesting question is thus: is it possible to improve further sulphidation (deeper and at lower temperature), for instance by using tungsten molecular precursors having sulphur-containing ligand, for instance by using $W(=S)_x(SR)_{6-2x}$ derivatives or/and sulphided surfaces ?

Besides, interactions between the surface of the support and tungsten surface species, as well as between the W species themselves have been proposed to partly explain the different behaviour upon sulphidation of materials (the weaker the interaction (supported dinuclear species *vs.* polyoxometallates *vs.* oxide) the more favoured the sulphidation). Therefore, probing and characterising these interactions between the ASA support and the (1) surface alkoxide species as well as the (2) WS_2 crystallites would probably help understanding phenomena taking place at the interface between ASA and tungsten species upon sulphidation and provide clues on how to improve this step with the objective to reach a pure sulphide phase. One approach would be to monitor the formation of the surface species at each step using ^{17}O-NMR on ^{17}O-doped ASA since oxygen-17 is highly sensitive to its environment (quadrupolar nuclei).

Another important observation of this PhD is that the sulphide phases are different between conventional and CSC sulphided catalysts according to IR(CO) spectroscopy at low temperature. Yet such differences are not understood, and complementary analyses and computational studies are clearly needed.

Concerning Ni-promoted samples, the use of a molecular approach in the preparation of NiWS/ASA materials proved to give highly active hydrogenation catalysts. Improved catalytic activities have been interpreted as a result from the balance between the strength and the amount of active sites observed on sulphide phases, which is probably influenced by the surface species formed upon impregnation of Ni and W molecular precursors. As previously performed on non-promoted samples, extensive spectroscopic studies are necessary to obtain insights in the characterisation of surface species along the catalyst preparation steps. NiW materials prepared by grafting of molecular complexes should be studied by NMR. Note however that considering the (probable) paramagnetic behaviour of Ni entities, NMR signals originating from tungsten and nickel surface species would probably be strongly broadened and difficult to interpret. However, IR, XANES and EXAFS combined with computational studies could help refining the structure of surface species. In addition, model mixed metal complexes could also be used to obtain spectroscopic signatures for interactions between Ni and W.

From a more industrial point of view, NiWS/ASA CSC catalysts have shown promising activity for the hydrogenation of toluene in the presence of aniline, typically greater than these observed for the conventional ones. Considering that catalytic tests on model molecules are far from realistic test conditions, catalytic tests on a more realistic feed, such as Vacuum Gas Oil, should be and will be performed to ascertain the high catalytic activity of CSC NiWS/ASA catalysts, in more practical hydrogenation reactions.

Finally, trimetallic phases are expected to be more active than bimetallic ones. Yet Ni-promoted CSC samples (prepared with Ni and W) display comparable hydrogenating activity as the trimetallic industrial reference samples (prepared with Ni, Mo and W). It is thus clear that the preparation of ASA supported NiMoW catalysts *via* a controlled surface chemistry approach should be the next step. One possibility, in the view of the results presented in this PhD, is to investigate the co- or successive impregnation of molybdenum alkoxides such as $Mo(OEt)_5$ with $[W(OEt)_5]_2$ and $Ni(acac)_2$ molecular complexes followed by the sulphidation step. Achieving the formation of well dispersed species for each metal should help the formation of high amount of active sulphide phases.

To conclude, the preparation of supported NiWS catalysts by "**CSC**" appears to provide more active catalysts for HYD reactions. While scarcely applied for the synthesis of HDS catalysts, such a molecular approach, using well-defined molecular precursors with tunable ligands and thereby tunable reactivities, could enable the preparation and improvement of

sulphide catalysts specifically designed for other hydrotreating processes such as HDN, or HDO.

VII.3. References

Chizallet, C. and Raybaud, P. *Angewandte Chemie International Edition* (2009), **48**, 16, 2891-2893

Chizallet, C. and Raybaud, P. *Chem.Phys.Chem*. (2010), **11**, 1, 105-108

Girleanu, M.; Alphazan, T.; Boudène, Z.; Raybaud, P.; Gay, A.S.; Ersen, O.; Bonduelle, A. and Legens, C. *in preparation*

Lesage, A.; Lelli, M.; Gajan D.; Caporini, M.; Vitzthum, V.; Miéville, P.; Alauzun, J.; Roussey, A.; Thieuleux, C.; Mehdi,A.; Bodenhausen, G.; Copéret, C. and Emsley, L., *Journal of the American Chemical Society (*2010), **132**, 15459.

Roussey, A., Gajan, D.; Maishal, T.K.; Mukerjee, A.; Veyre, L.; Lesage, A.; Emsley, L.; Copéret, C. and Thieuleux, C., *Physical Chemistry Chemical Physics* (2011), **13**, 4230-4233

Appendices

Outline of appendices

Appendix A: Tentative de dépôt sur ASA_{-300} de $W(CO)_6$ et d'un mélange « $W(CO)_6$ / $W(CO)_5(thf)$ ». 301

Appendix B: Decomposition of ^1H MAS solid state NMR spectra with Dmfit software.....305

Appendix C: Bar graphs obtained from TEM analyses of different non-promoted and Ni promoted catalysts. 309

Appendix D: IR and NMR spectra of samples obtained after contacting ethanol with SiO_{2-700}, Al_2O_{3-450}, and ASA_{-300}. 317

Appendix E: Contributions W 4f des catalyseurs WS_2/ASA préparés par voie CSC ou conventionnelle (séchés ou calcinés), en fonction de la température de sulfuration 319

Appendix F: NiWS crystallites data 320

Appendix A: Tentative de dépôt sur ASA_{-300} de $W(CO)_6$ et d'un mélange « $W(CO)_6$ / $W(CO)_5(thf)$ ».

A.1. Dépôt de $W(CO)_6$ par imprégnation ou par voie CVD

Le dépôt de **tungstène (0) hexacarbonyle** $W(CO)_6$ a été réalisé par deux méthodes distinctes : une imprégnation à sec, et un dépôt par voie CVD (chemical vapour deposition).

Préalablement à l'imprégnation, des tests de solubilité de $W(CO)_6$ dans le toluène, le pentane et le cyclohexane ont montré que le cyclohexane était le plus approprié pour solubiliser le précurseur, avec une solubilité évaluée à 0,30 mol/L à chaud (90°C, reflux). Une double-imprégnation à chaud a été effectuée afin de maximiser la faible quantité de W déposée. Cette imprégnation a été réalisée suivant la procédure générale, décrite dans la partie expérimentale.

Pour la voie de préparation CVD, 3 méthodes ont été testées :

- la 1ère a été réalisée en mettant en contact des extrudés d'ASA_{-300} et le complexe moléculaire dans un réacteur sous vide statique (10^{-2} mbar), chauffé à 110°C durant 4 à 6h. Durant la manipulation, le précurseur cristallise dans la partie supérieure du réacteur, froide car située en dehors du four. En fin de manipulation, la couleur initiale des extrudés (blanc) n'a pas changé.

- la 2nd a été effectuée en mélangeant des extrudés (ASA_{-300}) et le précurseur dans une ampoule scellée sous 5 à 10 mbar d'argon, et placée 4 à 6h dans un four chauffé à 110°C. L'intérêt de cette méthode est de mettre en contact intime le support avec le précurseur pour favoriser le dépôt du métal sur la surface du support. En fin de manipulation, les extrudés d'ASA étaient blancs. Le dépôt sur alumine (Al_2O_{3-300}) a quant à lui permis d'obtenir des extrudés jaunes.

- la 3ème et dernière méthode utilisée est une méthode sous flux. Pour cette expérience, les extrudés n'ont pas été manipulés en conditions inertes. Cette manipulation comprend une première étape de traitement thermique du support à 500°C sous flux d'azote durant 10h, à 10 L/h, pour éliminer l'eau physisorbée. La seconde étape est le dépôt du précurseur chauffé à 90°C sous flux d'azote (± 2 L/h), qui traverse le lit d'extrudés maintenus à 100°C pendant 4h. Les extrudés obtenus sur ASA comme sur alumine étaient blancs.

A.2. Caractérisation des matériaux

Les analyses IR effectuées ont révélé que **$W(CO)_6$** ne se greffait ni sur la silice-alumine, ni sur l'alumine, mais **était physisorbé à la surface des supports**. Sur ASA, le spectre infrarouge du catalyseur préparé par imprégnation est identique à ceux des catalyseurs préparés par dépôt en phase vapeur. Les spectres IR (exemple, voir **Figure A.a**) montrent **trois bandes de vibration attribuées aux vibrations ν(CO) de à $W(CO)_6$ physisorbé** (ν_1 ≈ 2123 cm^{-1}, ν_2 ≈ 2020 cm^{-1}, ν_3 ≈ 1992 cm^{-1}). Un épaulement vers 1955 cm^{-1} est vraisemblablement attribuable à une forme $W(CO)_5$. Néanmoins, la présence d'espèces sub-carbonyles $W(CO)_x$, x < 6 comme $W(CO)_5$ ou $W(CO)_5L$, L étant un oxygène de surface, est toujours sujette à discussion dans la littérature.

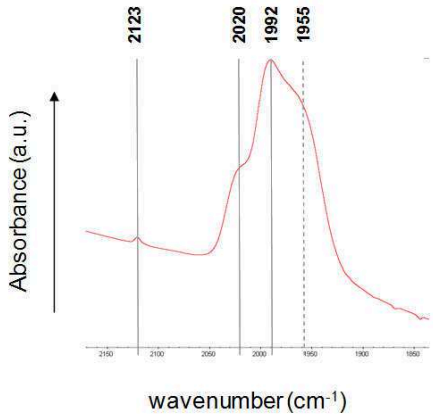

Figure A.a: Spectre IR (zone CO) d'un catalyseur préparé par double imprégnation sur ASA_{-300} de $W(CO)_6$ solubilisé dans le cyclohexane

Les travaux de modélisation moléculaire réalisés par Leydier [Thèse, Paris, 2012] ont permis de simuler en parallèle des configurations de $W(CO)_6$ physisorbé et chimisorbé sur un modèle théorique de surface d'ASA [Chizallet et Raybaud, 2009 ; Chizallet et Raybaud, 2010]. $W(CO)_6$ serait stable par physisorption sur des sites acides de Lewis ou acides de Brønsted. A titre d'illustration, la **Figure A.b** représente la configuration pour laquelle l'énergie d'adsorption entre le précurseur et un Al_{IV} est légèrement endothermique : +8 $kJ.mol^{-1}$. Toutes les tentatives pour greffer le complexe $W(CO)_5$ sur un oxygène de surface ont conduit à une énergie significativement plus défavorable (+154 $kJ.mol^{-1}$). Ce résultat est donc peu encourageant vis-à-vis du greffage de $W(CO)_6$ sur une surface d'ASA.

Appendix A : Tentative de dépôt sur ASA_{-300} de $W(CO)_6$ et d'un mélange « $W(CO)_6$ / $W(CO)_5$(thf) ».

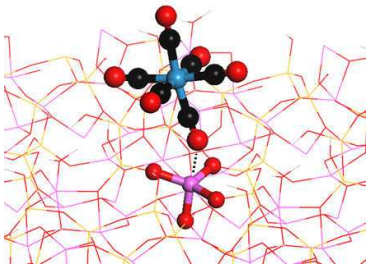

Figure A.b : Représentation de $W(CO)_6$ physisorbé sur un site acide de Lewis Al_{IV} (d'après Leydier, Thèse, Paris, 2012)

Les analyses IR des catalyseurs préparés par dépôt CVD de $W(CO)_6$/ASA dans un réacteur sous vide statique sont similaires à celles précédemment décrites.

Finalement, suite aux résultats peu encourageants obtenus pour le dépôt du précurseur sur ASA, les matériaux préparés sur alumine ont été analysés. Compte tenu des similitudes observées sur les spectres IR, il a été conclu que, dans les conditions expérimentales utilisées, l'emploi d'alumine comme d'ASA ne permettait que de physisorber le précurseur sur la surface du support.

Une tentative de sulfuration du matériau, préparé par double imprégnation de $W(CO)_6$ dans le cyclohexane, a révélé que le complexe préalablement physisorbé sur la surface se sublimait et cristallisait sur les parois du réacteur de sulfuration. Après sulfuration, l'impossibilité de quantifier le tungstène par XPS prouve que le complexe a totalement disparu durant la sulfuration, et n'a pas permis d'obtenir d'espèces de surface, sulfurées ou non.

En l'état, les travaux décrits dans la littérature (voir partie bibliographique) concernant le dépôt de $W(CO)_6$ n'ont pas pu être reproduits. Compte tenu de difficultés rencontrées par les auteurs et durant nos expériences, il semblait intéressant d'étudier un composé similaire à $W(CO)_6$, mais plus aisé à déposer comme $W(CO)_5$(thf). En effet, la meilleure labilité du ligand thf, proposée dans la littérature, est mise en évidence par les calculs DFT de Leydier (2012) : l'énergie nécessaire arracher un ligand carbonyle s'élève à environ +315 $kJ.mol^{-1}$ contre +153 $kJ.mol^{-1}$ pour un ligand tétrahydrofurane. La préparation et le dépôt de $W(CO)_5$(thf) ont donc été étudiés.

A.3. Préparation et dépôt sur ASA_{-300} d'une solution contenant $W(CO)_6$ et $W(CO)_5$(thf)

La préparation de $W(CO)_5$(thf) a été réalisée à partir d'un protocole décrit dans la littérature (Maeyama, K. and Iwasawa, N., *Journal of Organic Chemistry* (1998), **64**, 1344). Le précurseur moléculaire, $W(CO)_6$, mis en suspension dans un excès de thf (solution incolore), est irradié durant 10 minutes sous UV (lampe Hg) (3 répétitions) pour donner immédiatement une solution jaune. Des analyses RMN ^1H et $^{13}C\{^1H\}$ ont mis en évidence la présence de $W(CO)_5$(thf) mais $W(CO)_6$ reste significativement majoritaire (voir **Figure A.c**).

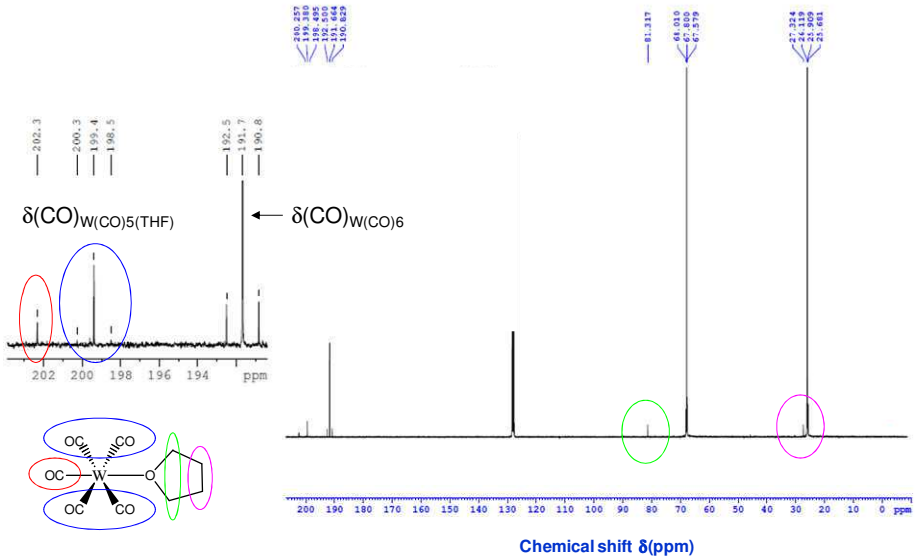

Figure A.c : Spectre $^{13}C\{^1H\}$ (298K, C_6D_6) de la solution obtenue par photo-irradiation de $W(CO)_6$ dans le thf.

Après imprégnation par excès de cette solution sur ASA_{-300}, les extrudés, lavés avec du thf, ont été sulfurés à 350°C (15 $\%_{mol.}$ H_2S/H_2, 2h). Aucune phase sulfure de W n'est observée en XPS. Les manipulations préliminaires révèlent donc que les dépôt/sulfuration de W ne sont pas significativement améliorés par l'emploi d'une solution de $W(CO)_6$ dans le thf, après 3x10 min d'irradiation sous UV. Compte tenu de ces résultats peu encourageants, l'utilisation de composés carbonylés n'a pas été approfondie.

Appendix B: Decomposition of ^{1}H MAS solid state NMR spectra with Dmfit software.

The ^{1}H spectrum of ASA_{-300} was decomposed with a good fit (sdev = 4.93) with a minimal number of sites: three peaks placed at *ca.* 0.5 ppm, 1.7 ppm and 3.0 ppm (see main text for details).

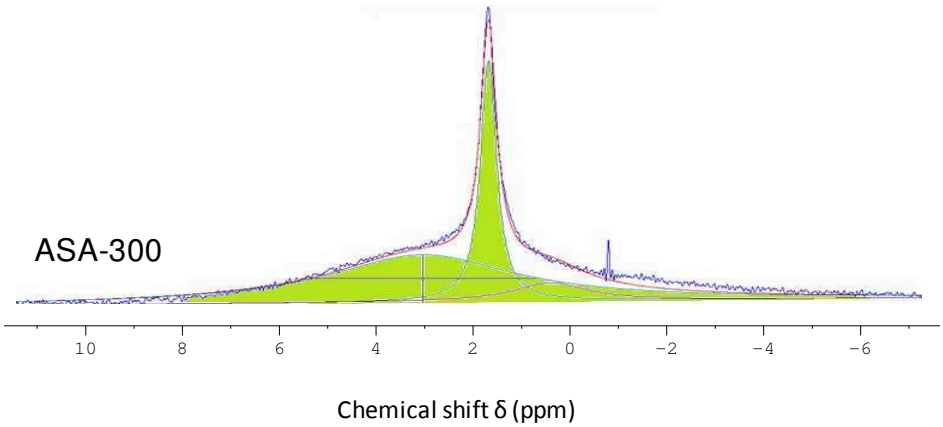

Data obtained with dmfit software:

#1 - SiOHn1"	"pos(ppm)"	1.7	"wid(ppm)"	0.4
#2 - SiOHn2	"pos(ppm)"	0.5	"wid(ppm)"	1.7
#3 - AlOH"	"pos(ppm)"	3.0	"wid(ppm)"	4.4

Model Integration:

#	Name	%
1	"SiOH n°1"	30.2
2	"SiOH n°2"	9.9
3	"AlOH"	59.9

For NMR spectra of the various $[W(OEt)_5]_2$-IWI-/ASA_{-300} materials, besides using the peak of silanols and aluminols described above for ASA_{-300}, additional peaks are introduced to include the signals associated with ethoxides bound to the ASA surface and these bound to tungsten.

Appendix B (continued): Decomposition of ^{1}H MAS solid state NMR spectra with Dmfit software.

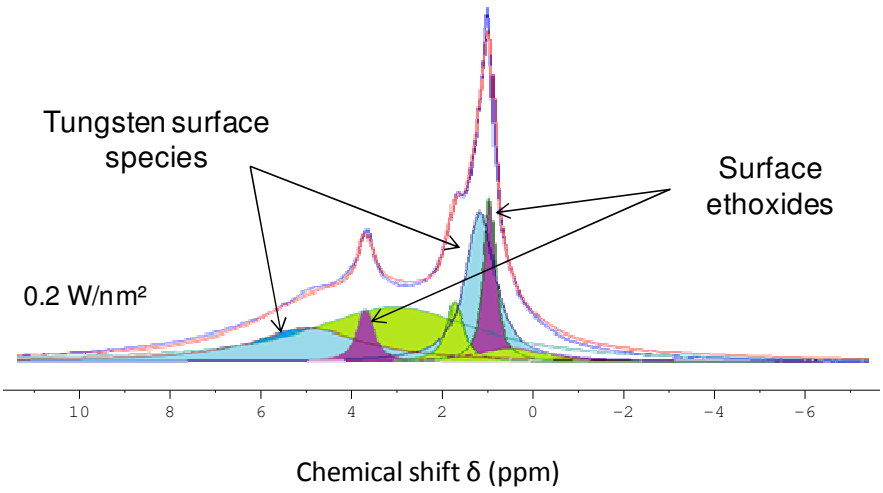

Data obtained with dmfit software:

#1 – SiOHn°1	"pos(ppm)"	1.8	"wid(ppm)"	0.4	
#2 – SiOHn°2	"pos(ppm)"	0.5	"wid(ppm)"	1.7	
#3 - AlOH	"pos(ppm)"	3.1	"wid(ppm)"	4.4"	
#4 - CH_3-C***H₂***-O-ASA	"pos(ppm)"	3.7	"wid(ppm)"	0.4	
#5 - CH_3-C***H₂***-O-W-O-ASA	"pos(ppm)"	5.0	"wid(ppm)"	3.0	
#6 - C***H₃***-CH_2-O-ASA	"pos(ppm)"	1.0	"wid(ppm)"	0.3	
#7 - C***H₃***-CH_2-O-W-O-ASA	"pos(ppm)"	1.2	"wid(ppm)"	0.8	

Model Integration:

#	Name	Peak Model	%	Intensity
1	"SiOHn°1"	"Gaus/Lor"	5.0	2268.2
2	"SiOHn°2"	"Gaus/Lor"	4.1	1869.6
3	"AlOH"	"Gaus/Lor"	38.1	17378.6
4	" CH_3-C***H₂***-O-ASA "	"Gaus/Lor"	4.4	2027.2
5	" CH_3-C***H₂***-O-W-O-ASA "	"Gaus/Lor"	17.2	7848.6
6	" C***H₃***-CH_2-O-ASA "	"Gaus/Lor"	9.5	4327.4
7	" C***H₃***-CH_2-O-W-O-ASA "	"Gaus/Lor"	21.6	9840.7

Decomposition process:

First, hydroxyles amplitudes were put at their maximum so as to maximize their quantity, especially for SiOH at *ca.* δ = 1.7 ppm. Then the others peaks were placed at their given chemical shift with an arbitrary width. At this point, only peak width and amplitude were allowed to be modified by the software. Positions were manually set at ± 0.1 ppm. After a first calculation by the software, width and amplitude were adjusted manually in order to respect the ratio CH_2 / CH_3 which should be close to 2 / 3. A tolerance of 10% was applied for this constraint. A similar constraint was applied to methylene and methyl protons assigned to each surface species, *e.g.* surface ethoxides and tungsten surface species. Little by little, the number of degree of freedom was diminished and calculations were run until reaching the 2 / 3 ratio expected.

Results obtained after ^{1}H NMR spectra decomposition by dmfit (peak position, peak width) are available in the following table:

	Assignment	0.2 W/nm²	0.2 W/nm²	0.2 W/nm²	0.5 W/nm²	0.6 W/nm²	0.7 W/nm²	0.8 W/nm²	1.7 W/nm²	Constraints
chemical shift δ (ppm)	SiOH 1	1.8	1.7	1.9	1.7	1.7	1.7	1.7	1,7	1.7 +/- 0.1
	SiOH 2	0.5	0.5	0.6	0.5	0.5	0.5	0.5	0.5	0.5 +/- 0.1
	AlOH	3.1	3.2	3.2	3.1	3,1	3.1	3.1	3,1	3.1 +/- 0.1
	CH3-***CH2***-O-ASA	3.7	3.7	3.8	3.7	3,7	3.7	3.7	3.8	3.7 +/- 0.1
	CH3-***CH2***-O-W-O-ASA	5.0	5.0	5.0	5.0	5.0	5.0	5.0	4.9	5.0 +/- 0.1
	CH3-CH2-O-ASA	1.0	0.9	0.9	0.9	0.9	0.9	0.9	1.0	0.9 +/- 0.1
	CH3-CH2-O-W-O-ASA	1.2	1.1	1.2	1.1	1.1	1.1	1.1	1.2	1.1 +/- 0.1
Peak width	SiOH 1	0.4	0.4	0.5	0.5	0.5	0.5	0.5	0.5	0.5 +/- 0.1
	SiOH 2	1.7	1.7	1.7	2.1	2.0	2.1	2.1	2.1	1.9 +/- 0.2
	AlOH	4.4	4.4	4.4	5.5	5.0	5.5	5.5	5.5	5.0 +/- 0.5
	CH3-***CH2***-O-ASA	0.4	0.6	0.7	0.5	1.0	1.0	1.0	0.8	0.7 +/- 0.3
	CH3-***CH2***-O-W-O-ASA	3.0	3.0	3.0	3.8	2.3	1.5	1.5	0.5	2.3 +/- 1.5
	CH3-CH2-O-ASA	0.3	0.5	0.8	0.8	0.8	1.2	1.2	1.1	0.7 +/- 0.5
	CH3-CH2-O-W-O-ASA	0.8	0.8	0.9	0.8	0.9	0.8	0.8	0.3	0.8 +/- 0.5

In the model, integration of each peak was given in %.

Calculation of the number of ethoxy ligand still linked to a W centre was deduced from the number of surface ethoxides. The number of surface ethoxides was calculated as follow:

$$N(ethoxy) = \frac{(CH_3CH_2 - O - ASA)CH_2}{CH_{2_{total}}} \times 5$$

where, if we take the example of the material with 0.2 W/nm², which data are available above:

- *N(ethoxy)* stands for the amount of ethoxides, bound to the surface
- *(*CH_3CH_2*-O-ASA)*CH_2 = 4.4, as calculated from CH_2 integration of CH_3CH_2-O-ASA species (δ = 3.7 ppm)

- CH_{2_total} = 4.4 + 17.2 = 21.6, as calculated from CH_2 integration of CH_3CH_2-O-ASA species (δ = 3.7 ppm) and CH_3CH_2-O-W-O-ASA species
- 5 represents the maximal amount of surface ethoxides which could be formed, considering 5 ethoxy ligands possibly released upon grafting of one W centre (only 5 ethoxy ligands are available on each tungsten centre in $[W(OEt)_5]_2$

Calculations gave *N(ethoxy)* = 1.0, which meant that the number of ethoxy ligands still linked to a W centre was *N(ethoxy on W)* = 5 – *N(ethoxy)* ⇔ ***N(ethoxy on W)* = 4.0**. Due to several uncertainties, a ± 0.5 approximation was added to each *N(ethoxy on W)* calculated.

The ratio $(CH_2 / CH_3)_{total}$ calculated as (4.4 + 17.2) / (9.5 + 21.6) was 0.70, which is close to 0.67, *e.g.* 2/3.

Calculation of the relative amount of free OH was performed as follow:

%free OH = %SiOHn°1 **+** %SiOHn°2 **+** %AlOH

Appendix C: Bar graphs obtained from TEM analyses of different non-promoted and Ni promoted catalysts.

Conventional calcined, 1.8 W/nm²
350°C (15 $\%_{mol.}$ H_2S/H_2)

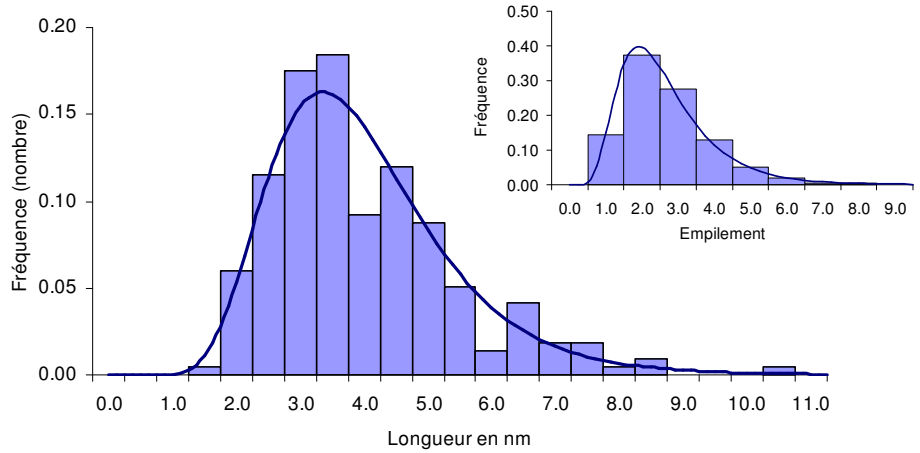

Conventional calcined, 1.8 W/nm²
600°C (15 $\%_{mol.}$ H_2S/H_2)

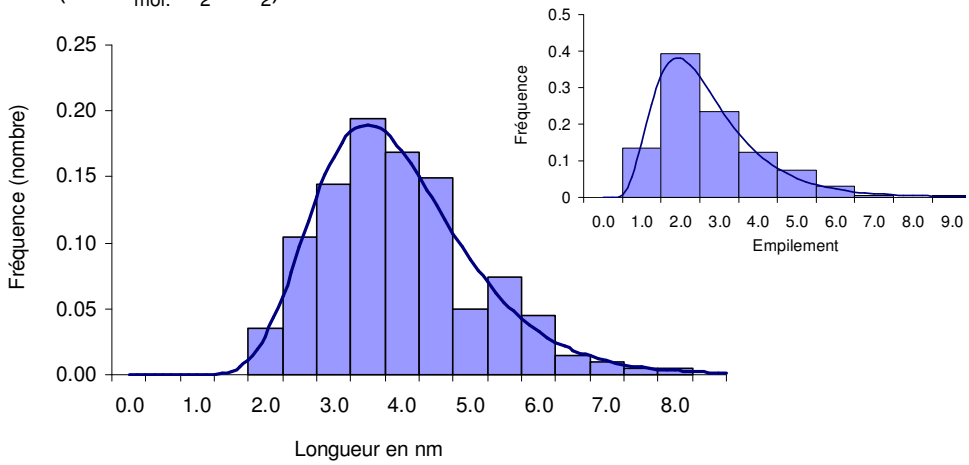

Conventional dried, 1.8 W/nm²
350°C (15 $\%_{mol.}$ H_2S/H_2)

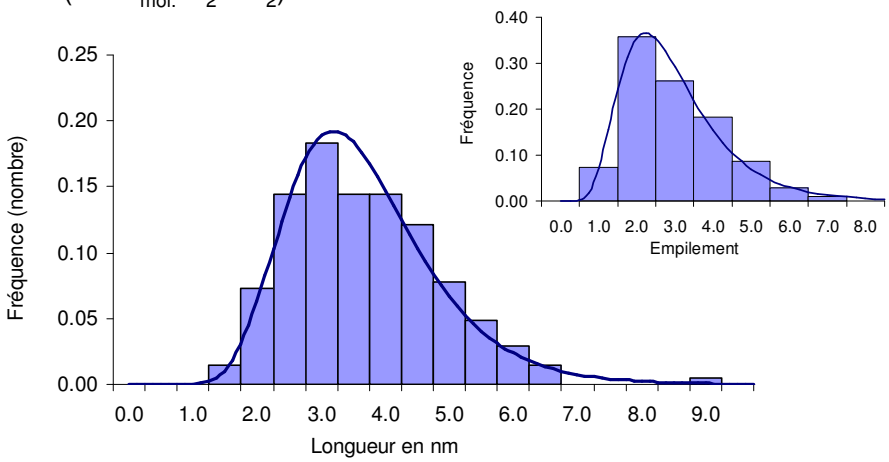

Conventional dried, 1.8 W/nm²
600°C (15 $\%_{mol.}$ H_2S/H_2)

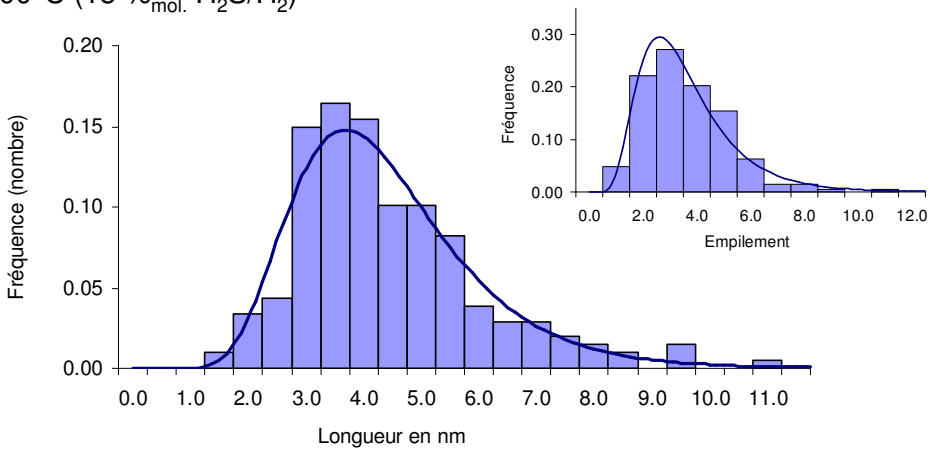

Appendix C (continued): Bar graphs obtained from TEM analyses of different non-promoted and Ni promoted catalysts.

Conventional calcined, 0.5 W/nm²
350°C (15 $\%_{mol.}$ H_2S/H_2)

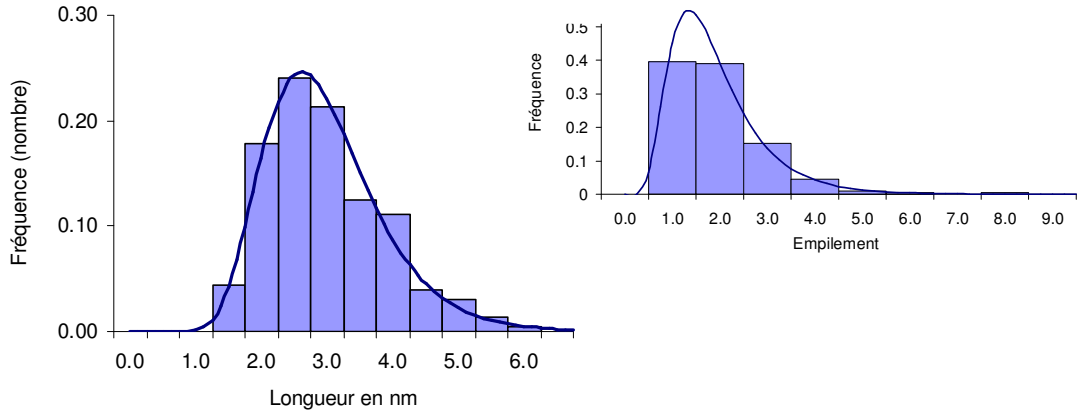

Conventional calcined, 3.7 W/nm²
350°C (15 $\%_{mol.}$ H_2S/H_2)

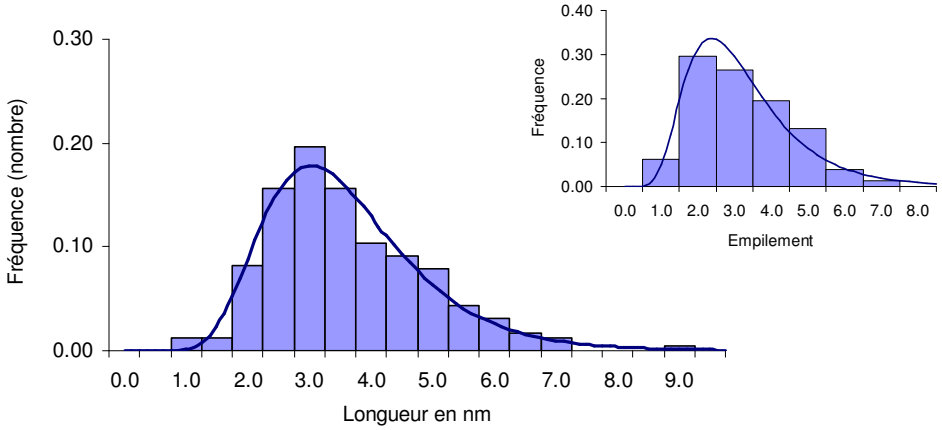

Appendix C (continued): Bar graphs obtained from TEM analyses of different non-promoted and Ni promoted catalysts.

Conventional dried, 0.5 W/nm²
350°C (15 $\%_{mol.}$ H_2S/H_2)

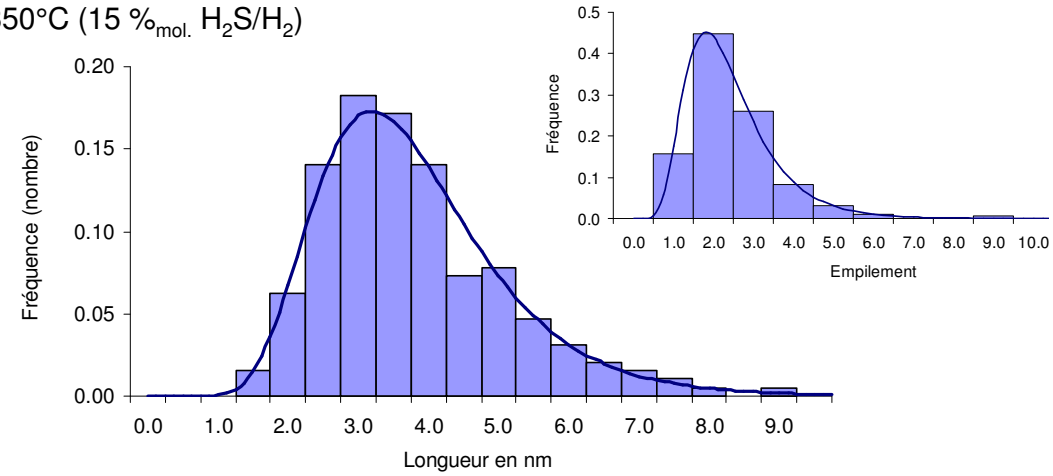

Conventional dried, 3.7 W/nm²
350°C (15 $\%_{mol.}$ H_2S/H_2)

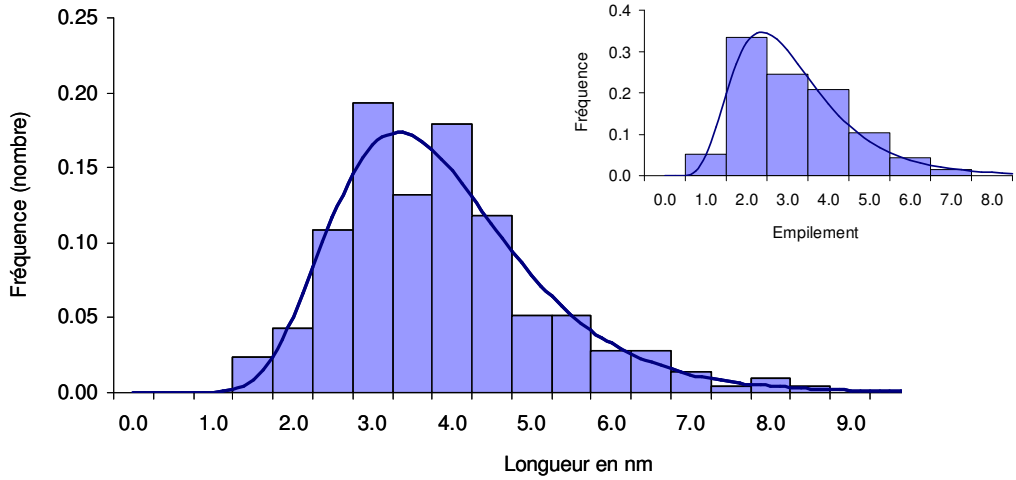

CSC 0.5 W/nm²
350°C (15 $\%_{mol.}$ H_2S/H_2)

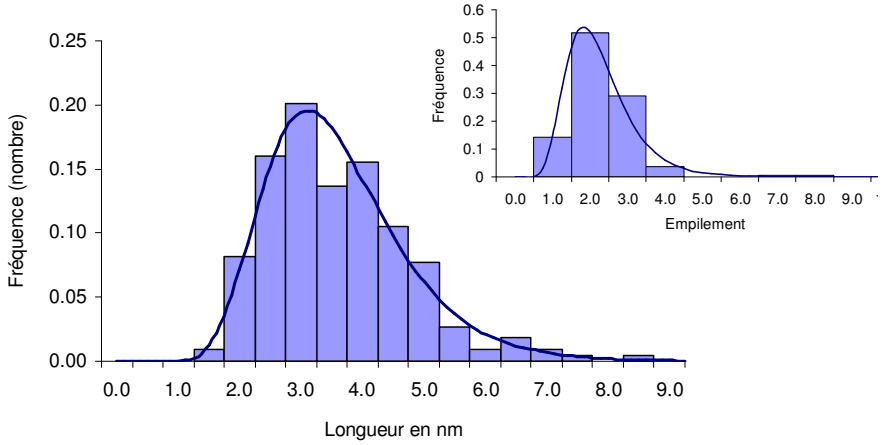

CSC 1.7 W/nm²
350°C (15 $\%_{mol.}$ H_2S/H_2)

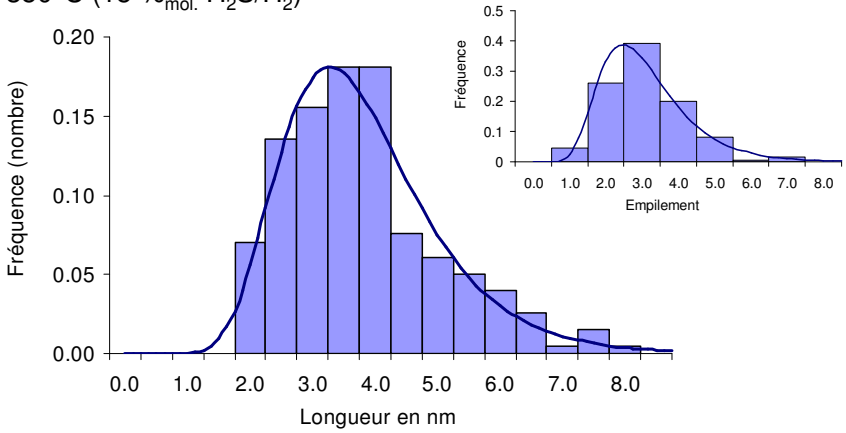

CSC 3.7 W/nm²
350°C (15 $\%_{mol.}$ H_2S/H_2)

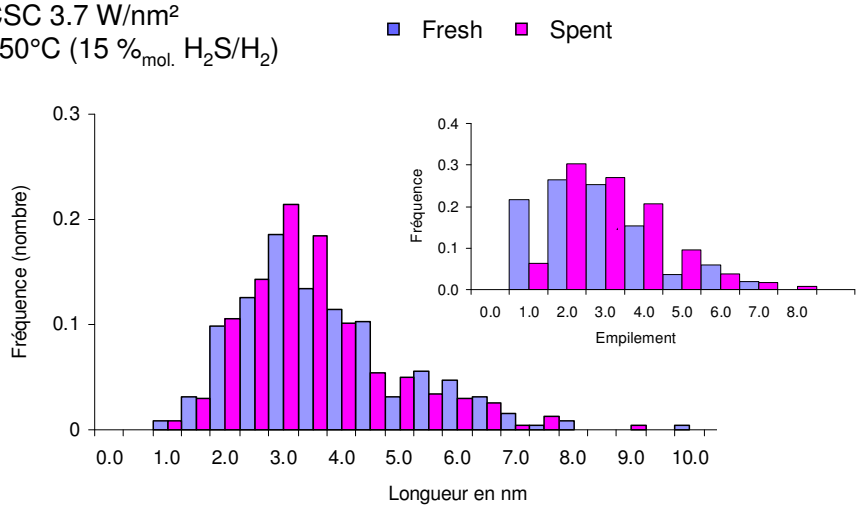

CSC 1.7 W/nm²
23°C (15 %mol. H_2S/H_2)

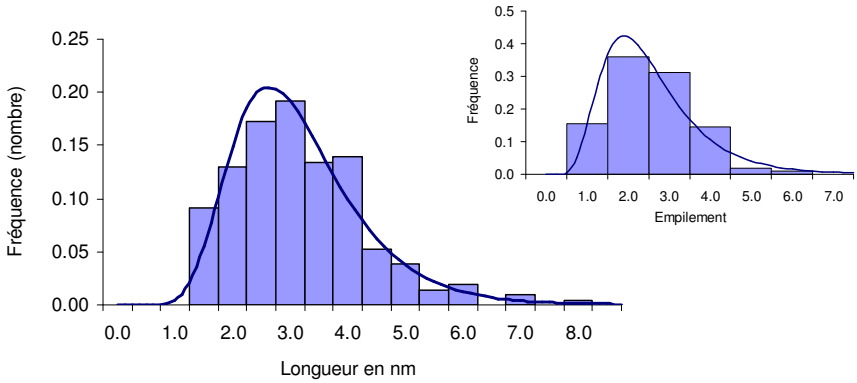

CSC 1.7 W/nm²
600°C (15 %mol. H_2S/H_2)

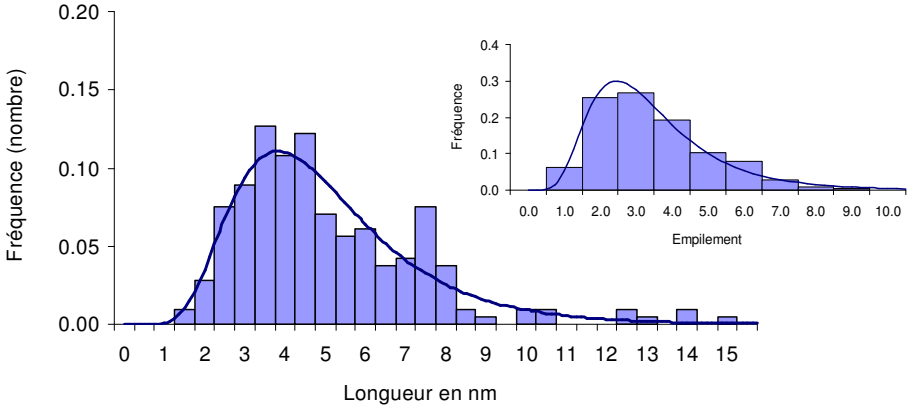

CSC NiWS *ex.* acac/$WS_{2\text{-}350°C}$/ASA
1.7 W/nm², Ni/W ≈ 0.2
350°C (15 $\%_{mol.}$ H_2S/H_2)

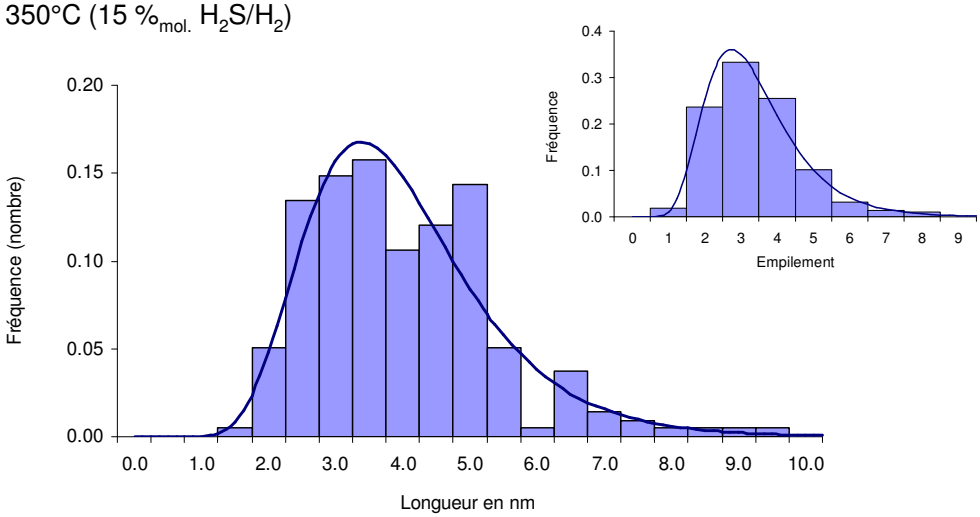

CSC NiWS *ex.* acac/$WS_{2\text{-}23°C}$/ASA
1.5 to 1.6 W/nm²
350°C (15 $\%_{mol.}$ H_2S/H_2)

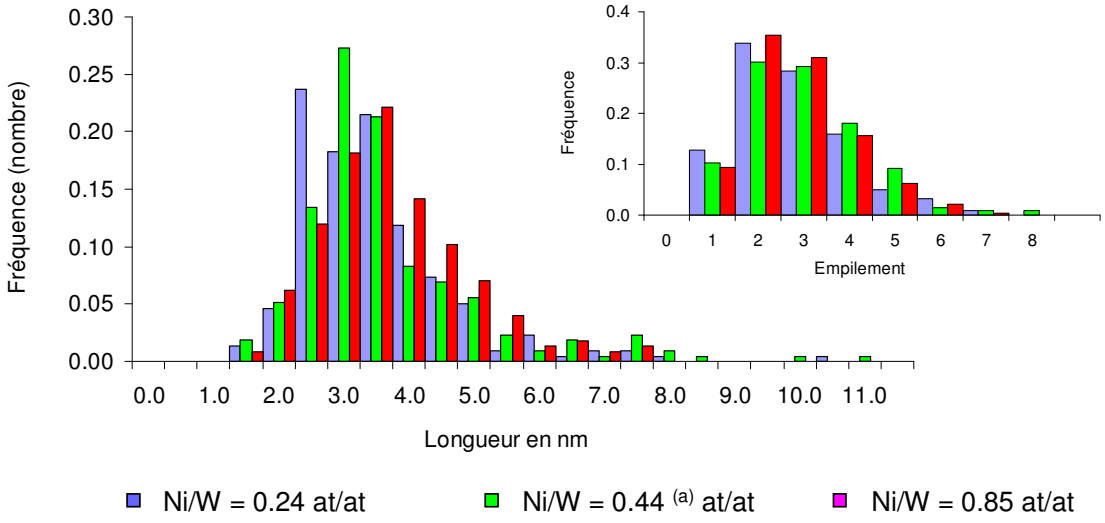

Ni/W = 0.24 at/at Ni/W = 0.44 [(a)] at/at Ni/W = 0.85 at/at

Note: [(a)] refers to a sample where the Ni content has to be confirmed by elemental analysis.

CSC NiWS *ex.* acac/$[W(OEt)_5]_2$/ASA
1.5 to 1.6 W/nm²
350°C (15 $\%_{mol.}$ H_2S/H_2)

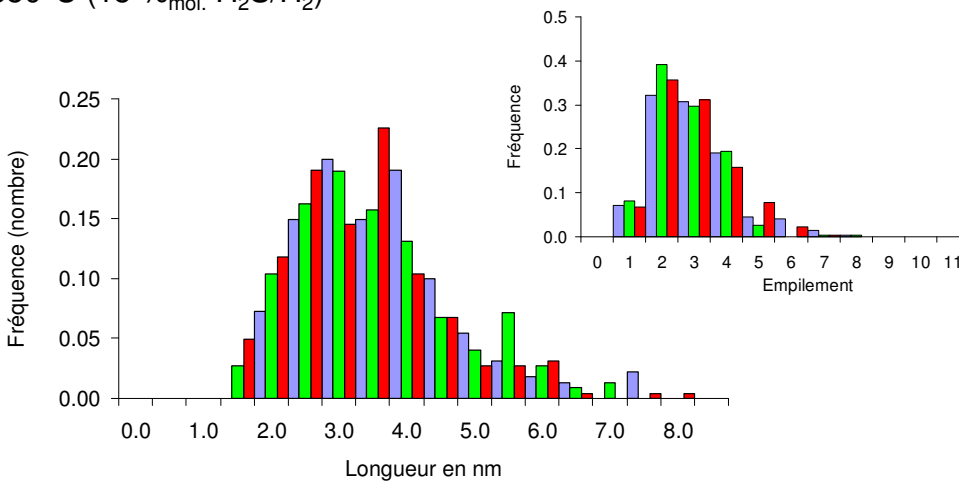

Ni/W = 0.21 at/at Ni/W = 0.44 at/at Ni/W = 1.00 at/at

Appendix C (continued): Bar graphs obtained from TEM analyses of different non-promoted and Ni promoted catalysts.

NiWS conventional dried

1.8 W/nm², Ni/W ≈ 0.22

350°C (15 $\%_{mol.}$ H_2S/H_2)

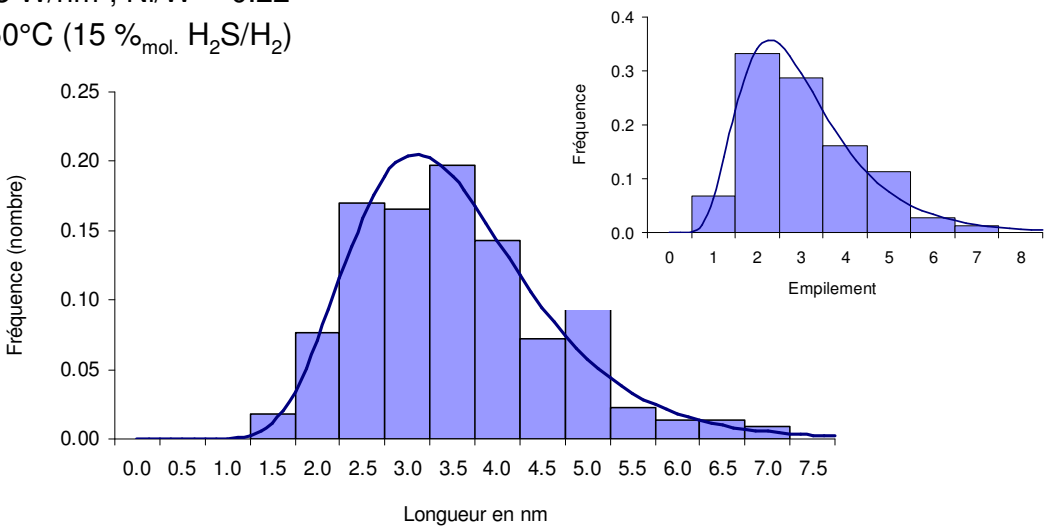

NiWS conventional calcined

1.8 W/nm², Ni/W ≈ 0.22

350°C (15 $\%_{mol.}$ H_2S/H_2)

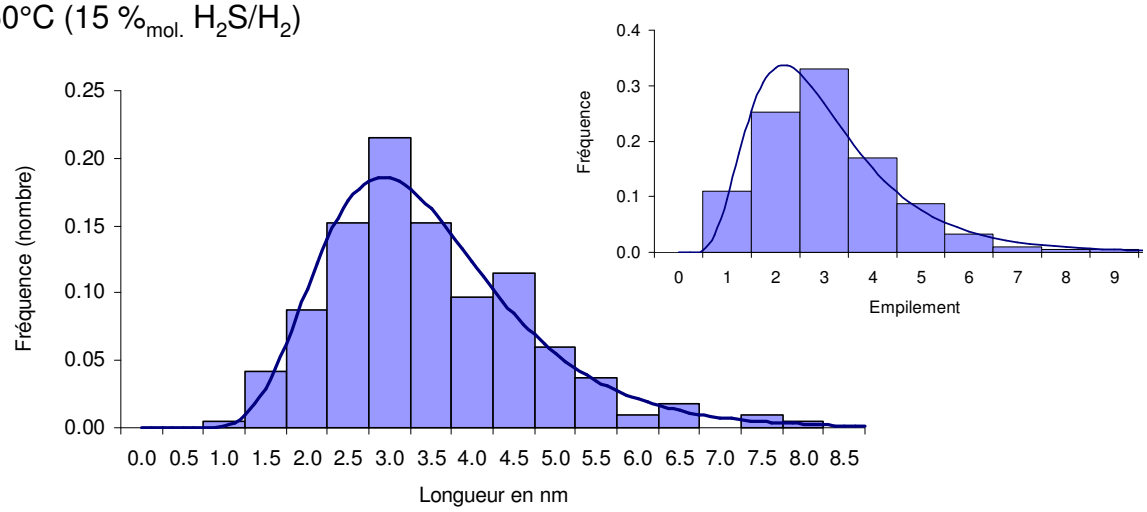

Appendix D: IR and NMR spectra of samples obtained after contacting ethanol with $SiO_{2\text{-}700}$, $Al_2O_{3\text{-}450}$, and $ASA_{\text{-}300}$.

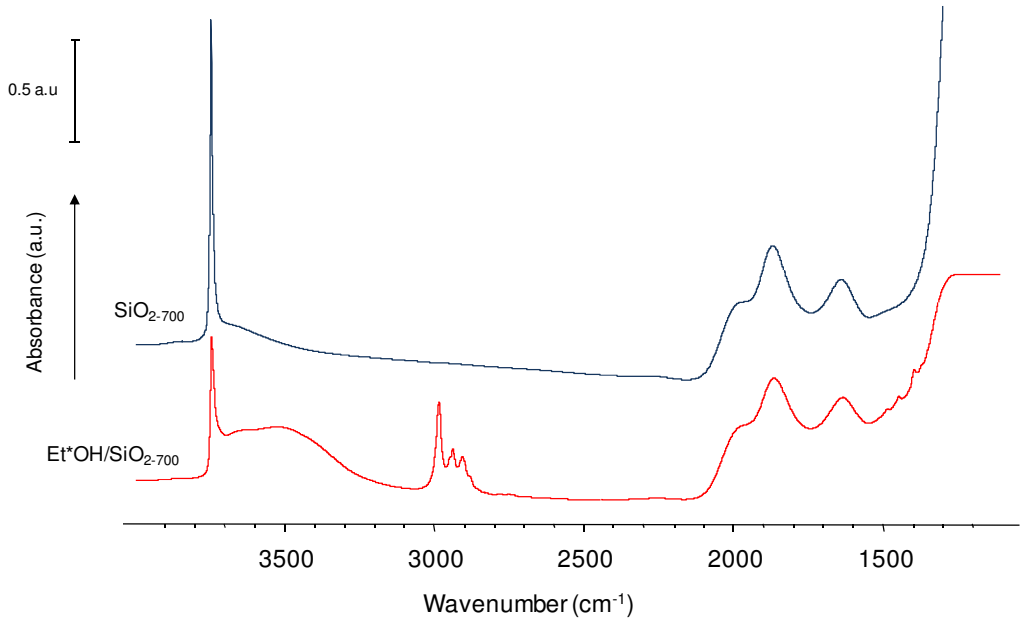

Figure D.a: IR spectra of $SiO_{2\text{-}700}$ and EtOH/$SiO_{2\text{-}700}$

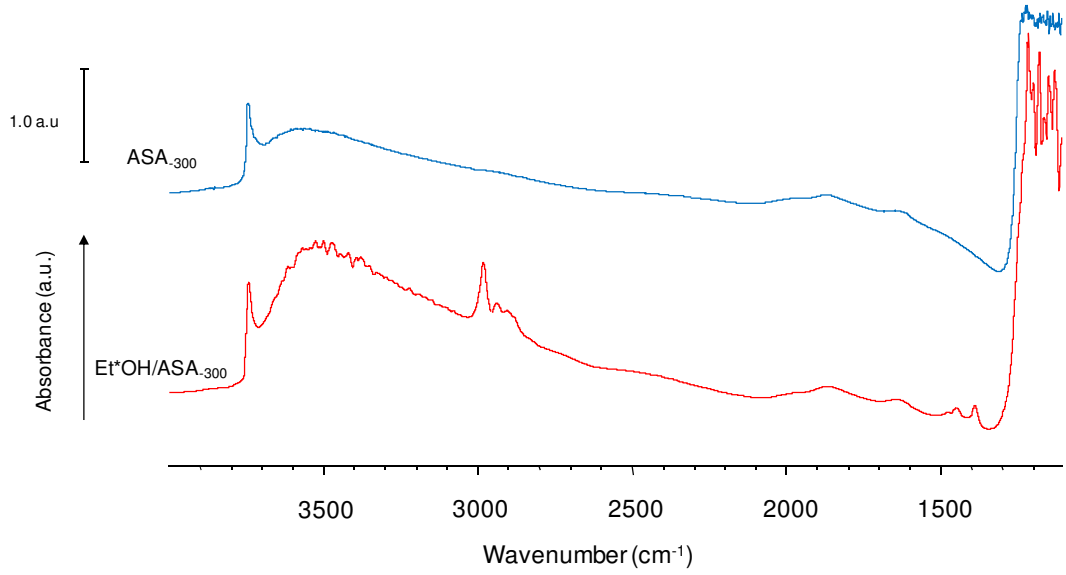

Figure D.b: IR spectra of $ASA_{\text{-}300}$ and Et*OH/$ASA_{\text{-}300}$

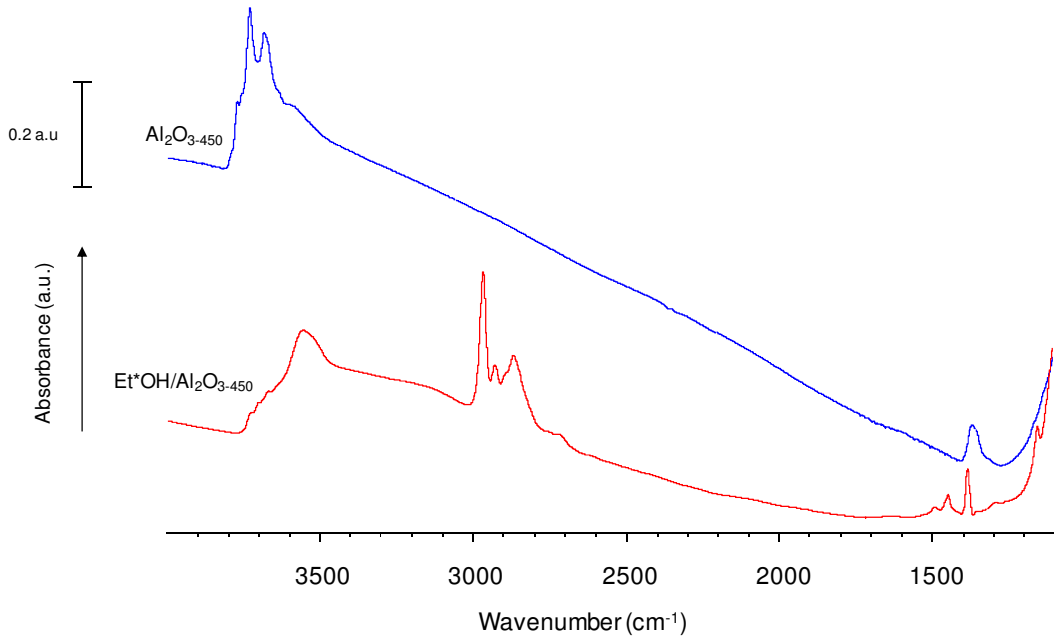

Figure D.c: IR spectra of $Al_2O_{3\text{-}450}$ and Et*OH/$Al_2O_{3\text{-}450}$

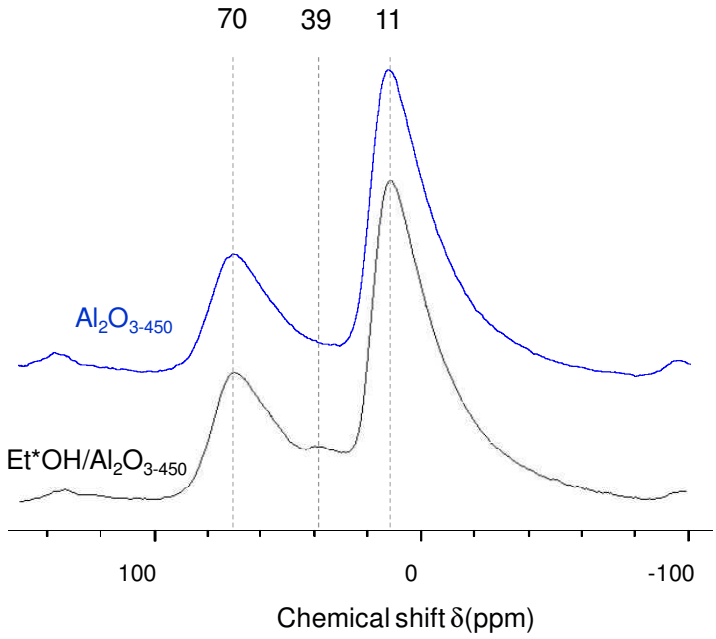

Figure D.d: ^{27}Al CPMAS Solid-State NMR spectra of $Al_2O_{3\text{-}450}$ and Et*OH/$Al_2O_{3\text{-}450}$

Appendix E: Contributions W 4f des catalyseurs WS_2/ASA préparés par voie CSC ou conventionnelle (séchés ou calcinés), en fonction de la température de sulfuration

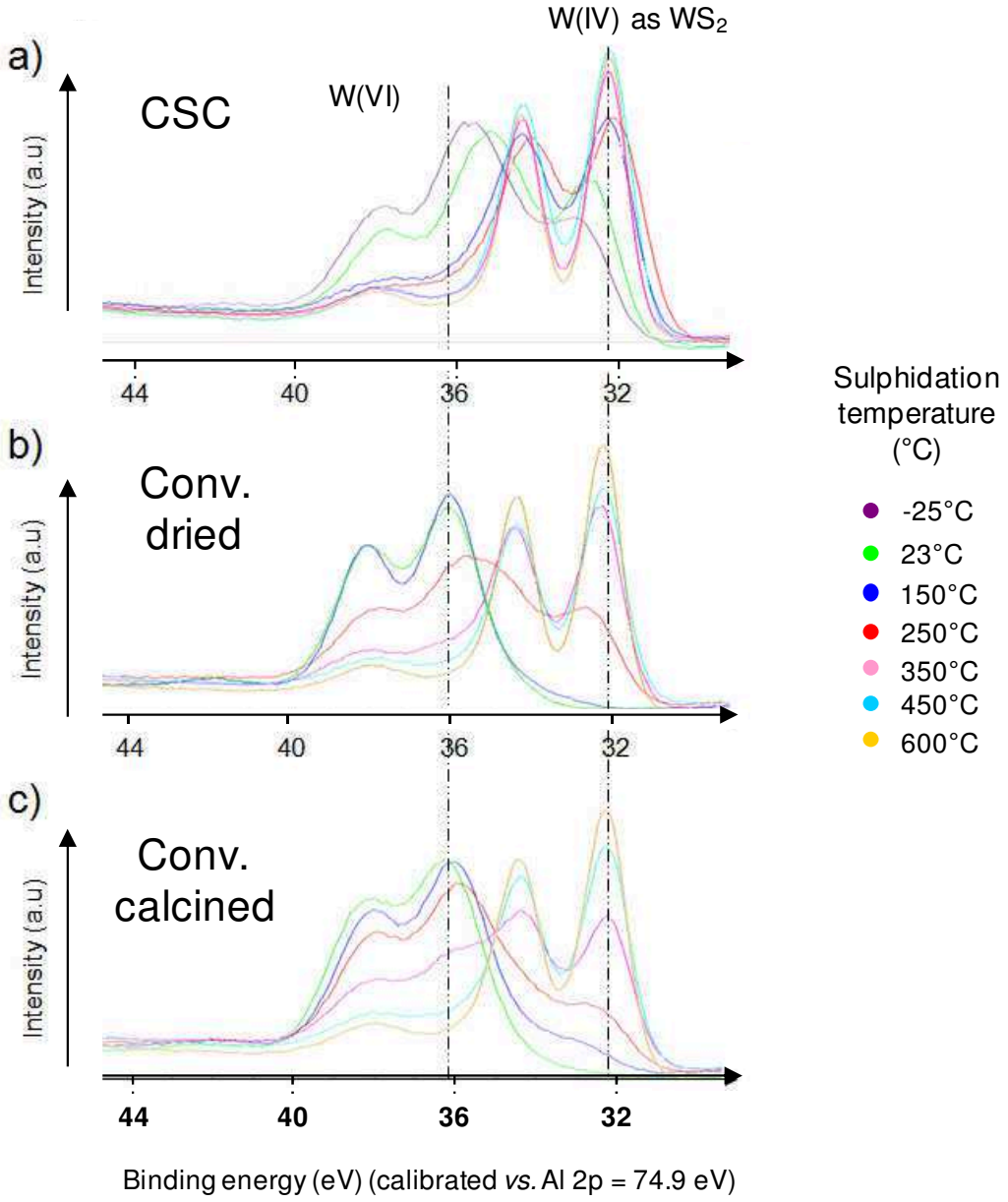

Appendix F: NiWS crystallites data.

Table F.a: NiWS crystallites data obtained from calculations based on geometrical models and theoretical values of (Ni/W)slab.

Experimental Ni/W (at/at)	Length L from TEM (Å)	Length L' from the model (Å)	*nM*	*nS*	$(Ni/W)_{slab}$ *(theo.)*	(number W atom)$_{total}$ for one slab	% W-edge [a]	% edge sites [b]	X_{subst} (%)
0.20	40	41	8	5	0.37	145	64	26.9	100
0.20	40	41	8	5	0.30	145	64	26.9	86
0.20	40	41	7	6	0.36	147	54	26.6	100
0.20	40	41	7	6	0.30	147	54	26.6	87
0.20	37	38	8	4	0.30	123	70	29.2	79
0.20	37	38	8	4	0.40	123	70	29.2	98
0.20	37	38	7	5	0.30	127	60	28.5	81
0.20	37	38	7	5	0.40	127	60	28.5	100
0.44	35	35	7	4	0.30	107	67	31.0	74
0.44	35	35	7	4	0.40	107	67	31.0	92
0.44	35	35	7	4	0.45	107	67	31.0	100
0.44	35	35	6	5	0.30	109	56	30.4	76
0.44	35	35	6	5	0.40	109	56	30.4	94
0.44	35	35	6	5	0.44	109	56	30.4	100
1.00	33	32	6	4	0.30	92	63	33.0	70
1.00	33	32	6	4	0.40	92	63	33.0	87
1.00	33	32	6	4	0.49	92	63	33.0	100
1.00	33	32	5	5	0.30	93	51	32.6	71
1.00	33	32	5	5	0.40	93	51	32.6	88
1.00	33	32	5	5	0.48	93	51	32.6	100

[a] Calculated from the number of W atoms on W-edge, relative to the total number of W atoms on edges (W-edge + S-edge)

[b] Calculated from the number of W atoms on W-edge, S-edge and corners, relative to the total number of W atoms in one slab.

Table F.b: NiWS crystallites data obtained from calculations based on geometrical models and experimental values of (Ni/W)slab, obtained from XPS analyses of spent catalysts.

	Experimental Ni/W (at/at)	Length L from TEM (Å)	Length L' from the model (Å)	*nM*	*nS*	$(Ni/W)_{slab}$ *(exp.)*	(number W atom)$_{total}$ for one slab	% W-edge [a]	% edge sites [b]	X_{subst} (%)
ex. acac/$WS_{2\_350°C}$	0.20	40	41	8	5	0.17	145	64	26.9	54
	0.20	40	41	7	6	0.17	147	54	26.6	55
ex. acac/$[W(OEt)_5]_2$	0.20	37	38	8	4	0.30	123	70	29.2	79
	0.20	37	38	7	5	0.30	127	60	28.5	81
	0.44	35	35	7	4	0.40	107	67	31.0	92
	0.44	35	35	6	5	0.40	109	56	30.4	94
	1.00	33	32	6	4	0.39	92	63	33.0	85
	1.00	33	32	5	5	0.39	93	51	32.6	86
Conv. dried	0.22	36	35	7	4	0.23	107	67	31.0	60
	0.22	36	35	6	5	0.23	109	56	30.4	62
Conv. calcined	0.22	36	35	7	4	0.27	107	67	31.0	69
	0.22	36	35	6	5	0.27	109	56	30.4	70

[a] Calculated from the number of W atoms on W-edge, relative to the total number of W atoms on edges (W-edge + S-edge)

[b] Calculated from the number of W atoms on W-edge, S-edge and corners, relative to the total number of W atoms in one slab.

Résumé

L'enjeu de cette thèse réside dans la compréhension et l'amélioration de la sulfuration de catalyseurs à base de W. Elle a pour objectif la rationalisation des différentes étapes de préparation de catalyseurs d'hydrotraitement de type NiWS depuis la préparation jusqu'au test catalytique par une approche moléculaire (appelée «chimie de surface contrôlée» ou CSC), ce qui permet de proposer de nouvelles voies pour lever le verrou majeur, lié à la mauvaise sulfuration du W. Au cœur de cette approche se situe l'utilisation d'une méthode de préparation originale, ayant recours à des composés moléculaires métallo-organiques bien-définis comme précurseurs de la phase sulfurée WS_2, combinée à une analyse poussée par spectroscopies multiples (IR, RMN, XPS) et chimie computationnelle.

La famille des alcoxydes de tungstène a été sélectionnée ; les précurseurs mono ou di-nucléaires tels que $W(OEt)_6$, $[W(=O)(OEt)_4]_2$ ou $[W(OEt)_5]_2$ ont été greffés sur silice-alumine partiellement deshydroxylée, et leur conversion en phase sulfure a montré que le type de précurseurs moléculaires influençaient peu les propriétés des catalyseurs non promus (WS_2/ASA), en termes de taux de sulfuration (déterminé par XPS) ou d'activité catalytique, en hydrogénation du toluène en présence d'aniline. Le composé $[W(OEt)_5]_2$ a ensuite été sélectionné pour approfondir l'étude des catalyseurs préparés par CSC.

L'approche visant à améliorer la compréhension des différentes espèces de surface formées a été réalisée par l'étude des matériaux avant et après sulfuration. L'augmentation de la quantité de W déposé sur les matériaux CSC a permis de révéler la formation de (1) une couche d'espèces greffées sur la surface de silice-alumine, puis (2) de couches successives, formées d'espèces plus mobiles. L'étude portant sur la sulfuration de ces matériaux en fonction de leur teneur en W, et de la température de sulfuration, a permis de les comparer aux catalyseurs sulfurés dits «conventionnels». Cette étude approfondie a mis en évidence une amélioration de la sulfuration du W pour les matériaux CSC aux températures habituellement utilisées (350°C). La vitesse intrinsèque d'hydrogénation des catalyseurs CSC, jusqu'à deux fois supérieure à celle des catalyseurs conventionnels, a en partie été expliquée par un meilleur taux de sulfuration, et par la morphologie 2D des feuillets WS_2 (STEM-HAADF), de forme triangulaire tronquée, dans le cas d'un catalyseur conventionnel.

Finalement, ayant démontré que l'emploi d'espèces moléculaires mono et binucléaires permettait d'améliorer les catalyseurs non promus par rapport à l'approche conventionnelle utilisant des clusters polyanioniques, les catalyseurs promus de type NiW/ASA ont été étudiés. Différents précurseurs ont été utilisés (par exemple $Ni(acac)_2$) ainsi que différentes méthodes de dépôt (dépôt du nickel sur un matériau sulfuré, ou non) et quantités de nickel. Ces travaux ont permis d'estimer l'influence de ces paramètres sur la sulfurabilité du W et du Ni, ainsi que sur l'activité catalytique des catalyseurs, et montrer que l'emploi d'une approche moléculaire dans la préparation des phases NiWS supportées permet d'améliorer la promotion des feuillets sulfures par le nickel, mais aussi d'accéder à des catalyseurs pouvant avoir des vitesses intrinsèques d'hydrogénation quatre fois supérieures celles de catalyseurs conventionnelles de référence. Ces résultats catalytiques sont très probablement liés à une balance optimisée entre «nature» et «quantité» de sites actifs mixtes Ni-W. Cela démontre l'intérêt d'une approche moléculaire pour la préparation de catalyseurs d'hydrotraitement plus performants.